



MONASH University

*Performance Enhancement of Two-Phase Closed Thermosyphon via
Carbon-Based Surface Functionalization*

Tong Wei Li

B. Eng. (Mechanical, Hons), M. Eng. Sc. (Res)

Monash University

A Thesis Submitted for the Degree of Doctor of Philosophy at
Monash University in 2016
School of Engineering

Under the Copyright Act 1968, this thesis must be used only under the normal conditions of scholarly fair dealing. In particular no results or conclusions should be extracted from it, nor should it be copied or closely paraphrased in whole or in part without the written consent of the author. Proper written acknowledgement should be made for any assistance obtained from this thesis.

I certify that I have made all reasonable efforts to secure copyright permissions for third-party content included in this thesis and have not knowingly added copyright content to my work without the owner's permission.

© Tong Wei Li 2016

Contents

Abstract.....	v
Declaration.....	viii
Acknowledgements.....	ix
List of Publications	x
1 Introduction	1
1.1 Two-phase closed thermosyphon	1
1.2 Surface wettability on phase-change heat transfer	3
1.2.1 Surface functionalization for enhanced evaporation.....	4
1.2.2 Surface functionalization for enhanced condensation	8
1.3 Research objectives and chapter outline	12
2 Literature Review	15
2.1 Nanofluid.....	15
2.2 Graphene, the future material.....	17
2.2.1 Synthesis of graphene and its derivatives	18
2.3 Graphene heat transfer	24
2.3.1 Graphene heat spreaders.....	27
2.3.2 Thermal interface materials	30
2.4 Graphene oxide and reduced graphene oxide nanofluids	31
2.5 Water permeation in graphene oxide.....	35
2.6 Phase-change heat transfer enhancement with fast water permeation of graphene derivatives	39
3 Coupled effects of hydrophobic layer and vibration on thermal efficiency of two-phase closed thermosyphons.....	41

4	Enhanced Evaporation Strength through Fast Water Permeation in Graphene-Oxide Deposition	66
5	Effective phase-change heat transfer through graphene-oxide surface functionalization	94
6	Effective phase-change heat transfer <i>via</i> graphene nanoplatelets coating in two-phase closed thermosyphon....	124
7	Conclusions and future work	158
	7.1 Conclusions	158
	7.2 Recommendations for future work.....	160
	References	162
	Appendix A	175
	Appendix B	185

Performance Enhancement of Two-Phase Closed Thermosyphon *via* Carbon-Based Surface Functionalization

Tong Wei Li

[REDACTED]

Supervisors:

A/Prof. Hung Yew Mun

[REDACTED]

Dr Tan Boon Thong

[REDACTED]

Abstract

Formidable challenges have been posed to the thermal management community in developing effective heat dissipation devices due to the exponential growth in heat generation of miniaturized electronics devices. With the continuous development of advanced microprocessors, convective phase-change heat transfer devices are insufficient to overcome the aggressive growth in heat generation in the coming future. Addressing the problem, extensive studies have been conducted to enhance the phase-change heat transfer *via* surface functionalization which facilitates effective evaporation and condensation. In general, hydrophilic surface is well-recognized to promote filmwise evaporation while dropwise condensation is observed across hydrophobic surface.

In this thesis, experimental studies were conducted with the objective of enhancing the thermal performance of a two-phase closed thermosyphon (TPCT) by exploring various innovative techniques through surface functionalization. The study begins with the circulation enhancement of the condensates by coating a hydrophobic thin film (Teflon AF-1600) on the condenser surface. Imperative information was obtained from the exposition of the size and distribution of condensate droplets in the analysis of the circulation effectiveness. The coupled effects of high acceleration induced vibration with the hydrophobic layer on the thermal performance of a TPCT

were also investigated. Interestingly, we observe that the formation of elongated liquid jets and the entrainment of droplets induced by the high-acceleration vibration counteract the enhancing effect from the increased body force of the condensed droplets.

In a separate study, graphene-oxide (GO) nanofluid was utilized as working fluid in TPCT to enhance its strength of evaporation. Surface morphology of GO layer inherently deposited on the evaporator surface was investigated. The consensus of high thermal conductivity nature of GO was demonstrated to be inadequate to explain the anomalous performance enhancement of TPCT. Water molecules are able to permeate through the nanocapillaries in GO deposition with ultralow friction. The thermal performance enhancement is primarily attributed to the water permeation across GO deposition which extends the effective evaporating region, leading to a significant increase in the evaporator heat transfer coefficient. To gain further insights in the water permeation effect, we analysed the dynamic behaviour of a droplet vaporizing on a GO-coated surface under various boiling regimes. The nanocapillaries embedded within the GO-coating provide effective dissipation channels for the vapour water molecules. Rapid transition of boiling regimes from transition boiling to contact boiling of a droplet vaporizing on GO-coated surface was observed. At high surface temperature, the Leidenfrost state was suppressed due to the water permeation effect across GO-coating. A significant increase of Leidenfrost point was obtained. The underlying physical mechanism of rapid water permeation was scrutinized to elucidate the outstanding capability of GO-coating in suppression of Leidenfrost state.

An unprecedented approach in enhancing the thermal performance of TPCT was also demonstrated with the introduction of graphene nanoplatelets (GNPs) thin film. GNPs-coating with high water permeability was coated on the inner wall of TPCT, forming a continuous layer across the evaporator and the condenser sections. Exceeding the water permeability of GO-coating, GNPs-coating with its implicit characteristic of rapid water permeation significantly augments the evaporation, condensation and circulation processes which govern the operation of TPCT. The optimized ratio of non-oxidized to oxidized regions endows GNPs-coating with excellent water permeability. Water molecules intercalating through the layered structure of GNPs-coating experiences more frictionless flow to a greater extent compared to its counterpart of

GO-coating. Evaporation is enhanced with the induced thin film evaporation and the effective distribution of water molecules across GNP-coated evaporator surface for suppression of dryout. GNPs-coating is endowed with unique surface characteristics. The circulation of condensates is enhanced through rapid water permeation while the nucleation of condensed droplets is promoted by its hydrophilic surface characteristic. The unique fast water permeation of functionalized graphene-based coating is appealing for practical implementation in effective phase-change thermal management systems. This study paves the way for a promising start of employing fast water permeation property of graphene-based coatings in thermal applications.

Declaration

I hereby declare that this thesis contains no material which has been accepted for the award of any other degree or diploma at any university or equivalent institution and that, to the best of my knowledge and belief, this thesis contains no material previously published or written by another person, except where due reference is made in the text of the thesis.

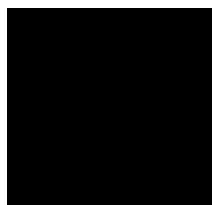
This thesis includes two original papers published in peer reviewed journals and two unpublished publications. The core theme of the thesis is performance enhancement of two-phase closed thermosyphon *via* carbon-based surface functionalization. The ideas, development and writing up of all the papers in the thesis were the principal responsibility of myself, the candidate, working within the School of Engineering under the supervision of A/Prof. Hung Yew Mun and Dr. Tan Boon Thong.

The inclusion of co-authors reflects the fact that the work came from active collaboration between researchers and acknowledges input into team-based research. In the case of Chapters 3-6 my contribution to the work involved the following:

<i>Thesis Chapter</i>	<i>Publication Title</i>	<i>Publication Status</i>	<i>Nature and Extent of Candidate's Contribution</i>
3	Coupled effects of hydrophobic layer and vibration on thermal efficiency of two-phase closed thermosyphons	Published	I was the chief investigator for this work. My contributions to this research were the design and fabrication of the experimental setup, conduct experiments, data analysis and preparation of manuscript.
4	Enhanced evaporation strength through fast water permeation in graphene-oxide deposition	Published	I was the chief investigator for this work. My contributions to this research were the design and fabrication of the experimental setup, conduct experiments, data analysis and preparation of manuscript.

I have renumbered sections of submitted or published papers in order to generate a consistent presentation within the thesis.

Student Signature:



Date: 1st June 2016

The undersigned hereby certify that the above declaration correctly reflects the nature and extend of the student's and co-authors' contributions to this work. In instances where I am not the responsible author I have consulted with the responsible author to agree on the respective contributions of the authors.

Main Supervisor Signature:



Date: 1st June 2016

Acknowledgements

I would like to extend my sincerest appreciation to A/Prof. Hung Yew Mun for his immeasurable support and dedicated mentoring throughout my Ph.D. candidature. His dedication to research, youthful passion to work and stunning positivity in life have become my inspiration. My accomplishments in the last four years would not be possible without his guidance. I am forever indebted for his indispensable advices and insights we gained in those infinite hours of brutal discussions. It is an honour to be part of this research team.

I would also like to thank Dr. Tan Ming Kwang, A/Prof. Chai Siang Piao and Dr. Kenny Tan for their continuous supports in my research. Their willingness to collaborate and to share years of research experiences has been crucial to my research completion. Special thanks go to Mr Ong Wee Jun, for his particular support in this cross-disciplinary collaboration – his knowledge in graphene and our cohesion in working together as a team are the key to this breakthrough.

Further, I want to thank my buddies – Anthony Tee, TeckWei Yeo and Adrian Yeo, for their endless encouragement in darkest moments of this research journey. Above all, to my family who offers warmth and complete trust that this research will see the light, I could not thank them enough. They have added meanings to my endeavour. I hope my achievements would make them proud. To my beloved Sing Li, her overwhelming love, trust and understanding have carried me through the times of loneliness, leading me to the completion of this important discovery. Last but not least, thank God for giving me the strength, hope, and courage of life.

Tong Wei Li

Monash University

June 2016

List of Publications

Journal papers

1. **Tong, W.L.**, Tan, M.K., Chin, J.K., Ong, K.S. & Hung, Y.M. Coupled effects of hydrophobic layer and vibration on thermal efficiency of two-phase closed thermosyphons. *RSC Advances* 5, 10332-10340 (2015).
2. **Tong, W.L.**, Ong, W.-J., Chai, S.-P., Tan, M.K. & Hung, Y.M. Enhanced evaporation strength through fast water permeation in graphene-oxide deposition. *Scientific Reports* 5, 11896 (2015).

Chapter 1

Introduction

1.1 Two-phase closed thermosyphon

Effective control and utilization of heat energy have been a constant challenge since the industrial revolution. Heat is both a welcome and unwelcome presence depending on the process at hand. In the case of electricity generation, heat conversion benefits many aspects in our daily life. On the other end of the spectrum, nuclear core damage arising from inadequate heat dissipation could threaten human lives. Heat is also a major pain point in ubiquitous electronic devices in modern society, and the quest for better, reliable and more effective thermal management systems is of the forefront of many research and development centres. The miniaturization of the high performance electronic components engenders exponential growth in power consumption, leading to an increase of operating temperature¹. The performance and the reliability are significantly reduced with the absence of an effective thermal management system. The pressing need is further emphasized with the projection of the exponentially increasing power density with the shrinking of the electronic devices². The thermal management system will be expected to dissipate greater heat energy with increasing compactness. To address the challenges above, thermal management systems operating on the principle of phase-change heat transfer have been widely utilized. These include the two-phase closed thermosyphon (TPCT), heat pipe, microchannel, jet impingement and spray cooling systems.

Out of all the thermal management systems, TPCT has been more commonly employed due to its effective heat transport capability, passive operation, and simplicity in design and operation^{3, 4}. Apart from the electronics cooling, TPCT is also found in the cooling of automobile engines, heat exchanger of solar heating systems, heat recovery in industrial refrigeration systems, and heat exchanger of chemical reactors^{3, 4}. Essentially, a basic TPCT consists of a tube filled with a working fluid in low-pressure

(vacuum) condition to reduce saturation temperature. The TPCT is divided into three sections: evaporator, adiabatic section, and condenser. It relies on the phase-change processes, namely evaporation and condensation, and the circulation of working fluid to function as heat transfer equipment (Figure 1.1). The heat applied to the evaporator section diffuses towards the liquid-vapor interface where it is taken up as the latent heat of evaporation by the liquid phase. The resultant vapor flows through the adiabatic section toward the condenser section, where the vapor condenses and the heat is dissipated to the surroundings. The condensate is then circulated back to the evaporator section *via* gravitational force and the cycle is perpetuated. Extensive studies on the operating characteristics of the TPCT have been conducted. The thermal efficiency of a TCPT is governed by several pertinent parameters such as the fluid properties and the filling ratio of the working fluid^{5, 6}, evaporator to condenser length ratio⁷, inclination angle⁸, operating limitations⁹ and the structure geometry¹⁰. On the other hand, the maximum heat transport capacity of a thermosyphon can be limited by a number of operating limitations such as burn-out or boiling limit, sonic limit and entrainment limit^{4, 11, 12}.

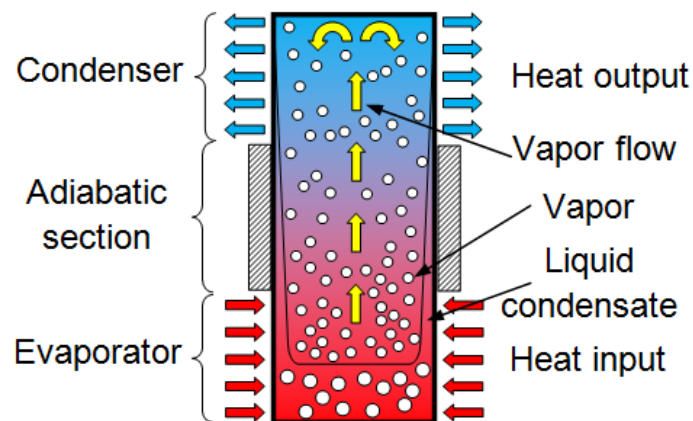


Figure 1.1| Schematic illustration of a TPCT working on the principle of phase-change heat transfer. The working fluid evaporates at the evaporator section and subsequently travels to the condenser section *via* thermal buoyancy. The liquid condensates then circulate back to the evaporator section through gravitational force.

In the practical operation, boiling limit and the entrainment limit determine the upper limits of the heat transport capability of the TPCT. The sustained evaporation of working fluid in a TPCT is replenished by the circulation of condensate from the

condenser section. A deficient circulation rate induces the occurrence of flooding at the condenser section, impeding the performance of TPCT. The flooding phenomenon in TPCT has been extensively investigated¹³⁻¹⁵. Major factors such as heat input, thermo-physical properties of the vapor, vapor velocity and the critical aspect ratio (defined as the radius over length) incur adverse effects on the circulation of the condensates^{14, 15}. Under high evaporation rate, extreme vapor velocity, and small critical aspect ratio, the countercurrent interfacial shear acting on the condensate surface prevents the circulation back to the evaporator. As a result, accumulation of condensate in the condenser greatly reduces the condensation heat transfer. The thermal efficiency of the TPCT operating beyond the entrainment limit significantly reduces. With the axial heat flux further increasing, the TPCT reaches its boiling limit with the depletion of working fluid in the evaporator section. The evaporator temperature exponentially increases with the formation of localized hotspots, hindering the operation of the TPCT. Thus, the operating limitations are vital considerations in the design of effective cooling system.

1.2 Surface wettability on phase-change heat transfer

The operation of the TPCT involves evaporation, condensation and the circulation of the working fluid. The continuity of the operating mechanisms is critical for the effective heat transfer across the TPCT^{3, 4}. The enhancement in either of the phase-change processes can result in the overall performance enhancement of the TPCT but only within a specific range of heat flux. For instance, enhancement in the strength of evaporation while maintaining the original condensation and circulation rates will result in the excessive accumulation of working fluid in the condenser, limiting the heat transfer at high heat flux condition. Thus, it is desirable that all operating mechanisms are simultaneously enhanced to maximize the overall performance of the TPCT. The surface wetting characteristics required for effective evaporation and condensation varies tremendously. Hydrophilic surface enhances evaporation while hydrophobic surface favours condensation. Surface wetting characteristic can be effectively manipulated with the introduction of micro/nanostructured surface to achieve either superhydrophilic/superwetting surface or superhydrophobic surface. Nevertheless, recent investigations showed that a two-tier hydrophobic and hydrophilic patterned surface provides better enhancements in evaporation as compared to a pure hydrophilic

surface¹⁶. Surprisingly, similar trend is obtained in the condensation enhancement with the combination of hydrophobic and hydrophilic networks¹⁷. It is therefore critical to understand the underlying working principles which promote the enhancement in evaporation and condensation. To elucidate such enhancements, the complex phase-change heat transfer processes will be discussed in detail in the following sections (section 1.2.1 & section 1.2.2). Evidently, phase-change heat transfer in both evaporation and condensation is significantly influenced by the surface wetting characteristic^{18, 19}. A minor enhancement in the surface characteristic in accordance with the respective surface wetting requirement can remarkably improve the heat transfer efficiency of the thermal management devices. In particular for the case of a TPCT, it is nearly impossible to accommodate both enhancements in evaporation and condensation with a single approach or using an identical functionalized surface. In general, enhancements in both evaporation and condensation of a TPCT often require separate surface treatments to obtain opposite wetting characteristics in the evaporator section and the condenser section²⁰. Furthermore, the practicality and fabricating limitations of incorporating micro/nanostructured surfaces into TPCT remains a significant bottle neck to the technological adoption. A more simplified, efficient approach is required to overcome the technological hurdles. The development of a single surface which favours both evaporation and condensation can severely impact the efficiency of various thermal management systems, not limited to the TPCT. Thus, this presents a tremendous challenge to the research society to search for a miracle material. Till date, none of the available materials or methods can be utilized to achieve both enhancements in evaporation and condensation with a single approach.

1.2.1 Surface functionalization for enhanced evaporation

It is well-recognized that hydrophilic surface facilitates the spreading of the liquid, resulting in the increase of the effective evaporation area. However, under pool boiling condition, the increased surface wetting can have detrimental effect on the vapour nucleation. Pool boiling refers to a mode of boiling where the heated surface is immersed in a stationary liquid²¹. As the temperature of the heated surface approaches the liquid saturation temperature, nucleation, growth and departure of vapour bubbles can be observed over the heated surface. This phenomenon in the pool boiling is also known as nucleate boiling. Nucleate boiling is responsible for the excellent phase-

change heat transfer in pool boiling. The variation in heat transfer of pool boiling is commonly illustrated with the boiling curve, as shown in Figure 1.2. The boiling curve relates the heat flux q with the wall superheat $T_w - T_{\text{sat}}$ whereby the wall superheat represents the temperature difference between the heated surface T_w and the liquid saturation temperature T_{sat} . Two major performance indicators can be derived from the boiling curve. Heat transfer coefficient (HTC) is calculated by dividing the heat flux with the wall superheat. Higher HTC indicates a greater heat transfer. On the hand, critical heat flux (CHF) represents the maximum heat flux prior to the formation of film boiling. As indicated in the boiling curve, the heat flux dramatically increases with the formation of vapour bubbles starting from point A to B, indicating the boiling regime of partial nucleate boiling. With the progressive increase of the wall superheat, the heat flux achieved its highest value at point C, also known as the CHF. Rapid nucleation and detachment of vapour bubbles can be observed under the fully developed nucleate boiling regime. In the design of effective boiling surface, high CHF is desirable as it indicates the suppression of the film boiling transition which reduces the efficient heat transfer. Further increase of the wall superheat triggers the momentary formation of vapour film. Under the transition boiling regime (from point C to D), coalesce of vapour bubbles forming momentary vapour film between the solid-liquid interface significantly impedes the heat transfer. The vapour film with ultra-low thermal conductivity forms thermal insulator which separates the solid-liquid contact. Reduction in the HTC can be noticed under the transition boiling regime. Unable to dissipate the heat energy, the wall superheat increases exponentially under constant heat flux (from point C to E). In practice, the rapid transition from nucleate boiling (point C) to film boiling (point E), skipping the transition boiling regime (point D) is often expected. The wall superheat in the film boiling regime is two orders of magnitude greater than that of the nucleate boiling regime, exceeding the melting temperature of most conventional metals. Such phenomenon of heat transfer restriction is often the sole reason of a nuclear disaster, also known as nuclear meltdown²². Thus, it is critical for any phase-change thermal management system to operate under its respective CHF to prevent overheating and system failure. To summarize, enhancing the nucleation of vapour bubbles increases the HTC while delaying the transition to film boiling increases the CHF. Surface characteristics which favour the nucleation of vapour bubbles and prevent the transition to film boiling are desirable for the development of effective heating surface.

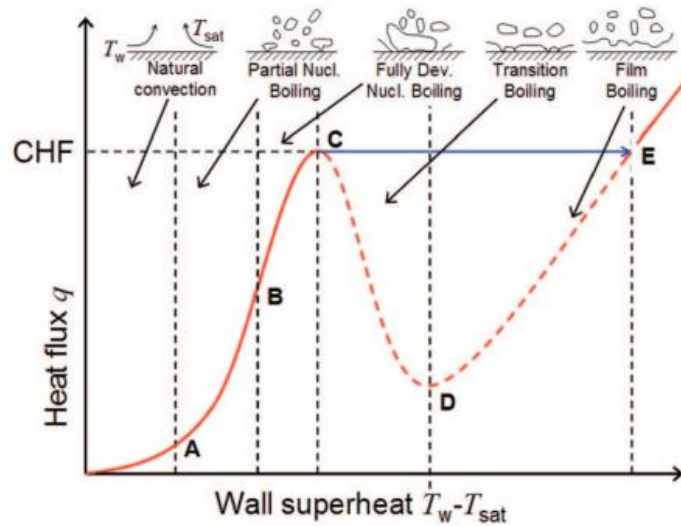


Figure 1.2] Boiling curve showing the variations in heat flux and vapour nucleation with respect to the increasing wall superheat (adapted from reference ²¹).

Extensive studies have been conducted on enhancing the boiling heat transfer. In particular of the nucleate boiling enhancement, various techniques which increase the surface wettability have been used. Apart from the aforementioned nanoparticles depositions^{23, 24}, high porosity surfaces²⁵⁻³³ also facilitate the nucleation of vapour bubbles with lower wall superheat. The enhancement of the nucleate boiling is attributed to the entrapment of gases in the porous medium or cavities^{21, 33-35}. In a recent study on macro-porous copper surface, the HTC increased by 17 times as compared to the reference roughed flat surface³³. High density nucleation of vapour bubbles was observed even at low heat flux of 1 W/cm². However, similar to the machined microgrooves on the copper plate^{36, 37}, the nucleate boiling enhancement in the porous mediums is only temporary with the flooding of the cavities after several heating cycles^{18, 28, 38}. As a result, the porous mediums are rarely accepted in the heat transfer industry due to its unpredictable reliability.

With the advancement in micro and nanostructures fabrication, new coating methods and materials have been utilized in the quest of delaying the transition to film boiling. A recent review regarding the pool boiling enhancement with nanostructured surfaces has been conducted³⁹. While the underlying mechanisms are yet to be conclusive, capillary pumping effect⁴⁰⁻⁴³, superwetting surface characteristic⁴⁴ and the extended effective heat transfer area⁴⁵ are believed to have contributed to the

augmentation of CHF. On the other hand, enhancement in the HTC can also be obtained over all nanostructured surfaces due to the entrapment of gasses in the cavities formed under the coating processes. Nanowires fabricated from copper^{41, 42}, silicon⁴¹ and carbon nanotubes⁴⁶⁻⁴⁸ showed overall enhancement in the pool boiling heat transfer. Regardless of the unprecedented augmentation in the HTC and CHF for both copper and silicon nanowires⁴¹, their superwetting characteristics remain a limitation to achieve onset of nucleation boiling at low wall superheat. It is well known that a hydrophobic surface promotes the onset of nucleation boiling but engenders the early transition to film boiling^{18, 34, 49}. Conversely, hydrophilic surface delays the transition to film boiling and also the onset nucleation boiling^{18, 34, 41}. Higher wall superheat is required for the occurrence of nucleation boiling with the increased surface wettability. Thus, it is desirable for a surface to possess both hydrophobic and hydrophilic wetting characteristics. In fact, the combination of hydrophobic and hydrophilic surfaces for boiling enhancement has been investigated with the enhancements of HTC and CHF by 100% and 65% as compared with a flat hydrophilic surface¹⁶. This justified that the hydrophobic areas are equally important in the boiling enhancement with the ability to enhance nucleation and departure of the vapour bubbles. Therefore, the common assumption of superwetting/superhydrophilic surface for excellent boiling enhancement will have to be re-evaluated. Notably, enhanced heat transfer *via* micro/nano fabrications have been experimentally demonstrated but remain incompatible due to the complex fabrication methods, surface contamination, and the reliability of the coating^{18, 19, 41, 42, 50}. A more simplified approach is in urgent need to address the overwhelming heat dissipation problem.

Recently, the discovery of graphene has attracted substantial interest in developing potential graphene-based applications. The high thermal conductivity nature of graphene has been positioned as a promising candidate to overcome the exponentially increasing heat generation following the advancement in electronic devices^{51, 52}. Nevertheless, harnessing the multifunctional characteristics of graphene often entails with massive challenges due to the scalability, production cost and the complexity in manufacturing processes⁵³. Particularly in the graphene-based thermal applications of heat spreader⁵⁴ and Thermal Interface Materials (TIMs)⁵⁵, apart from the complicated fabrication method which reduces its consistency and practicality, heat conduction in such devices are significantly mitigated by the heat transfer limitations of

phonons scattering effects at interfaces and boundaries^{52, 56}. In other words, the heat conduction is limited by the weak van der Waals coupling between the graphene and the coated substrate⁵⁶, leading to the drastic reduction in the thermal conductivity. Thus, the adoption of graphene-based thermal applications has been stagnant. Alternatively, scalable graphene derivatives of graphene-oxide (GO)⁵⁷ and reduced GO (rGO)^{58, 59} have demonstrated enhancement in boiling heat transfer. As phase-change heat transfer is more effective than conduction heat transfer, the development of phase-change based graphene thermal applications is highly desirable. This not only provides a more simplified method in enhancing the phase-change heat transfer as compared to the convectional micro/nano structured surfaces, but also directly overcomes the technological hurdle engendered in heat conduction of graphene. Thus, surface functionalization with graphene derivatives holds great potential in enhancing the phase-change heat transfer.

1.2.2 Surface functionalization for enhanced condensation

Condensation occurs at the saturation temperature when the vapor comes into contact with a cool surface. The latent heat of vaporization is released through the wall surface surrounding the condensate. Depending on the wetting condition of the surface, condensation may occur either in filmwise or dropwise mode. Film condensation takes place primarily on clean and uncontaminated surfaces while dropwise condensation materializes on non-wettable surfaces⁶⁰. Dropwise condensation is superior to film condensation as the heat transfer rate of the former is more than an order of magnitude larger than that of the latter^{17, 18, 60}. A multistage process is involved in dropwise condensation which includes nucleation of initial droplet, droplet growth, droplets coalesce, departure of droplet and coalesce of more droplets as the droplet sweeps downward.⁶¹ Under dropwise condensation, smaller body force of the condensed droplet is required to overcome the liquid-solid contact force, thus reducing the thermal resistance across the droplet^{17, 62}. Furthermore, rapid removal of condensed droplets also contributes to the higher droplet nucleation rate due to the rejuvenation of condensate-free surface. The enhancement of surface refreshment rate and droplet removal stimulates continuous condensation and consequently augments both the heat and mass transfer coefficients.⁶³ It is a common practice to utilize non-wettable (hydrophobic/superhydrophobic) surface coating with low surface energy to promote

dropwise condensation. However, flat hydrophobic coatings such as fluorinated materials can only achieve maximum contact angle of 120° ^{64, 65}. To obtain superhydrophobic surface with higher contact angle exceeding 150° , manipulating the surface roughness is the most effective method⁶⁶⁻⁶⁹. A huge variety of superhydrophobic rough surfaces inspired by the natural species with superhydrophobic wetting characteristic (for example the lotus leaves⁷⁰, Indian cress⁷¹ and water strider's legs⁷²) has been reported⁷³⁻⁸². Among those, square and circular micro/nanopatterned vertical pillars are more commonly reported^{74, 76, 78, 80-82}. Although rapid drop removal can be visualized from the superhydrophobic surfaces, several critical problems may disrupt the efficient dropwise condensation. As droplet condensates on a superhydrophobic surface, the high mobility of the droplet is promoted by the entrapment of air between the droplet and the textured surface, also known as the Cassie state of droplet or Cassie drop (Fig. 3a)^{67, 74, 83}. The superhydrophobic behavior is sustained with the presence of the air cushion underneath the droplet. However, the presence of the air layer also contributes to the additional thermal resistance which reduces the condensation heat transfer⁸⁰. A 71% heat flux degradation was measured over the Cassie drop as compared to the flat hydrophobic surface. Under practical operating condition, the increased thermal resistance of Cassie droplet residing on nanopillars with vapor entrapment is even more intense than the entrapment of air⁸⁴. Thus, the enhancement of condensation using superhydrophobic surfaces may not necessarily be the best strategy. This implies that the coupling of wetting surface with superhydrophobic surface is required to maximize the condensation heat transfer.

Apart from the condensation heat transfer reduction of Cassie drop, the rapid transition from Cassie state⁶⁷ to Wenzel state⁶⁶ of a droplet also hampers the practical use of superhydrophobic surface for dropwise condensation (Figure 1.3). The loss of superhydrophobic characteristic has been commonly observed over superhydrophobic surfaces depending on the variation in ambient humidity or external disturbances^{83, 85-89}. Penetration of liquid into the textured surface triggers the immediate transition from Cassie state to Wenzel state of a droplet. Droplets in Wenzel state are highly pinned to the surface with significant reduction in the droplet mobility⁸³, leading to the formation of filmwise condensation. High droplet contact angle hysteresis can also be noticed over a Wenzel drop. Droplet contact angle hysteresis is defined as the difference between the advancing and the receding contact angles whereas high droplet contact angle hysteresis

indicates strong droplet adhesion. This transition can also be observed on superhydrophobic lotus leaf depending on the surface conditions and how the water droplet materialized^{89, 90}. Nevertheless, the self-regeneration capability of the lotus leaf enables the transition from Wenzel drop to Cassie drop *via* the secretion of wax. For the less fortunate artificial superhydrophobic surfaces, the wetting transition is irreversible. The superhydrophobic surfaces remain wetted and require additional repair to regain its original state. Accumulation of surface contamination and more importantly the wear resistance of the micro/nanostructures also contribute to the degradation of the hydrophobicity over long period and eventually trigger the transition of Wenzel state⁸⁷. Thus, the uninhibited and irreversible transition of wetting state directly leads to the questions of reliability and practicality towards real life applications. Furthermore, the expensive and lengthy preparation procedures with limited large production scalability also contribute to the depreciation of superhydrophobic surfaces.

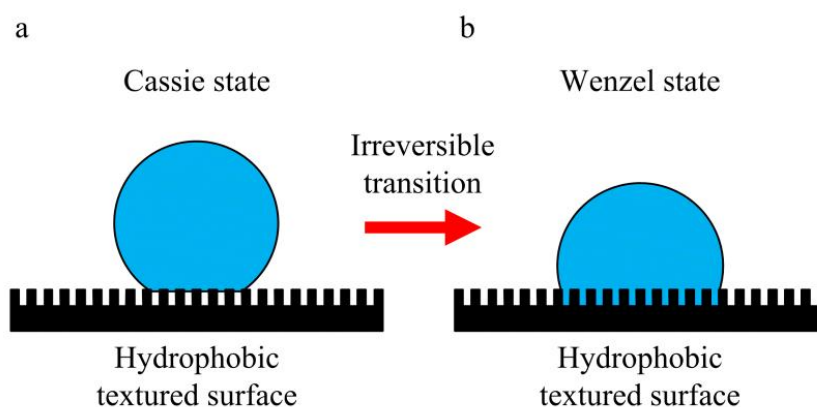


Figure 1.3| Schematic illustrations of the surface wetting modes of (a) Cassie state and (b) Wenzel state on a hydrophobic textured surface. As liquid penetrates the textured surface, irreversible transition from Cassie state to Wenzel state is observed.

Interestingly, the nucleation of droplet in dropwise condensation is confronted with similar dilemma as the nucleation of vapor bubbles in pool boiling with one concerning the liquid phase and the other the vapor phase. In the condensation heat transfer, hydrophilic surface favors the nucleation of droplet while superhydrophobic surface facilitates the rapid droplet removal and subsequently prevents filmwise condensation^{18, 91}. Several experimental studies on improving the dropwise condensation have been focused on incorporating regional hydrophilic surface with

global superhydrophobic surface⁷³. Mimicking the two-tier textured surface of a lotus leaf, carbon nanotubes were deposited on micropillars made of Silicon and then coated with hexadecanethiol⁷³. The final two-tier textured surface was capable of sustaining continuous dropwise condensation. In another study, multiscale nanograsped micropyramid Silicon microstructure was found to have increased the drop number density by 65% and augmented the droplet self-removal volume by 450% as compared with a superhydrophobic surface with only nanostructures¹⁷. The multiscale design satisfies both requirements of wetting surface for drop nucleation and superhydrophobic surface for rapid droplet removal. However, the surface was only tested under ambient condition of 22°C with a relative humidity of 70%. Under high vapor condition, transition to filmwise condensation may be unavoidable due to the excessive accumulation of condensates over the relatively tiny microstructures. To summarize, current available superhydrophobic surfaces are unable to be integrated in actual condenser section with high condensation rate. Particular in the TPCT, flat hydrophobic surface will be more appropriate to promote dropwise condensation. Similar to the strategy of using hydrophobic or superhydrophobic structures for rapid droplet removal, it is a common practice in the design of TPCT to utilize wick structure for enhancing the circulation of the condensates. Wick structure can be inserted in the TPCT to assist the flow of condensed liquids *via* capillary force. TPCT with the wick structure is also known as heat pipe. As of particular interest, we will only be focusing on the TPCT technology. Alternatively, the circulation rate can be improved by introducing centrifugal force,^{92, 93} electro-kinetic force,^{94, 95} magnetic force,⁹⁶ or, vibration force.⁹⁷ Amongst these approaches, inducing vibration on the TPCT is considered the most convenient approach to integrate with the conventional TPCT design. By inducing vibrations, the body force of the condensed liquids is increased due to the increase in acceleration, i.e., $F_b \propto m_f \ddot{\xi}$, where m_f is the mass of the fluids/droplets, and $\ddot{\xi}$ is the acceleration. However, very few prior studies dealt explicitly with the effect of vibration on the circulation effectiveness of a TPCT. Up to date, the only relevant study was focused on low-frequency vibrations ($f \sim 10^0 \text{ Hz}$).⁹⁷ While improved performance was observed, the increase of body force exerted on the liquids was only in a very small order of magnitude as a result of accelerations in the order of $\ddot{\xi} \sim 10^{-3} \text{ m/s}^2$. Thus, it is instructive to investigate the coupled effects of the hydrophobic surface and the high-acceleration induced vibration on the enhancement in the condensation heat transfer.

1.3 Research objectives and chapter outline

The main objective of the current research is to enhance the thermal performance of TPCT *via* carbon-based surface functionalization. TPCT relies on the phase-change heat transfer processes, namely evaporation and condensation, to function as an effective heat dissipation device. The circulation of the condensates is also essential in ensuring the perpetual operation of the device. In particular, this study focuses on enhancing the three essential processes of the TPCT using specific carbon-based materials such as Teflon and graphene derivatives. The thermal performance enhancement of TPCT is demonstrated experimentally with coatings of functionalized layers on the inner surface of customized TPCT. Specifically in the implementation of graphene derivatives, the research findings documented in this thesis reveal an exceptional and unprecedented phase-change heat transfer enhancement of TPCT. This leads to a novel approach for the adoption of graphene technology in thermal management systems. The underlying physical mechanism is elucidated schematically together with the supplementation of other published works to strengthen our postulations. Detailed literature reviews are documented in Chapter 2 with subsequent chapters (Chapter 3 to Chapter 6) reporting on a series of experimental investigations. Concluding remarks and recommendations for future work are included in Chapter 7. The brief summary of each chapter is given as follows.

Chapter 3

This study aims to enhance the condensation and the circulation of the condensates in a TPCT. The condensed droplets in the TPCT are subjected to two competing forces: contact line pinning force between the droplet and the condenser wall and the body force due to gravity. Either reducing the contact line pinning force or increasing the body force can lead to significant enhancement in heat transport capability, especially under high heat input condition. To reduce the contact line pinning force, thin hydrophobic layer made of Teflon is applied on the condenser wall. On the other hand, high-acceleration induced vibration is introduced to the coated TPCT to increase droplet's body force. The coupled effects of hydrophobic layer and high-acceleration induced vibration on the thermal performance of a TPCT are scrutinized. Nanofluid with distinguished thermo-physical properties is charged to the TPCT to further enhance

the thermal performance. We demonstrate that the formation of elongated liquid jets and entrainment of droplets induced by the high-acceleration vibration counteracts the enhancing effect from the increased body force of the condensed droplets. Factors contributing to the enhancement of the thermal performance of a TPCT are also identified and the underlying physical significance of the coupled effects is delineated.

Chapter 4

This study reports on the thermal performance enhancement of a GO nanofluid charged TPCT. The underlying physical mechanism which enhances the evaporation is associated with the fast water permeation across GO layers deposited on the evaporator surface. The fast water permeation of GO deposition extends the effective evaporation region and induces filmwise evaporation. The formation of hotspot at high heat input is delayed with the effective water distribution mechanism. As a result, GO deposition is more superior to metallic nanoparticles deposition in enhancing the evaporation strength of a TPCT. The thermal performance enhancement of GO nanofluid charged TPCT is inappropriate to be elucidated with the consensus of high thermal conductive nature of graphene. This study provides important insights into the anomalous phase-change heat transfer enhancement with GO deposition and demonstrates its enormous potential in thermal management applications with special relevance to the development of two-phase cooling devices.

Chapter 5

Inspired by the unique water permeation characteristic of GO, this study focuses on demonstrating the dramatic enhancement in phase-change heat transfer and the Leidenfrost state suppression with a simple and scalable surface functionalization technique of GO-coating. Complete vaporization of droplet on GO-coated surface is observed well above the predetermined Leidenfrost point of uncoated aluminium surface, indicating a significant shift in Leidenfrost point. Time-lapse images captured by the high speed camera reveals the rapid transition in boiling regimes from transition boiling to contact boiling as the droplet vaporizes. Effective cooling of the heated surface over a temperature range of 100°C to 320°C is recorded with an infrared thermal imaging spectrometer. Water molecules are found capable of permeating through the GO-coating irrespective to its state of matter (liquid or gas). In the contact

boiling regime, effective spreading of water droplet induces filmwise evaporation. Beyond the transition boiling regime, formation of vapour layer at the liquid-solid interface is effectively evacuated *via* the nanocapillaries embedded in the GO structure. As a result, GO-coating with its favourable attributes significantly augments the evaporation heat transfer, exceeding those of conventional surface functionalization approaches. Suppression of Leidenfrost state is discussed in conjunction with Laplace pressure gradient, temperature gradient and temperature induced structural alteration of GO. This study provides a comprehensive understanding on the phase-change heat transfer enhancement induced by GO-coating which demonstrates its unique water permeation property competent in the integration with current phase-change thermal management systems.

Chapter 6

As water permeation in graphene-based coating is closely associated with the populations of oxygenated functionalities, this chapter focuses on enhancing the thermal performance of TPCT using a graphene derivative with greater water permeability. With the optimized ratio of non-oxidized to oxidized regions, GNPs-coating exhibits greater water permeability as compared to its counterpart: GO-coating. Water molecules intercalating through the layered structure of GNPs-coating experiences more frictionless flow to a greater extent with smaller pinning effect from the oxygenated functionalities. This is evidenced with the higher reduction rate in static contact angle as compared to that of GO-coating. Water permeation also takes place in the antigravity direction across GNPs-coated glass tube. GNPs-coating coated across the TPCT enhances both the evaporation and the circulation of the condensates, leading to the dramatic enhancement in the thermal performance. This is demonstrated by comparing the thermal performance of a fully coated (evaporator section and condenser section) GNPs TPCT to that of a half coated (evaporator section) GNPs TPCT. The rapid water permeation effect across GNPs-coating induces filmwise evaporation in the evaporator section and enhances the circulation of condensates in the condenser section. This study introduces a novel and effective approach in enhancing the phase-change heat transfer *via* the utilization of GNPs-coating.

Chapter 2

Literature Review

As surface functionalization includes the surface deposition of metallic and non-metallic nanoparticles, the literature review begins with the recent development in the utilization of nanofluids for thermal performance enhancement of TPCT. The fundamental mechanisms responsible for the heat transfer enhancement are summarized. Next, the unique properties of graphene and potential graphene-based applications are introduced, followed by its diverse synthesis processes and alternative production of graphene derivatives (GO, rGO and graphene nanoplatelets (GNPs)). We then focus our attention on the heat transfer in graphene, in particular of the heat conduction in the crystal lattice and also the heat transfer limitations encountered by graphene-based thermal applications of heat spreader and TIMs. Nanofluids prepared by graphene derivatives with the capability of enhancing the boiling heat transfer are subsequently introduced. Various postulations on the underlying physical mechanisms which contribute to the anomalous boiling enhancement are summarized and evaluated based on the material's characteristics. Critical reviews on these postulations are also provided with the emphasis of the unique water permeation effect in GO. Various operating mechanisms behind the water permeation effect of GO are elucidated with several renowned studies. Lastly, we reconnect the missing link between the enhanced phase-change heat transfer with GO deposition and its fast water permeation effect. We propose that the fast water permeation effect of GO deposition can be utilized to induce filmwise evaporation and ultimately for Leidenfrost suppression.

2.1 Nanofluid

With the advancement of the nano-material fabrication technologies, nanofluid with the suspension of nano-sized metallic particles in base fluid has been utilized as a replacement for the conventional working fluids in many industries. Characterizations of the base fluids (water, ethylene glycol, alcohol and lubrication oil) added with small

dosage of nanoparticles exhibited extraordinary thermal conductivity enhancements⁹⁸⁻¹⁰⁴. Overwhelming number of studies has been reported on the thermal performance enhancement of the TPCT or heat pipe with nanofluids^{105, 106}. In general, nanoparticles used in the studies can be classified into three categories: pure metal, metal oxide and carbon based materials. Metal oxides such as copper oxide¹⁰⁷⁻¹¹², aluminium oxide^{109, 113-116} and iron oxide^{117, 118} are more commonly used than those of the pure metal (gold¹¹⁹, silver¹²⁰⁻¹²², titanium¹²³⁻¹²⁵ and aluminum¹²⁶). Carbon based materials such as diamond^{127, 128} and carbon nanotubes¹²⁹⁻¹³³ have also been reported. The high tendency of nanoparticles' agglomeration remains a major problem in the commercialization of nanofluid technology. This clustering effect of the nanoparticles is attributed to the van der Waals attraction between individual particles. Over a short period of time, severe agglomeration of nanoparticles can be observed in the nanofluid. In applications without involving phase change heat transfer (e.g. lubrication), the clustering of nanoparticles reduces the antiwear characteristic, inducing negative effect on the overall performance^{134, 135}. On the other hand, the clustering effect is favourable in applications involving single or two-phase heat transfer. The inevitable depositions of nanoparticles on the evaporator surface often engendered the enhancement in thermal performance of a TPCT or heat pipe charged with nanofluid^{105, 106}. This is intelligible that the porous layer formed through the deposition of nanoparticles strengthens the phase change heat transfer. However, it is yet inconclusive regarding the deposition effects of the nanofluid. In general, nanoparticles deposition on the heated surface is found to have significantly enhanced the nucleate boiling mechanism and surface wettability, which contributes to an increase in the evaporator heat transfer coefficient^{23, 136-142}. On the other hand, contradicting results have also been reported - mainly due to the additional thermal resistance imposed by the layer of nanoparticles on the heated surface and the filling of active nucleation cavities¹⁴³⁻¹⁴⁵. As a result, the thickness of the nanoparticles coating and the surface wettability have significant effects on the overall increase in the evaporator heat transfer coefficient. An ideal method is to pre-coat the heated surface with a layer of nanoparticles with optimum thickness and manage the surface wettability without using any nanofluids. Feasibility studies on such methods, controlling the coating thickness through the increase of heat flux, have been conducted but yet to be conclusive^{146, 147}. Based on the significant evaporation enhancement obtained from the nanoparticles coating, we focus our studies on enhancing the overall thermal performance of the TPCT *via* the manipulation of surface wettability.

2.2 Graphene, the future material

Graphene, a single layer of graphite formed with arrays of hexagonally arranged carbon atoms, is the thinnest material on earth. This fascinating material was discovered by Geim and Novoselov in 2004 with the display of unprecedented electronic properties¹⁴⁸. The atomically thick graphene was first isolated with the “Scotch-tape method”, technically known as micromechanical cleavage method, by peeling of bulk graphite with adhesive tape. The simplicity and inexpensive method of obtaining micro-sized graphene sheets has sparked the interest of the global scientific community to investigate other aspects of the amazing graphene. Regardless of the nanoscale thickness of only 0.33 nm, its distinctive structural features provide graphene with outstanding mechanical, thermal, electrical and optical properties¹⁴⁹. While being the thinnest material, graphene is also the strongest material with exceptional Young’s modulus of 1.0 TPa¹⁵⁰, which is 5 times greater than that of steel. The electron mobility of graphene ($2 \times 10^5 \text{ cm}^2 \text{V}^{-1} \text{s}^{-1}$)^{151, 152} is measured exceeding twice the value of conventional semiconductor and it is also optically transparent, making it an excellent material for conductive electrodes¹⁵³. Moreover, the extraordinary thermal conductivity of $5300 \text{ Wm}^{-1} \text{K}^{-1}$ also makes graphene an ideal material for heat spreader in thermal management devices^{51, 54, 154} and additive of thermal interface materials (TIMs)¹⁵⁵⁻¹⁵⁸. With all the spectacular physical properties, the rise of graphene has united researchers around the globe, working towards a common goal in developing potential graphene-based applications. These include graphene-based nanocomposites, sensors, electrical conductive films, heat dissipation films, photocatalytic applications, field-effect transistors, flexible touch-screen displays, supercapacitors, batteries, anticorrosion coatings, lubricants, water filtration membranes, solar cells and more¹⁵⁹⁻¹⁶². Nevertheless, harnessing the multifunctional characteristics of graphene often entails with massive challenges due to the scalability, reproducibility, production cost and the complexity in manufacturing processes⁵³. To date, most of the reported graphene-based products are still in the research and development phase with only a hand full managing to reach the open market. Tennis rackets made of graphene nanocomposites material, graphene-based nanofluids as coolant for drilling, graphene-based flexible displays, flexible heaters made with printable graphene ink and graphene coated light-emitting diode (LED) light bulbs are available but yet to be fully commercialized. It is estimated that the adoption and fully commercialization of graphene-based technologies may be

materialized in another two more decades⁵³. Indeed, most of the novel graphene-based applications are required to overcome various technical and economic difficulties to really benefit mankind. This also applies to the potential application of graphene as effective heat dissipation medium for advance electronics devices.

2.2.1 Synthesis of graphene and its derivatives

To realize the full potential of graphene for practical applications, manageable synthesis of graphene is utmost important. However, the growth of graphene is costly and involves complex techniques, which engender restricted control over the quality, size, shape, thickness, and more importantly the reliability and repeatability¹⁶¹. To overcome such technological hurdles, other graphene derivatives have been synthesized and capable of mimicking the excellent properties of graphene but only to certain extend. To be concise, other than the single layer or multilayer graphene film, common graphene derivatives include graphene-oxide (GO), reduced graphene-oxide (rGO) and graphene nanoplatelets (GNPs). Although the properties of the graphene derivatives are incomparable with the pristine graphene, their productions are more scalable and consistent. This makes graphene derivatives more popular and compatible to be integrated with potential applications. In the following section, the productions of graphene and graphene derivatives will be discussed. The productions of graphene and its derivatives can be categorized into four major approaches, i.e., micromechanical exfoliation of graphite, chemical vapour deposition (CVD), epitaxial growth on silicon carbide (SiC) and physical/chemical exfoliation of graphite¹⁶³.

Inspired by the Scotch tape method, graphene can be obtained from graphite *via* micromechanical exfoliation^{148, 164}. This method has been widely used in the study of the fundamental properties due to the yield of high quality single layer graphene^{51, 149, 159}. The simplicity of this method also facilitates the development of potential thermal application such as thermal heat spreader⁵⁴. However, shortcomings of inconsistent sheet size and restricted yield of large area graphene film have limited the utilization of such method¹⁵⁹. Graphene flakes obtained from micromechanical exfoliation are limited in the micrometer range¹⁶⁴. In the CVD approach, few layers of graphene can be grown on metal substrates. Two years after the discovery of graphene, one group demonstrated the first production of few layers graphene using CVD approach¹⁶⁵. Transition metals

such as Ni¹⁶⁶, Cu¹⁶⁷, Co¹⁶⁸, Pd¹⁶⁹, Ru¹⁷⁰ and Ir¹⁷⁰ are commonly used as catalyst in the synthesis of fine graphene film. However, the properties of the resulting graphene film are strongly affected by the catalyst used¹⁷¹. For example, in the comparison of graphene film grown on Ni substrate and Cu substrate, the latter exhibited greater grain size with lesser grain boundary^{166, 167}. This nanoscale differences can be crucial in determining the thermal characteristic of the graphene film, specifically in the context of graphene heat conduction¹⁷². Using Cu substrate as catalyst, several groups have demonstrated large area growth of high quality graphene sheets targeted to replace conventional transparent electrode made of indium tin oxide (ITO)^{167, 173, 174}. Yet, these large area graphene sheets are found to be polycrystalline. To enhance the heat conduction in graphene film, grain size, grain boundary, number of graphene layer and defect are important factors to be considered^{52, 56}. Unlike the requirement of metal catalyst in the CVD process, high quality graphene can be grown on SiC substrate with thermal annealing process under ultrahigh vacuum condition^{175, 176}. The presence of carbon atoms in the SiC substrate provides the starting material for the formation of graphene crystalline. Although such method is relatively clean without the involvement of metal, the resulting graphene films exhibited much smaller grain size of nanometer range (30-200nm) due to morphological alteration of SiC substrate under high temperature thermal annealing process and the utilization of SiC substrate with different atomic structures (Si-terminated or C-terminated basal plane)¹⁷⁷⁻¹⁷⁹. Furthermore, the thermal decomposition of SiC substrate at unconfined locations often produces graphene film with large variation in number of layers. Improved quality of graphene films with enlarged grain sizes (300-700 nm) were also reported using ex situ thermal annealing of Si-terminated SiC in argon enclosure under atmospheric pressure¹⁸⁰. Nevertheless, the grain size is insufficient for effective heat transfer with additional consideration of costly SiC substrate¹⁶². For practical utilization of graphene film growth by CVD method or on SiC substrate, relocation of graphene film on to other bulk materials is often required. The transferring of graphene film involves complex and precision transferring techniques which imposes significant bottleneck in practical applications in terms of scalability and repeatability.

Alternatively, graphene derivatives can be produced in significantly larger quantities with the combination of chemical treatments and physical exfoliation methods. These scalable methods often utilize inexpensive bulk graphite as precursor

which is relatively cost effective compared to the surface deposition techniques. In general, common graphene derivatives include GO, rGO and GNPs. With their scalability and affordability, graphene derivatives are well-suited to be integrated with large variety of practical applications. To be concise, standard synthesis methods of the graphene derivatives will be discussed. The production of GO involves a two-stage process whereby precursor graphite is first oxidized and subsequently exfoliated in solvent. Common oxidation methods of graphite include Brodie method, Staudenmaier method and Hummers method^{159, 163, 181}. These methods can be differentiated by the oxidizing agents utilized to achieve various level of graphite oxidation¹⁶³. Brodie and Staudenmaier methods utilize potassium chlorate (KClO₃) and nitric acid (HNO₃) as oxidizing agents while Hummers method utilizes potassium permanganate (KMnO₄) and sulphuric acid (H₂SO₄) for the oxidation^{159, 181}. The vigorous oxidizing process significantly disrupts the covalent sp² bonding of the carbon network with the binding of oxygenated functional groups (mainly hydroxyl and epoxy groups, with only minority of carbonyl and carboxylic groups located at the edge of the graphitic layer)^{163, 181}, yielding the product of graphite-oxide. To obtain the final product of GO, physical exfoliation of graphite-oxide in solvent is required. With the hydrophilic nature of the functional groups¹⁸², graphite-oxide can be easily dispersed in solvent *via* mechanical stirring or sonication treatment. Sonication treatment is commonly utilized due to the accelerated process and the yield of more uniform dispersion. Nevertheless, the sonication treatment also contributes to the disintegration of the GO sheets, forming GO dispersion with a large distribution of platelet sizes in nanometer range¹⁸¹. Notably, GO dispersion is capable of maintaining stable suspension without noticeable agglomeration¹⁸². The stable suspension is induced by the repulsive electrostatic forces between the negatively charged GO sheets^{163, 181, 183}. Regardless of the identical chemical composition, it is essential to differentiate GO from graphite-oxide with the huge structural differences. Graphite oxide remains in a multi-layered structure with interlayer distance of 6-12 Å, depending on the water content and the density of the oxygenated functional groups¹⁸⁴. On the other hand, single layer or few-layered stacks of GO sheets can be obtained from the exfoliation process¹⁸¹.

Although GO can be synthesized in a larger scale, the practical applications of GO are still limited due to the lattice disruption which significantly mitigates the thermal, electrical and mechanical properties¹⁸¹. To restore some of the favourable properties of

graphene, GO can be reduced through three types of reduction processes namely chemical reduction, thermal reduction and electrochemical reduction^{163, 181}. In the reduction processes, most of the oxygenated functional groups can be eliminated. GO with the removal of functional groups is known as rGO. Yet, the reduction process only partially rejuvenates some of the thermal conductivity due to the remaining lattice defects in the graphene sheets^{163, 181}. Thus, current rGO-based thermal applications such as heat spreaders and TIMs have much lower thermal conductivity as compared to the pristine graphene or even the bulk graphite^{52, 56}. The intuition of high thermal conductivity of rGO has been in constant debate whereby most of the research groups believed that the reduction process of GO was sufficient to recover its thermal conductivity. However, it is important to emphasize that the oxidization and sonication processes of manufacturing GO has critically damaged the carbon network for excellent in-plane heat conduction. To support our postulation, additional factors influencing the heat conduction in rGO-based thermal applications will be discussed in detail in the following section (section 1.5.1). Several comprehensive reviews on the reduction processes of GO have been reported^{159, 163, 181, 185}. In the chemical reduction processes of GO, reducing agents such as hydrazine monohydrate¹⁸⁶, sodium borohydride¹⁸⁷, ascorbic acid^{188, 189}, hydroquinone¹⁹⁰ and other strong alkaline solutions¹⁹¹ have been used. The most commonly used and also the first reported reduction method of GO is the utilization of hydrazine monohydrate¹⁸⁶. As GO is suspended in solvent (water), reducing agent which is inert to water is desired during the reduction process. This makes hydrazine monohydrate a suitable candidate for the reduction of GO. However, the removal of the oxygenated functional groups with hydrazine monohydrate also engenders the introduction of heteroatomic impurities to the graphene sheets such as hydrazines, amines and aziridines¹⁸⁷. The removal of such impurities is often challenging without any direct approach. Therefore, the reactivity of the reducing agent with solvent and the yield of impurities to the graphene sheets are common dilemmas in the selection of reducing agent for the reduction of GO¹⁸¹. Other than the chemical reduction paths, GO can be reduced *via* thermal approaches^{192, 193}. Under high temperature environment (>1000°C), the oxygenated functional groups are converted into carbon oxides and water. It is believed that for few-layered GO platelets, the gaseous entrapments within the graphitic structures generated sufficient pressure (130 MPa at 1000°C based on state equations) for the exfoliation of GO platelets or in extreme case, the rupturing of graphitic layer with the gases discharge¹⁹². Furthermore,

the final yield of rGO was found to have decreased 30% in mass as compared to the initial mass of unreduced GO¹⁹³. In other words, a total of 30% of initial mass was lost undergoing the thermal reduction process. As a result, thermal reduction process of GO not only reduces the final yield of rGO but also engenders significantly more defective sites throughout the layered structure¹⁸¹. Although thermal reduction of GO is relatively simple without involving strongly toxic chemicals, the product may not be suitable for the utilization in thermal applications, especially for heat transfer by conduction.

Lastly, the reduction of GO can be achieved *via* the electrochemical reduction process. Using common electrochemical cell with aqueous buffer solution, the electrochemical gradient is capable of removing the oxygenated functional groups. GO thin film can be deposited onto targeted surface of any substrate (by spray coating, casting or electrostatic interaction) and subsequently reduced with the charging of the electrochemical cell¹⁹⁴⁻¹⁹⁸. Employing the linear sweep voltammetry on GO deposited substrate immersed in sodium phosphate buffer, the rapid reduction of GO initiated at -0.60 V and obtained maximum at -0.87 V in a short period of 300 s¹⁹⁸. The continuous decrease in reduction efficiency prolonged 1700 s and gradually settled at 5000 s. Effective reduction of GO with a C/O ratio of 23.9 was obtained which marked the highest reduction effect among all related studies using the electrochemical approach¹⁹⁸. Alternatively, with the direct submersion of electrodes into GO dispersion, GO deposition and reduction can be obtained simultaneously¹⁹⁹. As the current passed through the GO dispersion, initial deposition of GO was first noticed on the anode, followed by the reduction of the GO within 30 s. However, the resulting rGO film was incomparable to those obtained from the chemical reduction using hydrazine. In general, electrochemical reduction of GO is relatively cleaner, faster and safer as compared to the chemical or thermal reduction processes²⁰⁰. Yet, the effectiveness of obtaining high level of reduction in GO still limits the adoption of such approach. In the context of graphene heat transfer, regardless of the available reduction processes, the adoption of rGO for practical thermal applications is still restricted by the inevitable lattice defects formed during its synthesis.

To overcome the introduction of defective sites through the oxidation and exfoliation processes, graphene sheets can be obtained from thermal exfoliation of graphite intercalation compounds (GICs) or expanded graphite. The fundamental

objective of oxidizing graphite into GO is to facilitate the exfoliation of graphene sheets from bulk graphite. The introduction of oxygenated functional groups weakens the layer-to-layer van der Waals interactions of graphite. Similar to the principle behind the oxidation of graphite, the intercalation of alkaline atoms or acid molecules between the graphitic layers widens the interlayer distance and allows greater yield of single layer graphene under rapid thermal treatment^{163, 185, 201}. Using commercially available expanded graphite, one group demonstrated the production of high quality graphene nanoribbons with the combination of rapid thermal treatment and sonication treatment²⁰². Expanded graphite was first exposed to temperature of 1000°C for 1 minute in forming gas of argon with 3% hydrogen and subsequently dispersed in dichloroethane solution with dissolved aromatic polymer. Polymer coated graphene sheets and graphene nanoribbons of single-layer and few-layer were found in the dispersion after 30 minutes of the sonication treatment. To further enhance the final yield of single-layer graphene, the same group proposed another approach which involved a second intercalation of oleum (fuming sulphuric acid) and tetrabutylammonium hydroxide²⁰³. Similar to the previous study, expanded graphite intercalated with sulphuric and nitric acids was first exfoliated with rapid thermal treatment under the same condition. The exfoliated graphite was then treated with oleum and followed by the insertion of tetrabutylammonium hydroxide in N,N-dimethylformamide solution. The re-intercalation process lasted 4 days to ensure the full insertion of intercalants. Aided by surfactant, homogeneous suspension with 90% single-layer graphene was obtained after the sonication treatment. In the characterization of the graphene sheet obtained from this approach, the X-ray photoelectron spectroscopy (XPS) spectrum of the graphene sheet was identical to that of the highly oriented pyrolytic graphite (HOPG) crystal. This indicated the high quality of the graphene sheet with significantly less lattice defects. Microwaves irradiation can also be utilized for the exfoliation of expanded graphite²⁰⁴. Expanded graphite was submerged in aqueous ammonia solution and subjected to microwave irradiation. The microwave irradiation was maintained in a temperature range of 120°C to 200°C for 120 minutes. Although traces of few-layer graphene sheets (8 wt%) were obtained from the process, solid residual of expanded graphite still remained in the mixture. The authors attributed the successful exfoliation of expanded graphite at low temperature condition to the insertion and decomposition of ammonia solution in the graphitic structure.

To summarize, the selection of graphene or graphene derivatives for the integration in practical applications is totally dependent on the required material's properties. For example, single-layer graphene synthesized with the CVD approach is more appropriate to be utilized as heat dissipation medium¹⁷² while GO synthesized from the Hummers' method is used as aromatic drug carrier due to its excellent water solubility²⁰⁵. Therefore, it is utmost important to understand the fundamental chemistry and the functionality of graphene related materials for the future development of novel graphene-based technologies.

2.3 Graphene heat transfer

Since the discovery of ultra-high thermal conductivity of graphene, heat conduction in low dimensional material has been extensively studied with the emergence of various hypotheses. Recently, a comprehensive review of the thermal conduction in carbon materials has been published which provides valuable insight into the heat transfer limitations of graphene⁵². In general, the effectiveness of heat conduction of a material is characterized by its thermal conductivity. Thermal conductivity is governed by the Fourier's law of heat conduction defined as $q = -K\nabla T$, where q represents the heat flux, K denotes the thermal conductivity and $-\nabla T$ is the negative temperature gradient. For anisotropic material, K is significantly influenced by structural orientation. As heat energy can be transferred *via* acoustic phonons (oscillation of atoms in a crystal lattice) and electrons in solid materials, K is therefore the sum of K_p and K_e which represents the contribution from the phonons and the electrons. For metallic materials, heat transfer is dominated by electrons due to the abundance free carriers. Under room temperature, K for pure copper reads $400 \text{ Wm}^{-1}\text{K}^{-1}$, in which the contribution by phonons K_p is only 1-2% of the total K ^{52, 206}. Opposing to the heat transfer in metals, heat transfer in graphene and carbon-based materials are dominated by phonons. The unique thermal characteristics of graphene are attributed to the strong covalent sp^2 bonding connecting the carbon atoms which empowers efficient heat transfer *via* lattice vibrations^{52, 56}.

In general, the heat transfer by phonons can be limited by intrinsic effects and extrinsic effects. In the intrinsic effects, crystal lattice defects, impurities and the

anharmonicity of the phonons interaction mitigate the ballistic heat transfer^{52, 56}. This explains the significant reduction in thermal conductivity of GO due to the vigorous oxidation process, which engenders lattice defects and attachment of functional groups (impurities)^{181, 207, 208}. The anharmonicity phonons interaction is also known as the Umklapp process^{209, 210}. Under normal scattering process of two incoming phonons, the collided phonons generate one phonon with a momentum of the sum of the former two phonons without going over the Brillouin zone, energy conservation can be observed. As the phonons momentum continuously increases, the combined total momentum of the collided phonons exceeds the Brillouin zone which affects the resulting total phonon momentum. The loss of energy due to the Umklapp scattering limits the thermal conductivity of the graphene-based materials^{52, 211}.

The extrinsic effects mainly include the phonons scattering at interfaces and grain boundaries^{52, 56}. Particularly in the interfacial phonons scattering, the heat transfer is significantly reduced between the graphene sheet and the adjacent substrate due to the weak van der Waals coupling. This postulation has been justified by a recent study on the reduction in thermal conductivity of graphene supported by SiO₂ substrate²¹². Graphene was obtained using mechanical exfoliation technique and subsequently deposited onto the SiO₂ substrate. The thermal conductivity of the combined structure yielded a value of 600 Wm⁻¹K⁻¹ under room temperature. The authors attributed the significant reduction in thermal conductivity to the phonons leakages across the van der Waals couplings between the graphene sheet and the SiO₂ substrate. Moreover, the adhesive between the graphene sheet and the SiO₂ substrate also plays a critical role in the resulting thermal conductivity. As the surface morphology of the SiO₂ is presented with nanoscale roughness, the interactions between the graphene sheet and the SiO₂ substrate are only limited to the peaks of the rough surface through the van der Waals forces (Figure 2.1). As a result, the graphene sheet deposited on flat surface will eventually lead to a much lower thermal conductivity. The leakage of phonons was also comprehended with another experimental investigation of graphene sheet embedded in SiO₂ substrate²¹³. A thermal conductivity of 160 Wm⁻¹K⁻¹ was measured from the graphene sheet embedded in SiO₂ substrate. On the other hand, the thermal conductivity progressively increased with the number of graphene layers. At the thickest sample of 20 graphene layers, the thermal conductivity achieved that of the bulk graphite. This indicated that the interfacial phonons scattering effect of ultrathin graphite (multilayer

graphene) reduced significantly as compared to that of a single layer graphene embedded in similar SiO_2 substrate. In the development of effective graphene heat spreaders, a minimum layer thickness of 10 nm is necessary to avoid excessive interfacial phonons leakages while maintaining high in-plane thermal conductivity beyond $1000 \text{ Wm}^{-1}\text{K}^{-1}$. These also explain the unusual phenomenon of relative low in-plane thermal conductivities measured over various graphene heat spreaders deposited on or embedded in bulkier materials. More details on the experimental studies of graphene heat spreaders will be comprehended in the following section (section 1.5.1). Heat transfer in graphene is also found to be size-dependant. A reduction of 85% in the thermal conductivity was obtained by reducing the graphene size from $5 \mu\text{m}$ to $1 \mu\text{m}$ ²¹⁴. The phonons scattering effect at grain boundary was also illustrated in other studies^{172, 215}. In the growth of graphene using CVD method, the resulting graphene grain size is dependent on the grain size and the material of the metal substrate which varies from nanometer to micrometer¹⁷¹. For example, the graphene grain sizes on commonly used copper substrate yielded $10 \mu\text{m}$ to $60 \mu\text{m}$ while Ni substrate was found in the range of only $1 \mu\text{m}$ to $2 \mu\text{m}$ ¹⁷². Higher graphene grain size with lower number of grain boundaries is preferable in the reduction of phonons scattering effect at grain boundary²¹⁵. In the next section, we summarize the recent developments of graphene-based heat dissipation devices (heat spreaders and TIMs) and illustrate the fundamental heat transfer restrictions of graphene.

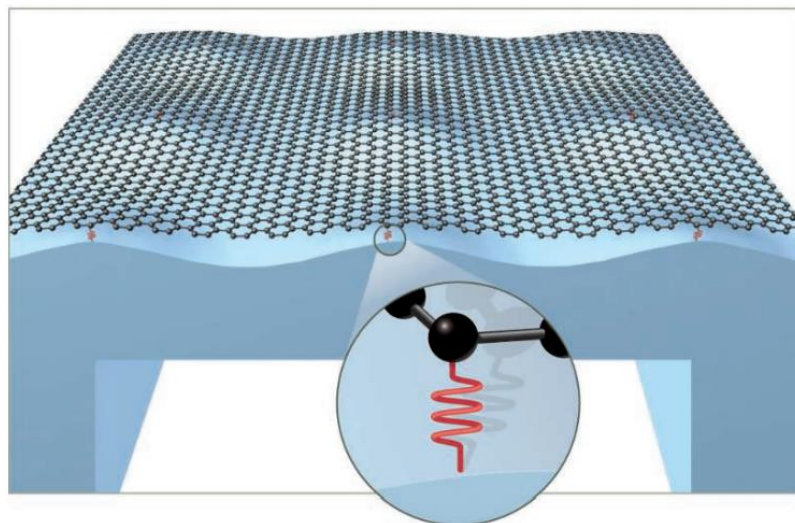


Figure 2.1| Schematic illustration of the van der Waals couplings (red springs) between the graphene sheet and the peaks of the SiO_2 substrate. The reduction in the thermal

conductivity is attributed to the phonons leakages across the van der Waals couplings (adapted from reference²¹²).

2.3.1 Graphene heat spreaders

The high thermal conductivity nature of graphene has been positioned as a promising candidate to overcome the exponentially increasing requirement in heat dissipation of microelectronics devices^{52, 212, 216, 217}. In which, one relevant study explored the potential application of graphene as effective heat dissipation device for high-power gallium nitride (GaN) electronic⁵⁴. By introducing additional heat dissipating channels made of few-layer graphene on top of the GaN transistors operating at 13 Wmm^{-1} , reduction in hotspots temperature of 20°C was reported. The enhanced heat dissipation of GaN transistors not only prolonged the device's lifetime by an order-of-magnitude but also unravelled the current limitation of excessive heat generation in nitride-based technology. Nevertheless, fabricating such thermal conducting layers requires precision and complex transfer techniques which raises doubt against the consistency and reliability of each graphene device. The mechanical exfoliation technique used to obtain few-layer of graphene can be difficult to control. Followed by the development of few-layer graphene heat conductor for GaN transistors cooling, similar cooling technique was also used for the cooling of GaN visible light-emitting diodes (LEDs)²¹⁸. Instead of using graphene for the fabrication, a more scalable material of GO was used. Prior to the deposition of GaN nucleation layer, GO was first spray coated on to the sapphire substrate (base) and underwent thermal annealing process at high temperature to yield the final product of rGO. As compared to the conventional counterpart, rGO embedded LED indicated reductions in both the junction temperature and thermal resistance of 25.7% and 34%, respectively. Although this relatively simple approach can be used for effective heat removal, the high temperature thermal annealing process at 1100°C may not be suitable for other heat sensitive microelectronics. Furthermore, the thermal conductivity of rGO is incomparable with its precursor graphene. The thermal reduction process of GO is insufficient to rejuvenate the oxidized graphene sheets back to its original state of high thermal conductivity^{52, 181}. The oxidization process induces permanent disruptions in the covalent sp^2 bonding and lattice defects to the graphene sheet which significantly impede the anisotropic heat conduction. Although the thermal conductivity of rGO is

much lower than that of the graphene sheet, the authors suggested that the rGO layer was able to maintain partial of its initial thermal conductivity, which is approximately about the thermal conductivity of bulk graphite ($2000 \text{ Wm}^{-1}\text{K}^{-1}$)²¹⁸. However, the mechanical property of the rGO layer decreases dramatically due to the detachment of functional groups under the thermal annealing process. Thus, the thermally reduced GO layer is often brittle and requires delicate handling while coating onto other substrates. On the other hand, contradicting result on the mechanical strength of rGO-based heat spreader was also reported²¹⁹. The rGO layer fabricated from vacuum-filtration of GO in aqueous solution and subsequently heated at 1200°C yielded high tensile strength of 13.62 MPa with a thermal conductivity of $1043.5 \text{ Wm}^{-1}\text{K}^{-1}$. The authors emphasized that the thermal annealing process above 1000°C triggered the reconnection of major sp^2 clusters with newly materialized minor sp^2 domains, thus re-establishing the original state of graphene. Although it is in accordance with one of the recent study²²⁰, it is yet conclusive and requires further investigation. The differences in the GO deposition technique and the deposition thickness may have influenced the mechanical strength of the rGO layer. Yet, it is more acceptable that the thermal annealing process of GO which induces random expansions in the graphitic structures due to the generation of various gases from the escape of functional groups, leading to the brittle fracture of the rGO layer. To overcome the reduction in mechanical strength of rGO, another study was conducted by integrating carbon fibres with rGO, forming a new kind of composite layer for heat dissipation devices²²¹. The resulting carbon/carbon composite layer exhibited high tensile strength of 15.3 MPa with a thermal conductivity of $977 \text{ Wm}^{-1}\text{K}^{-1}$ determined at ambient temperature with laser flash method. The carbon fibres provide essential reinforcement to the composite layer while the rGO sheets effectively transfer heat *via* lattice vibration. Meanwhile, GNPs was also used for the fabrication of effective heat spreader to counteract the performance deficiencies of rGO layer²²². Unlike the unavoidable reduction in mechanical strength of rGO layer, GNPs layer was directly prepared with vacuum-filtration of GNPs in aqueous suspension (with surfactant) and subsequently graphitized at high temperature. The final product of GNPs layer was more mechanically flexible but yielded lesser thermal conductivity of $220 \text{ Wm}^{-1}\text{K}^{-1}$. Although the flexible GNPs layer is weaker in term of thermal transport capability, the relatively simple fabrication process together with the controllable layer thickness through the regulation of filtration volume provide GNPs-based heat spreaders with competitive features over rGO-based heat spreaders. Furthermore, the

production of GNPs is relatively scalable as compared to graphene growth by surface deposition technique. Thermally exfoliated from GICs or expandable graphite, GNPs can be manufactured in large quantities⁵³.

To preserve the high thermal conductivity nature of graphene, one study focused on implementing continuous graphene films with various thicknesses as effective heat spreaders¹⁷². Using chemical vapour deposition technique, monolayer graphene and multilayer graphene were deposited onto Cu thin film and Ni thin film respectively. The graphene films were then transferred onto a thermal evaluation chip (electrically powered platinum micro-heater) using wet chemical process. This involved the coating of graphene deposited substrate (Cu or Ni thin film) with polymethylmethacrylate (PMMA) layer, followed by the chemical etching process of the substrate and finally the removal of the PMMA layer with hot acetone while leaving the graphene film on the heater surface. Based on the evaluation of hotspot temperature, the monolayer graphene heat spreader indicated a better thermal performance with a reduction of 13°C under the highest heat flux of 430 Wcm⁻². Under similar heat flux, the multilayer graphene heat spreader only showed a reduction of 8°C. These findings contradicted with the postulation of enhanced in-plane thermal conductivity with the increase of the number of graphene layers as a result of the reduction in phonon-scattering²¹³. Interestingly, the authors explained their findings with the variation in graphene grain size corresponding to the different substrates used for the graphene synthesis. The Cu thin film yielded a grain size one order of magnitude larger than the Ni thin film. The reduction in grain size increases the grain boundaries and amplifies the boundary phonon-scattering effect²¹⁵, leading to the reduction in thermal performance of multilayer graphene heat spreader. Thus, the chemical vapour deposition technique is yet to be envisaged as an excellent synthesis method for continuous graphene conducting thin film due to the random formation of grain boundary and the inevitable transferring process. The final removal of the PMMA layer often engenders additional boundaries due to the cracking effect on irregular coated surface. Moreover, the reduction in the in-plane thermal conductivity due to the fundamental phonon-scattering effects at the graphene-substrate interfaces and the grain boundaries can be considered as significant bottlenecks in harnessing the full potential of single layer graphene.

2.3.2 Thermal interface materials

Apart from the graphene-based lateral heat spreaders, other advance thermal transport graphene-based materials also include the TIMs. TIM is the effective heat transfer medium applied at the interface between the heat source and the heat sink of modern electronics. Conventional TIMs utilize polymers or greases as base material mixed with thermally conductive particles such as silver²²³, aluminium oxide^{224, 225} and aluminium nitride²²⁶. High volume fraction of the particles up to 50% is often required to achieve low thermal conductivity of $1\text{-}3\text{ Wm}^{-1}\text{K}^{-1}$ for the resulting composites^{158, 227}. Reduction in mechanical strength of the resulting composite with high loadings of filler material is also a limiting factor in the development of efficient TIMs. Recently, carbon-based materials have been utilized as filler material for the development of next generation TIMs with extraordinary enhancement in the thermal conductivity. In general, the thermal performance of the TIM is characterized by the thermal conductivity enhancement ratio $\eta = (K_{\text{eff}} - K_{\text{base}}) / (K_{\text{eff}})$, where K_{eff} denotes the thermal conductivity of the resulting composite layer and K_{base} is the thermal conductivity of the original base material⁵². While carbon nanotubes have been proposed as filler in TIM, the weak thermal coupling between the filler material and the base material significantly undermined the thermal conductivity of the resulting composite as compared to other carbon-based composites²²⁸⁻²³⁰. For a 1 wt% of carbon nanotubes added epoxy composite, the thermal conductivity only augmented by 125% at room temperature²²⁹. On the other hand, carbon-based filler materials of graphene⁵⁵ and GNPs¹⁵⁵ obtained astonishing enhancements in thermal conductivity of 1000% and 3000% under filler loadings of 5 vol% and 25 vol% in epoxy composites, respectively. With the significantly lower filler loadings, carbon-based TIMs are relatively cost effective as compared to their conventional counterparts. Nevertheless, the corresponding thermal conductivities of the carbon-based TIMs are mostly lower than $10\text{ Wm}^{-1}\text{K}^{-1}$, which are two to three orders of magnitude lesser than the pristine graphene sheet. The low heat conduction property of the carbon-based TIMs is attributed to the phonons scattering effect at the interfaces and the disconnected lattices.

As we can see, the development of advance heat dissipation devices such as heat spreaders and TIMs are strongly limited by the weak thermal coupling between the graphitic surfaces and the substrate interfaces. Currently, it is impossible to unleash the

full potential of a single layer graphene with its ultrahigh thermal conductivity. Thus, the progress in developing graphene-based thermal applications has rapidly slowed down as more studies indicated its weakness. Nevertheless, heat transfer need not necessary to be limited in conduction mode, another efficient and more superior mode of heat transfer is convection. To be specific, under convection mode, boiling heat transfer is considered as the most effective form of heat transfer due to the associated phase-change heat transfer. Recently, many studies indicated the enhancement in boiling heat transfer with GO and rGO nanofluids through the observation of enhanced critical heat flux. The interesting phenomenon immediately triggers the debate on the physical mechanism behind the boiling enhancement of carbon-based nanofluids. Till now, majority of the postulations has been attributed to the high thermal conductivities of GO and rGO. Nevertheless, literatures have indicated experimentally and theoretically that GO and rGO have very low thermal conductivities, which are three to four orders of magnitude lower than its precursor graphite^{207, 208, 231}. The devastating damages of the GO and rGO crystal lattices were evidenced with the high-resolution transmission electron microscopy (HRTEM)²³². While the reduction process is capable of removing the oxygenated functional groups, it also contributes to the large area of defective sites observed over the rGO. Additionally, the limiting factor of phonons scattering effects is not considered in the postulations. Thus, a more conclusive mechanism is required to connect the missing link. In the next section, we summarize all available studies on the boiling enhancement using GO and rGO nanofluids.

2.4 Graphene oxide and reduced graphene oxide nanofluids

In the attempts of enhancing the phase-change heat transfer *via* graphene-based material, GO has been selected for its water affinity characteristic. GO, a functionalized graphene derivative which contains flakes of monolayer and few-layered graphene, is prepared with a gentle sonication of graphite oxide in various solvents for facile and mass production^{233, 234}. The excellent solubility and stable dispersion in aqueous solution is attributed to the presence of the oxygen functionalities^{182, 235}. GO nanofluid – fluid containing GO nanoparticles suspension, has been investigated and shown to be capable of enhancing the CHF of an immersed heated surface deposited with GO layers⁵⁷. Unlike metal-based nanofluids, GO nanofluid illustrated a reduction in surface

wettability with the measurement of a hydrophobic contact angle of 85° on the GO deposition. The enhanced surface wettability is therefore insufficient to elucidate the boiling enhancement. The authors then attributed the enhancement in boiling heat transfer to the excellent thermal conductivity of GO which facilitated the heat dissipation of the hot spots. To illustrate the boiling enhancement, thermal activity S is utilized for the explanation. The thermal activity, which characterizes the conduction in heater, is defined as $S = \delta \sqrt{\rho_h c_h k_h}$, where δ denotes the heater characteristic dimension, ρ_h is the density of GO, c_h is the specific heat of GO and k_h is the thermal conductivity of GO. Without the available data for the thermal conductivity of GO, the authors used the thermal conductivity of graphene instead and obtained high value in thermal activity, which concluded the CHF enhancement. The authors also linked the CHF enhancement to the hydrodynamic liquid-choking limit/ hydrodynamic instability theory which involved the estimation of the Rayleigh-Taylor instability wavelength. Yet, it is inconclusive as the aforementioned theory is only applied to metallic porous layers. To our knowledge, the graphene-based materials have diverse properties as compared to conventional metals. Therefore, many questions arise on the underlying mechanism of CHF enhancement with GO nanofluid. Followed by this published work, a sharp rise in the experimental studies on boiling heat transfer enhancement with GO and rGO nanofluids is observed.

In the context of GO nanofluid, several studies have shown similar CHF enhancements with low weight percentages of GO nanoparticles added to the aqueous solution²³⁶⁻²³⁹. However, some measurements of static contact angle on GO deposition contradicted the early study⁵⁷. Several studies showed enhanced surface wettability²³⁷⁻²³⁹ while only one was in accordance to the early study of reduced surface wettability²³⁶. Yet, in both cases, the scanning electron microscopy (SEM) images of the GO deposition illustrated a well-ordered, layer-by-layer formation of laminated GO sheets with abundant nucleation sites for vapour bubble formation. Hereby, the CHF enhancement can be attributed to two different postulations corresponded to the static contact angle analysis. For the studies with reduced surface wettability, the CHF enhancement was attributed to the high thermal activity^{57, 236}. Thermal reduction of GO was also proposed to further increase the thermal conductivity as GO reduced to rGO, leading to the additional augmentation in the thermal activity with progressive heat

loading²³⁶. On the other hand, postulation of enhanced surface wettability which contributed to the CHF enhancement was also proposed²³⁷⁻²³⁹.

Similar boiling enhancements have also been demonstrated using rGO nanofluid. However, most of the postulations on CHF enhancement were similar to that of the GO nanofluid with all studies conducted by only one research group. Enhanced thermal activity^{58, 59, 240-242}, modulation in the Rayleigh-Taylor instability wavelength²⁴¹ and enhanced surface wettability²⁴⁰ were all attributed to the CHF enhancement. The thermal conductivity of rGO is often envisaged to be similar to that of the bulk graphite. Postulation derived in most of the studies explaining the boiling heat transfer enhancement of rGO nanofluid were based on such conjecture which ultimately led to the augmented thermal activity^{58, 59, 240-242}. Thus, it is necessary to understand the synthesis of rGO and most importantly its thermal conductivity. Generally, rGO deposited layer is synthesized from chemical²⁴³ or thermal reduction²⁴⁴ of graphene oxide deposited layer. Yet, the reduction processes of rGO deposited layer are insufficient to rejuvenate the oxidized graphene sheets due to the permanent disruptions in the covalent sp^2 bonding and lattice defects yielded in the oxidization process^{52, 181}. Moreover, the size of individual rGO sheets is in the range of 0.5 μm - 1 μm ⁵⁸. This directly contributes to the heat transfer limitation of phonons scattering effect at the grain boundaries²¹⁵. Not to mention the weak thermal coupling of the rGO deposited layer with the substrate (interfacial phonons scattering effect)^{52, 56}, it is impossible for rGO deposited layer to obtain similar thermal conductivity as bulk graphite. Notably, the thermal conductivity of rGO was often compared to that of the ultrathin graphite embedded in SiO_2 substrate studied by Jang et al²¹³, whereby the in-plane thermal conductivity increased with the graphite thickness. However, this comparison is inappropriate due to the diverse synthesis methods of ultrathin graphite and rGO, producing significant differences in the heat transfer characteristic. To strengthen our postulation, the actual thermal conductivity of rGO is in the range of 0.14 - 2.87 $\text{Wm}^{-1}\text{K}^{-1}$, which is four orders of magnitude lesser than the pristine graphene²⁰⁷. Furthermore, we emphasize that the enhancement in boiling heat transfer is strongly associated with the effective nucleation and departure of the vapour bubbles. The consensus of enhanced heat conduction across rGO deposition with insignificant thickness may not contribute to the dramatic enhancement in CHF. Therefore, the modulation in surface wettability of rGO deposition is more suitable to elucidate the

CHF enhancement. In one of the study⁵⁹, reduction in surface wettability was identified from the rGO deposition with the surface contact angle measured at 81.5°. Regardless of the reduced surface wettability, analysis on the vapour bubbles generated from the rGO deposition indicated a smaller bubble diameter with significantly larger nucleation site density and bubble frequency as compared to the uncoated surface. Indeed, hydrophobic surface promotes the onset of nucleation boiling, leading to the enhancement in boiling heat transfer at lower wall superheat. However, this is insufficient to explain the enhanced CHF of rGO nanofluid as hydrophobic surface also engenders the early transition to film boiling^{18, 34, 49}. Thus, the presence of an essential mechanism which fundamentally enhances the CHF of rGO nanofluid is yet to be determined.

Interestingly, water absorption on rGO deposition was observed in several studies^{58, 240, 241}. In the measurement of the contact angle on the rGO deposition, abnormal reduction in the contact angle was noted over time. As graphene oxide is well-known to be hydrophilic in nature, the authors speculated that some of the hydrophilic functional groups may have remained in the rGO due to the incomplete reduction process^{58, 240}. The water absorption phenomenon was attributed to the remaining functional groups embedded in the rGO deposition. Thus, this explains the contradicting findings in surface wettability of rGO deposition and also GO deposition. With the water absorption characteristic, the precise measurement of static contact angle on GO/rGO deposition can be challenging. Furthermore, the rough and high porosity surface morphologies of the depositions may have triggered different wetting states of the droplet. As water recedes into the deposition, irreversible transition from Cassie state to Wenzel state will be observed. Therefore, water saturated GO/rGO deposition exhibits a hydrophilic characteristic while the dry GO/rGO deposition demonstrates a hydrophobic characteristic. In order to characterize the water absorptivity of such surface, the measurement of static contact angle is more appropriate to be performed on dry deposition with the analysis of reduction in droplet's contact angle over time. However, most of the studies only measured the contact angle at an instant with no quantitative evidence supporting the water absorptivity of GO/rGO deposition. The reduction in contact angle of a droplet residing on the GO/rGO deposition will provide useful evidence and information to justify the postulation of enhanced CHF *via* water absorption. The water absorptivity of GO/rGO deposition may be similar to the

capillary pumping effect observed over micro/nanostructured surface⁴⁰⁻⁴³, which is capable of enhancing the CHF. Thus, the anomalous water absorption of GO/rGO deposition plays a critical role in overcoming the heat transfer limitations^{52, 56} encountered in the development of graphene-based heat spreaders and TIMs. Novel thermal management applications based on the enhancement in phase-change heat transfer rather than the heat conduction can be materialized in the near future.

2.5 Water permeation in graphene oxide

The anomalous water absorption characteristic of GO/rGO deposition can also be observed over their precursor graphite oxide. Apart from the strong affinity to water, graphite oxide with the abundance oxygenated functional groups is capable of absorbing liquid water and vapour when subjected to humid environment or submerged in aqueous solution^{184, 245-247}. The hydrophilic functional groups in graphite oxide act as spacers between the graphitic planes which contributed to the widening of the interlayer distance. The interlayer distance increased from the dehydrated state of 6 Å towards the hydrated state 12 Å with the intercalation of water bilayer between the graphitic planes^{184, 245-247}. Moreover, the structural expansion of the hydrated graphite oxide was sensitive to temperature variation²⁴⁵. The interlayer distance reduced with the increase of the temperature. On the other hand, the structural variation of graphite oxide upon compression was observed to be similar to those of the auxetic materials²⁴⁸. Under pressurized condition, auxetic material such as zeolite sodium aluminosilicate experiences structural expansion due to the pressure induced hydration²⁴⁹. Thus, the water intercalation effect of graphite oxide can be manipulated with the variations in temperature and also pressure. As graphite oxide consists of multilayer stacks of GO, the unique water absorption characteristic is also applied to GO deposition.

In the advancement of nanofiltration technology, fast water vapour permeation across laminated GO membrane while impeding the permeation of Helium atom was discovered by Nair et al.²⁵⁰. In the permeation experiments, GO membranes with interlocking layered structures and thickness of 0.1 µm to 10 µm were fabricated on copper substrates using spin and spray coating techniques. Freestanding GO membranes were then obtained by the chemical etching of copper. These GO membranes were then

used for the sealing of metal containers charged with gases or liquids. The permeability of GO membrane on various gases and liquids was evaluated using mass spectrometry analysis and gravimetric analysis, respectively. Permeation of He through the GO membrane was found to be much lower than that of a 1mm thick glass barrier. On the other hand, GO membrane was also impermeable to various organic liquids such as ethanol, hexane, acetone, decane and propanol. Yet, these impermeable membranes were highly permeable to water. Significant weight reduction was observed over the container filled with water. The weight reduction was identical to the case of an exposed container. In comparison with the permeability of He, the water permeability through GO membrane was found to be 10 orders of magnitude greater. The authors attributed the rapid water permeation of GO membranes to the frictionless flow of water monolayer along the non-oxidized regions embedded within the graphitic structure. The oxygenated functional groups also contributed to the water intercalation with the expanding of the interlayer distance (10 Å) but found to have vigorously interacted with the intercalating water molecules. The dependency of water permeability with GO interlayer distance was identified with the thermal annealing of GO membrane at 250°C in hydrogen-argon enclosure. The thermal reduced GO membrane yielded an interlayer distance of only 4 Å. The reduction in capillaries width impeded the intercalation of water monolayer, leading to the dramatic reduction in the water permeability. Theoretical modelling of water intercalating in graphene nanocapillaries was also conducted using atomistic simulations to strengthen the postulation of rapid water permeation. As GO membrane holds great potential in separation applications, understanding the fundamental mechanism of rapid water permeation is of great interest. Nevertheless, various postulations on the fast water permeation mechanism have been proposed both experimentally and theoretically. Among all the relevant studies, two studies reviewed several contradicting postulations and provided useful insight into the governing principles of the water permeation.

The water permeability of GO membrane with respect to the structural alteration under temperature variation was studied extensively by Andrikopoulos et al.²⁵¹. Progressive thermal treatment of GO membranes at two different temperatures of 160°C and 200°C were used for the analysis, simulating reduction in the interlayer distance with partial elimination of oxygenated functional groups and water content. The characterizations of thermally treated GO membranes were conducted using XRD, X-

ray photoelectron spectroscopy (XPS) and Fourier-transform infrared spectrometer (FTIR) whereby the affiliated variations in the interlayer distance and density of oxygenated functional groups with the water permeability of GO membranes were elucidated. Initially, the hydration behaviour of the GO membranes was investigated. Under high humidity environment (relative humidity of 85%) for 1 hour, the 100°C thermally treated GO membrane with interlayer distance of 6.19 Å was capable of recovering back to its untreated state with the interlayer distance of 7.38 Å. The structural alteration of GO membrane with the absorption and desorption of water molecules into the graphitic structure was found to be repeatable. This indicated the unique and reversible structural alteration of GO membrane which was commonly acknowledged in other studies^{184, 245-248}. In contrast, the 200°C thermally treated GO membrane revealed a significant different behaviour as compared to the 100°C thermally treated GO membrane. The interlayer distance (4.91 Å) remained unchanged even after prolonged period in humid environment. This marked the critical temperature which controlled the water permeability of the GO membranes in which the elimination of oxygenated functional groups with thermal treatment reduced the water intercalation capability of the graphitic structures. Based on the temperature and annealing time of the thermal treatment, the GO membranes were separated into three different sets (mild reduction, intermediate reduction and extreme reduction), each representing different range of interlayer distance (>7.5 Å, ≈ 6 Å and ≈ 5 Å). High water permeability of $2315 \text{ gd}^{-1}\text{m}^{-2}$ was measured over the GO membrane of mild reduction. The corresponded interlayer distance of more than 7.5 Å was critical in providing sufficient spacing between the graphite structures for fast water permeation. GO membranes from the intermediate reduction set yielded only half of the initial water permeability and reduced sharply with the prolonged annealing time of 300 minutes under the temperature of 160°C. The drastic reduction in the water permeability was attributed to the reduced interlayer distance measured at 5 Å. Similar water permeability and interlayer distance were obtained from the GO membranes of the extreme reduction set. By heating the GO membranes at 200°C for 60 minutes, the interlayer distance reduced to 4.91 Å with a water permeability of only $170 \text{ gd}^{-1}\text{m}^{-2}$. As a result, oxygenated functional groups embedded between the graphitic planes play a critical role in ensuring the fast water permeation. The authors associated the step-like behaviour in the water permeability to the reduction in interlayer distance to a recent molecular dynamic simulation indicating the presence of ice bilayer intercalating in GO membrane. In this

theoretical study, the fast water permeation was attributed to the formation of well-ordered bilayer ice between the graphitic structures together with the melting transition at the edges of the GO flakes²⁵². Although the formation of ice bilayer may be controversial, the number of water layers intercalating through the graphitic structures is adequate to elucidate the step-like behaviour in water permeability of the GO membranes. For GO membranes of the mild reduction set, the interlayer distance above 7.5 Å allowed the intercalation of water bilayer through the graphitic layers. The water permeability then decreased by half for the intermediate reduction set as the interlayer distance reduced to 6 Å which only allowed the formation of water monolayer. This was in accordance with the minimal interlayer distance for hydrated graphite oxide^{184, 245-247}. As the interlayer distance reduced below the minimal interlayer distance for water intercalation, the fast water permeation of GO membrane vanished.

Intuitively, the liquid permeability of GO membrane is assumed to be identical with its precursor graphite oxide powder as they are chemically identical. In other words, only water molecules are able to permeate through the GO membrane as well as the graphitic layers of the graphite oxide flakes. Surprisingly, graphite oxide flakes were capable of intercalating four ethanol monolayers while GO membrane only allowed one ethanol monolayer²⁵³. The one ethanol monolayer was found to have strongly pinned to the graphitic structures which explained the limited permeation of GO membranes found in the earlier study by Nair et al.²⁵⁰. State-of-art synchrotron radiation X-ray diffraction equipment was utilized in the study of structural variation with respect to various liquids (water, ethanol and water-ethanol mixtures) and temperature (-133°C to 27°C)²⁵³. The uniqueness of Synchrotron is the capability of measuring the interlayer distance of a material in the excess of liquid. As compared to the previous study²⁵¹, the interlayer distance of the GO membrane was estimated in the dehydrated state due to equipment limitation. Thus, it is difficult to visualize the actual structural alteration of the GO membrane under hydrated state. In this study, the structural alteration of hydrated GO membrane can be well analysed. Coupled with a chiller, the structural alterations of GO membrane and graphite oxide powder submerged in various liquids under progressive cooling were systematically determined. To be concise, we focus our review only on the structural alteration of GO membrane in water. The initial characterization of GO membrane indicated an interlayer distance above 7.5 Å. As the GO membrane was submerged in excessive water at room temperature, the interlayer

distance expanded to 12.3 Å with the intercalation of at least two water monolayers (estimated 2.7 Å per water monolayer). With the solidification of water at low temperature, reduction in the interlayer distance (1.7 Å) was obtained. This reduction was attributed to the de-insertion of liquid-like water monolayer from the graphitic structures. Although the reduction was much lower than the estimated diameter of a water monolayer, the authors suggested that only a fraction of the GO membrane experienced the de-insertion as a result of the highly packed graphitic layers. Thus, GO membrane immersed in excessive water at ambient temperature is capable of intercalating two water monolayers. Under low temperature, one solidifies while the other having liquid-like property can be de-inserted from the graphitic planes. The insertion and de-insertion of water monolayer are reversible with temperature variation. As a matter of fact, several studies have emphasized that the intercalation of first water monolayer strongly interacted with the graphitic planes while the second water monolayer exhibited a translation motion over the first layer^{184, 246}. These findings contradict the postulation of fast water permeation through the networks of interconnecting graphene nanocapillaries formed by the non-oxidized regions of GO^{250, 252}. Furthermore, GO under HRTEM showed only a 16% coverage of the non-oxidized regions per side²³². The functional groups dominated graphitic planes of GO are therefore unlikely to facilitate the formation of interconnecting graphene nanocapillaries. As for the postulation of bilayer ice formation²⁵², the authors emphasized the invalidity based on the absences of additional reflections in the XRD analysis and infrared spectra of ordered water structure. The fast water permeation of GO membranes was attributed to the lattice expansion with the intercalation of water molecules across the non-oxidized regions as well as the oxidized regions. The rapid insertion and de-insertion of second water monolayer over the highly pinned water monolayer is identified as the fundamental mechanism of fast water permeation across GO membranes.

2.6 Phase-change heat transfer enhancement with fast water permeation of graphene derivatives

With the inherent characteristic of fast water permeation in GO membranes, the anomalous CHF enhancement of GO nanofluid can be fundamentally explained. Herein, the missing link between the phase-change heat transfer enhancement and the fast water

permeation of GO deposition is reconnected. The fast water permeation of GO deposition mimics the capillary pumping effect of micro/nano hydrophilic structures^{41, 42, 50}, preventing the formation of hotspot through effective water distribution. The water distribution mechanism of GO deposition is believed to be far more effective than those experienced under the capillary pumping effect of micro/nano hydrophilic structures. Furthermore, the permeation of GO membrane is not limited by the states of matter, i.e., apart from liquid water, water vapour is also capable of permeating through the GO membrane. This unique characteristic of GO deposition may hold great potential in suppressing the Leidenfrost effect commonly encountered in high power thermal management systems. While GO deposition is capable of intercalating with water molecules, the controllable microscopic to macroscopic thickness of the deposition can be utilized to induce filmwise evaporation²⁵⁴⁻²⁵⁶. Filmwise evaporation is far more superior to pool boiling and only occurs at liquid meniscus of thickness $<10\ \mu\text{m}$ on a heated surface. The evaporation in microchannel is predominated by filmwise evaporation. Regardless of the relatively small region of micro-meniscus, more than 50% of the total evaporation heat transfer and 90% of the reduction in solid-liquid interface temperature were contributed by the evaporation of micro-meniscus²⁵⁵. In the absence of the capillary pressure, region with micro-meniscus from a liquid droplet on flat surface will be significantly smaller, only at the droplet's edge, which is insufficient to facilitate filmwise evaporation. Thus, hydrated GO layers in nanometer range can be utilized to enhance the evaporation heat transfer of a heated surface. Till now, the utilization of such favourable attribute of GO is only available for CHF enhancement using GO nanofluid. Not to mention that in all related studies, none has attributed the augmentation of CHF to the fast water permeation of GO. The unique water permeation characteristic of GO will inspire the future development of novel graphene-based thermal management systems. The limiting factors in current graphene-based thermal management systems (heat spreaders and TIMs) can be eliminated by the substitution of conduction heat transfer with phase-change heat transfer. Moreover, the water absorption phenomenon is not limited to GO, but also includes the deposited layers of other graphene derivatives. Anomalous water absorption phenomenon has been frequently reported across depositions of graphite²⁵⁷, reduced graphene oxide (RGO)^{258, 259}, GNPs²⁶⁰ and carbon nanotubes²⁶¹. Thus, apart from GO deposition, other graphene derivatives also hold great potential in enhancing the phase-change heat transfer.

Chapter 3

Coupled effects of hydrophobic layer and vibration on thermal efficiency of two-phase closed thermosyphons

Tong, W.L., Tan, M.K., Chin, J.K., Ong, K.S. & Hung, Y.M. Coupled effects of hydrophobic layer and vibration on thermal efficiency of two-phase closed thermosyphons. *RSC Advances* 5, 10332-10340 (2015).

URL: <http://pubs.rsc.org/en/content/articlelanding/2015/ra/c4ra14589e>

DOI: 10.1039/C4RA14589E

3.1 Outline

With the water-repellent characteristic, hydrophobic or superhydrophobic surfaces are commonly used to facilitate dropwise condensation on a condenser surface. Unfortunately, the condensation in a TPCT is a typical example of filmwise condensation where thick liquid condensate layers cover the surface, incurring a larger thermal resistance to heat transfer between the vapor and the condenser wall^{7, 262}. Apart from the much lower heat transfer coefficient as compared to dropwise condensation^{17, 18, 60}, filmwise condensation also engenders flooding of condensates in the condenser at high heat input¹³⁻¹⁵. Thus, surface inducing dropwise condensation is desirable to be integrated in the condenser section of a TPCT. As mentioned in the literature reviews, condensation on superhydrophobic surface is associated with several critical problems. These not only reduce the condensation heat transfer⁸⁰, but also constitute a significant barrier in the technological adoption. In short, the effective droplet removal of superhydrophobic surface is momentary and quickly converts into the less favorable filmwise mode with the penetration of liquid into the textured surface^{83, 85-89}. The loss of superhydrophobicity is expected to be more severe under high humidity condition, which is similar to the vapor saturated condition in a TPCT. Therefore, the contemporary artificial superhydrophobic surfaces are not suitable for integration with TPCT. In this study, flat hydrophobic layer of Teflon AF-1600 is utilized to induce dropwise condensation in a TPCT.

Similar to the hydrophobic layer, the introduction of vibratory force also contributes to the reduction in contact forces between the condensed liquids and the TPCT wall⁹⁷. Thus, the thermal performance of a TPCT with coupled effects of hydrophobic layer and vibration is expected to be substantially enhanced. A well-defined parameter for the falling rate of condensed droplets and the strength of evaporation is proposed to elucidate their relationship. To ensure these approaches are working with different working fluids, water and silver-oxide nanofluid are employed. The use of nanofluid, which is essentially a base fluid with nanoparticle suspension²⁶³, has been reported to be able to enhance the heat transfer characteristic of the conventional fluids^{264, 265}. Nanofluid poses distinct thermal and hydrodynamic characteristics from the conventional fluid associated with its distinguished transport properties such as thermal conductivity, heat capacity, viscosity and surface tension. It

is instructive to investigate the coupled effects of the hydrophobic surface at condenser wall and the high-acceleration induced vibration on the nanofluid judging from the prominent changes induced in its thermo-physical properties. In this study, imperative information is obtained from the exposition of the size and distribution of condensate droplets in the analysis of circulation effectiveness. The underlying physical significance of the coupled effects of hydrophobic layer and vibration on the thermal efficiency is outlined.

Monash University
Declaration for Thesis Chapter 3

In the case of Chapter 3, the nature and extent of my contribution to the work was the following:

Nature of contribution	Extent of contribution (%)
I was the chief investigator for this work. My contributions to this research were the design and fabrication of the experimental setup, conducting experiments, data analysis and preparation of manuscript.	80

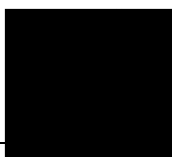
The following co-authors contributed to the work.

Name	Nature of contribution
A/Prof. Hung Yew Mun*	Overall supervision
Dr. Tan Ming Kwang	Overall supervision
Dr. Chin Jit Kai	Overall supervision
Prof. Ong Kok Seng	Overall supervision

The undersigned hereby certify that the above declaration correctly reflects the nature and extent of the candidate's and co-authors' contributions to this work*.

**Candidate's
Signature**

Tong Wei Li



Date: 1 June 2016

**Main
Supervisor's
Signature**

A/Prof. Hung Yew Mun



Date: 1 June 2016

3.2 Experimental investigation

3.2.1 Preparation of hydrophobic coating

Teflon AF-1600 amorphous fluoroplastics which was purchased from DuPont, Inc. is used to form a hydrophobic layer in TPCT. The hydrophobic coating is deposited onto the inner section of a standard glass tube *via* spin-coating technique to assure the uniformity of the coating. A total of 10 millilitres of Teflon solution is gently flushed through the glass tube which is then spin coated at a constant speed of 1500 rpm for 30 minutes. Subsequently, the coated glass tube is heated in a furnace with a gradual increase in temperature to a maximum of 250°C for 30 minutes. Finally, a uniform thin transparent layer of hydrophobic coating on the inner wall surface of TPCT is obtained.

3.2.2 Experimental setup

A schematic diagram of the experimental setup is illustrated in Figure 3.1. The setup includes a mini TPCT, electrical heater, water cooling jacket, vibrator and measuring instruments. The TPCT is fabricated with a glass tube of inner diameter of $d_i = 13.5\text{mm}$ and length of $L = 110\text{mm}$. The glass tube is sealed by using a rubber stopper connected with an access valve for charging of working fluid into the tube (Figure 3.1(a)). To ensure the TPCT is airtight, epoxy is applied at all connections. Two different types of working fluid are selected: distilled water and a nanofluid. For nanofluid preparation, silver-oxide (Ag_2O) nanoparticles (Sigma-Aldrich, Inc.) with an average particle size of 30 nm and volume fraction of 1% are dispersed in deionized water under mild ultrasonication treatment. The mixtures are ultrasonicated (20 kHz, 700 W) with an ultrasonic processor (Q700 Sonicator[®], Qsonica, LLC.) for 5 hours with fluid temperature maintained below 80°C to prevent evaporation. The TPCT is charged with 1ml of working fluid, which is equivalent to 16.67% of volume fill ratio. It is a common practice to charge the TPCT with a volume fill ratio which is in the range of 13.5% - 20%.^{5, 266} This range of fill ratio is considered as the optimal fill ratio in which case there is neither dryout nor flooding taking place in the TPCT. Once the working fluid is charged into the tube, the pressure within the tube is reduced using a vacuum pump, which is connected to the access valve, as shown in Figure 3.1(a). The pressure in the tube prior to heating is maintained at 0.2 Pa for all tests. The evaporator section is

heated with an electrical heating element, whereas the condenser section is cooled with a water cooling jacket, as depicted in Figure 3.1(b).

The experiments are conducted in a controlled environment with a room temperature maintained at 26°C with a fluctuation of $\pm 1.5^\circ\text{C}$. Power input to the electrical heater is controlled by a DC power supply (EA-PSI 8160-04 LCD, EA Elektro-Automatik). Surface temperature on the TPCT is measured using six type-T thermocouple wires with an overall accuracy of 2%, which are connected to a MIDI logger (GL820, Graphtec Co.), with an accuracy of 0.05%. Figure 3.1(a) shows the locations of the thermocouple wires. For each test, the temperatures are recorded for 60 minutes, with an interval of two seconds between each recording. To investigate the effect of vibrations, the TPCT is positioned on a vibrating plate excited by a speaker (vibrator), which is connected to an amplifier and a function generator, as shown in Figure 3.1(b). The TPCT is placed atop a thin plate attached to a speaker (TD 8", Motivity[®]), to provide lateral vibration to the system. The signal generated by the function generator (TG5011, Thurlby Thandar Instruments limited) is amplified by an amplifier (LZY-22, Mini-Circuits[®]) before it is transmitted to the speaker. The frequency of excitation is 63Hz.

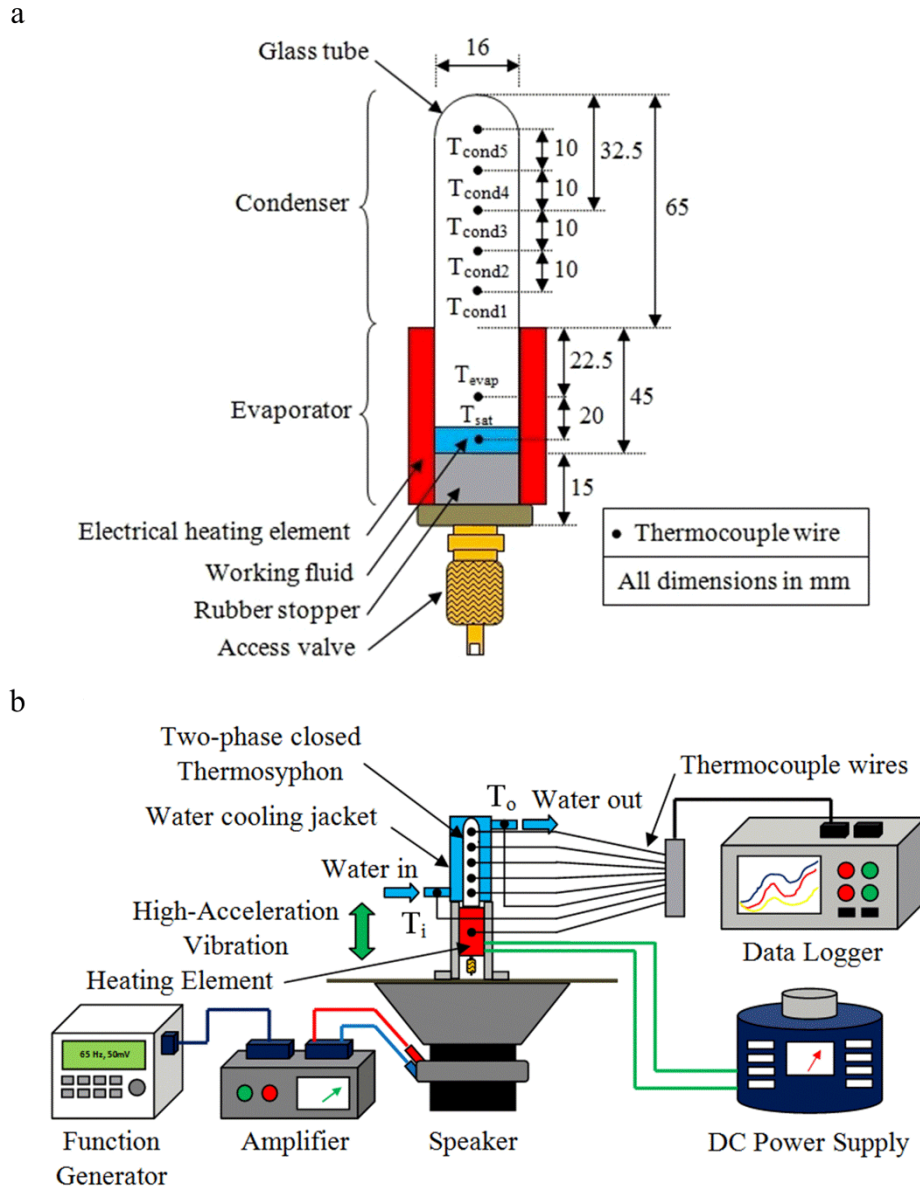


Figure 3.1| (a) Schematic diagram of the basic components of a two-phase closed thermosyphon (TPCT). (b) Experimental setup for the thermal efficiency evaluation of TPCT.

3.2.3 Thermal efficiency of TPCT

The thermal efficiency of a TPCT is governed by the circulation effectiveness and the strength of latent heat of evaporation of the working fluid. The thermal efficiency of a TPCT can be quantified with the performance indicators such as the effective thermal resistance R_{eff} and the average evaporator heat transfer coefficient \bar{h}_e . Lower thermal resistance indicates better overall thermal performance while larger value of evaporator

heat transfer coefficient manifests higher strength of latent heat of evaporation. The overall thermal performance can be characterized using the effective thermal resistance which is obtained by evaluating the axial temperature drop, $\Delta T = T_{\text{evap}} - T_{\text{cond}}$, along the longitudinal direction of TPCT for a heat input. The effective thermal resistance is calculated as

$$R_{\text{eff}} = \frac{T_{\text{evap}} - T_{\text{cond}}}{\dot{Q}_a} \quad (3.1)$$

where T_{evap} is the temperature at the evaporator, T_{cond} is the temperature at the condenser, and \dot{Q}_a is the heat transport rate of the TPCT. Notably, T_{cond} is taken here as the average temperatures measured across the condenser section. The heat transport rate, \dot{Q}_a , which is calculated based on the principle of energy conservation whereby the net heat transported across the TPCT is equivalent to the heat dissipated from the condenser section. The total convection heat transfer of the water flowing across the water jacket is determined as $\dot{Q}_a = \dot{m}c_p(T_o - T_i)$, where \dot{m} represents the mass flow rate of the water flow, c_p is the specific heat capacity of water. T_i and T_o denote the inlet and outlet water temperatures of the cooling jacket mounted onto the condenser section.

The average evaporator heat transfer coefficient, \bar{h}_e , is used to quantify the strength of evaporation, given by $\bar{h}_e = \dot{Q}_a / (\pi d L_e (T_{\text{evap}} - T_{\text{sat}}))$, where T_{sat} is the saturation temperature of the working fluid, d is the inner diameter of the TPCT and L_e is the axial length of the evaporator section. During the experiments, the heat input is kept at a constant value and the evaporator heat transfer coefficient augmentation ratio can be expressed as

$$\eta = \frac{\bar{h}_e}{\bar{h}_{e,0}} = \frac{(T_{\text{evap},0} - T_{\text{sat},0})}{(T_{\text{evap}} - T_{\text{sat}})} \quad (3.2)$$






where $\bar{h}_{e,0}$ is the average evaporator heat transfer coefficient for the case of uncoated TPCT using water as working fluid. To scrutinize the heat transfer enhancement at the evaporator section, η is the relative comparison of the evaporator heat transfer

coefficients by using the value of uncoated TPCT as the basis for comparison. The heat transfer is enhanced when η is greater than unity and vice versa.

3.2.4 Evaluation of static contact angle

The static contact angle θ_s between the liquid and the substrate under different conditions are measured using a standard goniometer (Model 590, Ramé-Hart Instrument Co.) under atmospheric pressure and a room temperature of 26°C. Table 3.1 shows the results of the contact angle measurements under different conditions. For glass coated with a thin hydrophobic layer, the contact angle is slightly lower for nanofluid ($\theta_s \approx 118^\circ$) as compared to the distilled water ($\theta_s \approx 120^\circ$). With the addition of surfactant to the distilled water on the hydrophobic surface, the static contact angle decreases ($\theta_s \approx 73^\circ$). The reduction in static contact angle of the nanofluid was studied by Wasan and Nikolov²⁶⁷. It was found that the nanoparticles near the liquid-contact line tend to increase the spreading of the nanofluid, resulting in the decrease of the static contact angle.

Table 3.1 Static contact angle measurement for two different working fluids: distilled water and nanofluid, on glass surfaces with and without the hydrophobic coating.

				
Water on uncoated glass	Water with surfactant on coated glass	Water on coated glass	Nanofluid on uncoated glass	Nanofluid on coated glass
$\theta_s = 24^\circ$	$\theta_s = 73^\circ$	$\theta_s = 120^\circ$	$\theta_s = 40^\circ$	$\theta_s = 118^\circ$

3.2.5 Experimental uncertainty

The experimental uncertainties associated with the calculation of the heat transport rate, \dot{Q}_a , effective thermal resistance R_{eff} and the heat transfer coefficient \bar{h}_e were calculated according to the monograph by Holman²⁶⁸ and displayed in Table 3.2. The following equations were implemented for the uncertainty analysis:

$$\frac{\Delta \dot{Q}_a}{\dot{Q}_a} = \sqrt{\left(\frac{\Delta \dot{m}}{\dot{m}}\right)^2 + \left(\frac{\Delta T_o}{T_o}\right)^2 + \left(\frac{\Delta T_i}{T_i}\right)^2} \quad (3.3)$$

$$\frac{\Delta R_{\text{eff}}}{R_{\text{eff}}} = \sqrt{\left(\frac{\Delta \dot{Q}_a}{\dot{Q}_a}\right)^2 + \left(\frac{\Delta T_{\text{evap}}}{T_{\text{evap}}}\right)^2 + \left(\frac{\Delta T_{\text{cond}}}{T_{\text{cond}}}\right)^2} \quad (3.4)$$

$$\frac{\Delta \bar{h}_e}{\bar{h}_e} = \sqrt{\left(\frac{\Delta \dot{Q}_a}{\dot{Q}_a}\right)^2 + \left(\frac{\Delta T_{\text{evap}}}{T_{\text{evap}}}\right)^2 + \left(\frac{\Delta T_{\text{sat}}}{T_{\text{sat}}}\right)^2} \quad (3.5)$$

Table 3.2| Estimation of uncertainty.

Parameter	Uncertainty (%)
Heat transport rate \dot{Q}_a	2.43
Effective thermal resistance R_{eff}	2.62
Heat transfer coefficient \bar{h}_e	2.81

3.3 Results and discussion

3.3.1 Effect of hydrophobic surface

Figure 3.2 shows the plots of the effective thermal resistances R_{eff} as a function of heat transport rate, \dot{Q}_a , for three different contact forces between the working fluid and the TPCT wall: water on bare glass ($\theta_s \approx 24^\circ$), water added with surfactant on coated glass ($\theta_s \approx 73^\circ$), and, water on coated glass ($\theta_s \approx 120^\circ$), representing the cases for high, mid, and low contact force, respectively. In the cases of low and mid contact force, R_{eff} is lower compared to that of high contact force. At $\dot{Q}_a = 15.5\text{W}$, for the cases of low and mid contact force, R_{eff} records a reduction of 16.9% and 11.4%, respectively. A smaller R_{eff} indicates a higher heat transport capability of the TPCT.

The reduction in the R_{eff} can be attributed to the presence of hydrophobic coating that lowers the contact force F_c , which then facilitates the falling of condensed droplets back to the evaporator. It is observed that by reducing the contact force F_c between the condensed droplets and the wall of TPCT, the effective thermal resistance R_{eff} is further reduced due to the enhanced flow circulation of the working fluid.

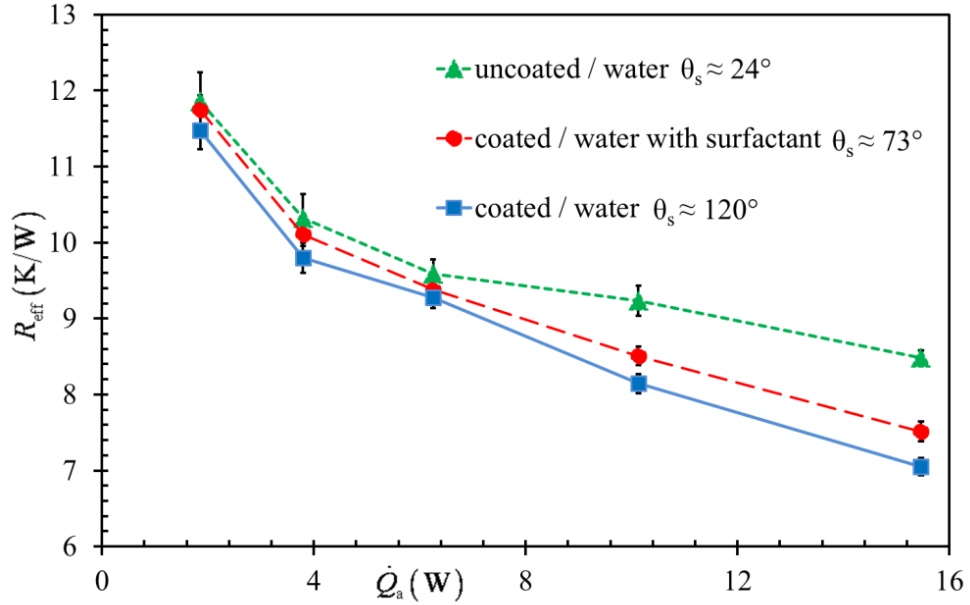


Figure 3.2 Effective thermal resistance, R_{eff} , as a function of heat transport rate, \dot{Q}_a , for three different cases: water on uncoated glass ($\theta_s \approx 24^\circ$), water added with surfactant on coated glass ($\theta_s \approx 73^\circ$), and, water on coated glass ($\theta_s \approx 120^\circ$).

On the other hand, the strength of evaporation is observed to be indirectly affected by the contact force, as shown in Figure 3.3, which depicts the evaporator heat transfer coefficient augmentation ratios η for two cases: water added with surfactant on coated glass ($\theta_s \approx 73^\circ$), and, water on coated glass ($\theta_s \approx 120^\circ$), using the case of water on bare glass ($\theta_s \approx 24^\circ$) as the baseline for comparison. For the range of heat transport rate under investigation, we can observe that the enhancement of heat transfer coefficient increases with the decrease in the contact force. For the case of smaller contact force (water on coated glass), the enhancement in the heat transfer coefficient can exceed 20.4% at high heat transport rate. It is shown that the enhancement in circulation effectiveness and strength of evaporation is inherently simultaneous.

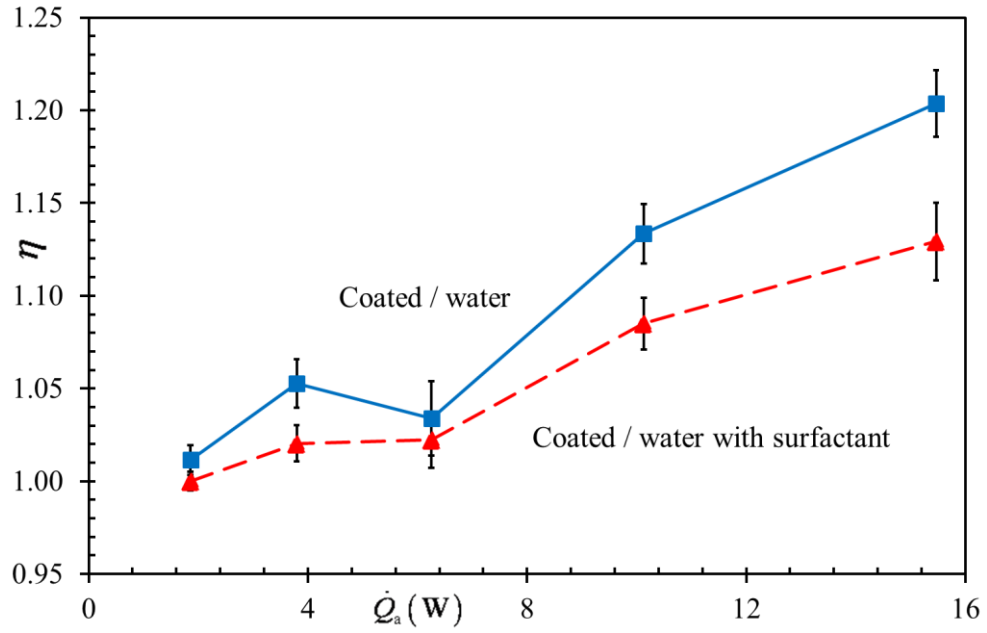


Figure 3.3 Evaporator heat transfer coefficient augmentation ratio, η , as a function of heat transport rate, \dot{Q}_a , for two different cases: water added with surfactant on coated glass ($\theta_s \approx 73^\circ$) and water on coated glass ($\theta_s \approx 120^\circ$).

The size and distribution of the droplets are important factors in governing the mechanism of condensation heat transfer in a TPCT. We shall, therefore, be concerned with the size and distribution of the droplets in the following. Figure 3.4(a, b) shows the time-lapse images of the morphology of condensed droplets on the interior wall of the uncoated and coated TPCT with the hydrophobic layer, respectively. Evidently, the diameters of the condensed droplets on the coated glass tube are observed to be significantly smaller than those on the uncoated glass. We also note that dropwise condensation is prevalent in the former while film condensation occurs in the latter. As observed in Figure 3.4(b) for dropwise condensation, when the droplet size increases to a diameter of $650 \mu\text{m}$ (as indicated with an arrow), the droplet starts to detach from the wall surface and move downwards coalescing with other droplets. The sliding speed increases as more droplets are combined. Subsequently, nucleation of new droplets can be observed as illustrated in the dashed circles. This shows that the surface refreshment rate (departure rate of condensed droplets on a hydrophobic surface) is high, allowing a continuous dropwise condensation to occur on the wall surface. On the contrary, Figure

3.4(a) illustrates the droplet growth cycle of an uncoated glass surface. The departure diameter is found to be larger than that of the hydrophobic surface. The largest droplet diameter is measured to be more than $2500\ \mu\text{m}$ with no sign of droplet departure. It has been shown that the typical droplet departure diameter on an uncoated glass surface under film condensation is between $2\ \text{mm}$ to $3\ \text{mm}$ ¹⁷. Continuous coalescence of neighbouring droplets forms non-circular droplets, indicating a weak three-phase contact line with a large contact angle hysteresis^{269, 270}. The large droplets on the wall surface form a thermal barrier which inhibits the condensation of the vapour, and hence reducing the overall condensing heat transfer coefficient. Furthermore, large droplets which occupy the surface reduce the area for vapour condensation, hindering the droplet growth rate in a TPCT.

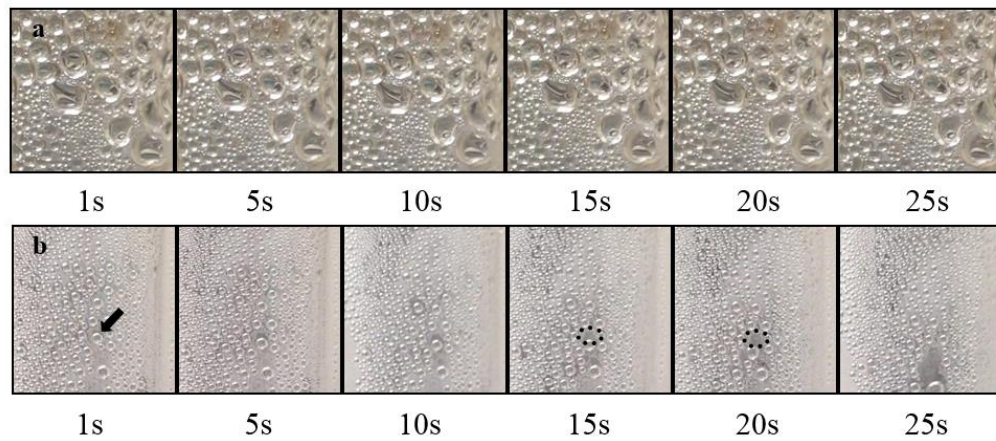


Figure 3.4| Time-lapse images of the morphology of condensed droplets on the interior wall of the (a) uncoated TPCT, and, (b) coated TPCT.

To have a detailed view on the size and distribution of droplets on the mechanism of condensation, we quantify the average diameter range and the number of droplets condensing on the TPCT wall surface. SigmaScan[®] Pro (Systat Software, CA, USA) is used for image processing and analysis of droplet distribution and droplet size. Figure 3.5(a, b) depicts the average droplet count, N , as a function of droplet diameter, D , for the uncoated and coated surfaces, respectively. The diameters of the condensed droplets on the uncoated glass tube ($100\ \mu\text{m} - 2500\ \mu\text{m}$) are observed to be significantly larger than those on the coated glass ($50\ \mu\text{m} - 650\ \mu\text{m}$).

To scrutinize the droplet distribution over the entire wall surface of the condenser, we use the total surface area of condenser as the basis for comparison. A relative comparison parameter between the covering surface area of droplet, A_d , and the total surface area, A_t , is quantified as $\delta = A_d/A_t$. The δ value is evaluated by analyzing the marked surface area covered by the droplets on the condenser wall using SigmaScan[®] Pro image processing software. At a fixed heat transport rate of 15.5 W, high definition images are taken continuously for every minute during the steady state of the experiments. To ensure the accuracy of the measurement of randomly distributed droplets on the surface, a total of 24 images from 3 independent sets of experiment are analyzed. The surface area covered by the droplets, A_d , on a specific region on the condenser wall with an area of $A_t = 10\text{mm} \times 10\text{mm}$, is marked. By setting a reference length scale, SigmaScan[®] Pro is used to measure the total surface area covered by the droplets. The δ value is calculated based on the statistical mean of a sample size of 24. It is found that at an instant of steady operation of a TPCT, we measure $\delta = 33.7\%$ for the coated hydrophobic surface and $\delta = 67.7\%$ for the uncoated surface. This attests the fact that the hydrophobic surface which repels water molecules yields higher circulation rate for the condensate from the condenser to the evaporator. In addition, the hydrophobic surface provides larger liquid-free and sub-cooled surface for nucleation of new droplets and hence the condensation rate is enhanced.

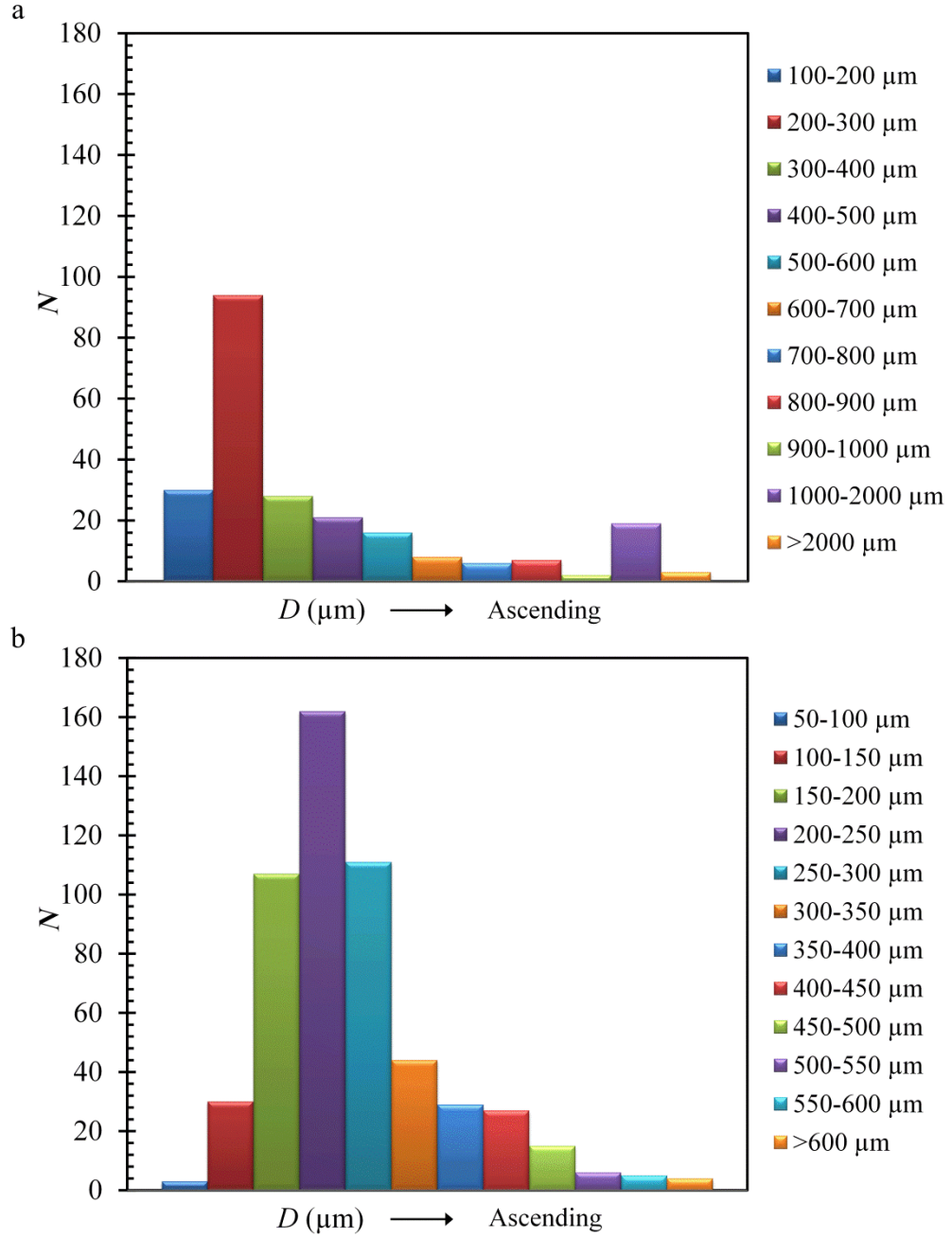


Figure 3.5| Average droplet count, N , as a function of droplet diameter, D , for the (a) uncoated and (b) coated surfaces.

As the condensate liquids accumulate and increase in size at the condenser, two dominant competing forces - body force F_b and the contact line pinning force F_c exert on these condensed liquid. The shear force at the liquid-vapor interface F_s is assumed to be negligible. This point has been justified by comparing the order of magnitude of the interfacial shear force and that of the body force in an independent set of experiments.

By virtue of low relative velocities associated with the vapor flow and the droplet motion, it is found that the body force F_b is at least 10^4 times of the shear force F_s . Therefore, together with the assumption of a uniform vapor temperature, the interfacial shear force acting on the surface of the liquid droplet can be neglected. To characterize the two dominant forces acting on a droplet, the Bond number is used and it is given by $Bo \equiv \rho_l g \ell^2 / \gamma (\cos \theta_A - \cos \theta_R) \equiv F_b / F_c$, where ρ_l is the liquid density, g is the gravitational acceleration, ℓ is the characteristic length defined as the radius of droplet, γ is the coefficient of interfacial surface tension, θ_A is the advancing contact angle and θ_R is the receding contact angle of the droplet. When the body force becomes larger than the contact line pinning force, i.e., $F_b > F_c$ or $Bo > 1$, the condensed liquids fall to the evaporator, completing a loop circulation from evaporator to condenser. The contact line pinning force increases with the decrease of contact angle. The decrease in static contact angle greatly affects the dynamic behaviour of the droplet. The contact line of the three phases (solid, liquid, and vapour) deteriorates with the decrease of the static contact angle, increasing the contact area of the droplet²⁶⁹. As a result, the contact line can be easily deformed, resulting in an increase of contact angle hysteresis. Contact angle hysteresis is defined as the difference between the advancing and the receding angles. High contact angle hysteresis impedes the movement of the droplet and higher external force is required for the droplet to overcome the pinning force F_c . Hence, for the droplet to depart, accumulation in size is required to increase the body force F_b . As noted earlier that $Bo \equiv F_b / F_c$ and the liquids start to fall back to the evaporator when $F_b > F_c$. Therefore, by reducing the F_c , the condensed droplets begin to fall back to the evaporator at a smaller body force. Since the body force is directly proportional to the volume of the condensed liquid, i.e., $F_b = mg = \rho Vg$, for the TPCT coated with the hydrophobic layer, the diameter of the condensed droplets should be much smaller than those without coating. This is consistent with the experimental images shown in Figure 3.4 for condensed droplets on the interior wall of the TPCT with and without the hydrophobic coating. The diameters of the condensed droplets on the uncoated glass tube are observed to be significantly larger (100 μm – 2500 μm) than those on the coated glass (50 μm – 650 μm), inferring that the former is film condensation whereas the latter is dropwise condensation. For film condensation, a thick layer of condensed liquid covers the wall surface, lowering the heat transfer rate. On the other hand,

dropwise condensation allows for more continuous condensation to occur on the wall surface. This in turn results in high surface refreshment rate, i.e. the departure rate of condensed droplets, thereby improving the resultant heat transfer rate. It has been shown that the heat transfer coefficient for dropwise condensation is an order of magnitude higher than that for film condensation¹⁷. Therefore, the hydrophobic surface not only improves the circulation by increasing the falling rate of condensed droplets, it also facilitates the formation of dropwise condensation, which further improves the heat transport capability of the TPCT.

To elucidate the relationship of the falling rate of condensed droplets and the strength of evaporation, in the uncoated and coated TPCT, we recast the experimental data in terms of a new dimensionless number

$$\Psi \equiv \frac{\text{Bo}}{\text{Ja}} \equiv \frac{\rho_l g \ell^2}{\gamma (\cos \theta_A - \cos \theta_R)} \frac{h_{fg}}{c_p (T_{\text{evap}} - T_{\text{sat}})} \quad (3.6)$$

where Ja is the Jakob number, defined as⁶⁰ $\text{Ja} = c_p (T_{\text{evap}} - T_{\text{sat}}) / h_{fg}$, with h_{fg} being the latent heat of vaporization and c_p the specific heat capacity. In the context of present work, a larger Jakob number represents the case of higher sensible heat absorbed from the evaporator and hence a more intense evaporation rate, whereas, a larger Bond number represents the case of higher falling rate of condensed droplets to the evaporator. The plots of Ψ as a function of heat transport rate \dot{Q}_a for uncoated and coated TPCTs are shown in Figure 3.6. At each fixed heat transport rate, the Ψ for the coated (hydrophobic) TPCT is higher than that for the uncoated (hydrophilic) TPCT, indicating the falling rate of condensed droplets in the coated TPCT is higher than that in the uncoated TPCT. On the other hand, as the heat transport rate is proportional to the heat input power of the heater, for both uncoated and coated TPCT, the Ψ reduces with the increase of the heat input power due to the increase in the evaporation rate (higher Ja).

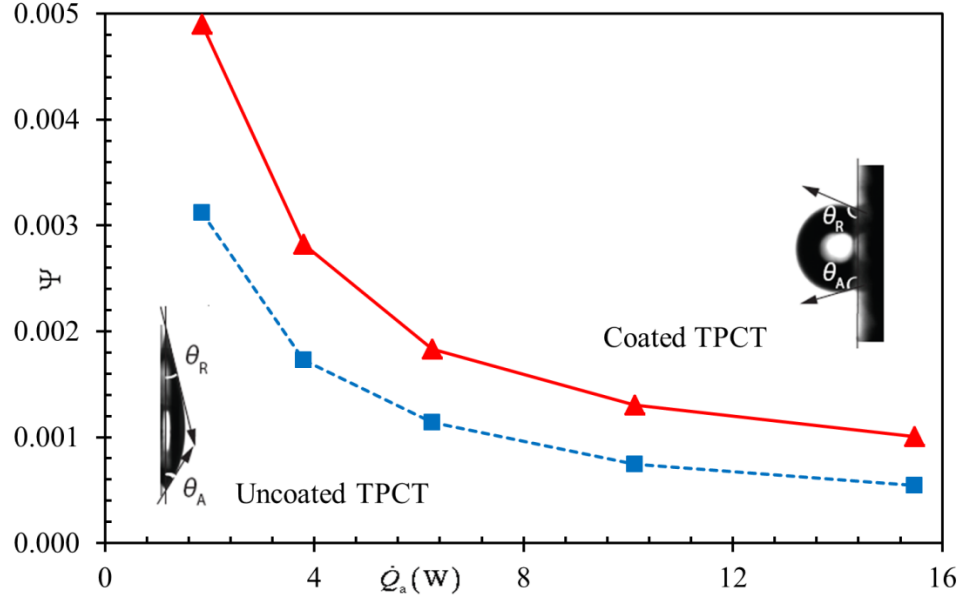


Figure 3.6 | Relation between the dimensionless number and the heat transport rate for coated (hydrophobic) and uncoated (hydrophilic) TPCT. The insets show the estimation of the advancing angle and receding angle for a sessile droplet on a hydrophobic and hydrophilic substrate

3.3.2 Coupled effects of hydrophobic surface and high-acceleration vibration

As discussed earlier, to further increase the circulation rate, we can either reduce the contact force F_c by introducing a thin layer hydrophobic coating (Figure 3.2), or, increase the body force F_b by inducing vibrations. Figure 3.7(a, b) shows the experimental results of the effect of vibrations on the effective thermal resistance. The results show that for all cases, the effective thermal resistance R_{eff} is reduced once the vibration is introduced. The reduction in R_{eff} is within the range to 1.9% to 5.8% for uncoated hydrophilic TPCT, as depicted in Figure 3.7(a). Interestingly, for coated hydrophobic TPCT shown in Figure 3.7(b), the reduction in R_{eff} which ranges from 5.2% to 21.9% is almost triple to that of the uncoated TPCT. The reduction in R_{eff} is attributed to the increase in the rate of falling of condensed droplets to the evaporator. When the TPCT tube is subjected to vibratory force, the body force increases due to the additional acceleration generated by the vibrating plate, i.e., $F_b \approx m(g + \ddot{\xi})$. For a 65Hz excitation with surface displacement in the order of 10^{-3}m , the estimated surface acceleration is in the order of $\ddot{\xi} \sim 10^3 \text{ m/s}^2$, which is two order of magnitudes higher

than the gravitational acceleration $g \sim 10^1 \text{ m/s}^2$, therefore the falling rate of droplets is enhanced. As these droplets slide along the condenser wall, more liquid free sub-cooled surfaces are available for the nucleation of new condensate droplets. In light of its distinguished transport properties, Ag_2O -water nanofluid is also used as a working fluid in the uncoated and coated TPCTs. The results demonstrate a similar trend of improvement, as shown in Figure 3.7(a, b). Under similar experiment conditions (uncoated with vibration), the TPCT filled with nanofluid as working fluid has lower thermal resistance as compared to the TPCT filled with water; the reduction in thermal resistance is in the range of 18.3% to 21.2%.

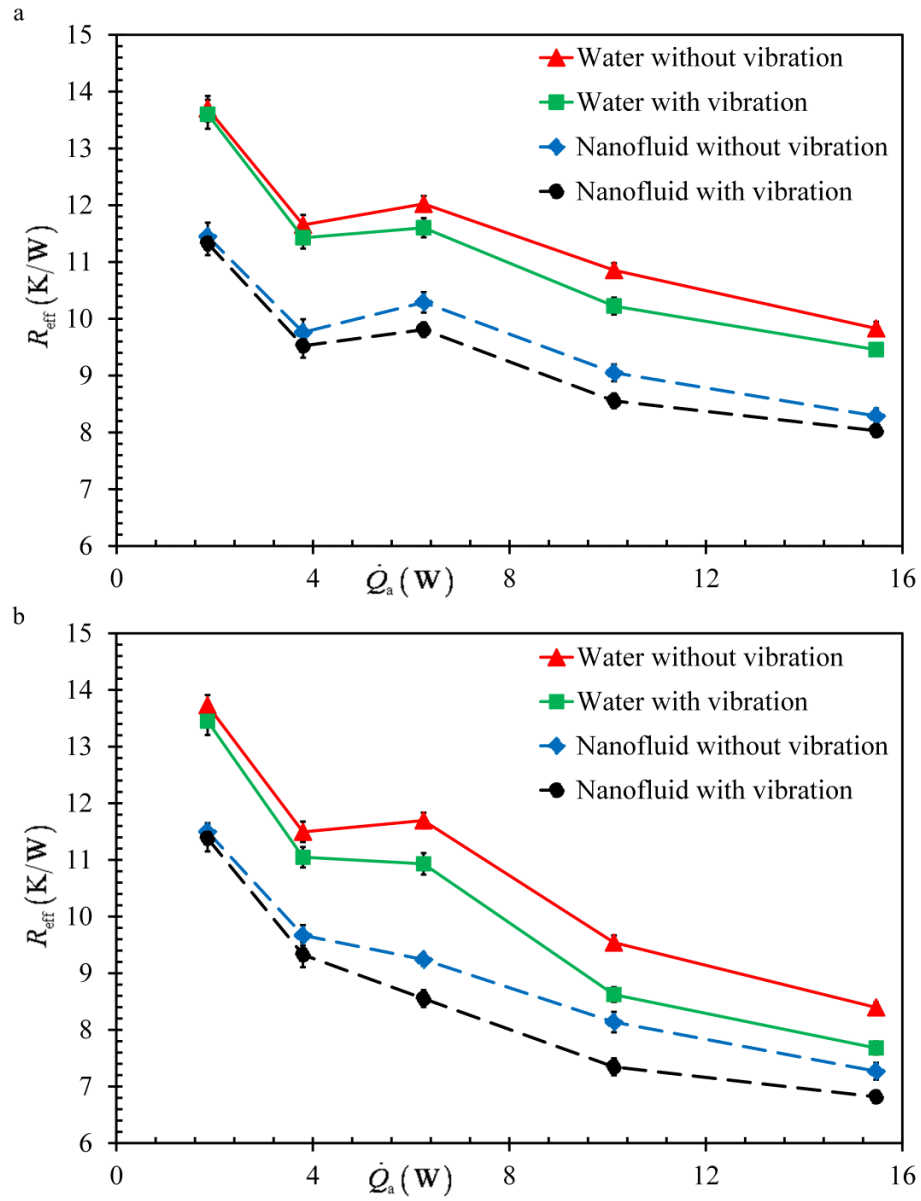


Figure 3.7| Effect of vibration on the effective thermal resistance of (a) uncoated TPCT and (b) coated TPCT using water and nanofluid as working fluid.

The effect of vibration on the strength of evaporation is investigated and the evaporator heat transfer coefficient augmentation ratios are evaluated using Equation (3.2) and plotted as a function of heat transport rate for both uncoated and coated TPCTs in Figure 3.8(a, b). As discussed earlier, the contact force between the droplets and the condenser wall is associated with the circulation effectiveness of condensate. We observe that the effect of vibration on the strength of evaporation is also prevalent although it is not dominant. This observation is congruous with a recent study investigating the effect of electrically induced droplet oscillation on evaporation²⁷¹. However, interestingly, it is observed that the suspension of nanoparticles significantly augments the heat transfer coefficient augmentation ratio which characterizes the strength of evaporation, for both cases without and with vibration. The increases in heat transfer coefficient are observed to exceed 35.2% and 47.7% for the cases without and with vibration, respectively, in a coated TPCT, as depicted in Figure 3.8(b). This augmentation is attributed to the deposition of nanoparticles on the evaporator surface which significantly enhances the nucleate boiling mechanism and surface wettability^{23, 105, 136}. The effect of deposition of nanoparticles on the performance enhancement is worth further investigation.

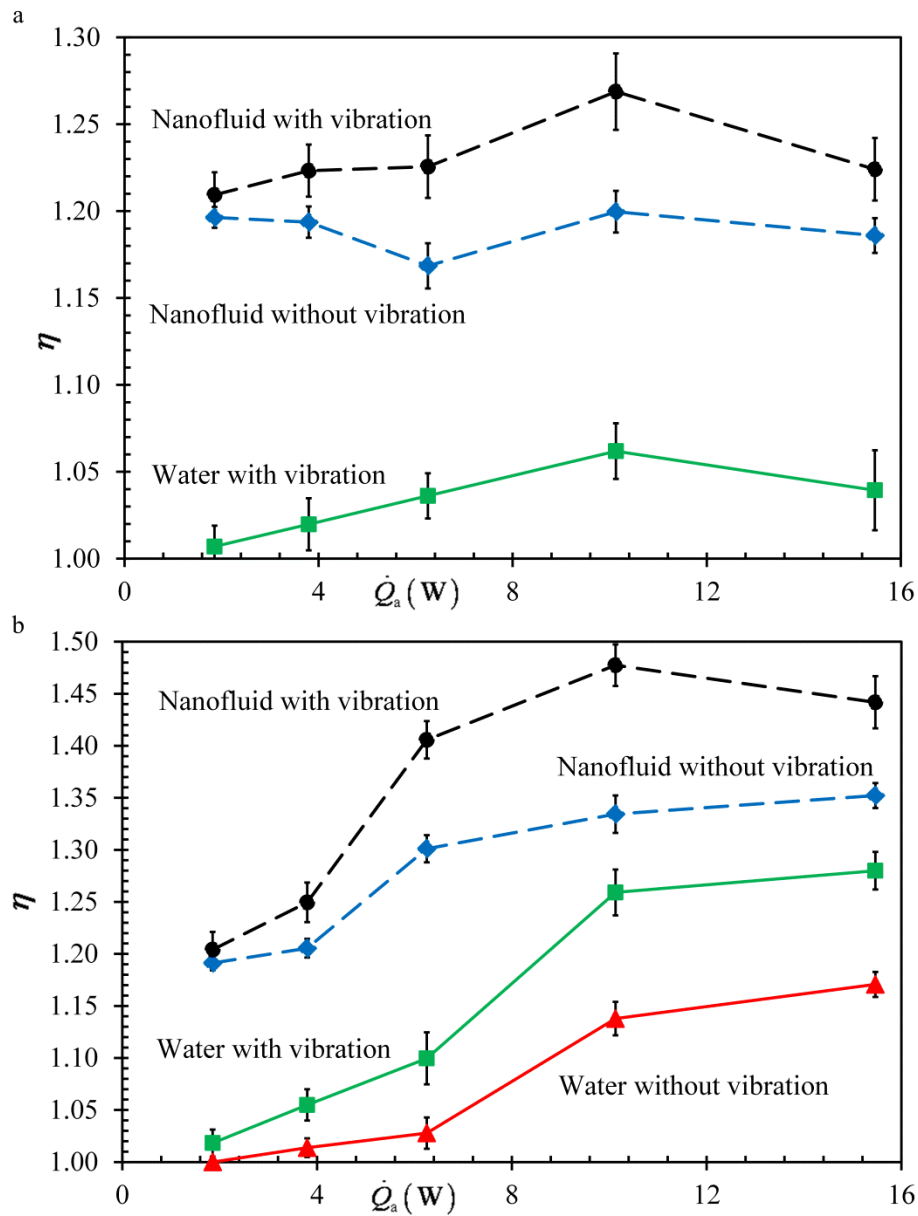


Figure 3.8| Effect of vibration on the evaporator heat transfer coefficient augmentation ratios of (a) uncoated TPCT and (b) coated TPCT using water and nanofluid as working fluid.

Despite these favorable factors enhancing the circulation of the condensate, the maximum reductions in thermal resistance R_{eff} are only about 12.1% and 14.3% for water charged TPCT and nanofluid charged TPCT, respectively. It is evident that the effect of vibration on the improvement of overall circulation rate is not as significant as predicted. To investigate the underlying physical justification of the marginal increase in the circulation effectiveness rendered by the high-acceleration vibration, a digital high-speed camera (Phantom Miro M 310, Vision ResearchTM) coupled with a long-distance microscope is employed to record the high-speed events of transient phenomena in the TPCT with particular attention paid to the liquid-vapor interfacial structure.

It is observed that in addition to higher body force experienced by the condensed droplets at the evaporator, the high acceleration induced by the vibrator generates elongated jets which subsequently break up into multiple droplets, as illustrated in Figure 3.9. The diameter of these droplets is between 2 to 3 mm. Based on the images recorded at 1000 frames per second, the estimated jet Weber number We_j is approximately 100, indicating a strong inertial force dominating the jet motion. The jet Weber number is defined as $We_j \equiv \rho U_j^2 R_j / \gamma$, where R_j is the radius of the jet, and U_j is the velocity of the jet. The excitation from the vibration induces large surface waves at the liquid-vapor interface at the evaporator section, creating instabilities in the liquid flow. This leads to the formation of elongated jets which eventually break up into finer droplets. The droplets formed from the break-up of the elongated jets are observed to be entrained in the vapor flow and returned to the condenser. This entrainment of liquid droplets induced by the high-acceleration vibration can be analogous to the typical entrainment phenomenon caused by high shear forces developed at the liquid-vapor interface due to the high relative velocity between the counter-current liquid and vapor flows when the axial heat flux imposed on a TPCT is substantially high^{11, 272, 273}. The latter which is associated with the entrainment limit in the operation of a TPCT provokes a depletion of liquid supply to the evaporator, incurring a local dry-out at the evaporator and flooding at the condenser if the entrainment is sufficiently intense¹¹. When the entrained droplets deposit on the condenser wall surface, the thermal resistance increases and the condensation heat transfer deteriorates. Consequently, the axial heat flux and the performance of the TPCT decline. In the present study, the

vibration-induced entrainment of droplets acts in a similar manner in returning the liquid back to the condenser, impeding the circulation rate of the condensate. Up to this point, the marginal increase in the circulation effectiveness rendered by the high-acceleration vibration can be reasoned out. The high-acceleration vibration yields two opposing effects on the liquid circulation effectiveness in a TPCT. The increase in the rate of falling of condensed droplets to the evaporator is apparent and explicit while the entrainment of droplets back to the condenser is a subtle phenomenon. The former is viable in enhancing the circulation effectiveness while the latter generates an adverse effect that counteracts with the enhancing effect of the increased falling rate of condensed droplets, inhibiting the circulation rate. The observation of liquid jets and entrained droplets provides valuable experimental insights into the physical process of the liquid-vapor interaction induced by the high-acceleration vibration in a TPCT.

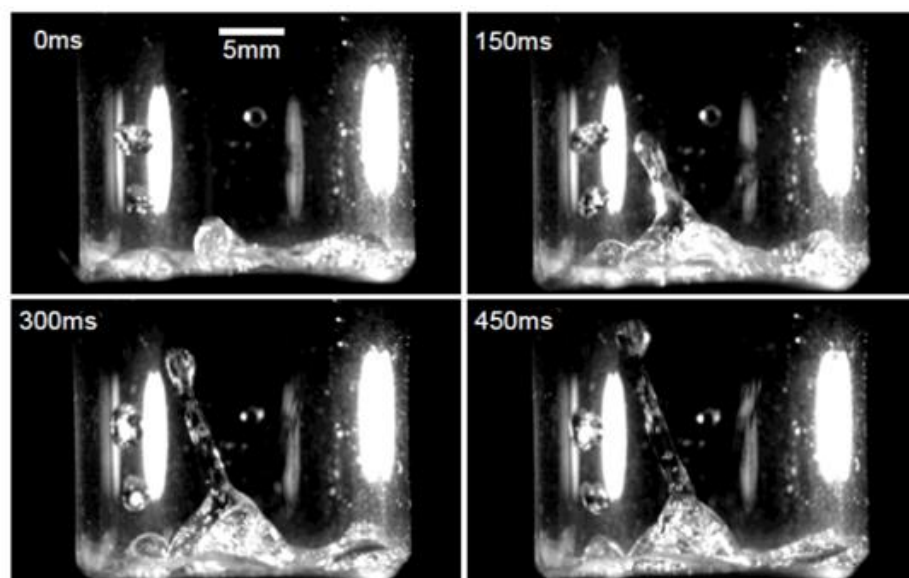


Figure 3.9| Elongated liquid jet generated at the evaporator due to the strong vibration. The jet breaks up into multiple finer droplets which are entrained in the vapor flow.

3.4 Conclusions

Experimental study has been performed to investigate the coupled effects of contact forces and vibrations on the thermal efficiency of TPCTs. By comparing the experimental results for uncoated (hydrophilic) glass tube and coated (hydrophobic) glass tube, the reduction in the effective thermal resistance R_{eff} , which is used to characterize the overall thermal performance, is between 3.2% and 16.9%. This reduction is primarily due to the increase in the falling rate of the condensed droplets and the formation of dropwise condensation. The strength of evaporation which is characterized by the evaporator heat transfer coefficient augmentation ratio is observed to be indirectly affected by the contact force. The enhancement in the circulation effectiveness and the strength of evaporation is inherently simultaneous. The high-acceleration vibration ($\ddot{\xi} \sim 10^3 \text{ m/s}^2$) on the TPCT also reduces the R_{eff} ; the reduction is between 1.9% and 5.8%. By combining both the effects of contact force and vibration, the total reduction of R_{eff} is between 5.2% and 21.9%. For nanofluid, the effects of contact force and vibration on the reduction in R_{eff} are similar. However, it is observed that the utilization of nanoparticles substantially increases the heat transfer coefficient augmentation ratios, exceeding 35.2% and 47.7% for the cases without and with vibration, respectively, in a coated TPCT. Interestingly, the observation of elongated liquid jets and entrained droplets from the liquid-vapor interface induced by the high-acceleration vibration delineates the underlying physical justification of the marginal increase in the circulation effectiveness. This observation provides valuable experimental insights into the physical process of the liquid-vapor interaction phenomena induced by the high-acceleration vibration in a TPCT. To eliminate the entrainment of droplets back to the condenser which impedes the circulation rate of the condensate, high-frequency and low-acceleration vibrations ($f > 100 \text{ kHz}$) can be employed in the future investigation.

Chapter 4

Enhanced Evaporation Strength through Fast Water Permeation in Graphene-Oxide Deposition

Tong, W.L., Ong, W.-J., Chai, S.-P., Tan, M.K. & Hung, Y.M. Enhanced evaporation strength through fast water permeation in graphene-oxide deposition. *Scientific Reports* 5, 11896 (2015).

URL: <http://www.nature.com/srep/2015/150623/srep11896/full/srep11896.html>

DOI: 10.1038/SREP11896

4.1 Outline

In the view of the excellent thermal properties determined in experiments, GO is a promising candidate for replacing metal-based nanoparticles in the preparation of nanofluid. Characterization of graphene-based nanofluid showed extraordinary thermal conductivity enhancement with a small dosage of graphene^{274, 275}. The choice of working fluid has been a key area of interest in enhancing the phase-change heat transfer of thermal management devices. While numerous postulations have been proposed to elucidate the underlying physical mechanism of the anomalous boiling heat transfer enhancement with GO nanofluids, most of the studies attributed the enhancement to the high thermal conductivity nature of GO deposited layer^{57-59, 236, 240-242}. Speculation of thermal reduction of GO was also suggested due to the progressive thermal annealing process, yielding higher thermal conductivity²³⁶. However, the characterization of individual GO sheet revealed its low thermal conductivity nature as a result of the abundant oxygenated functional groups and lattice defects on the graphitic plane^{207, 208, 231}. Regardless of the reduction process, the thermal conductivity of rGO was even lesser than GO due to the induction of additional defective sites with the detachment of functionalities²³². Furthermore, the superior conduction heat transfer in graphene is also significantly reduced by the phonons scattering effects on the interfaces and the grain boundaries^{52, 56}. Interestingly, several studies indicated the water absorptivity of GO deposited layer^{58, 240, 241}. Yet, this phenomenon is often neglected to have contributed to the boiling enhancement. Thus, the presence of an essential mechanism which fundamentally enhances the boiling heat transfer is yet to be identified.

Recently, fast water transport across laminated GO membrane while blocking even the smallest gas atom of helium has been discovered by Geim and co-workers²⁵⁰. Anomalous high permeation of water through GO laminates having vacant spaces formed between non-oxidized regions of graphene sheets was observed. Two factors contribute to this unusual water permeation – the capillary driven force and the remarkable boundary slip of ultralow-friction passage. The oxidized regions act as spacers to form a network of nanocapillaries that vigorously interact with the intercalating water while the two-dimensional graphene nanocapillaries allow low-friction flow of monolayer water. Water flowing through the empty region between the

pristine graphene sheets experiences an ultra-fast, low-friction flow similar to those reported in the water permeation of carbon nanotubes²⁷⁶. The fast water transport confined in the nanocapillary is ascribed to the frictionless interaction between the atomically smooth, hydrophobic carbon wall and the well-ordered hydrogen bonds of water molecules^{250, 277, 278}. For GO membranes immersed in liquid water, the mechanism of fast water permeation is not limited to non-oxidized regions²⁵³, based on the fact that no interconnecting network forms in these regions for water permeation²³². Water intercalation through an immersed GO membrane engenders expansion of the interlayer distance between the graphitic planes^{245, 251, 253}. As the interlayer distance expanded over 9 – 10 Å, the first water monolayer was found to be attached firmly to the oxidized region while the second water monolayer manifests its rapid movement in a translational motion^{246, 279}. It was also suggested that fast water permeation could be attributed to the permeation across defective holes laid across the GO sheets²⁵³. By virtue of vigorous oxidation of precursor graphite and sonication treatment, GO sheets were introduced with high percentage of defective sites, allowing the permeation of water molecules across the graphitic plane. The mechanism of fast water permeation was also stimulated *via* molecular modelling. Till now, it is yet conclusive to fully comprehend the underlying physical phenomenon of the anomalous fast water permeation of GO.

Based on the water absorption phenomenon of GO/rGO depositions and the fast water permeation effect over GO membranes, the anomalous enhancement in CHF of a heated surface immersed in GO nanofluid can be fundamentally elucidated. Resembling the capillary pumping effect of micro/nano hydrophilic structures^{41, 42, 50}, the fast water permeation of GO deposition effectively saturates dry regions with water, preventing the formation of hotspots. The inevitable surface deposition of GO sheets on heated surface provides an alternative approach in enhancing the boiling heat transfer, which is relatively simple and practical as compared to the more complex approach of micro/nanostructure fabrication. The water permeation effect of GO deposition inspires its application in enhancing the evaporation *via* surface functionalization. Such surface functionalization is also observed over TPCT charged with conventional metallic oxide nanofluid whereby nanoparticles progressively deposited on the heater surface and augmented the surface wettability, leading to the evaporation enhancement^{23, 136-142}. However, the augmentation in the surface wettability of the GO deposition is far more

superior to that of the metallic oxide nanoparticles deposition. The unique water permeation characteristic of GO deposition offers exceptional evaporation enhancement through the formation of water thin film.

In this study, GO nanofluid is introduced as a working fluid for the TPCT. The thermal performance of GO nanofluid charged TPCT is then benchmarked with the thermal performance of silver oxide nanofluid and DI water charged TPCTs operating under identical condition. The effect of nanofluid concentration on the thermal performance is also studied using five different weight percentages of GO nanofluid. The underlying mechanism of evaporation enhancement in TPCTs is scrutinized with the characterization of the nanofluids, surface morphology analysis and surface wettability analysis (evaluation of static contact angle) of the deposited layers. In addition, based on the structural studies of GO membrane in water of prior investigations^{250, 251, 253}, we are able to comprehend the heat transfer characteristics induced by different thicknesses of GO deposition and different operating temperatures. Under low heat input condition, the water permeation effect of GO deposition extends the effective evaporation region with the formation of water thin film across the evaporator surface. On the other hand, at high heat input, hotspots formation is delayed with the effective water distribution mechanism.

Monash University
Declaration for Thesis Chapter 4

In the case of Chapter 4, the nature and extent of my contribution to the work was the following:

Nature of contribution	Extent of contribution (%)
I was the chief investigator for this work. My contributions to this research were the design and fabrication of the experimental setup, conducting experiments, data analysis and preparation of manuscript.	80

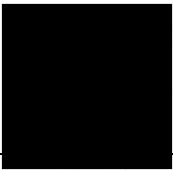
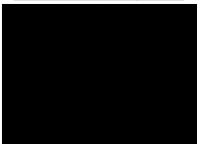
The following co-authors contributed to the work. If co-authors are students at Monash University, the extent of their contribution in percentage terms must be stated:

Name	Nature of contribution	Extent of contribution (%) for student co-authors only
A/Prof. Hung Yew Mun*	Overall supervision	-
Dr. Tan Ming Kwang	Overall supervision	-
A/Prof. Chai Siang Piao	Overall supervision	-
Ong Wee Jun	Assisted in the synthesis of graphene-oxide and advised on the material's characterization	5

The undersigned hereby certify that the above declaration correctly reflects the nature and extend of the candidate's and co-authors' contributions to this work*.

**Candidate's
Signature**

**Main
Supervisor's
Signature**

Tong Wei Li		Date: 1 June 2016
A/Prof. Hung Yew Mun		Date: 1 June 2016

4.2 Experimental investigation

4.2.1 Experimental Setup and Data Reduction

A schematic diagram of the experimental setup is illustrated in Figure 4.1. Briefly, the apparatus includes a TPCT, electrical heater element, water cooling jacket, data logger and direct-current (DC) power supply. The TPCT was fabricated using standard laboratory glass tube with an inner diameter of 13.5 mm and a length of 110 mm. The glass tube was sealed using a rubber stopper, which was embedded with an access valve. To ensure the glass tube was airtight, high strength epoxy was applied at all connections²⁸⁰. A 1 ml of working fluid, equivalent to 16.7% of fill ratio, was charged into the TPCT through the access valve. Two different types of working fluids were prepared: silver oxide (SO) nanofluids (solutions with weight ratios of 0.01% and 0.5%), and GO nanofluids (solutions with weight ratios of 0.01%, 0.025%, 0.05%, 0.075% and 0.1%). SO nanofluids refer to aqueous solutions with suspension of SO nanoparticles of diameter 30 nm (Sigma Aldrich), whereas GO nanofluids refer to aqueous solutions with suspension of graphite oxide. The graphite oxide was synthesized using the high purity graphite powder of size 45 μm (Sigma Aldrich); the protocol for synthesizing the graphite oxide powder is described in the next section, followed by the preparation of graphite oxide nanofluids. Once the charging was completed, the absolute pressure in the glass tube was reduced to 0.2 Pa using a vacuum pump. The evaporator section of the TPCT was in direct contact with a uniform electrical heating element, whereas the condenser section was cooled *via* a water cooling jacket, as shown in Figure 4.1(b). The electric power input to the electrical heating element was controlled by adjusting the switch on the DC power supply. To minimize the heat loss from the electrical heating element to the surrounding, several layers of insulating materials were wrapped around the element. For performance analysis of the TPCT, the axial temperature distribution of the TPCT was measured using six type-T thermocouple wires, which were all connected to a data acquisition system. The liquid saturation temperature, T_{sat} , was also measured by inserting a type-T thermocouple wire into the bottom section of the evaporator. In each test, the temperatures were recorded for a duration of 60 minutes and at a sampling rate of 2 readings per second.

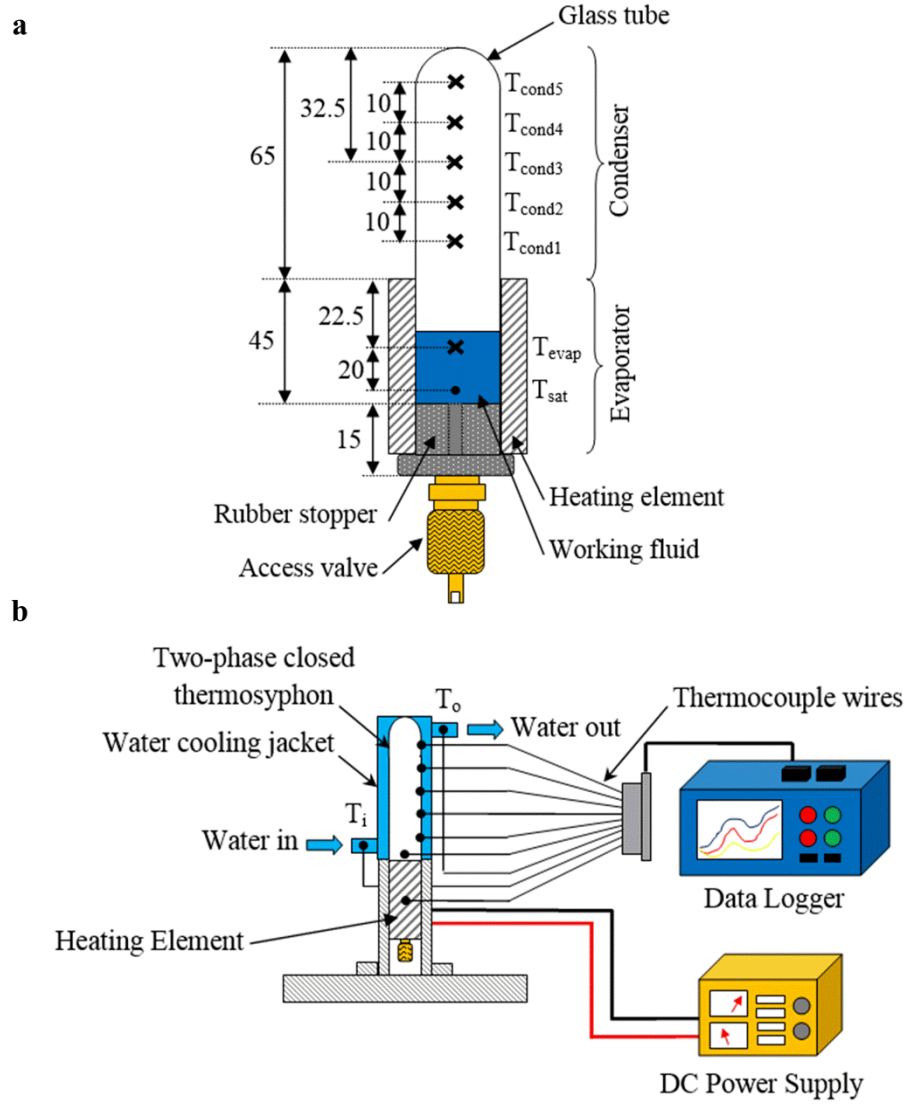


Figure 4.1| (a) Schematic diagram of a TPCT with temperature measurement points. **(b)** The experimental setup for the evaluation of performance of nanofluid charged TPCT.

Using the measured temperatures, the overall thermal performance can be characterized using the effective thermal resistance, given by

$$R_{eff} = \frac{\Delta T}{\dot{Q}_a} \quad (4.1)$$

where \dot{Q}_a is the heat transport rate, $\Delta T = T_{evap} - T_{cond}$ is the axial temperature difference between the evaporator and the condenser, with T_{evap} the temperature at the evaporator and T_{cond} the temperature at the condenser. We note here that

$T_{\text{cond}} = (T_{\text{cond1}} + T_{\text{cond2}} + T_{\text{cond3}} + T_{\text{cond4}} + T_{\text{cond5}})/5$, is the average temperature of the condenser and \dot{Q}_a is calculated based on the principle of energy conservation, i.e., the net heat transported across the TPCT is equivalent to the heat dissipated from the condenser section, $\dot{Q}_a = \dot{m}c_p(T_o - T_i)$, with the assumption of a well-insulated water cooling jacket. Two thermocouples are employed to measure the inlet and outlet water temperatures, T_i and T_o . Here, \dot{m} is the water mass flow rate and c_p is the specific heat capacity.

The average evaporator heat transfer coefficient, $\bar{h}_e = \dot{Q}_a / (\pi d L_e (T_{\text{evap}} - T_{\text{sat}}))$, is used to quantify the strength of evaporation, where T_{sat} is the saturation temperature of the working fluid in the evaporator, d and L_e are the inner diameter and length of the evaporator, respectively. During the experiments, under a constant heat input, the evaporator heat transfer coefficient augmentation ratio is given by

$$\eta = \frac{\bar{h}_e}{\bar{h}_{e,0}} = \frac{(T_{\text{evap},0} - T_{\text{sat},0})}{(T_{\text{evap}} - T_{\text{sat}})} \quad (4.2)$$

where $\bar{h}_{e,0}$ is the average heat transfer coefficient of DI water charged TPCT. Here, η represents the relative comparison of the heat transfer coefficients by using the value of DI water charged TPCT as the basis for comparison. Enhancement in heat transfer at the evaporator can be noticed with η exceeding the value of one and vice versa.

4.2.2 Synthesis of Graphite Oxide

Graphite oxide powder was synthesized *via* the modified Hummers' method with the following procedures^{244, 281}. 3 g of graphite powder (Sigma Aldrich, <45µm, >99.99%) was added into an 80°C mixture containing 12 ml of concentrate H_2SO_4 (Chemolab supplies, 95-97%), 2.5 g of P_2O_5 (Sigma Aldrich, $\geq 98\%$) and 2.5 g of $\text{K}_2\text{S}_2\text{O}_8$ (Sigma Aldrich, $\geq 99\%$). The mixture was then stirred for 4.5 hours and cooled to room temperature before diluted with 500 ml of DI water. The mixture was continuously washed with DI water until the pH of the filtrate became neutral. The product was dried at 70°C overnight. The pre-oxidized graphite was re-dispersed into

120 ml of cold concentrated H_2SO_4 together with 15 g of KMnO_4 (Sigma Aldrich, $\geq 99\%$). The mixture was then stirred for 2 hours with the temperature kept below 20°C . Next, the mixture was diluted with 250 ml of DI water in an ice bath to keep the temperature below 50°C . After 2 hours of stirring, the solution was diluted again with 700 ml of DI water. 20 ml of H_2O_2 (R&M Chemicals, 30%) was further added into the final mixture which was then washed with 1 l of HCL (Merck, 37% diluted to 10%) followed by DI water for several times to completely remove the acid content. After filtration, the graphite oxide was air-dried at a temperature of 60°C for 24 hours. The graphite oxide was then grounded into fine powder form. The X-ray diffraction (XRD) spectrum of GO powder indicates a peak at 9.1° corresponding to an interlayer distance of 9.72 \AA , which is consistent with those of prior studies^{251, 253}.

4.2.3 Preparation of GO and SO nanofluids

In order to obtain the final product of GO nanofluid, graphite oxide powder was dispersed in DI water and underwent ultrasonication treatment. Through sonication process, graphite oxide suspended in the aqueous solution exfoliates to yield a large distribution of nanometer-sized GO sheets. GO nanofluids were prepared with five concentrations measured by the weight of graphite oxide powder added to the dispersion (Figure 4.2). The weight percentages were maintained at 0.01 wt%, 0.025 wt%, 0.05 wt%, 0.075 wt% and 0.1 wt%. The mixtures were ultrasonicated (20 kHz, 700 W) with an ultrasonic liquid processor (Q700 Sonicator[®], Qsonica, LLC.) for 5 hours with fluid temperature maintained below 80°C to prevent evaporation. To quantify the superiority of the GO nanofluid, SO nanofluid was prepared in two concentrations of 0.01 wt% and 0.5 wt%. Similar ultrasonication treatment was used for the preparation of SO nanofluids to ensure the homogeneity.

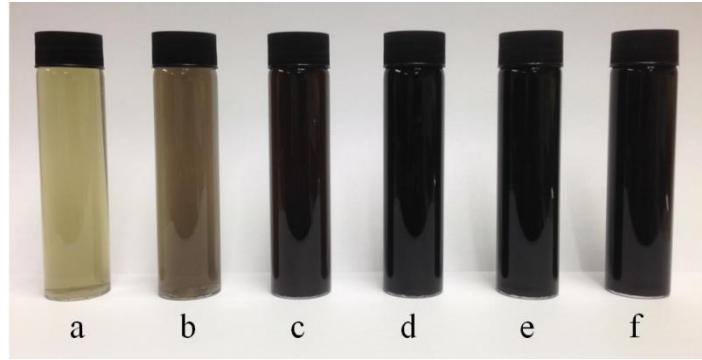


Figure 4.2| Digital images of nanofluids with various nanoparticles concentrations: **(a)** 0.01 wt% SO, **(b)** 0.01 wt% GO, **(c)** 0.025 wt% GO, **(d)** 0.05 wt% GO, **(e)** 0.075 wt% GO, and **(f)** 0.1 wt% GO.

4.2.4 Characterization of GO and SO nanofluids

The heat transfer capability of a TPCT is governed by thermophysical properties such as the thermal conductivity and the viscosity of working fluid. The thermal conductivity of the nanofluid was measured using thermal property analyzer (KD2Pro, Decagon Devices, Inc., Canada) with an uncertainty of $\pm 5\%$. The device measured the thermal conductivity using transient hot wire method with a probe sensor of 60 mm in length and 1.3 mm in diameter. Thermal bath was used to prevent temperature fluctuation and all samples were measured at the temperatures ranging from 25°C to 45°C. Prior to the taking of measurements, the KD2 Pro device was calibrated with glycerol. Ten measurements were taken for each sample at the targeted temperature to ensure the accuracy and reliability. The measured thermal conductivities of the GO and SO nanofluids were compared with thermal conductivities of the base fluid (DI water) measured under the same conditions.

Figure 4.3(a) shows the thermal conductivity enhancement ratios of GO and SO nanofluids as a function of nanofluid concentration and temperature. The thermal conductivity enhancement ratio is defined as k_{nf}/k_o where k_o is the thermal conductivity of the based fluid and k_{nf} is the thermal conductivity of the nanofluid. The SO nanofluid with 0.01 wt% has nearly no enhancement for the range of temperature from 25°C to 45°C. However, the GO nanofluids achieve an overall enhancement in

thermal conductivity. Different trends in the change of enhancement ratio at different temperatures are observed for SO and GO nanofluids. At a high GO content of 0.1 wt%, the enhancement ratio increases exponentially. However, the enhancement ratio of 0.5 wt% SO nanofluid remains almost constant at different temperatures. The constant enhancement ratio with the increase of temperature implies that the base fluid has more dominant effect on the increase in thermal conductivity rather than the thermal transport behaviour associated with the suspended nanoparticles. The thermal transport mechanisms such as micro-convection due to Brownian motion, ballistic phonon transport and clustering effect of nanoparticles are among those commonly affecting the increase in thermal conductivity of nanofluids⁴³. Nevertheless, the factors affecting the thermal conductivity of GO nanofluids are distinguishable. For GO nanofluids, strong temperature dependence of thermal conductivity enhancement ratio is observed in the concentrations of 0.05 wt%, 0.075 wt% and 0.1 wt%. This can be attributed to the high thermal conductivity nature and the high surface area to volume ratio of GO sheets. As GO sheets have significantly larger contact area with the fluid molecules, the contact resistance at the graphene-fluid interface is substantially reduced. In light of high thermal conductivity nature of GO sheets, the thermal energy can be effectively transported across the solid-fluid interface, creating an excellent heat conduction path. Due to the high thermal conductivity and the 2D structure of GO sheets, a substantial thermal conductivity enhancement is attainable even at a low concentration of GO. On the other hand, the viscosity increases with concentration of nanoparticles. Figure 4.3(b) depicts the viscosities of the GO and SO nanofluids at different concentrations. The viscosity decreases with increasing temperature. At higher temperatures (above 60°C), the viscosities of nanofluids rapidly decrease and approach the viscosity of base fluid (DI water). As the TPCT operates at temperatures higher than 60°C, the effect of increase in viscosity on the thermal performance of TPCT can be deemed to be marginal.

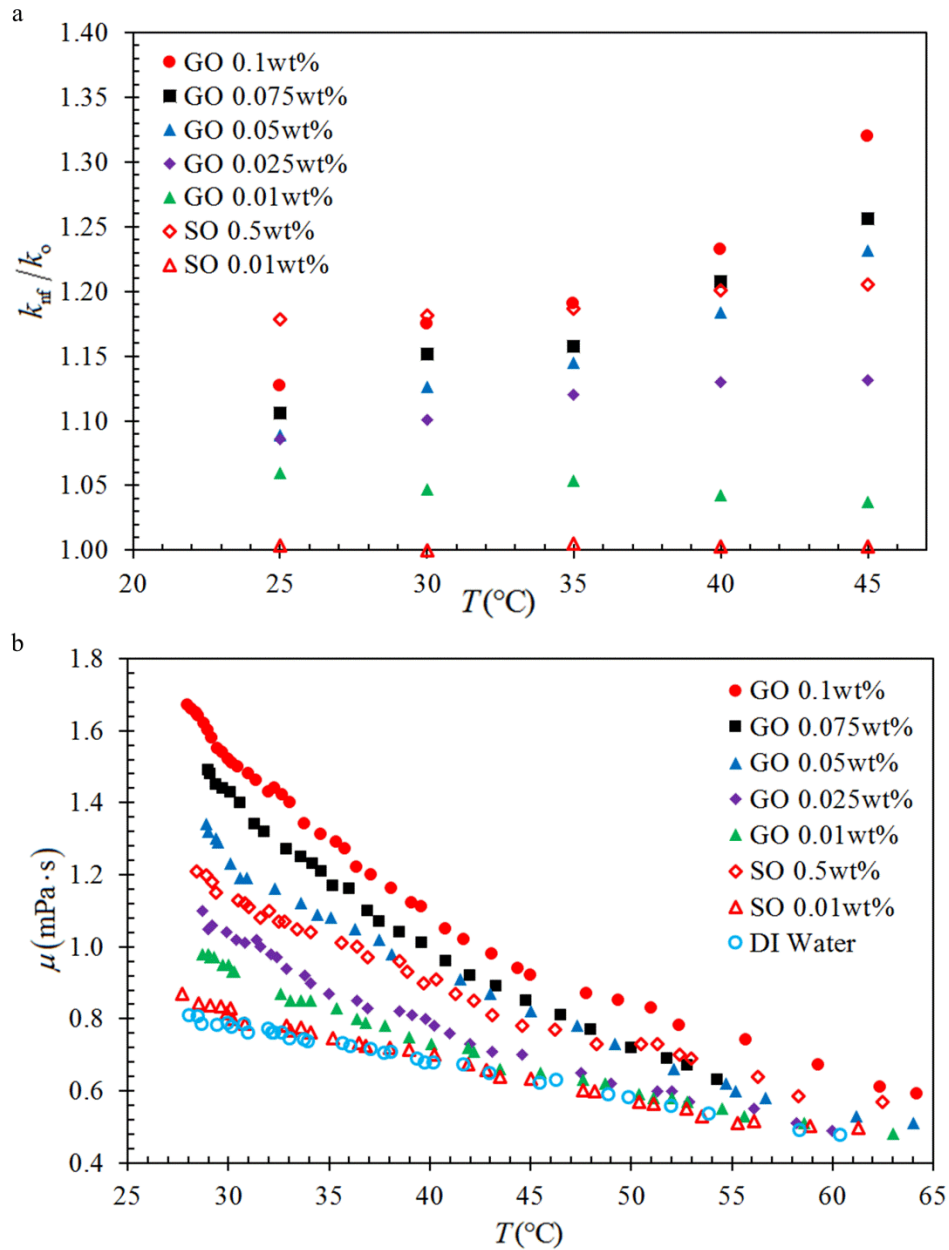


Figure 4.3| (a) Effective thermal conductivity enhancement ratio, and (b) viscosity, of GO and SO nanofluids as a function of temperature for different nanofluid concentration.

4.2.5 Surface Morphology of Nanoparticles Deposition

During the two-phase heat transfer process, a thin layer of nanoparticles was observed depositing on the heated evaporator surface. A variation in colour or colour intensity of the deposition was clearly noted for different weight percentages and different nanofluids. Samples of the deposition were prepared by gently breaking the glass structure of TPCT to obtain the wall of evaporator section where the deposition

took place. To assure the consistency of the results, the samples were obtained at a location 5 mm from the bottom of the evaporator. Observation of surface morphology of deposited layers was carried out using a SU-8010 field emission scanning electron microscope (FESEM, Hitachi Ltd., Japan). Static contact angle θ_s between DI water and the deposition was measured using a standard goniometer (Model 590, Ramé-Hart Instrument Co.) under atmospheric pressure and a room temperature of 26°C.

4.3 Results and discussion

4.3.1 Performance comparison of GO and SO nanofluids

The temperature difference, $\Delta T = T_{\text{evap}} - T_{\text{cond}}$, manifests itself as a convenient indicator in quantifying the heat transport rate along the axial direction. In accordance with the Fourier's law of heat conduction, under the same heat transfer rate, smaller ΔT indicates higher heat transport capability of the specimen. A low ΔT infers a low thermal resistance across the evaporator and condenser sections. We observe that ΔT of a GO-nanofluid charged TPCT is lower than that of a DI water charged TPCT. Figure 4.4 shows the variations of ΔT reduction ratio, $\psi = (\Delta T_{\text{nf}} - \Delta T_o) / \Delta T_{\text{nf}}$, of GO and SO nanofluids charged TPCTs as a function of \dot{Q}_a , with the nanofluid concentration being a parameter. Here, ΔT_o is the temperature difference of the base fluid (DI water) charged TPCT, ΔT_{nf} is the temperature difference of the nanofluid charged TPCT, and ψ is regarded as a comparison of the change in ΔT of nanofluid charged TPCT with ΔT of a base fluid charged TPCT, indicating an enhancement in the performance of a nanofluid charged TPCT. The GO nanofluids charged TPCTs have higher ΔT reduction ratios than that of SO nanofluids charged TPCTs. At a very high concentration of SO (0.5 wt%), the performance of TPCT is comparable with that of 0.1 wt% GO nanofluid charged TPCT. This shows that the GO nanofluid TPCTs outperform the SO nanofluid ones. For GO nanofluid TPCTs charged with higher concentrations (0.05 wt%, 0.075 wt% and 0.1 wt%), we observe that ψ decreases with increasing \dot{Q}_a at low \dot{Q}_a and starts to increase when \dot{Q}_a exceeds 6.5 W. This indicates that the GO nanofluid TPCTs perform better at a higher heat input, which will be discussed later.

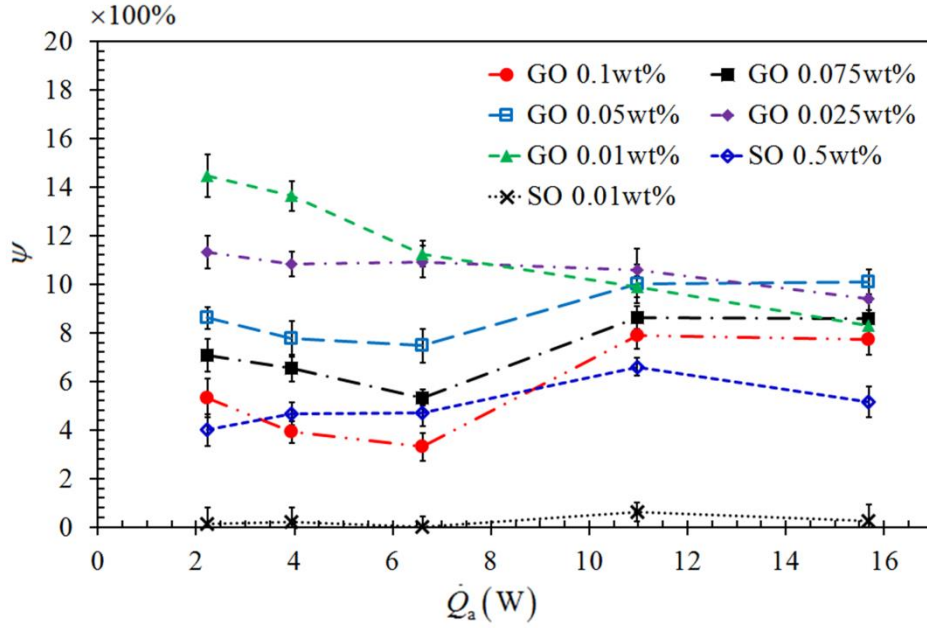


Figure 4.4 Variations of ΔT reduction ratio, $\psi = (\Delta T_{nf} - \Delta T_o) / \Delta T_{nf}$, of GO and SO nanofluids charged TPCTs as a function of \dot{Q}_a , with the nanofluid concentration being a parameter.

To evaluate the overall performance of TPCT, the effective thermal resistance, R_{eff} , which is a function of ΔT is analyzed. Figure 4.5(a, b) depicts the variations of R_{eff} with \dot{Q}_a , for different concentrations of GO and SO nanofluids charged TPCTs, respectively. The effective thermal resistance of the DI water ($\phi = 0$) charged TPCT is used as a benchmark to illustrate the enhancement in thermal performance of nanofluid charged TPCTs. A lower R_{eff} indicates higher performance. The decrease in R_{eff} is essentially attributed to the enhancement of either evaporation strength at the evaporator or circulation effectiveness of condensed liquid back to the evaporator or of both. Basically the effective thermal resistance decreases with increasing \dot{Q}_a . We observe that R_{eff} of GO nanofluid TPCTs is overall lower than that of DI water charged TPCT while R_{eff} of SO nanofluid TPCTs is only marginally lower than that of DI water charged TPCT even at high concentration of SO. Hence, comparatively the GO nanofluid TPCTs outperform the SO nanofluid TPCTs. Remarkably, for the case of GO nanofluids, R_{eff} increases with GO concentration ϕ at low \dot{Q}_a (2.23 W, 3.94 W and 6.6 W) and becomes independent of ϕ at high \dot{Q}_a (10.97 W and 15.69 W). Referring to

Figure 4.3(a) which shows that the effective thermal conductivity of nanofluid increases with GO concentration, we expect that R_{eff} of TPCT should decrease with increasing GO concentration. However, the finding in Figure 4(a) is contrary to what was anticipated based on the characterization of effective thermal conductivity of GO nanofluid as discussed in Figure 4.3(a). In this regard, the reduction of R_{eff} is not entirely attributed to the increase in effective thermal conductivity of GO nanofluid. Other factors might have contributed to this astonishing result. As mentioned, nanoparticles agglomerate in the base fluid and thin porous layers are formed on the inner surface of the evaporator. The nanoparticles deposition manifests significant enhancement in the surface wettability and nucleate boiling mechanism²⁸²⁻²⁸⁴. To this end, in what follows, we investigate the underlying physical significance of GO deposition and its anomalous characteristics in affecting the thermal performance of TCPT.

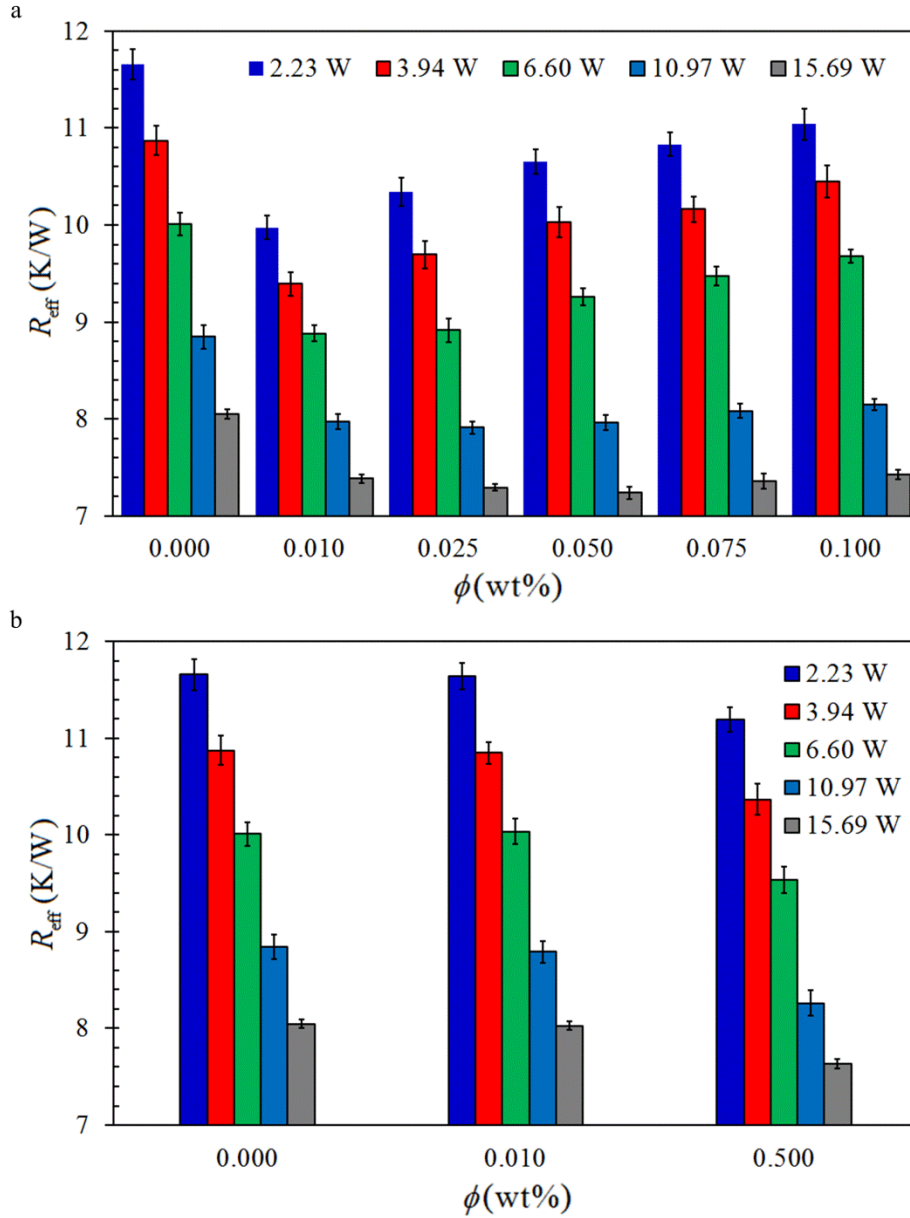


Figure 4.5| Effective thermal resistance, R_{eff} , as a function of nanoparticles weight ratio, ϕ , of (a) GO nanofluids, and (b) SO nanofluids, charged TPCTs at different \dot{Q}_a .

4.3.2 Fast Water Permeation Property of GO Deposition

To exclusively elucidate the role of thermal conductivity of nanoparticles deposition on the evaporator wall surface, we first examine the effective thermal conductance of uncharged TPCTs that had been coated with GO and SO during the experiments. The working fluids were evacuated from the TPCTs to exclude the two-phase heat transfer process. Simple heat conduction experiments were conducted. The

primary objective is to examine the heat conduction contribution of the nanoparticle deposited layer. Except for the specimens, the experimental setup is identical to that in Figure 4.1(b). The thermal conductance which can be considered as the effective thermal conductivity of specimen is calculated as $k^* = (\dot{Q}_a L) / (A_c \Delta T)$, where L is the distance between the two measured temperatures, A_c is the cross section area of the evacuated glass tube and $\Delta T = T_{\text{evap}} - T_{\text{cond}}$ is the temperature difference. Figure 4.6(a) depicts the results of the heat conduction experiments. Although the thermal conductance of GO deposition is slightly higher than that of SO deposition, they are only marginally higher (with a maximum of 6%) than that of the uncoated surface. This is not surprising as GO intrinsically has significantly lower thermal conductivity as compared to the pristine graphene with high in-plane thermal conductivity nature.^{52, 208} Due to the introduction of oxygenated functional groups and defects in GO during vigorous oxidation process, in-plane heat transfer through lattice vibrations is impeded^{52, 181}. High in-plane thermal conductivity of graphene is attributed to the covalent sp^2 bonding between the carbon atoms and the heat flow is anisotropic⁵². On the other hand, the layered structure of GO is governed by the cross-plane van der Waals force and the repulsive electrostatic force which is induced by the negatively charged functional groups^{56, 183}. As a result, the cross-plane heat transfer is extremely ineffective as compared to the in-plane heat transfer. In fact, based on non-equilibrium molecular dynamics simulations, the thermal conductivity of GO with an oxygen coverage of 20% was estimated to be 8.8 W/m·K which is three orders of magnitude lower than the thermal conductivity of pristine graphene²⁰⁸. In addition, at the interface between the glass substrate and the adjacent GO sheets, poor van der Waals coupling limits the heat transfer⁵⁶ and a high thermal resistance (hence a low thermal conduction) is induced between the GO sheets and the glass substrate. This shows the insignificant contribution of thermal conductivity of the GO deposition, which is essentially associated with heat conduction, to the thermal performance enhancement of TPCT. Hence we postulate that the performance enhancement and the effects of GO deposition are entailed by the two-phase heat transfer process.

As mentioned earlier, the two-phase heat transfer in a TPCT is governed by the evaporation process and the circulation of condensate. As the nanoparticles deposition takes place at the evaporator section, the evaporation process is convinced to be

uniquely contributing to the performance enhancement. It has been pointed out that the thermal performance enhancement of a nanofluid-charged TPCT is essentially attributed to the formation of nanoparticles deposition on the heated surface which modifies the surface wettability and enhances the nucleate boiling mechanism^{23, 136-138}. We analyse the strength of evaporation by evaluating the evaporator heat transfer coefficient augmentation ratio, η , as defined in Equation (4.2). Figure 4.6(b) plots η as a function of \dot{Q}_a for different GO and SO concentrations. It can be observed that the average evaporator heat transfer coefficient, \bar{h}_e , enhances in TPCTs with GO deposition, with a minimum of 11.4% and a maximum of 83.3% of enhancement as compared to the uncoated TPCT (charged with DI water). For SO deposition, no \bar{h}_e enhancement is observed for low SO concentration (0.01 wt%) and even at a high SO concentration (0.5 wt%), the enhancement is relatively small compared to that of GO deposition. This discrepancy between TPCTs with GO and SO deposited layers is likely due to the distinct surface morphologies and characteristics of the depositions.

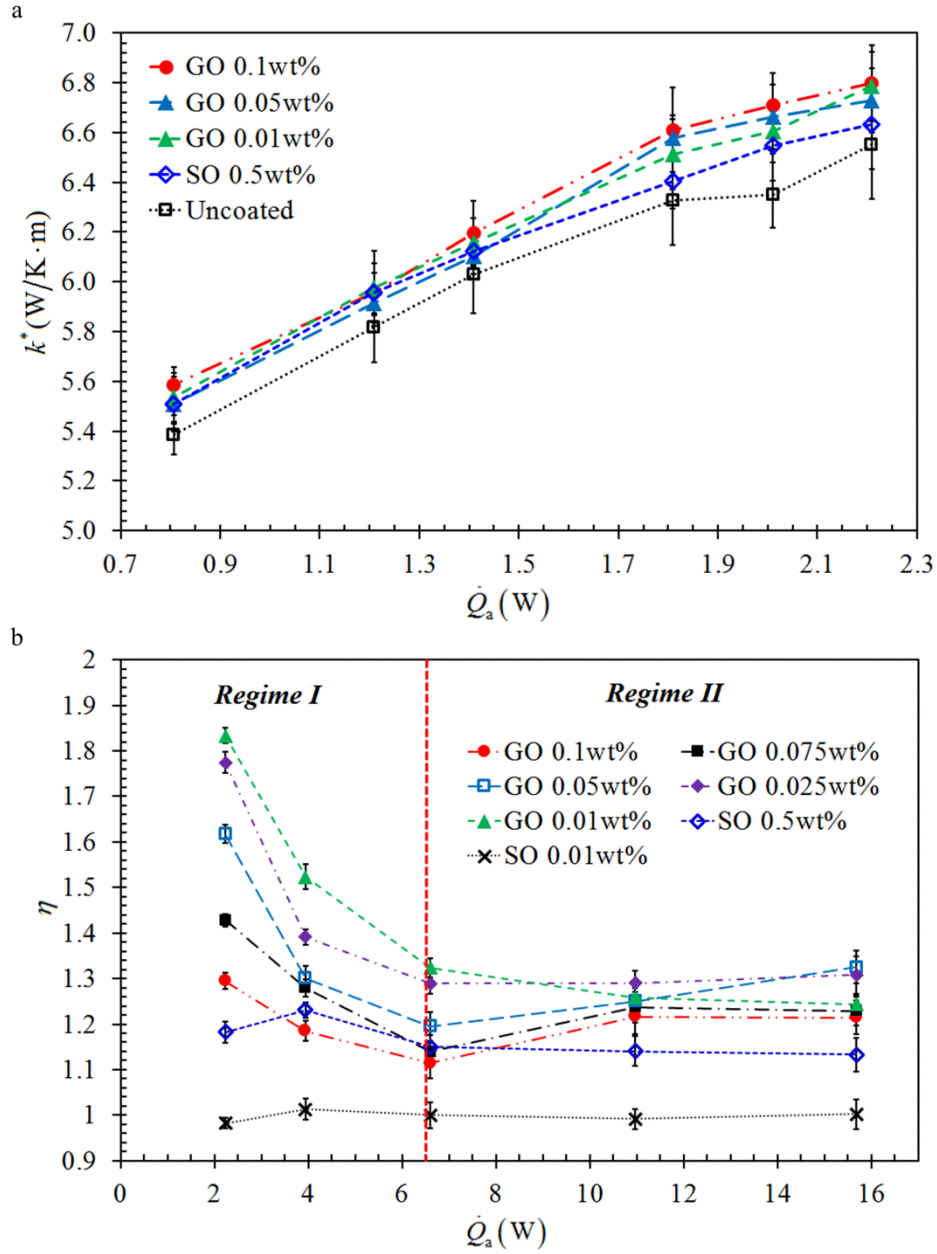


Figure 4.6| (a) Thermal conductance of uncharged TPCTs coated with thin GO and SO nanoparticles depositions as a function of \dot{Q}_a during the heat conduction experiments. (b) The evaporator heat transfer coefficient augmentation ratio, η , as a function of \dot{Q}_a with nanoparticles weight ratio as a parameter. Two distinct regimes – $\dot{Q}_a < 6.5$ W and $\dot{Q}_a > 6.5$ W can be clearly identified.

To this end, we investigate the surface wettability of deposited layer with a DI water droplet (2 μ l) through measurement of its static contact angle on the substrate to observe how water spreads out. A low contact angle manifests high surface wettability which induces a higher evaporation rate as the liquid-solid contact area increases. Figure 4.7 displays the variations of contact angle on GO, SO deposited layers and uncoated glass surface over a time frame of 300 seconds. Although the GO deposition is the most hydrophobic (with the highest contact angle among the three cases), its decrease in contact angle over the time of 300 seconds is the highest with a rate of 0.099 $^{\circ}$ /s. On the other hand, SO deposition which is the most hydrophilic (with the smallest contact angle) indicated a decrease in contact angle with a rate of 0.051 $^{\circ}$ /s. For the uncoated glass surface, the contact angle decreases with a rate of 0.053 $^{\circ}$ /s. The contact angle reduction rate of GO deposition is more than 1.9 times higher than that of SO deposition. As compared to the uncoated surface, the evaporation enhancement of SO deposited TPCTs is due the enhanced hydrophilicity of SO deposition. Of particular interest is the case of GO deposition. The anomalous enhancement in evaporation strength with GO deposited layer which is more hydrophobic than uncoated glass surface is contrary to the intuitive understanding. The factor of surface wettability is insufficient to explain this unusual phenomenon. In this case the unique fast water permeation property of GO comes into play. During the contact angle measurement of water droplet on GO deposition, for a longer time span, we observed that the contact angle continuously and gradually contracts over time and eventually the water droplet was completely absorbed into the GO deposited layer which is comparable to a sponge-like material.

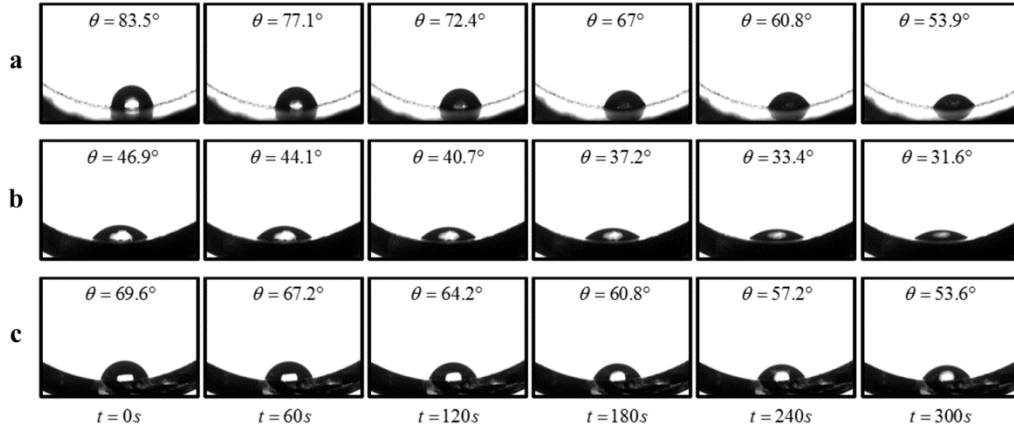


Figure 4.7| Time-lapse images of a 2- μ l water droplet residing on (a) 0.1 wt% GO deposited layer, (b) 0.5 wt% SO deposited layer, and (c) uncoated glass surface, over a time span of 5 minutes. For each 60-s interval, the corresponding contact angle is recorded and depicted.

To ascertain the cause of evaporation enhancement of GO deposition, in an individual experiment conducted under standard atmosphere, we compare the evaporation rates of water droplets on GO-coated surface and uncoated aluminium surface with a surface temperature of 130°C. To prepare the GO-coated surface, 30 ml of 0.1wt% GO nanofluid was progressively applied onto an aluminium surface heated at a temperature of 110°C. The solvent (water) is then evaporated leaving a uniform layer of GO deposition. To conduct the experiment, a 30- μ l water droplet was dropped onto the uncoated surface and also the GO-coated surface with a surface temperature of 130°C (a typical wall temperature of the evaporator of TPCT). Figure 4.8 shows the time-lapse images of a droplet evaporating on the uncoated surface and the GO-coated surface. It was observed that due to permeability of water through the GO deposition, the water droplet evaporates much faster on the GO-coated surface than on the uncoated surface. The water permeability of GO deposition significantly enhances the evaporation rate by rapidly spreading the water droplet. The respective time required for evaporation of a water droplet on the surface was calculated from the recorded videos. The estimated time for complete evaporation on the GO-coated surface is 2.6 s while that on the uncoated surface reads 10.3 s. The evaporation rate, \dot{m} , is evaluated as $\dot{m} = m_d/t$, where m_d denotes the mass of droplet and t is the estimated time. The evaporation rate of GO-coated surface and uncoated surface are 13.9 mg/s and 3.5 mg/s, respectively. The evaporation rate of the former is 4 times of that of the latter, justifying

the role of the fast water permeation in GO deposition in enhancing the evaporation strength.

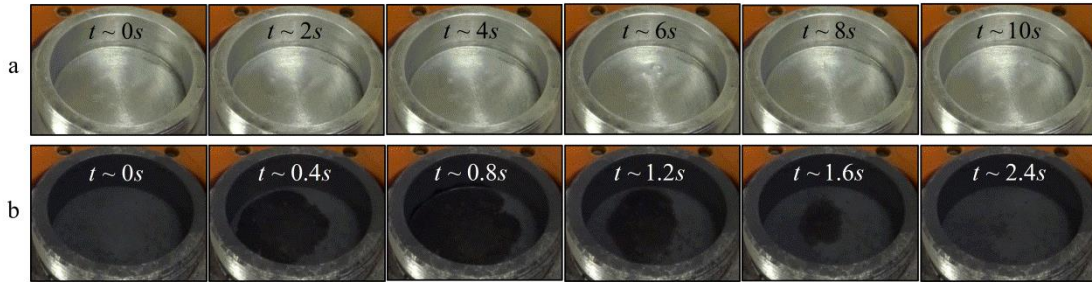


Figure 4.8| Time-lapse images of a 30- μ l water droplet impinging and evaporating on (a) uncoated aluminium surface and (b) GO-coated surface heated at a controlled surface temperature of 130°C. The droplet evaporation is significantly enhanced with the presence of the GO deposition. Fast water permeation of the GO deposition induces filmwise evaporation through the rapid spreading of the water droplet.

Here we illustrate the nanoparticle depositions schematically. Referring to Figure 4.9(a, i), The SO deposition is observed depositing in the submerged region and the effective evaporation region is only limited to the liquid-vapour interface. On the other hand, GO deposition spreads out across the evaporator wall above the liquid-vapour interface. The negatively charged hydroxyl groups at the edges of immersed GO sheets generate strong repulsive force between each individual GO sheet¹⁸³. Concurrent with the upward liquid and vapour flows, the deposited GO sheets are spread across the wall surface covering substantially larger surface area. By virtue of water intercalation in the GO deposition, the effective evaporation region is extended to the wall surface where the GO sheets deposited, above the liquid-vapour interface (highlighted with red colour) as depicted in Figure 4.9(a, ii). As water intercalates between the GO interlayers, a thin film of water forms at the GO deposited layer. Evaporation occurs in a thin film is more effective than that in a pool of water due to larger surface area of the former. Even though it is in an antigravity direction, the water thin film formed at the GO deposition is continuously replenished from the pool of water through the operation of water permeation in the GO structure. In what follows, we denote the evaporation taking place at the GO deposited layer as filmwise evaporation.

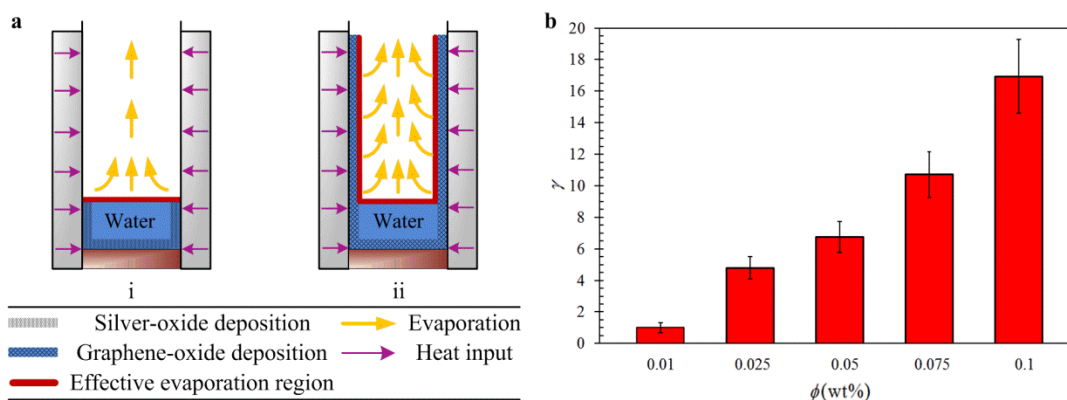


Figure 4.9| (a) Schematic illustration of evaporation process occurring at the effective region of a TPCT with (i) SO deposition, and (ii) GO deposition. In light of the fast water permeation effect, the effective evaporation region for TPCT with GO deposition is significantly extended across the evaporator wall surface (highlighted with red colour) where filmwise evaporation is induced. (b) Relative deposition thicknesses of various GO nanofluid concentrations. The average thickness of 0.01 wt% GO deposition is used as a baseline for comparison.

To gain better insight into the mechanism of water permeation of GO deposition on the evaporator wall, we examine the surface morphologies of the deposited layers. FESEM was used to capture images of the deposited layers. Figures 4.10(a, b, c, d) illustrates the FESEM images of 0.5 wt% SO, 0.01 wt% GO, 0.05 wt% GO, and 0.1 wt% GO deposited layers, respectively. It is observed in Figure 4.10(a) that spherically structured SO nanoparticles agglomerated and deposited disorderly on the surface. Although such deposition enhances the surface wettability, the enhancement of evaporation strength is not profound as discussed earlier. On the other hand, the GO depositions consist of well distributed, closely-packed layered structure of GO sheets which are responsible for the property of fast water permeation. For higher concentration of GO deposition (Figure 4.10(d)), relatively thicker strands that can be easily distinguished from those of lower concentration (Figure 4.10(b)) are observed. It is implied that the thickness of the GO layers depends on the nanofluid concentration.

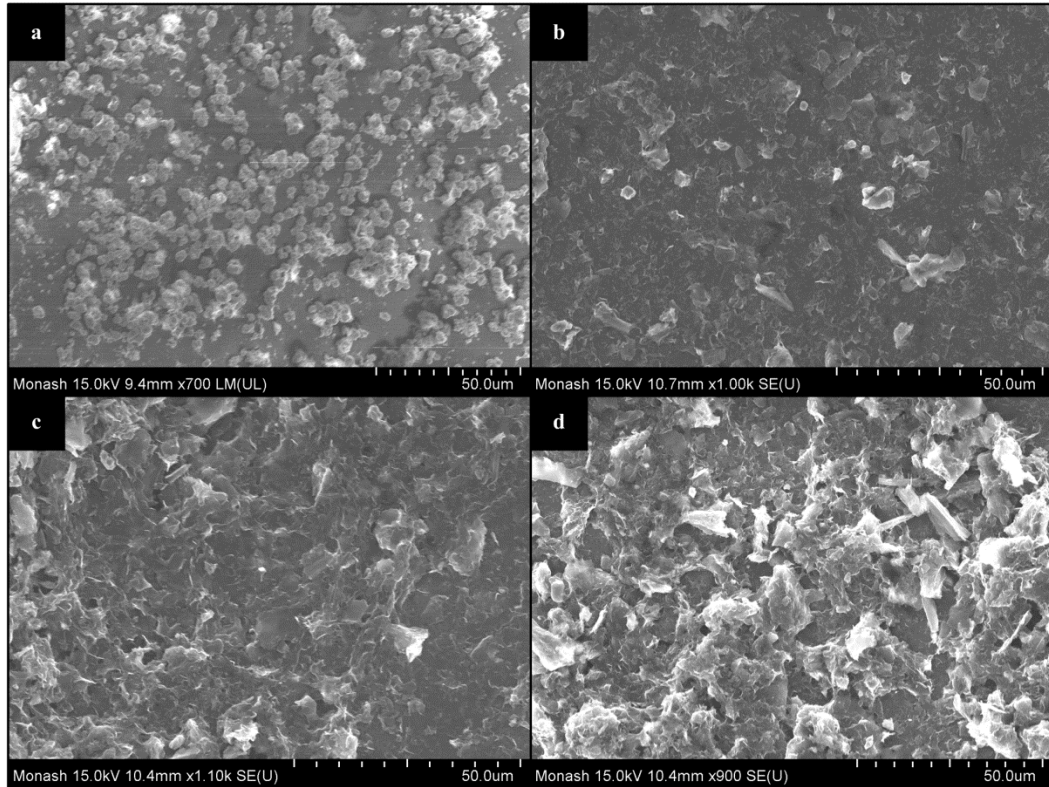


Figure 4.10 FESEM images of SO nanoparticles and GO sheets deposited on the glass surface of the evaporator section of TPCT: (a) 0.5 wt% SO nanoparticles, (b) 0.01 wt% GO sheets, (c) 0.05 wt% GO sheets and (d) 0.1 wt% GO sheets. The well distributed, closely-packed layered structure of GO sheets can be easily distinguished from the disorderly distributed spherical SO nanoparticles deposition. Higher concentration of GO sheets deposition is manifested in thicker strands.

To compare the GO deposition thicknesses of various nanofluid concentrations, we estimate the relative deposition thickness as $\gamma = t_1/t_0$, where t_1 is the average thickness of GO deposition and t_0 is the average thickness of 0.01 wt% GO deposition (lowest concentration) which is used as a baseline for comparison. The average thickness was approximated from the FESEM cross-section image of GO deposition which was then analysed using the SigmaScan[®] Pro (Systat Software, CA, USA) image processing software. For each concentration, a total of 15 cross-section images from 5 independent sets of experiment were captured. The average thickness of the baseline was estimated as 0.2 μm , corresponding to approximately 300 layers of GO sheets. Figure 4.9(b) depicts the relative deposition thickness of various GO nanofluid concentrations. The GO deposition thickness increases with nanofluid concentration and

the thickness of 0.1 wt% GO deposition is 17 times of that of 0.01 wt% GO deposited layer.

It has been reported that water intercalation through GO membrane results in the expansion of the interlayer distance between the graphitic planes^{245, 251, 253}. The X-ray diffraction (XRD) analysis of the hydrated GO membrane showed an increase in the interlayer distance from 7.7 Å to 12.29 Å²⁵³, capable of intercalating bilayer of water for fast water permeation^{246, 279}. Thus, the water permeability of GO membrane is appreciably enhanced when the interlayer spacing increases^{253, 279}. The variation of the interlayer spacing is temperature dependent^{251, 279}. Referring to Figure 4.6(b), the \bar{h}_e enhancement decreases with the increase in heat input and simultaneously the operating temperature that spans from 87°C to 136°C for the GO charged TPCT. The operating temperature is below the critical temperature of 200°C where the interlayer spacing completely collapses for the minimum clearance of water monolayer (≈ 5 Å) due to excessive thermal annealing²⁵¹. The decrease in the \bar{h}_e enhancement can be explained by the temperature variation which causes the structural transformation of GO deposition²⁵¹, a phenomenon termed as thermohydration. As the temperature increases, structural alteration of the GO deposition takes place where the interlayer distance progressively decreases. The reduction in the interlayer distance greatly affects the water vapour permeability as less water monolayer is able to permeate through the narrowing gap. Thus, η reduction can be observed as the heat input increases.

In Figure 4.6(b), it is obvious that two different regimes for the variation of η - Regime I ($\dot{Q}_a < 6.5\text{W}$) and Regime II ($\dot{Q}_a > 6.5\text{W}$) determine the evaporation enhancement for GO deposition. For a small \dot{Q}_a in Regime I, the \bar{h}_e enhancement of TPCT with GO deposition decreases with both increasing \dot{Q}_a and GO concentration. This is intelligible that at low heat input, the evaporation rate at the liquid-vapour interface of the pool of water is relatively low while the filmwise evaporation from the extended GO thin film is vitally significant. Particularly for thinner deposited layer (lower GO concentration), the evaporation becomes more intense due to larger surface area. When the heat input increases, the contribution of evaporation at the GO deposited layer diminishes as its counterpart of the liquid-vapour interface intensifies. For thick

deposited layer (high GO concentration), the effect of water permeation deteriorates, as elucidated in the following. In the oxidation process, GO sheets are attached by reactive oxygenated functional groups namely hydroxyl and carboxyl²⁴⁴ which enhance the hydrophilicity and act as a separation between two stacked GO sheets, allowing water molecules to travel between the interlayer of the two stacked GO sheets²⁵⁰. In regions with non-oxidized graphene sheets, fast water permeation prevails as water molecules slip through the atomically smooth carbon walls. When water molecules approach the oxidized regions with oxygenated functional groups, they are pinned down due to the strong hydrophilic nature of the functional groups, impeding the in-plane water permeation effect^{250, 277, 285}. Stronger pinning effect prevails in thicker GO deposited layer. This explains the decreasing trend of η with increasing \dot{Q}_a and the diminishing effect of GO deposited layer thickness on \bar{h}_e enhancement.

In Regime II for higher \dot{Q}_a , except for that of the thinnest GO deposited layer (0.01 wt%), η increases with \dot{Q}_a and approaches an asymptotic value at high heat input, as depicted in Figure 4.6(b). At high heat input ($\dot{Q}_a = 15\text{W}$), the 0.05 wt% and 0.025 wt% GO depositions (of middle thicknesses) manifest the highest η . This phenomenon is a compromise resulting from the deteriorative effects on the evaporation strength associated with the thickness of GO deposition. When the deposited layer is too thin, the filmwise evaporation is too intense for water to be replenished through permeation in GO sheets to sustain the evaporation that dryout might take place and hinder the filmwise evaporation. As the evaporation at the liquid-vapour interface is relatively intense at high heat input, the significance of filmwise evaporation is not profound and therefore the evaporation enhancement due to the deposited layer is decreased. On the other hand, when the deposited layer is too thick, the fast water permeation deteriorates due to the water pinning effect of the hydrophilic functional groups, as discussed earlier. In this case, the effect of the thickness of GO deposition on the enhancement of evaporation is marginal at high heat input. Thus, the fast water permeation characteristics of the GO deposition, which is intimately related to the structural alteration under temperature variation and deposition thickness, are key factors in affecting the evaporation strength and hence the thermal performance of a GO/water nanofluid charged TPCT.

4.4 Conclusions

In summary, we demonstrated the fast water permeation effect of immersed GO deposition on the evaporation strength of a GO/water nanofluid charged TPCT. The operation of fast water permeation in the nanocapillaries was attributed to the frictionless interaction between the atomically smooth, hydrophobic carbon wall and the well-ordered hydrogen bonds of the water molecules that gives rise to capillary force which is strong enough to overcome the gravitational force to form a thin water film on the GO deposited layers. The water intercalation induces the expansion of the interlayer distance between the graphitic planes which is temperature dependent. As a result, filmwise evaporation which is more effective than its interfacial counterpart is induced and the overall performance of TPCT is greatly enhanced. This study provides important insights into the mechanism of water permeation of immersed GO that exhibits an enormous potential in thermal management applications with special relevance to the development of two-phase cooling devices.

Chapter 5

Effective phase-change heat transfer through graphene-oxide surface functionalization

5.1 Outline

Graphene with its high thermal conductive nature has often been positioned as an excellent heat conducting material for high power electronics. Advanced heat dissipation devices such as heat spreaders and thermal interface materials (TIMs) have been extensively investigated but remain less effective with the inevitable limitations in heat conduction^{52, 56}. Firstly, the excellent thermal conductivity is significantly reduced with the inadvertent introduction of lattice defects from the initial chemical vapour deposition (CVD) process and transferring process of graphene thin film, or the case of graphene derivatives - oxidation and reduction. Secondly, the reduction in thermal conductivity worsens as graphene or graphene derivatives are deposited onto bulkier substrates^{212, 213}. The weak thermal coupling between the graphitic layer and the adjacent substrate greatly reduces the effective heat conduction in graphene-based heat spreaders. For TIMs, the resulting thermal conductivities of the composites are mostly lower than $10 \text{ Wm}^{-1}\text{K}^{-1}$, which are two to three orders of magnitude lower than the pristine graphene sheets^{52, 56, 158, 286}. As a result, this crippling weakness in graphene heat conduction has limited the advancement of graphene-based thermal applications.

In chapter 4, the strength of evaporation is enhanced with the deposition of GO layer on the evaporator surface, which not only extends the effective evaporation region but also facilitates the filmwise evaporation. Besides that, the fast water permeation of GO deposition has been identified as the primary mechanism which contributes to the anomalous boiling enhancement. The early postulation of high thermal conductivity of deposited layer in several related studies will have to be reassessed^{57-59, 236, 240-242}. Rather than the conventional approach of enhanced heat conduction with graphene, this study demonstrates graphene utilization for phase-change heat transfer enhancement. New generation of graphene-based heat dissipation devices operating on the principle of phase-change heat transfer can be developed.

In this study, we demonstrate an effective and scalable method of producing uniformly distributed GO deposition on any metallic substrate. Enhancement in phase-change heat transfer is evaluated based on the observation of droplet vaporizing dynamics on the GO-coated surface under various surface temperatures. Three surface temperatures are utilized to simulate three different types of boiling regimes: contact

boiling, transition boiling and film boiling. Quantitative analysis of the phase-change heat transfer enhancement is also conducted with an infrared thermal imaging spectrometer. The GO-coated surface demonstrates significant vaporization enhancement across all boiling regimes. Under the film boiling regime, droplets vaporizing on the GO-coated surface exhibit unique droplet dynamics which corresponds to the rapid transition of boiling regimes from film boiling to contact boiling. Complete vaporization of droplets can be observed on the GO-coated surface whereas the Leidenfrost effect can be observed on the uncoated aluminium surface. The effective vaporization enhancement and Leidenfrost state suppression are attributed to the fast water vapour permeation of the GO deposition. The underlying driving mechanisms which support the water vapour permeation across GO deposition are also discussed – namely the Laplace pressure gradient, temperature gradient and the temperature induced structural alteration of GO. This study provides a comprehensive understanding of the phase-change heat transfer enhancement of GO deposition.

Monash University
Declaration for Thesis Chapter 5

In the case of Chapter 5, the nature and extent of my contribution to the work was the following:

Nature of contribution	Extent of contribution (%)
I was the chief investigator for this work. My contributions to this research were the design and fabrication of the experimental setup, conducting experiments, data analysis and preparation of manuscript.	80

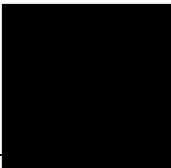
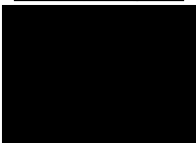
The following co-authors contributed to the work. If co-authors are students at Monash University, the extent of their contribution in percentage terms must be stated:

Name	Nature of contribution	Extent of contribution (%) for student co-authors only
A/Prof. Hung Yew Mun*	Overall supervision	-
Dr. Tan Ming Kwang	Overall supervision	-
A/Prof. Chai Siang Piao	Overall supervision	-
Ong Wee Jun	Assisted in the synthesis of graphene-oxide and advised on the material's characterization	5

The undersigned hereby certify that the above declaration correctly reflects the nature and extent of the candidate's and co-authors' contributions to this work*.

**Candidate's
Signature**

**Main
Supervisor's
Signature**

Tong Wei Li		Date: 1 June 2016
A/Prof. Hung Yew Mun		Date: 1 June 2016

5.2 Experimental investigation

5.2.1 Preparation of graphene-oxide nanofluid

Graphite oxide powder was synthesized using precursor graphite powder *via* the modified Hummers' method with the following procedures^{243, 244}. 3 g of graphite powder (Sigma Aldrich, <45 μ m, >99.99%) was added into an 80°C mixture containing 12 ml of concentrate H₂SO₄ (Chemolab supplies, 95-97%), 2.5 g of P₂O₅ (Sigma Aldrich, \geq 98%) and 2.5 g of K₂S₂O₈ (Sigma Aldrich, \geq 99%). The mixture was then stirred for 4.5 hours under a constant temperature of 80°C. Upon cooling to room temperature, the mixture was diluted with 500 ml of DI water. Filtered with Nylon membrane of 0.2 μ m pore size, the remaining was continuously washed with DI water until the pH of the filtrate water turned neutral. The product was dried at 70°C overnight. The pre-oxidized graphite was re-dispersed into 120 ml of cold concentrated H₂SO₄ together with 15 g of KMnO₄ (Sigma Aldrich, \geq 99%) with the temperature of the mixture kept below 20°C. A viscous dark green paste was formed. The mixture was then stirred for 2 hours at room temperature and subsequently diluted with 250 ml of DI water. An ice bath was required to maintain the mixture's temperature below 50 °C. With additional 2 hours of stirring, the dark brownish mixture was diluted with 700 ml of DI water. 20 ml of H₂O₂ (R&M Chemicals, 30%) was further added into the final mixture with the formation of a yellowish paste. Next, the mixture was washed with 1 l of HCL (Merck, 37% diluted to 10%) followed by DI water to completely neutral the acid content. Lastly, the graphite oxide solid was air-dried at a temperature of 60°C for 24 hours. The graphite oxide was then grounded into fine powder form for easy dispersion in water. X-ray diffraction (XRD) analysis of the graphite oxide powder indicated a sharp peak at 9.1°, corresponding to an interlayer distance of 9.7 Å. The exfoliation of graphite oxide was performed using ultrasonication treatment. Measured amount of graphite oxide powder was dispersed in DI water and underwent ultrasonication treatment. The weight percentage used in our studies was maintained at 0.1 wt%. The GO nanofluid was sonicated for 5 hours with an ultrasonic liquid processor (Q700 Sonicator®, Qsonica, LLC.) at 20 kHz and 700 W. A schematic diagram indicating the preparation of GO nanofluid is illustrated in Figure 5.1.

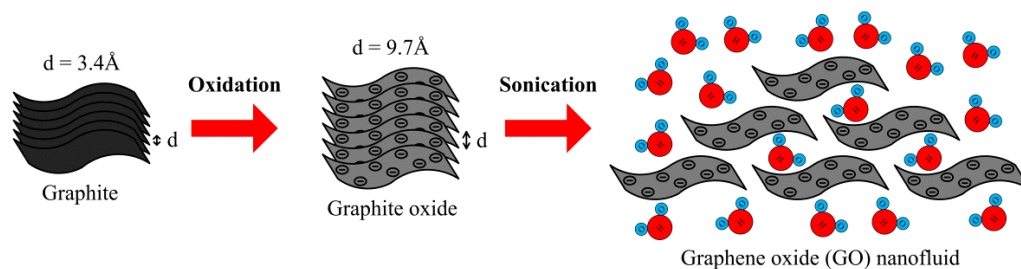


Figure 5.1| Schematic illustration of the preparation of GO nanofluid. The increase in the interlayer distance is attributed to the presence of oxygenated functional groups across the graphitic planes. The negatively charged functional groups induce electrostatic repulsion among the GO sheets.

5.2.2 Fabrication of graphene-oxide coated layer

Prior to the fabrication of the GO-coated layer, the aluminium surface was repeatedly cleaned with acetone, ethanol and DI water to remove any impurities. The aluminium surface was then heated using a hot plate. With the surface temperature maintained at 110°C , 50 ml of 0.1 wt% GO nanofluid was progressively supplied to the targeted surface. A circular hollow frame with an internal diameter of 28 mm was used to shape the GO-coated layer over the aluminium surface. As the solvent (DI water) evaporated, a homogeneous silvery layer of GO was formed. The GO-coated layer was further maintained at 110°C for 30 minutes to assure the complete removal of the remaining solvent. Such fabrication method has also been used in the preparation of GO thin film²⁸⁷. The negatively charged GO crystallites facilitates the formation of island like deposition¹⁸³. The Langmuir-Blodgett assembly of GO crystallites is also governed by the van der Waals force, forming interlocked layered structure^{250, 253}. Therefore, the proposed GO coating technique can be easily applied to any substrate by virtue of evaporating GO nanofluid on the targeted surface. By regulating the concentration and the volume of the GO nanofluid, controllable thickness of GO-coated layer can be achieved. Figure 5.2 shows the GO coating technique used in our studies.

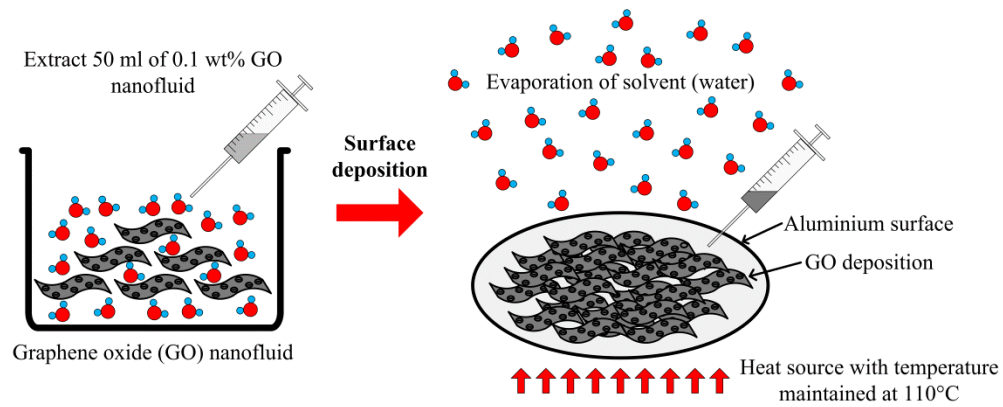


Figure 5.2| Schematic illustration of GO coating technique by the evaporation of GO nanofluid.

5.2.3 Experimental details for the evaluations of droplet dynamics and phase-change heat transfer enhancement

A photographic view of the setup for the visualization of the dynamic transformation of droplet vaporizing on various surfaces is shown in Figure 5.3. The main components consist of a power supply for the heating elements, controllable syringe pump, high speed camera, high intensity illuminator, thermocouple wires connected to a data logger and infrared thermal imaging spectrometer. To simulate phase-change heat transfer in different boiling regimes, the surface temperature of the substrate was varied with two embedded electrical heating elements connected to a power supply (PS 8160-04T, Elektro-Automatik, Viersen). Four different surface temperatures were selected in our studies namely 130°C, 180°C, 220°C and 260°C in the extreme case. The average surface temperature and the ambient temperature were measured using four type-T thermocouple wires. All temperature measurements were recorded with a data logger (GL820, Graphtec, California) at a sampling time of 2 seconds. To evaluate the rapid temperature variation of the substrate underneath the droplet, infrared thermal imaging spectrometer (thermoIMAGER TIM 160, Micro-Epsilon, Germany) was used (frame rate of 100 Hz). The thermal imaging spectrometer is calibrated with the adjustment of emissivity based on a reference temperature measured with the thermocouple wire. A consistent 10- μ l droplet was dispensed from the syringe charged with DI water and controlled by a syringe pump (EW-74900-05 series, Cole Parmer, Malaysia). The syringe needle was fixed 30 mm above the substrate throughout the experiments. The droplet's dynamic transformation was

captured using a high speed camera (M310, Phantom, New Jersey) coupled with a long distance magnifying lens (1-50486, Navitar, Rochester, USA). Back-lighting imaging method was utilized for the video capturing with a high intensity illuminator (41723-series, Cole Parmer, Malaysia). The droplet dynamics was captured at 1000 frames per second. Notably, the GO-coated layer was able to withstand continuous heating and cooling without any noticeable structural defect.

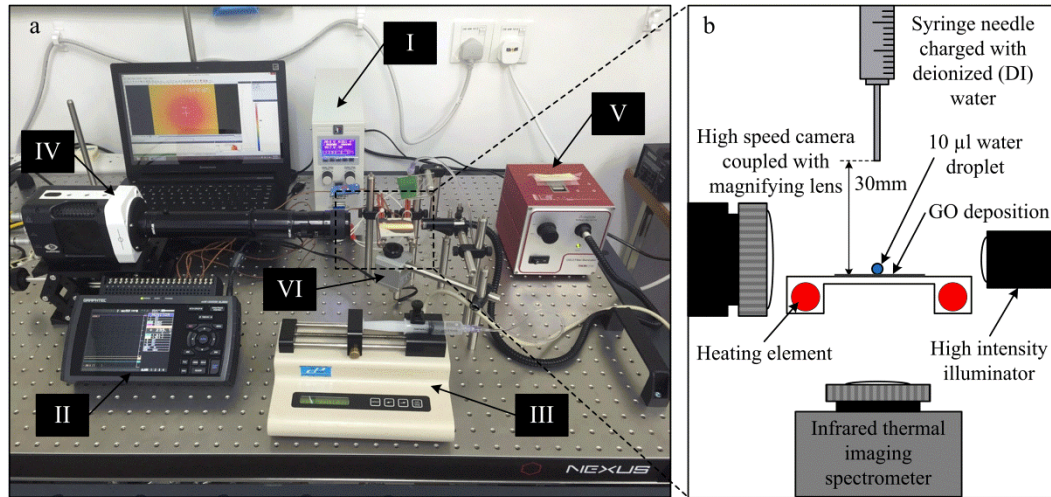


Figure 5.3| Experimental setup for the visualization of dynamic transformation and the thermal evaluation of droplet impinging on GO-coated surface and uncoated surface under various boiling regimes. **(a)** Photographic view of the experimental setup consisting of several main components: **(I)** direct current power supply, **(II)** data logger, **(III)** syringe pump connected with a syringe needle, **(IV)** high speed camera coupled with long distance magnifying lens, **(V)** high intensity illuminator and **(VI)** infrared thermal imaging spectrometer. **(b)** Schematic illustration of the experimental setup.

5.2.4 Experimental details for the characterization of phase-change heat transfer enhancement using spray cooling system

The experimental setup for the evaluation of phase-change heat transfer enhancement using a spray cooling system is shown in Figure 5.4(a). Two cylindrical heating elements were utilized for the heating of GO-coated surface and uncoated surface (aluminium surface) to the targeted temperatures. GO deposition was coated onto the aluminium surface with a diameter of 28 mm using the aforementioned coating technique. Both GO-coated surface and the uncoated surface have identical surface area

for the evaluation of effective cooling. The heating elements were powered by a power supply (PS 8160-04T, Elektro-Automatik, Viersen) with five fixed power inputs throughout each experiment. By positioning the heated surfaces (GO-coated surface and aluminium surface) above the spray cooling system at a fixed distance of 20 mm, the heated surfaces were subsequently cooled. Notably, both heated surfaces were well insulated with Polytetrafluoroethylene (PTFE) insulation block. Prior to the activation of the spray cooling system, the average surface temperature T_{nc} and the ambient temperature $T_{nc,\infty}$ under natural cooling were measured using four type-T thermocouple wires. The average surface temperature T_{sc} and the ambient temperature T_{sc} were then measured with the subsequent activation of the spray cooling system. The ambient temperatures were measured at a fixed location 15 mm away from the heated surface. All temperature measurements were recorded with a data logger (GL820, Graphtec, California) at a sampling time of 2 seconds over a period of 45 minutes. All temperature measurements used for the calculation of the evaporation enhancement ratio (EER) were selected under steady state condition. The spray cooling system consists of a circular disk piezoelectric module coupled with stainless steel diaphragm covered with 570 micro-sized orifices ($\phi_o=5\sim6\ \mu\text{m}$), capillary tube ($\phi_{ct}=10\ \text{mm}$, $L_{ct}=55\ \text{mm}$) and a water reservoir ($V_w=65\ \text{ml}$), as shown in Figure 5.4(c, d, e). The capillary tube was closely attached to the vibrating diaphragm which generated an average water droplet size of $10\ \mu\text{m}$. The piezoelectric module was excited by a function generator (TG5011, Thurlby Thandar Instruments limited, United Kingdom) connected to an amplifier (LZY-22, Mini-Circuits, United States). The resonance frequency was kept constant at 115 kHz. The actual power input to the piezoelectric module was measured using an oscilloscope (DS1102E, Rigol, United States) coupled with an alternating current probe (P6022, Tektronix, United States). A more detailed schematic illustration of the spray cooling system and the heated surface is shown in Figure 5.4(b).

Figure 5.4| Spray cooling experimental setup for the evaluation of phase-change heat transfer enhancement. **(a)** Photographic view of the spray cooling setup consisting of several main components: **(I)** spray cooling system, **(II)** direct current power supply, **(III)** data logger, **(IV)** function generator, **(V)** amplifier, and **(VI)** oscilloscope. **(b)** Schematic diagram of the spray cooling system. **(c)** Photographic view of the piezoelectric module used for the atomization of water droplets. **(d)** High-magnification optical microscopic image of the micro-sized orifices ($\phi_o=5\sim6\text{ }\mu\text{m}$). **(e)** Cross-sectional view of the piezoelectric module.

5.3 Results and discussion

5.3.1 Characterization of graphene-oxide coated layers

Figure 5.5(a) represents the GO-coated aluminium surface used in our experiments. A total of 50 ml of 0.1 wt% GO nanofluid was progressively supplied to the heated surface (110°C) with a diameter of 28 mm to yield an average coating thickness of 40 μm (Figure 5.5(d)). FESEM images indicate a large distribution of micro-sized cavities over the multi-layered GO deposition which served as active nucleation sites for vapour formation [Figure 5.5(b, c, e, f)]. In the nucleate boiling regime, rapid formation and detachment of tiny vapour bubbles are crucial to prevent the transition to film boiling.

5.3.2 Water absorption of graphene-oxide coated layers

To illustrate the water permeation effect on the GO-coated layers, static contact angle analysis is conducted on GO-coated surface and aluminium surface to observe the spreading of a water droplet. The variations in static contact angle of aluminium surface and GO-coated surface over a period of 300 seconds were measured with a standard goniometer under ambient temperature [Figure 5.5(g, h)]. In general, boiling heat transfer enhancement can be achieved with the increase in surface wettability which involves surface modification to lower the static contact angle and increase the liquid-solid contact. A lower contact angle is more desirable in promoting phase-change heat transfer. However, with the water absorbing characteristics of the GO-coated layer, the postulation of enhanced surface wettability for phase-change heat transfer enhancement is inadequate to elucidate with the apparent contact angle. GO-coated surface behaves similar to a super-wetting surface yet exceeding the capability of forming a thin film only at the edge of the deposited droplet. Water permeation across the GO-coated layer continuously reduces the droplet size by spreading the liquid towards the unsaturated area, forming a water thin film which is equivalent to the thickness of the deposition (upon total intercalation of water droplet). With the controlled thickness of the GO-coated layer, we are able to manipulate the thickness of the water layer to form an ultra-thin water film for ultra-effective vaporization. As an evidence of the water permeation

across GO-coated surface, the static contact angle reduces 48% at a rate of $0.112\text{ }^{\circ}\text{s}^{-1}$ while the reduction for aluminium surface is only registered 18.8% at a rate of $0.052\text{ }^{\circ}\text{s}^{-1}$.

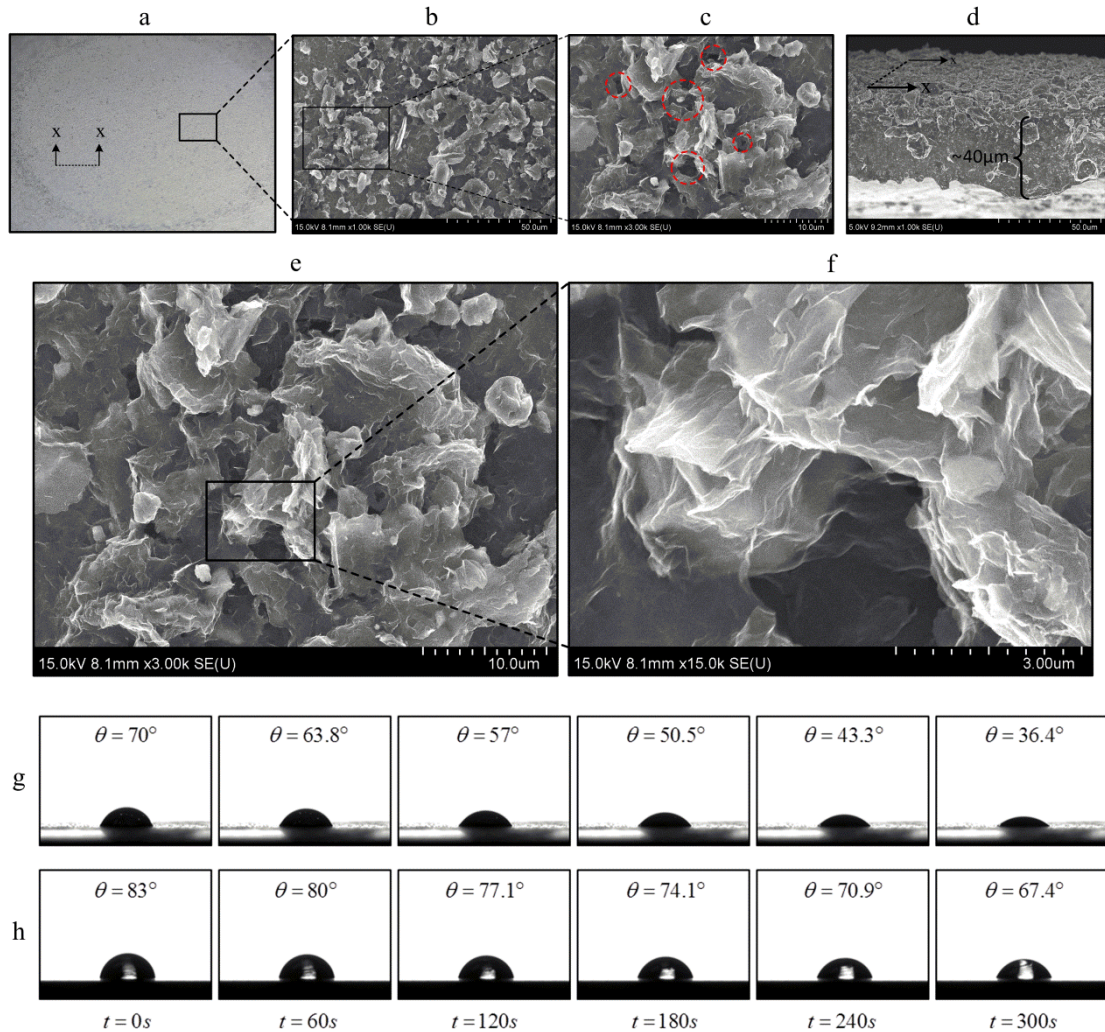


Figure 5.5| Characterization of GO depositions. (a) Photograph of uniformly distributed GO-coated layer on aluminium surface. (b) FESEM image of GO-coated layer at low-magnification. (c) FESEM image of GO-coated layer at high-magnification showing micro-sized cavities of active nucleation sites for vapour formation (red-dotted circles). (d) Cross-sectional view of GO-coated layer with an estimated thickness of 40 μm. (e) Enlarged view of the FESEM image of GO-coated layer at high magnification. (f) FESEM image of GO-coated layer at ultrahigh magnification revealing its layered structure. Time-lapse images of a 2-μl water droplet resting on (g) GO-coated surface and (h) aluminium surface, over a time span of 5 minutes under room temperature. The corresponding contact angles and dynamic of the droplet are captured with an interval

of 60 s. For GO-coated surface, complete absorption of water droplet can be observed within 10 minutes.

5.3.3 Evaporation enhancement of graphene-oxide coated layers

To evaluate the efficacy of water thin film vaporization over GO-coated substrate, we examine the dynamic transformation of droplet impinging on GO-coated surface under various surface temperatures. The experimental setup is illustrated in Figure 5.3. Three surface temperatures are utilized to simulate three different boiling regimes namely contact boiling, transition boiling and film boiling. Surface temperature above the boiling point of water with nucleation of vapour bubbles accounts for contact boiling heat transfer. By increasing the surface temperature, transition boiling is characterized by the merge of vapour bubbles forming intermittent vapour layer. Above the Leidenfrost point, film boiling takes place where a continual vapour layer is formed between the droplet and the surface. The dynamics of a 10- μ l droplet impinging on a surface coated with and without the GO coating were captured with a high speed camera under different surface temperatures. The variation of surface temperature underneath the droplet was measured with an infrared thermal imaging spectrometer.

The most effective phase-change heat transfer can be obtained in the contact boiling regime where direct contact between the droplet and the surface are essential for effective two-phase heat transfer. Formation of vapour bubbles is observed. By increasing the surface temperature to 130°C, the variations of droplet dynamics during initial impingement, vapour bubble size and vaporization time of a droplet vaporizing on GO-coated surface and aluminium surface can be clearly discerned [Figure 5.6(a, b)]. For GO-coated surface, the time taken for complete vaporization of a 10- μ l droplet is approximately 252 ms. On the other hand, aluminium surface requires more than 1100 ms (4 times of GO-coated surface) for the complete vaporization of a same-sized droplet. Furthermore, we notice that the droplet deposited on the aluminium surface generates larger vapour bubbles as compared to those of GO-coated surface. Formation of large vapour bubbles extending above the spreading lamella of the droplet can be undesirable due to the increased tendency of early transition to film boiling. The burst of vapour bubble at the liquid interface generates capillary waves, resulting in the ejection of tiny elongated liquid jets when the bubbles cohere²⁸⁸. For aluminium

surface, the burst of large vapour bubbles generates liquid jets which incur adverse effect on heat transfer due to the reduction of droplet's volume. In an extreme case, violent bursting of large vapour bubbles generates substantial repulsive force that completely propels the remaining droplets away from the heated surface. Such phenomenon is a classic example of transition boiling where the heat transfer rate is significantly reduced prior to the formation of vapour layer. Moreover, the edge of the droplet impinging on GO-coated surface manifests a sharp acute angle with a contact angle of $\theta_d = 33.6^\circ$. On the other hand, for the aluminium surface, a rounded edge is observed with a contact angle of $\theta_d = 84.2^\circ$. This indicates different interaction of water droplet on the two surfaces. The anomalous heat transfer enhancement of micro/nano structured surfaces is essentially attributed to the dramatic increase in density of active nucleation site of vapour bubbles and capillary pumping strength across the wicking structure extending the liquid-solid contact^{41, 42, 50}. Nevertheless, the actual mechanism contributed to the effective phase-change heat transfer of GO coating can be different due to its unique property of fast water vapour permeation. To comprehend the effect of water permeation on the heat transfer enhancement, the surface temperatures of GO and aluminium were further increased to 180°C , operating under the transition boiling regime.

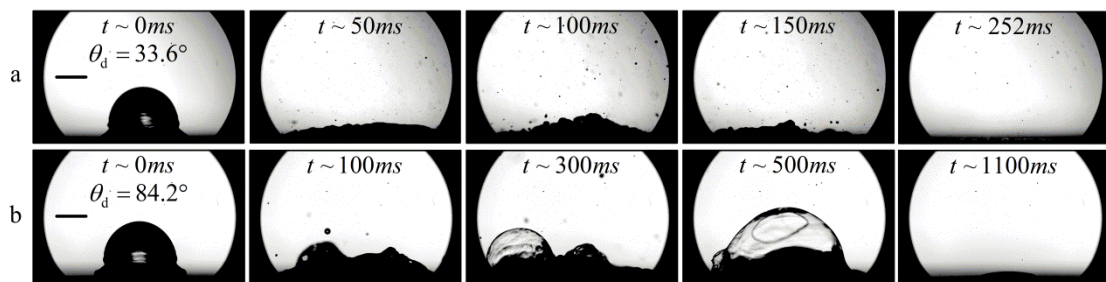


Figure 5.6| Sequential high-speed photography images of 10- μl water droplet impinging and vaporizing on (a) GO-coated surface, and (b) aluminium surface, heated to a controlled surface temperature of 130°C in contact boiling regime. The droplet dynamics at the initial impingement manifests distinct surface characteristic with a variation in contact angle θ_d . Scale bar, 1 mm.

Compared to the aluminium surface, the dynamic transformation of a droplet on a GO-coated surface is distinctive in the transition boiling regime as depicted in Figure

5.7(a, b). For GO-coated surface, we notice that the geometry of droplet changes from an initial hemisphere to a column where the solid-liquid contact area is reduced. As a result, the evaporation time is almost double of that of contact boiling regime. Formation of vapour bubbles inside the droplet is found occupying a partial area of solid-liquid interface and the droplet is partially in contact with the GO-coated surface. On the other hand, a droplet on aluminium surface is subjected to a typical transition boiling process whereby vapour bubbles burst vigorously at the liquid-vapour interface, as shown in Figure 5.7(b). Shortly after the droplet impinges on the aluminium surface (50 ms), it is ejected from the surface due to the bursting of vapour bubbles. The dynamics of a droplet under such circumstance are governed by two dominant forces, i.e. vapour force F_v associated with the vapour pressure prevalent underneath the droplet and the body force F_b of droplet. The vapour force is estimated as $F_v \equiv \pi p_v R_c^2$, where p_v denotes the vapour pressure and R_c is the critical radius of the vapour bubble prior to the burst. The body force is taken as $F_b = m_d g$, where m_d is the droplet mass and g is the gravitational acceleration. The bursting of vapour bubbles substantially reduces the droplet's body force. As the vapour force exceeds the droplet's body force, the droplet is ejected and bounces off the surface (110 ms). Therefore, in the transition boiling regime, the droplet is only partially vaporized and the thermal efficiency is reduced. However, droplet on GO-coated surface vaporizes completely regardless of the partial contact. This implies that the vapour force prevailing underneath the droplet is always smaller than its body force due to the fact that vapour dissipates and gets away from being confined underneath the droplet. The fast dissipation of vapour can be essentially attributed to the property of fast water vapour permeation of GO^{250, 253, 277, 289, 290}. The GO-coated surface provides nanocapillaries (nanoscale interconnecting networks) which serve as rapid flow passages for water vapour. As discussed in Figure 5.5(g), the droplet's contact angle continuously and gradually contracts over time on the GO-coated surface. The fact that water droplet is completely absorbed into GO-coated layer indicates that the fast water permeation property of GO is effectual to the dissipation of vapour underneath the vaporizing droplet. We shall discuss this point in a more detailed manner later.

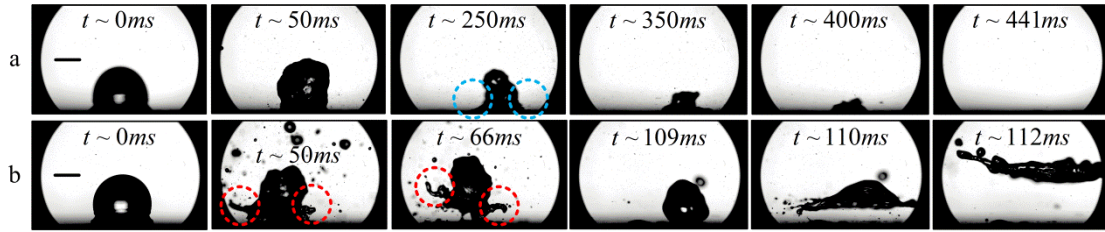


Figure 5.7| Sequential high-speed photography images of 10- μ l water droplet impinging and vaporizing on **(a)** GO-coated surface, and **(b)** aluminium surface, heated to a controlled surface temperature of 180°C in transition boiling regime. Water droplet on the GO-coated surface progressively vaporizes while complete droplet ejection is observed over the aluminium surface. For the droplet on aluminium surface, elongated liquid jets (red dotted circles) are ejected from the bottom section of the droplet due to the bursts of large vapour bubbles. On GO-coated surface, no burst of large vapour bubble (blue dotted circles) was observed. Scale bar, 1 mm.

As a result of the contact boiling, tiny droplets are ejected from the surface associated with the bursting of vapour bubbles at the liquid-vapour interface, as depicted in Figure 5.7(a). The size of tiny droplets ejected from the bursting of vapour bubbles is comparatively smaller, which is a typical characteristic of contact boiling. The size distributions of the ejected droplets induced by the bursting of vapour bubbles are tabulated in Table 5.1. For GO-coated surface, majority of the ejected droplet size is below 100 μ m, accounting for 94.6% of the total ejected droplets. For aluminium surface however, 53.6% of ejected droplets are large than 100 μ m, ranging from 100 μ m to 650 μ m.

Table 5.1| Size distributions of ejected droplets induced by bursting of vapor bubbles on GO-coated surface and aluminum surface at 180°C in the transition boiling regime.

Type of surface	Droplet size (μm)	Number of droplet (N)
GO	<100	384
	100-200	20
	200-300	1
	300-400	0
	400-500	0
	500-600	1
	>600	0
Aluminium	<100	111
	100-200	73
	200-300	31
	300-400	16
	400-500	3
	500-600	3
	>600	2

By increasing the surface temperature to 220°C above the Leidenfrost point for water, the droplet rebounds on the aluminium surface after the first impact [Figure 5.8(a)]. The formation of a vapour film at the instance of the first impact generates sufficient vapour force to levitate the droplet. This is a typical phenomenon observed in the film boiling regime. Figure 5.8(b) shows a water droplet vaporizing on GO-coated surface at 220°C. The droplet vaporizes completely without indication of rebounding. The Leidenfrost effect is suppressed where the droplet is always in contact with the surface and contact boiling is still prevailing. Therefore, it shows that the transition temperature (Leidenfrost point) is increased and the onset of film boiling regime is delayed.

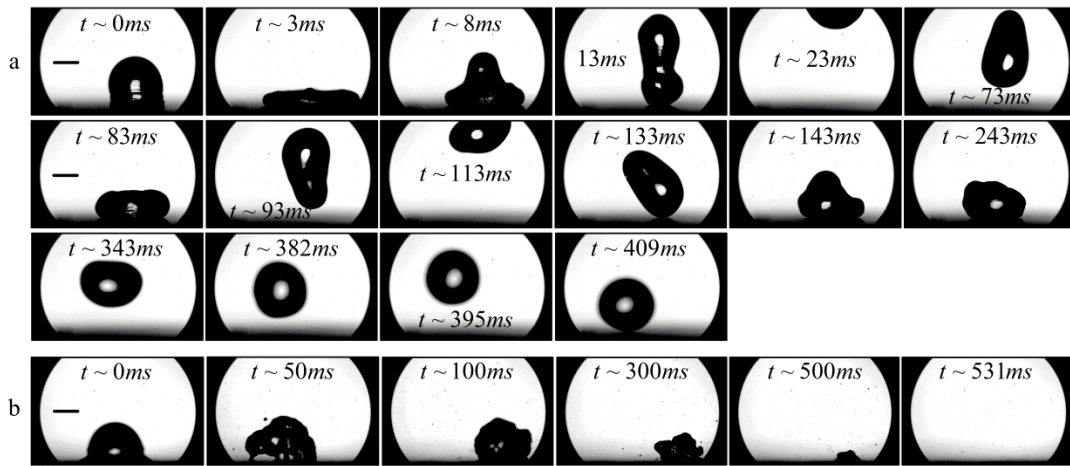


Figure 5.8| (a) Sequential high-speed photography images of 10- μ l water droplet rebounding after the first impact on aluminium surface heated at a controlled surface temperature of 220°C simulating heat transfer in the film boiling regime (beyond Leidenfrost point). The formation of a stable vapour film prevents the droplet from vaporizing and generates sufficiently large vapour force for continuous droplet levitation. The water droplet bounced off the heated surface after several impingements. (b) Complete vaporization of water droplet on GO-coated surface heated at a controlled surface temperature of 220°C with no indication of droplet rebounding. Scale bar, 1mm.

To understand the driving mechanism of Leidenfrost state suppression, we investigate the intriguing characteristic of the GO layer. As micro-sized GO crystallites deposited on a surface, the negatively charged functional groups repel each other and island like deposition is formed¹⁸³. The Langmuir-Blodgett assembly of GO crystallites is closely pulled by van der Waals force, forming interlocked layered structure^{250, 253}. Further characterization of the GO layer indicates an interlayer distance of 9.71 Å through X-ray diffraction (XRD) analysis (Figure 5.9). The oxygenated functional groups increase the interlayer distance of the GO structure, forming a network of nanocapillaries. Vigorous interaction between the water molecules and the hydrophilic surfaces along the nanocapillaries impedes the permeation while hydrophobic carbon surfaces favour the fast water permeation^{250, 251, 253}. Nevertheless, the rigidly attached water monolayer empowers the translation movement of the adjacent water monolayer, allowing further expansion of the graphitic planes with the intercalation of water multilayers^{246, 279}. As a consequence, fast water vapour permeation is prevalent in the GO layer.

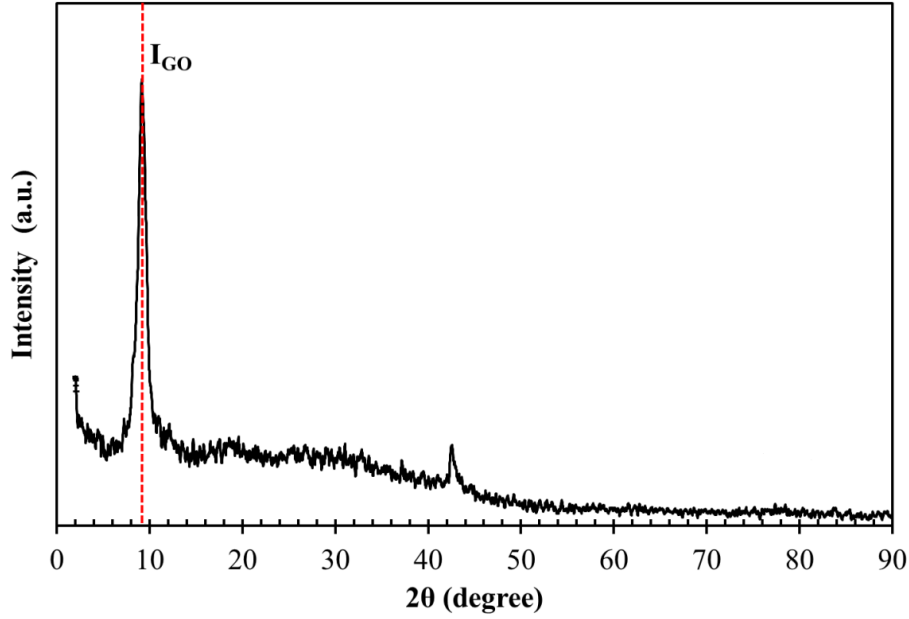


Figure 5.9| XRD pattern of the precursor graphite oxide. The peak position is located at 9.1° corresponding to the interlayer distance of 9.71 \AA . The increase in the interlayer distance illustrates the presence of the oxygenated functional groups. The XRD pattern is obtained using Bruker D8 Discover X-ray diffractometer with Cu K α ($\lambda=1.54056 \text{ \AA}$) and a scanning rate of $0.02^\circ \text{ s}^{-1}$.

Next, we describe the driving forces for the initiation of intercalation of water molecules in GO structure. The resultant vapour is capable of travelling into the GO layer through the nanocapillaries. Two possible driving mechanisms enable the constant flow of water molecules through the GO nanocapillaries, i.e. Laplace pressure gradient and temperature gradient. Notably, the droplet impact force is assumed to be negligible. This point has been justified by comparing the order of magnitude of the vapour pressure accumulating in the vapour bubble and the impact pressure of the impinging droplet in our experiments. The magnitude of the vapour pressure is estimated from the simplified Young-Laplace equation²⁹¹ given as $p_v = p_s + (2\gamma/R_c)$, where p_s is the surrounding pressure and γ is the surface tension. For a droplet evaporating on a GO-coated surface, the critical radius of the vapour bubble estimated in the order of 10^{-4} m (Figure 5.10). On the other hand, the impact pressure is estimated as $p_i = \rho R_m^2 U_i^2 / \pi R_d^2$, where ρ is the liquid density, R_m is the maximum radius of the spreading lamella, U_i is the impact velocity and R_d is the radius of the impinging droplet²⁹². The impact velocity is calculated in the order of 10^{-1} ms^{-1} while the radii of the spreading lamella

and the impinging droplet are in the order of 10^{-3} m. By virtue of low impact velocity and small spreading radius associated with the impinging droplet, it is estimated that the vapour pressure is at least 10^3 times of the impact pressure. Therefore, we rule out the droplet impact force as the driving force for water permeation in GO layer.

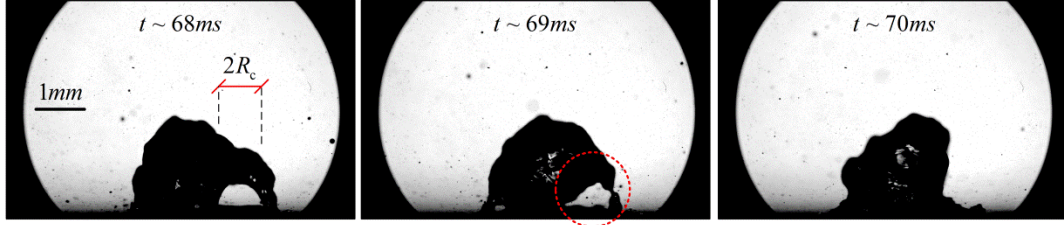


Figure 5.10| Size estimation of the bursting of vapour bubbles from a water droplet vaporizing on a GO-coated surface heated at 180°C (transition boiling regime). The critical radius R_c of the vapour bubble was measured in the order of 10^{-4} m. The vapour bubble collapses after reaching the critical radius (red-dotted circle) and the pressure of vapour is decreased. The water vapour permeability of the GO layer hinders the bursting of vapour bubbles, leading to the absence of elongated liquid jets. The formation of elongated liquid jets is a conventional phenomenon in the transition boiling regime due to the bursting of large vapour bubbles. Scale bar, 1 mm.

To initiate a burst, the pressure inside the vapour bubble is required to overcome the critical pressure, which is the resultant pressure of the surrounding pressure and the pressure induced by surface tension of the liquid-gas interface, i.e., $p_v > p_s + (2\gamma/R_c)$. Attributed to the property of fast water vapour permeation of GO layer, the pressure inside the vapour bubble drives the vapour through the nanocapillaries formed among the stacked graphitic planes. Therefore, no accumulation of vapour takes place and the pressure of vapour bubble is smaller than the critical pressure of bubble bursting. Subsequently, the thin vapour layer is unlikely to form underneath the droplet.

The water vapour permeability of GO membrane has been proven to be prevalent even under a differential pressure of 10 kPa²⁵⁰. For tiny nucleating vapour bubbles with radius in the order of 10^{-5} m, the differential pressure between the vapour pressure and the surrounding pressure is estimated as 11.8 kPa using the Young-Laplace equation. Thus, smaller nucleating vapour bubbles are more likely to facilitate the vapour

permeation across the nanocapillaries. We explore the effect of temperature on the structural alteration of GO deposition. Based on the literatures, the water vapour permeability of the GO membrane varies with the surrounding humidity and the pre-exposed heat treatments^{250, 251, 293}. Structural alteration, particularly the variation in the interlayer distance, significantly affects the water vapour permeability^{250, 251, 293}. Rapid water permeation can be achieved with the expansion of the interlayer distance between the graphitic planes, allowing the intercalation of multilayers water molecules^{251, 253}. As the GO membrane is constantly heated, the interlayer distance decreases together with the water vapour permeability^{250, 251}. Nevertheless, the structure alteration in GO is reversible with water immersion or exposure to humid environment^{250, 251}. Prior to the droplet impingement, the interlayer distance of the GO deposition remains at its minimum due to the heat treatment. As the droplet touches the surface, water vapour permeation is initiated with the intercalation of monolayer of water molecules and subsequently multilayers. The water vapour permeation rate increases gradually overtime to its maximum. After the complete vaporization of droplet, the interlayer distance resumes to its original condition.

Apart from the Laplace pressure gradient across the GO layer, the temperature gradient across the GO layer is also another driving mechanism. As the droplet impinges on the GO-coated surface, the surface temperature underneath the droplet in the centre of GO-coated layer rapidly reduces as the liquid vaporizes [Figure 5.11(c)]. A maximum temperature variation of 23.1°C can be obtained as the droplet vaporizes on the GO-coated surface heated at ≈180°C. Under the influence of temperature gradient, the thermophoretic force drives the water molecules from low temperature region to high temperature region²⁹⁴. Such driving force has also been determined to have driven the aerosol thermophoresis and more recently, being identified as the working mechanism of the self-propelled Leidenfrost droplet travelling across hot ratchets²⁹⁵. The thermophoretic force enhances the movement of water molecules intercalating among the nanocapillaries of GO layer from the underside of droplet radially to the region of higher temperature. This augments the seepage of vapour from the bubble through the nanocapillaries [as shown by yellow arrows in Figure 5.11(a)] to the exposed region (not covered by liquid droplet), from where the water vapour molecules emanate.

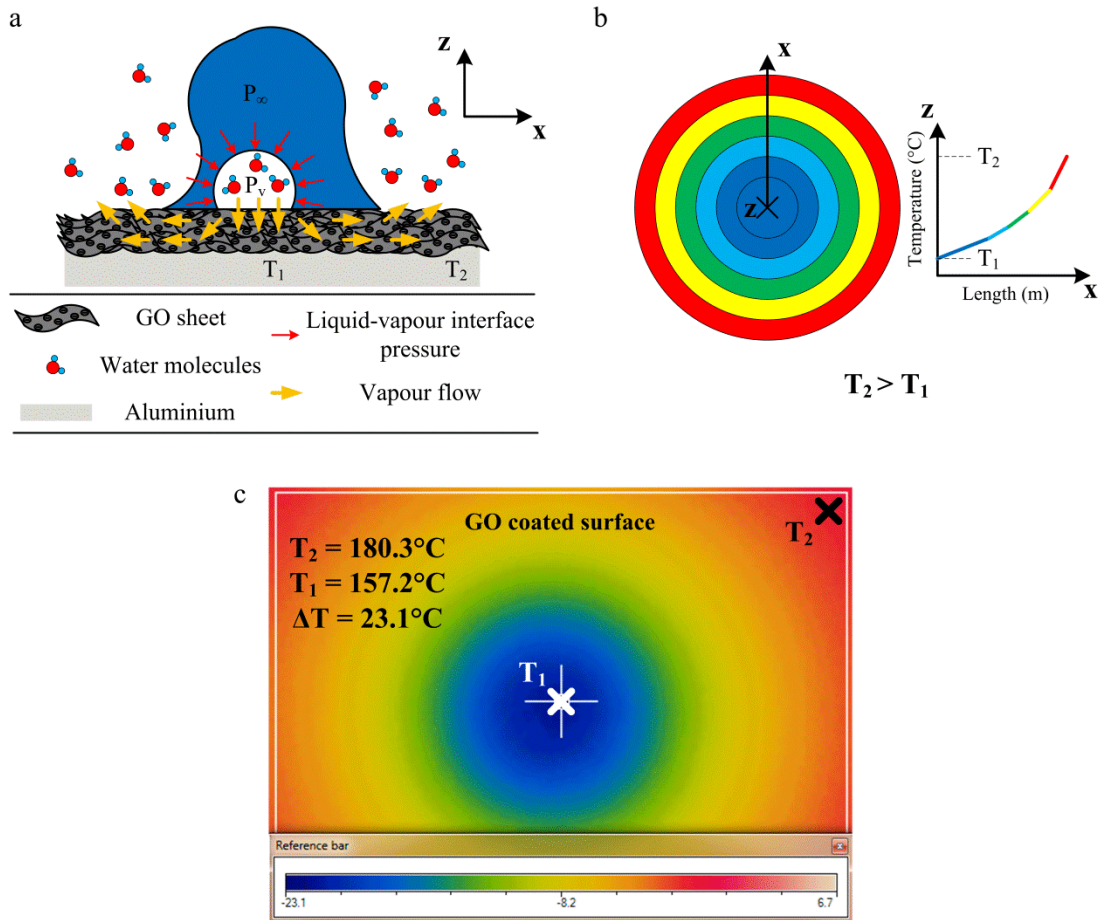


Figure 5.11| Schematic illustrations of the driving forces across nanocapillaries embedded within the GO-coated layer, (a) Laplace pressure gradient and (b) temperature gradient. (c) Temperature variation of 180.3°C heated GO-coated surface under the vaporization of a droplet. A maximum temperature variation of 23.1°C was recorded as a $10\text{-}\mu\text{l}$ water droplet vaporized from the GO-coated surface.

We analyse the dynamics of a droplet vaporizing on GO-coated surface at a surface temperature of 260°C (Figure 5.12). Sequential variation in droplet dynamics is observed as droplet impinges on the GO-coated surface. Initially, large vapour bubbles burst vigorously into tiny droplets. Shortly following this, due to more violent burst of large vapour bubbles, the droplet is divided into two whereby one of the daughter droplets is levitated. Eventually as a result of the collapse of vapour layer, the droplets reattach to the GO-coated surface and vaporize completely in 440 ms. Despite a significant increase in surface temperature, the droplet's lifetime is still equal to that at a surface temperature of 180°C . Benefiting from the inherent water vapour permeability,

GO deposition can be an excellent coating to enhance the phase-change heat transfer, essentially for Leidenfrost state suppression.

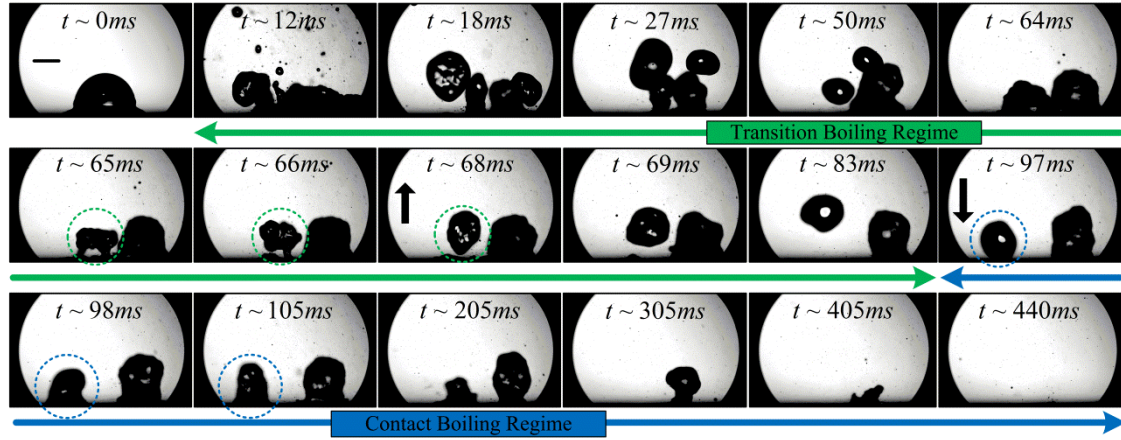


Figure 5.12| Rapid transition of boiling regimes of a droplet vaporizing on GO-coated surface heated at controlled surface temperature of 260°C. The water vapour intercalation triggers the expansion of the interlayer distance as the droplet impinged the GO interface, leading to the increase in the water vapour permeability and suppressing the formation of vapour film. Complete vaporization of water droplet can be noticed regardless of the initial Leidenfrost effect. In the transition boiling regime, partial droplet ejection is observed due to the bursting of large vapour bubble (green-dotted circles). The black arrow indicates the upward movement of the ejected droplet at 68 ms. The same ejected droplet subsequently impinges on the GO-coated surface at 97 ms and continuously remains pinned (blue-dotted circles) throughout the period of vaporization (98 ms- 305 ms) under the contact boiling regime. Scale bar, 1 mm.

5.3.4 Leidenfrost state suppression of GO-coated layer

To quantitatively analyse the phase-change heat transfer enhancement, variations in surface temperature of GO-coated surface and aluminium surface heated at controlled surface temperature of 260°C under the vaporization 10- μ l droplet are measured. The maximum temperature variations are illustrated in Figure 5.13(a, b), respectively. Under high surface temperature of approximately 260°C, the cooling effects induced by vaporization of a water droplet on GO-coated surface and aluminium surface can be clearly differentiated. Here, we employ the surface temperature variation, $\Delta T_{s,if} = T_{s,i} - T_{s,f}$, as a performance indicator, where $T_{s,i}$ is the initial surface temperature

and $T_{s,f}$ is the minimum surface temperature after the droplet impingement. For GO-coated surface, the highest surface temperature variation is recorded at 0.5 s from the initial droplet impingement. A surface temperature variation of 18.5°C was recorded.

On the other hand, due to the prevalence of Leidenfrost effect, droplet vaporization on the aluminium surface is impeded as a result of the formation of vapour barrier, leading to an insignificant temperature drop of only 1°C. The temperature variations of GO-coated surface and aluminium surface of droplet vaporization are plotted against time in Figure 5.13(c). We observe that the surface temperature of GO coating achieves its minimum point, $T_{s,f}$, in 0.5 s compared to 0.1 s of aluminium surface. This is attributed to the fact that the water droplet spreads on the GO-coated surface and vaporizes, in comparison with the droplet rebound and subsequently bounces off the aluminium surface. The $T_{s,f}$ temperature distributions of GO-coated surface and aluminium surface are depicted in Figure 5.13(d). In comparison with the case of aluminium surface, the cooling effect of water droplet on the GO-coated surface is more evident, prevalent at the centre of the droplet's impact point, where the droplet spreads to a larger locality and vaporizes completely. The latent heat of vaporization is absorbed effectively by the water droplet during vaporization and hence the surface temperature is reduced significantly. On the other hand, the water droplet bounces off the aluminium surface and the cooling effect is marginal with a temperature drop of less than 1°C.

To investigate the cooling effect imposed by a single water droplet over a feasible range of surface temperature, we evaluate the surface temperature variation, $\Delta T_{s,if}$, for GO-coated surface and aluminium surface, and the results are depicted in Figure 5.13(e). Each data point is the average of 10 runs of experiment. Typically, three different boiling regimes can be identified on the aluminium surface - contact boiling, transition boiling and film boiling. Contact boiling regime begins at the water boiling temperature of 100°C toward the point at approximately 150°C. Phase-change heat transfer intensifies with the formation of vapour bubbles nucleating at the liquid-solid interface. The highest surface temperature variation of 25.1°C is obtained at the termination of the contact boiling regime. Further increase in the surface temperature initiates the transition boiling, where the surface temperature variation drops drastically.

Beyond the surface temperature of 181.6°C, in the film boiling regime, Leidenfrost effect prevails and the formation of a continuous vapour layer can be observed underneath the droplet. In the film boiling regime, the surface temperature variation becomes insignificant and remains constant at approximately 1°C with increasing surface temperature. The change of surface temperature variation with the surface temperature is consistent with the typical boiling curve.

On the other hand, the change of surface temperature variation of GO-coated surface with increasing surface temperature is unique. There is no distinct transition and film boiling regimes. The surface temperature variation increases with the surface temperature in the contact boiling regime, achieving its maximum value at approximately 140°C. Beyond this temperature point, the surface temperature variation decreases with increasing surface temperature with a small gradient. The surface temperature variations are maintained at relatively high values due to the suppression of Leidenfrost effect by the fast water vapour permeation property of GO layer. This finding paves the way for great potential in enhancing the phase-change heat transfer rate of spray cooling on surface heated beyond the Leidenfrost point of water.

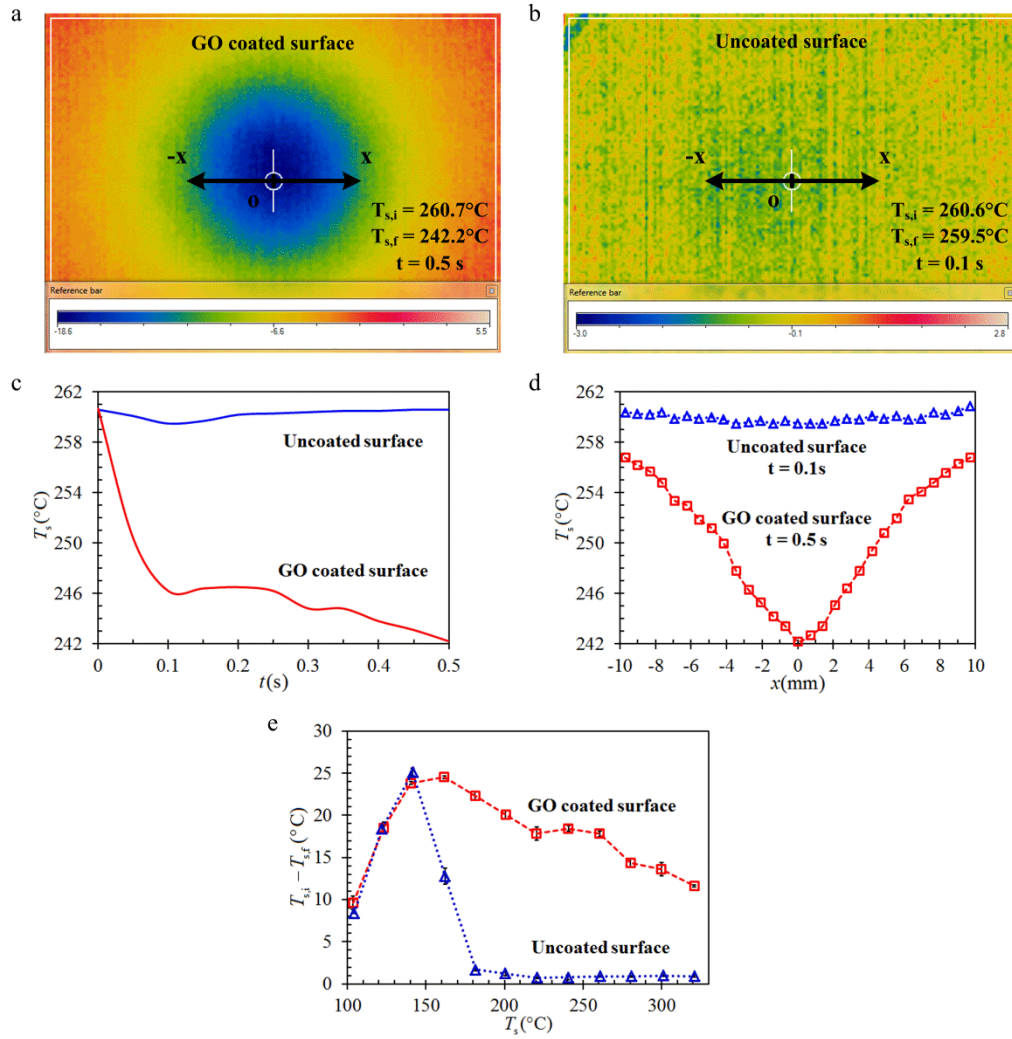


Figure 5.13 Heat transfer enhancement and Leidenfrost state suppression on GO-coated surface. Surface temperature variations of (a) GO-coated surface heated at a surface temperature of 260.7°C and (b) aluminium surface heated at a surface temperature of 260.6°C , under the vaporization of $10\ \mu\text{l}$ water droplet. (c) Surface temperature variations of GO-coated surface and aluminium surface with respect to time, under the vaporization of $10\ \mu\text{l}$ water droplet. (d) Surface temperature distributions of GO-coated surface and aluminium surface at $0.5\ \text{s}$ and $0.1\ \text{s}$, respectively. (e) Surface temperature variation, $T_{s,i} - T_{s,f}$, of GO-coated surface and aluminium surface, with respect to a feasible range of surface temperature. The experimental results verify the suppression of Leidenfrost effect with the use of GO coating on the aluminium surface.

With the successful demonstration of a single water droplet evaporating on the GO-coated surface at high temperature, we extend our study on the vaporization of continuous stream of micro-sized water droplets for practical application. To demonstrate the role of fast water vapour permeability of GO coating on the phase-change heat transfer enhancement, a spray cooling system (Figure 5.4) is utilized. Using the aforementioned coating technique, GO layer is coated onto an aluminium surface with a diameter of 28 mm. With the pressure induced atomization, water droplets of average size of 10 μm are generated by the piezoelectric module vibrating at high frequency. Three different mass flow rates are used in this study: 1.88 mgs^{-1} , 3.03 mgs^{-1} and 4.40 mgs^{-1} , as shown in Figure 5.14.

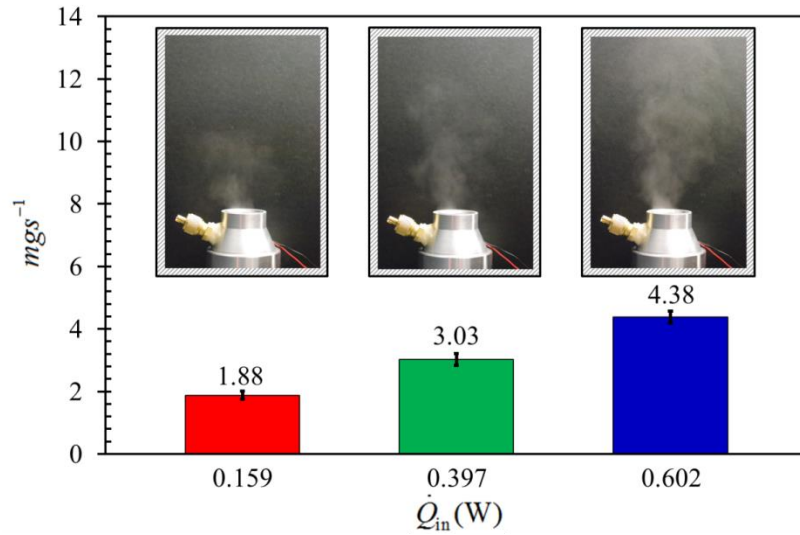


Figure 5.14| Mass flow rates of the atomized water droplets delivered to the heated surface under three different power inputs. The power inputs supplied to the piezoelectric module were measured using an oscilloscope. The three insets represent the variations in the droplet atomization strength for three power inputs.

The heat transfer enhancements of coated and uncoated surfaces are evaluated by comparing the vaporization enhancement ratio VER, under the same heat transfer rate. Based on the Newton's law of cooling, the convection heat transfer coefficient can be written as $h = [\dot{Q}(T_s - T_\infty)]/A$, where \dot{Q} , T_s , T_∞ and A are the heat transfer rate, the surface temperature, the ambient temperature and the surface area, respectively. With a constant heat transfer rate, the VER denotes the ratio of the convection heat transfer coefficient with spray cooling h_{sc} to the natural convection heat transfer h_{nc} as,

$$VER = \frac{h_{sc}}{h_{nc}} = \frac{T_{nc} - T_{nc,\infty}}{T_{sc} - T_{sc,\infty}} \quad (5.1)$$

where T_{nc} is the surface temperature under natural convection (without spray cooling), $T_{nc,\infty}$ is the ambient temperature of natural convection, T_{sc} is the surface temperature under spray cooling and $T_{sc,\infty}$ is the ambient temperature under spray cooling. The enhancement in phase-change heat transfer can be correlated with the increase in the VER. Figure 5.15 shows the VER for GO-coated surface and uncoated surface under various heat inputs. The effect of mass flow rate of the coolant is also elucidated. The phase-change heat transfer is significantly enhanced in the presence of GO coating. For a coolant's mass flow rate of 4.40 mgs^{-1} with a heat input of 14.3 W , the GO-coated surface amplifies the vaporization efficiency by 102% while the uncoated surface only shows an enhancement of 57.4%. At the highest heat input of 40.2 W , the VER is dramatically reduced to 35.4% and 18.8% for GO-coated surface and uncoated surface, respectively. The low vaporization enhancement at high heat inputs is attributed to the accumulation of excessive vapour on the heated surface, as a result of the limited clearance between the heated surface and the piezoelectric module (Figure 5.4(b)). For higher vaporization enhancement, the heater section can be redesigned to prevent vapour accumulation. Notably, the GO coating remains well-intact on the surface after several cycles of heat loading.

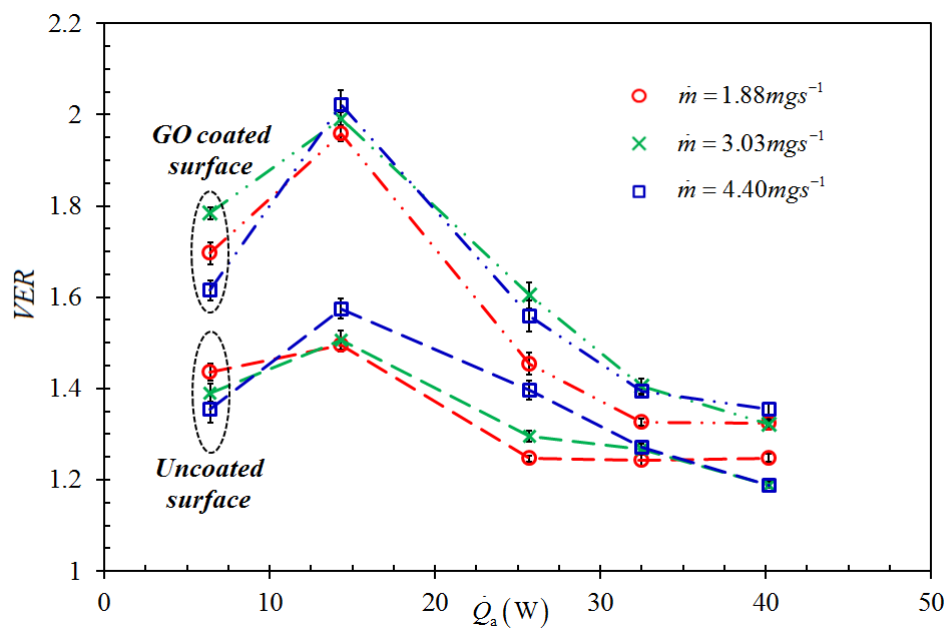


Figure 5.15| VER of GO-coated surface and uncoated surface (aluminium) under different heat inputs, \dot{Q}_a , and coolant's mass flow rates, \dot{m} .

5.4 Conclusions

To summarize, we introduced a cost effective and scalable method using GO coating for phase-change heat transfer enhancement. GO coating facilitates filmwise evaporation and capable of Leidenfrost state suppression through the excellent attribute of water vapour permeation. We successfully explained the enhancement in phase-change heat transfer and provided deeper insights on the physical mechanisms which assist the permeation of water molecules across GO coating. Contributing factors such as pressure gradient, temperature gradient and temperature induced structural alteration dramatically influence the permeability of the GO coating. The enhancement in phase-change heat transfer with the implementation of GO coating would be more appropriate to elucidate with the rapid water vapour permeation. Speculations of enhanced surface wettability and high thermal conductivity nature of GO should be reassessed. The unique water vapour permeation of GO deposition is appealing for practical implementation in effective phase-change thermal management systems, including heat exchangers, steam boilers, cooling power plants and electronic cooling devices, where GO engenders substantial leading edge over conventional metal surfaces.

Chapter 6

Effective phase-change heat transfer *via* graphene nanoplatelets coating in two-phase closed thermosyphon

6.1 Outline

With the inherent property of fast water permeation, hydrated GO deposition on heated surface offers significant evaporation enhancement and Leidenfrost state suppression. Using the proposed coating technique in this research, GO layers can be easily coated onto a heated surface of arbitrary geometry with the preparation of GO nanofluid. This provides a better and cost-effective alternative in surface functionalization for phase-change enhancement as compared to using conventional porous materials or micro/nanostructured surfaces. Furthermore, other important attributes of GO, such as structural integrity and thermal shock resistance are essential in the adoption of GO in phase-change thermal management devices. In general, the abundant oxygenated functional groups embedded within the graphitic layers of GO are considered to be the origin of fast water permeation with the intercalation of water bilayer in the expanded lattices. However, continuous heat loading at high temperature on GO membranes is perceived to have detrimental effect on the effective water permeation due to the reduction of oxygenated functional groups^{250, 251}. Similar to the thermal reduction process of GO, oxygenated functional groups are eliminated from the graphitic layers under prolonged thermal annealing treatment^{163, 181}. This process significantly reduces the density of the oxygenated functional groups, leading to a reduction of GO interlayer distance and thus its water permeability. Despite the shortcoming of interlayer distance reduction at high temperature, our investigation in Chapter 5 shows that phase-change heat transfer enhancement can be achieved with the unique property of fast water permeation of GO-coated surface under a surface temperature of 300°C. The role of oxygenated functionalities of GO on phase-change heat transfer enhancement has to be justified.

Intuitively, removal of oxygenated functionalities and restoration of non-oxidized carbon-walled surface are critical for greater water permeability. Apart from GO, Graphene nanoplatelets (GNPs) exhibits similar water absorption property²⁶⁰. It is therefore crucial to characterize the water permeability of GNPs-coating. Moreover, study also indicates the superwetting characteristic of GNPs-coating after progressive thermal treatment beyond 300°C²⁶⁰. The thermo-sensitive characteristic of GNPs-coating with respect to its wetting transition from hydrophobic to superhydrophilic

provides better insight in the fundamental mechanism behind water permeation in graphitic structures. The reduction in hydrophilic functionalities also endows the unimpeded flow of water molecules across GNPs-coating. The rapid water transport confined in the nanocapillaries is ascribed to the frictionless interaction between the atomically smooth, hydrophobic carbon wall and the well-ordered hydrogen bonds of water molecules^{250, 277, 278}.

In this study, we focus on investigating the water permeation effect in GNPs-coating and ultimately its integration with TPCT for thermal performance enhancement. Initial surface characterization of the GNPs-coating with FESEM and XRD analysis reveals its highly stacked and multi-layered structures. X-Ray Photoelectron Spectroscopy (XPS) analysis is used to elucidate the extraordinary water permeability of GNPs-coating as compared to that of the GO-coating. The accelerated water permeability and the antigravity flow of water molecules in GNPs-coating are confirmed by partially submerging the bottom end of a GNPs-coated glass tubes into a pool of water. Its permeability is quantified by the weight gain over time of the GNPs-coated glass tubes of various coating's thicknesses. In the integration of GNPs-coating in TPCT, the thermal performance is evaluated by measuring the thermal conductance and the evaporator heat transfer coefficient. The significance of phase-change heat transfer in TPCT is demonstrated with and without charging the working fluid, eliminating the possibility of heat transfer enhancement due to heat conduction across GNPs-coated TPCT. This study also illustrates the unprecedented condensation enhancement in TPCT with the rapid removal of condensates from the condenser section. The rapid water permeation effect across GNPs-coating resembles the rapid droplet removal on superhydrophobic surface, leading to the dramatic enhancement in thermal performance. This postulation is strengthened by comparing the thermal resistances of fully-coated and half-coated GNPs TPCTs. GNPs-coating exhibits two favourable characteristics which enhance both evaporation and condensation in a TPCT, being distinct from conventional approaches of introducing two different surfaces with opposite wettability. This study provides new insight into the potential role of GNPs-coating in enhancing thermal performance of TPCT and highlights the underlying physical mechanism of the anomalous wetting behaviour as well as the water permeation in graphitic structures.

Monash University
Declaration for Thesis Chapter 6

In the case of Chapter 6, the nature and extent of my contribution to the work was the following:

Nature of contribution	Extent of contribution (%)
I was the chief investigator for this work. My contributions to this research were the design and fabrication of the experimental setup, conducting experiments, data analysis and preparation of manuscript.	90


The following co-authors contributed to the work.

Name	Nature of contribution
A/Prof. Hung Yew Mun*	Overall supervision
Dr. Tan Ming Kwang	Overall supervision

The undersigned hereby certify that the above declaration correctly reflects the nature and extent of the candidate's and co-authors' contributions to this work*.

**Candidate's
Signature**

**Main
Supervisor's
Signature**

Tong Wei Li		Date: 1 June 2016
A/Prof. Hung Yew Mun		Date: 1 June 2016

6.2 Experimental investigation

6.2.1 Fabrication of GNPs-coated TPCT

The conductive graphene dispersion containing GNPs of thickness less than 7 nm was purchased from Graphene Laboratories, Inc. (United States). As indicated in the synthesis method provided by the supplier, GNPs were obtained by rapidly heating graphite intercalation compound (GIC) and subsequently grinded into fine powder form. 23 wt% of GNPs were then mixed with n-Butyl Acetate and Ethyl Cellulose, followed with mild ultrasonication treatment to yield homogeneous suspension of multilayer graphene. The Raman spectra of the GNPs deposition provided by the supplier is consistent with that of the multilayer graphene sheets with well-ordered defect free structures²⁹⁶. The coating technique of the GNPs layer is illustrated in Figure 6.1. Standard laboratory glass tube (Iwaki, Indonesia) with an inner diameter of 17.5 mm and length of 150 mm was used for the fabrication of the TPCT. The GNPs dispersion was deposited onto the inner section of the glass tube *via* spin-coating technique to assure the uniformity of the coating. 5 millilitres of GNPs dispersion was progressively applied onto the rotating glass tube. GNPs layer was spin-coated onto the inner wall of the glass tube which was clamped to a mechanical stirrer and rotated at a constant speed of 1200 rpm for 30 minutes to withdraw excessive GNPs dispersion from the coated surface. Subsequently, the GNPs-coated glass tube underwent thermal annealing process at 350°C for 45 minutes to completely remove the remaining solvent. Nitrogen gas was then utilized for surface cleaning. Finally, a dark silver coloured GNPs deposition was obtained. The thickness of the GNPs deposition was varied by repeatedly coating the surface with the above method. Four individual glass tubes were coated with different layers of GNPs to evaluate the effect of coating thickness on the thermal performance of a TPCT. A rubber stopper embedded with an access valve and a thermocouple wire was then inserted into the GNPs-coated glass tube²⁸⁰. The access valve allows subsequent vacuuming of excess air and charging of working fluid into the TPCT. The thermocouple wire measures the liquid saturation temperature inside the TPCT. High strength epoxy was then applied to all connections to ensure they are airtight. With the hardening of the epoxy, the GNPs-coated TPCT was subjected to leak test by evacuating the TPCT and measuring the variation in vacuum pressure over a

day. The reference TPCT (without GNP-coating) was fabricated with identical design for thermal performance comparison purpose.

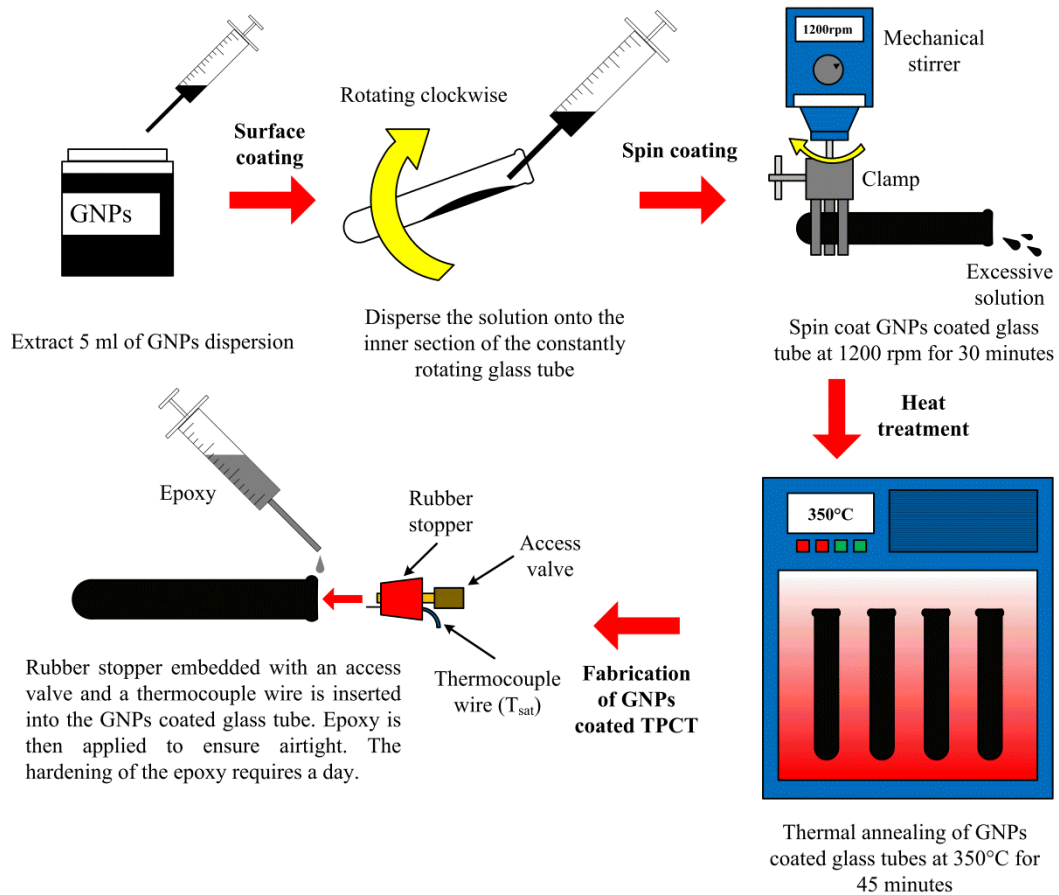


Figure 6.1| Fabrication of GNP-coated TPCT. The GNP dispersion was spin-coated onto the inner section of the glass tube and graphitized at a temperature of 350°C. The thickness of the GNP-coating was varied by repeatedly coating the glass tube with the aforementioned technique. A total of four different thicknesses of the GNP-coating was used in the study. The fabricated TPCTs were capable of maintaining the vacuum pressure without any sign of seepage.

6.2.2 Experimental setup

The schematic illustration of the experimental setup is shown in Figure 6.2. The apparatus includes a TPCT, electrical heating element, water cooling jacket and instrumentations. A fill ratio of 16.7% equivalent to 1 ml of deionized (DI) water was charged into the TPCT, followed by evacuation of excessive air with a vacuum pump (RV5, Edwards, United Kingdom) *via* the access valve. The vacuum pressure was

maintained at 0.2 Pa for all tests. The evaporator section of TPCT was enclosed with a uniform electrical heating element powered by an adjustable direct current power supply (PS 8160-04T, Elektro-Automatik, Germany). A water cooling jacket connected to a submersible water pump was mounted at the condenser section of TPCT for heat removal. The performance of TPCT was characterized through surface temperature measurements of the evaporator and the condenser section, together with the liquid saturation temperature located at the inner section of the evaporator. The heat transport rate along the TPCT was determined by measuring the temperature difference between the water inlet and outlet temperatures of the cooling jacket and the water mass flow rate. The water mass flow rate was measured with a volumetric flow meter. All temperature measurements were captured using type-T thermocouple wires connected to a data logger (GL820, Graphtec, United states) with an overall uncertainty of $\pm 0.25^\circ\text{C}$. For each test, the temperature measurements were recorded for 60 minutes with a sampling time of 2 seconds.

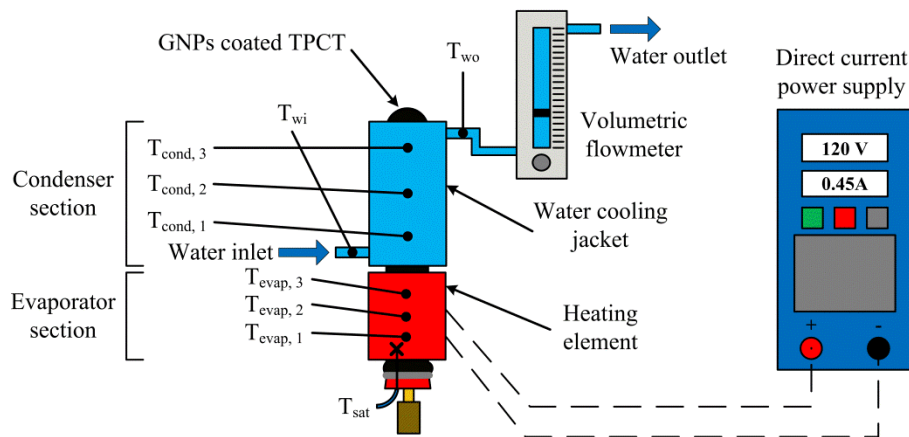


Figure 6.2| Experimental setup for the thermal performance characterization of GNPs-coated TPCT.

6.2.3 Characterization of GNPs-coating

The samples for the characterization of GNPs-coatings were obtained by gently breaking the GNPs-coated glass tubes into smaller segments of 10 mm x 10 mm. The surface morphologies of GNPs-coatings were characterized by SU-8010 FESEM (Hitachi Ltd., Japan). The thicknesses of GNPs-coatings were obtained by analysing the cross-sectional FESEM images of the respective GNPs-coatings. XRD data was

collected using X-ray diffractometer (Bruker D8 Discover) with Cu K α ($\lambda=1.54056$ Å) and a scanning rate of 0.02 °s $^{-1}$.

6.2.4 Evaluation of effective thermal conductivity of GNPs-coated surface via conduction (without two-phase heat transfer)

For benchmarking purpose, the effective thermal conductivities of GNPs-coated surfaces with various thicknesses were evaluated without the presence of the two-phase heat transfer (only heat transfer in conduction). Prior to the experiment, the uncharged GNPs-coated TPCTs were heated at 150°C for 30 minutes with the access valves opened to remove any remaining water. Subsequently, the TPCT was evacuated using vacuum pump without charging working fluid. Heat conduction experiment was then conducted using the same experimental setup with the evaporator temperature kept below 200°C . The effective thermal conductivity k_{eff} was calculated as $k_{\text{eff}} = (q''L)/(A_c\Delta T)$, where q'' is denoted as the measured heat flux, L is the distance spanning across ΔT , which is the temperature difference, and A_c is the cross section area of the glass tube (6.85×10^{-5} m).

6.2.5 Evaluation of static contact angle on GNPs-coating

The static contact angles were measured using a standard goniometer (Model 590, Ramé-Hart Instrument Co., United States) equipped with a dispensing micro syringe. GNPs-coated surface and a reference surface of glass were used for comparison purpose. 2 µl of DI water droplet was gently supplied to the targeted surface. Experiments were conducted at room temperature ($\sim 26^{\circ}\text{C}$) under standard atmospheric pressure. The variation in static contact angle for each surface was analysed using the DROPImage Advanced software (Ramé-Hart Instrument Co., United States) over a fixed time period of 2.5 minutes. As moisture content of the tested surfaces significantly alters the apparent contact angle measurement, surfaces were preheated at 70°C for 15 minutes prior to each testing. The experiment was repeated five times for each surface to ensure the consistency of the results.

6.2.6 Evaluation of water permeation across GNPs-coating

The water permeability of GNPs-coating with different thicknesses was characterized by the water absorption capability of the coating over a fixed period of time. The schematic illustration of the evaluation of water permeation across GNPs-coating is shown in Figure 6.3. To simulate the water permeation in the GNPs-coated TPCTs, open ended glass tubes of length 100 mm were deposited with GNPs-coating through similar procedures aforementioned. A glass dish filled with 20 ml of DI water and a depth of 5 mm was prepared for the experiment. The initial weight of the GNPs-coated glass tube was first measured. By submerging the bottom section of the GNPs-coated glass tube into the water filled glass dish, water permeation was immediately noticed. The GNPs-coated glass tube was then removed after 300 seconds and immediately weighted. The total water mass gain, which characterizes the water permeability of the GNPs-coating, was calculated as $\dot{m}_{\text{gain}} = (m_f - m_i)/t$, where m_i and m_f are the initial and final weight of the GNPs-coated glass tube measured over a time period t . For each GNPs-coated glass tube, the experiment was repeated five times to ensure consistency of results. Prior to each experiment, the GNPs-coated glass tube was preheated at 80°C to remove any possible moisture content. The GNPs-coated glass tube was then air cooled to room temperature. The water permeation across GNPs-coatings of different thicknesses was also captured with a recording camera.

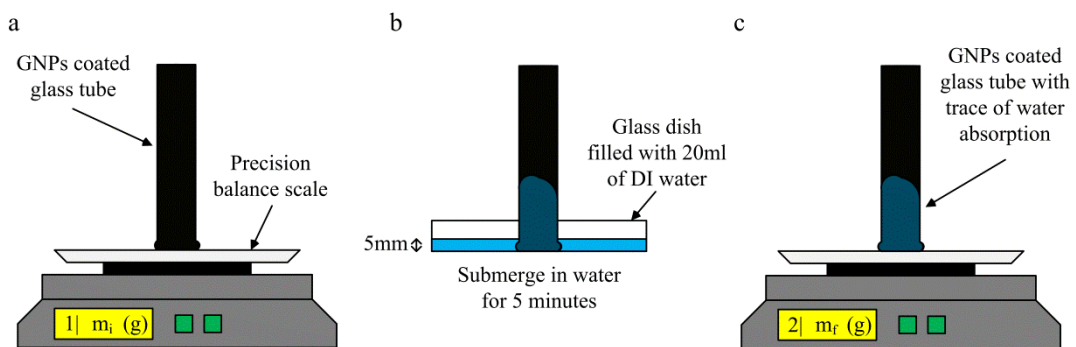


Figure 6.3| Schematic illustration of evaluation of water permeation rate across GNPs-coating.

6.2.7 Thermal performance characterization of TPCT

The thermal performance of TPCT was evaluated using the effective thermal resistance and the evaporator heat transfer coefficient. The effective thermal resistance, which quantifies the overall performance of the TPCT, was obtained by evaluating the temperature difference along the longitudinal direction of TPCT for a particular heat input, and was calculated as $R_{\text{eff}} = (T_{\text{evap}} - T_{\text{cond}}) / \dot{Q}_a$, where T_{evap} is the temperature of evaporator, T_{cond} is the temperature of condenser, and \dot{Q}_a is the heat transport rate. The heat transport rate, \dot{Q}_a is calculated based on the principle of energy conservation whereby the net heat transported across the TPCT is equivalent to the heat dissipated from the condenser section. With the assumption of a well-insulated water cooling jacket, its total convection heat transfer of water is determined as $\dot{Q}_a = \dot{m} c_p (T_{\text{wo}} - T_{\text{wi}})$, where \dot{m} represents the mass flow rate of water, c_p is the specific heat capacity of water. T_{wi} and T_{wo} denote the water inlet and outlet temperatures of the cooling jacket, respectively. The average evaporator heat transfer coefficient, \bar{h}_e , was used to quantify the strength of evaporation, given by $\bar{h}_e = \dot{Q}_a / [\pi d L_e (T_{\text{evap}} - T_{\text{sat}})]$, where T_{sat} is the liquid saturation temperature, d and L_e are the inner diameter (17.5 mm) and length (50 mm) of the evaporator section, respectively.

6.3 Results and Discussion

6.3.1 Characterization of GNPs-coatings

Figure 6.4(a) depicts a partial section of a three-coating GNPs-coated TPCT used in the study. A coarse-textured layer of GNPs was found covering the glass surface. The FESEM images reveal a layer-by-layer stacked structure of GNPs-coating (Figures 6.4(b, c, d, e)). The thermal treatment of GNPs-coating at high temperature removes the solvent and allows the graphitization of GNPs. The platelet-platelet interactions are restored with the reformation of a stacked structure similar to graphite, which is governed by the van der Waals coupling between adjacent graphene sheets¹⁸¹. Moreover, the surface morphology of the GNPs-coating indicates an abundant distribution of micro-sized cavities (red-dotted circles). This is of particular importance for the enhancement in nucleation boiling by virtue of providing sites for rapid formation of fine vapour bubbles¹³⁶. A thickness of 33 μm is measured from the cross-sectional image of the GNPs-coating (Figure 6.4(f)). Empty regions and cavities embedded in the entangling structure of GNPs are deemed to have facilitated the water permeation. We shall discuss this point in the next section (6.3.2). The XRD pattern of the GNPs-coating indicates a sharp peak at $2\theta = 26.1^\circ$ corresponding to the well-ordered graphitic planes with an interlayer spacing of 3.41 \AA (Figure 6.4(g))²⁹⁷. However, the graphite-like interlayer distance need not necessary represent its low water permeability as widening of the interlayer distance is often observed with the re-intercalation of water molecules. The interlayer distance of the deposited layer is also influenced by its curing temperature whereby prolong thermal annealing greatly reduces the interlayer distance with the removal of intercalated water molecules²⁵¹. Regardless of the graphite-like structure, a water molecule with a diameter of 2.5 \AA is still capable of permeating through the interlayer^{250, 253}. Thus, characterization of water permeability based only on the interlayer distance may not be effective with the insertion and de-insertion of water molecules.

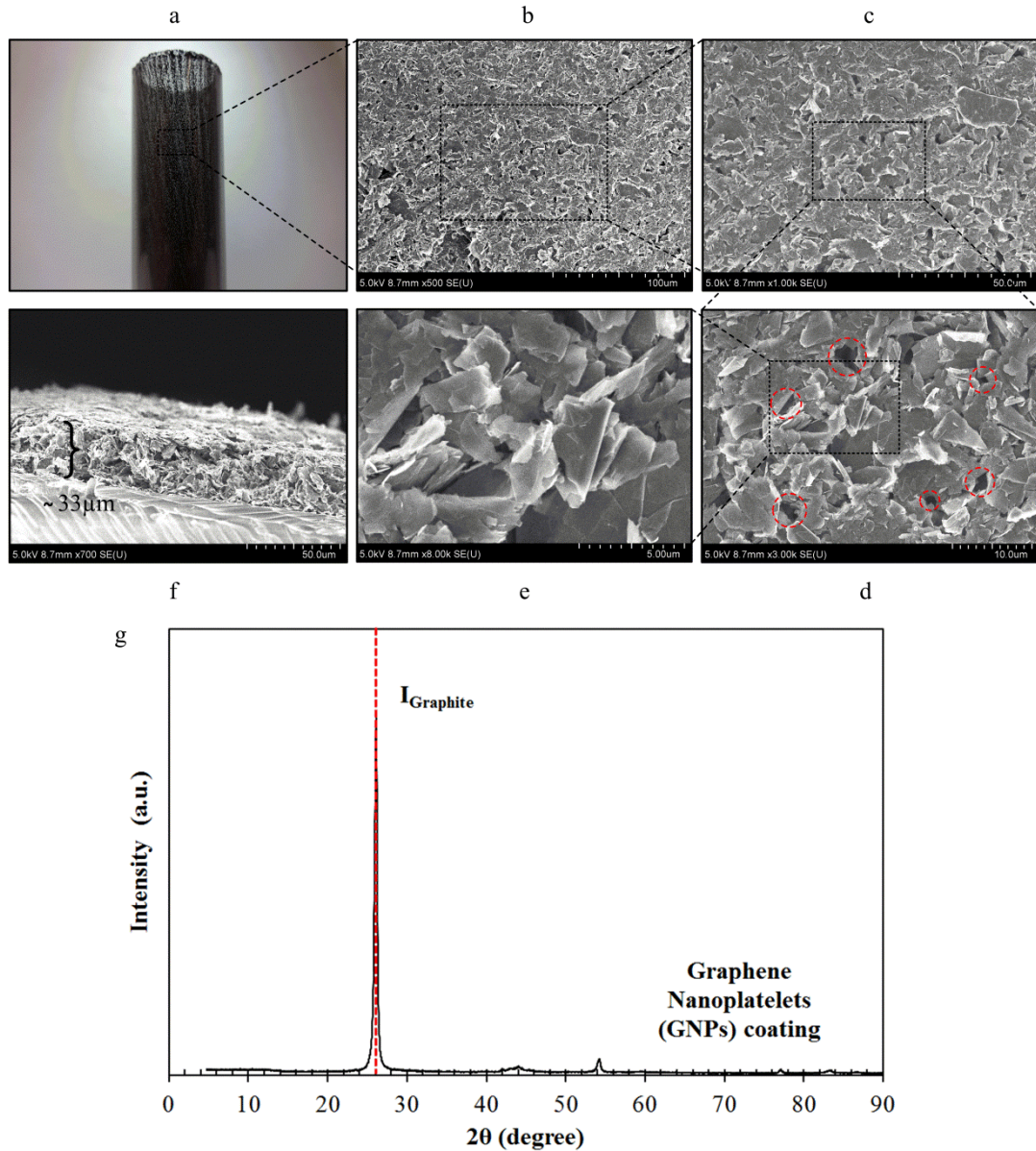


Figure 6.4| Characterization of GNPs-coatings. (a) Photograph of the coarse-textured three-coating GNPs-coated glass tube. (b, c) FESEM image of GNPs-coating at low-magnification. (d, e) FESEM images of GNPs-coating at high-magnification showing micro-sized cavities of active nucleation sites for vapour formation (red-dotted circles). (f) Cross-sectional view of GNPs-coating indicating an estimated thickness of 33 μm with an entangled structure. (g) XRD pattern of the thermally annealed GNPs-coating demonstrating a close approximation with that of the precursor graphite. The peak position is located at 26.1° corresponded to the interlayer distance of 3.41 \AA .

6.3.2 Wetting behaviour of GNPs-coating

To illustrate the excellent water permeation across GNPs-coating, we compare the variation of static contact angle on GNPs-coated surface, GO-coated surface and a reference glass surface. The reduction rates in static contact angle over a period of 150 seconds are illustrated in Figure 6.5(a, b, c). For glass surface, a reduction rate of 0.02 °/s was measured. Surprisingly, GNPs-coating with the graphite-liked interlayer distance yielded the highest reduction rate of 0.15 °/s. On the other hand, GO-coated surface obtained lower reduction rate of 0.11 °/s regardless of the larger interlayer distance measured in the previous studies^{290, 297}. This discrepancy contradicts with the understanding on water permeability of GO deposited layer based on the variation in interlayer distance whereby graphite-liked interlayer distance impedes the water transport. Therefore, apart from the interlayer distance, a more dominant factor may have governed the water permeability of graphene-based deposited layer. Hydrophilic functionalities has been renowned for its critical role in the water permeation of GO deposited layer. In general, GO sheet consists of non-oxidized and oxidized regions. In the non-oxidized region, smooth carbon-walled surface allows unimpeded flow of water molecules over the frictionless surface. On the other hand, oxidized region is filled with randomly distributed hydrophilic functionalities such as hydroxyl, epoxy and carboxyl. The driving force of water permeation in GO structure is attributed to the strong interaction between these hydrophilic functionalities and water molecules, where the latter is attracted to and pinned against the former. Therefore, the hydrophilic functionalities engender driving force for fast water permeation across the non-oxidized region. As a result, a combination of both non-oxidized and oxidized region is essential to endow the fast water permeation. Herein, we examine the populations of hydrophilic functionalities in GO-coating and GNPs-coating using XPS analysis.

In our analysis, the C1s spectra was assigned with four hydrophilic functionalities which generally includes sp^3 C-C bonding at 284.8 eV, C-O at 285.86 eV, C=O at 286.74 eV and O-C=O at 288 eV. The populations of the hydrophilic functionalities in GO and GNPs-coatings were subsequently evaluated *via* the measurement of area under representative curves. Figure 6.5(d, e) summarize the population of hydrophilic functionalities embedded among the GNPs and GO structures, respectively. The sp^3 C-C bonding representing non-oxidized region accounted for 64.96% in GNPs and

52.07% in GO. This implies that GNPs has more non-oxidized region proving frictionless passages for the effective transport of water molecules. Concerning the oxidized region allocated with C-O functional group, GNPs has significantly lower percentage as compared to GO with a difference of 30.61%. However, GNPs has additional 15.54% more C=O functional group than GO and only marginal amount of O-C=O can be determined from both GO and GNPs samples ranging from 1.24% to 3.41%, respectively. Based on the populations of hydrophilic functional groups and non-oxidized region in the two samples, GNPs-coating transcends over GO-coating in terms of water permeability. Although there are more oxidized regions providing stronger driving force for water intercalation in GO, the resistance incurred due to the pinning effect of functional groups are also more intense. On the contrary, more frictionless passages for rapid transport of water molecules prevail in GNPs-coating with less oxidized region to resist the flow. Therefore, the water permeability in GNPs-coating is more optimized compared to that of GO. This is in accordance with the greater reduction rate in static contact angle measured over GNPs-coated surface.

Apart from the high reduction rate, the initial static contact angle measurement of a droplet resting on the GNPs-coating also implies its water permeation property. A low contact angle of 36.7° was measured over the GNPs-coating in spite of the hydrophobic nature (Figure 6.5 (a)). Similar observation of low contact angle on high-temperature thermal annealed GNPs surface was also reported²⁶⁰. The reduction in static contact angle of GNPs-coating corresponding to the increased curing temperature revealed its thermo-sensitive nature. Lastly, we investigate the wetting behaviour of GNPs-coating based on its unique surface morphology. In general, the wetting behaviour of a hydrophobic surface is governed by two phenomena: Wenzel state²⁹⁸ and Cassie state⁶⁷ (Figure 6.5(f, g)). In Wenzel state, the increase in roughness of a hydrophobic surface, which increases the surface area, enhances its hydrophobicity. The Wenzel state prevails under the circumstance of a fully wetted rough or textured surface. On the other hand, the Cassie state describes the superhydrophobic behaviour of a droplet residing on a hydrophobic rough surface with air cavities trapped underneath the droplet. The Cassie state is often short-lived due to the high tendency of liquid impregnation into the air filled cavities^{67, 83}. For the case of GNPs-coating, the FESEM images indicate a rough, cavities infested surface which favours the entrapment of air below a residing droplet (Figure 6.4(c, d, e)). Based on the two models, hydrophobic or

superhydrophobic wetting behaviour is expected over GNPs-coated surface. Unfortunately, both Wenzel and Cassie models are unable to explain the superhydrophilic behaviour of GNPs-coating. A plausible explanation of this phenomenon is the rapid water permeation property of GNPs-coating. As the droplet touches the GNPs-coated surface, the droplet body force pushes the water molecules into the nanocapillaries and initiates the frictionless water permeation (Figure 6.5(h)). This force is similar to the external disturbance which causes the wetting transition from Cassie to Wenzel state^{67, 83}. In this case, the water permeation property of GNPs-coating significantly alters the wetting behaviour of a convectional rough surface which is intrinsically hydrophobic. As a matter of fact, the anomalous superhydrophilic wetting behaviour has been frequently reported for depositions of graphite²⁵⁷, reduced graphene oxide (rGO)^{258, 259}, GNPs²⁶⁰ and carbon nanotubes²⁶¹. In particular, rGO deposition, with the removal of oxygenated functional groups through thermal reduction, forms similar surface morphology and wetting behaviour with GNPs-coating. The wetting behaviour of rGO deposition was attributed to the residual hydrophilic functional groups which closely interact with water molecules^{15, 16}. Yet, the water permeability of rGO deposition is incomparable with GNPs-coating due to the prevalence of defective sites on the graphene sheets²³², reducing the non-oxidized carbon-walled regions. Next, we conduct feasibility study on utilizing GNPs-coating to enhance the thermal performance of a TPCT.

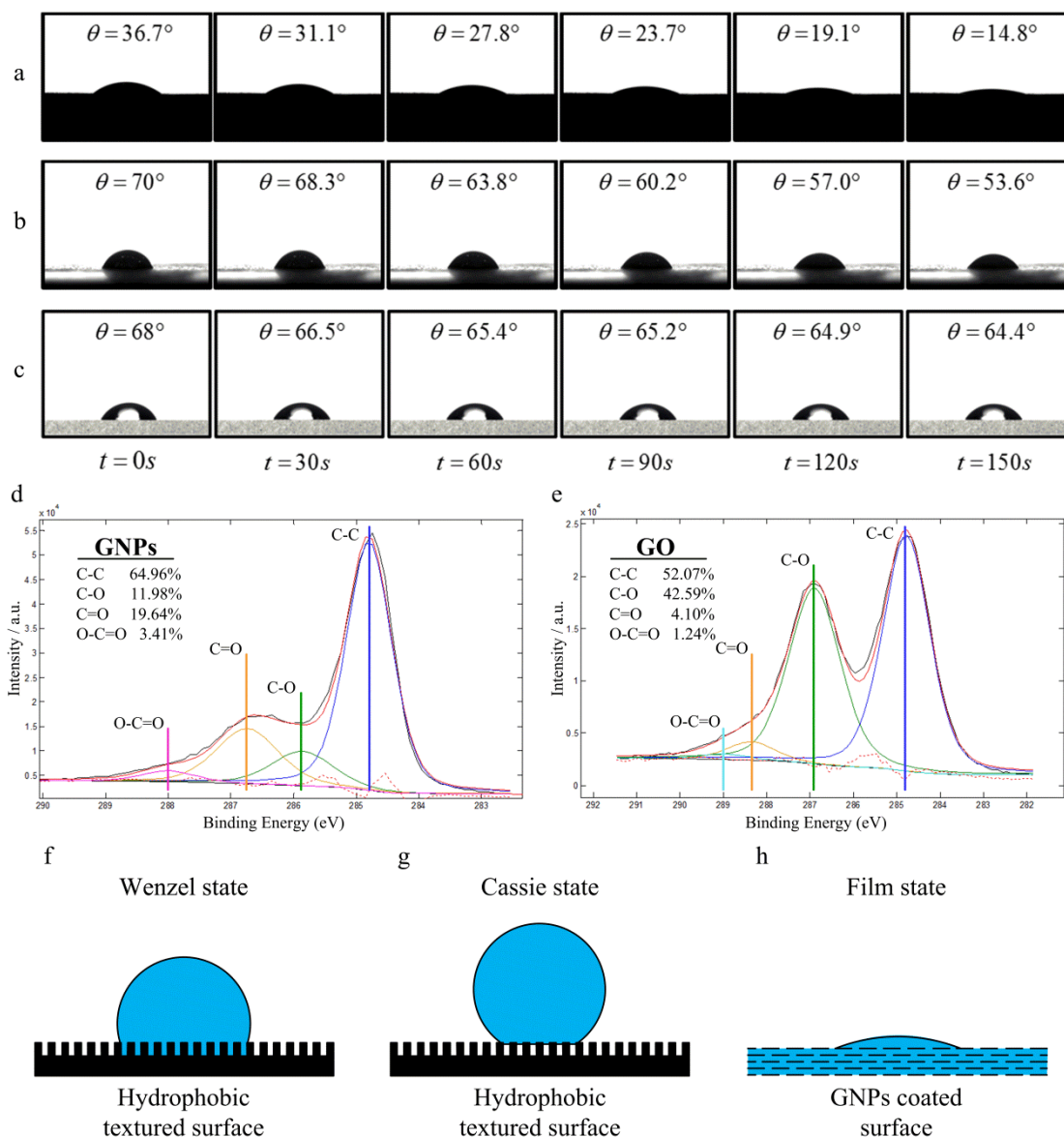


Figure 6.5| Wetting behaviour of GNPs-coating. Time-lapse images of a 2- μ l water droplet resting on (a) GNPs-coated surface, (b) GO-coated surface, and (c) glass surface, over a time span of 2.5 minutes under room temperature. The corresponding contact angles and droplet dynamics are captured with an interval of 30 seconds. Complete water absorption was observed about 3 minutes for a GNPs-coated surface. The well optimized ratio of non-oxidized regions to oxidized regions endows GNPs-coating with high water permeability. XPS C1s spectra of (d) GNPs-coating and (e) GO-coating. Specific oxygenated functionalities are labelled accordingly in the spectra together with its populations. Higher water permeability of GNPs-coating is evident through the larger population of C-C bonding and lower populations of other oxygenated functionalities. Schematic illustrations of the surface wetting modes of (f)

Wenzel state and (g) Cassie state on a hydrophobic textured surface. (h) Film wetting state of a droplet residing on GNPs-coated surface. In contrast to the hydrophobic nature of graphene, water molecules are capable of permeating through the nanocapillaries embedded across the GNPs-coating.

6.3.3 Water permeation of GNPs-coating

To justify the excellent water permeation, water absorption rate was measured for different thickness of GNPs-coating. The rate of water mass gain \dot{m}_{gain} representing the water absorption rate over a time period of 5 minutes for different thickness of GNPs-coating is shown in Figure 6.6(a). The water permeability increases gradually with the increase of the GNPs-coating thickness. This is explained with the growth in the GNPs-coating thickness as shown in Figure 6.6(c, d, e, f). In the coating process of the fourth coating, the increased cohesion between the GNPs dispersion and the three-coating GNPs-coated surface reduces the spreading of the GNPs dispersion. As a result, more GNPs dispersion (15 ml) was required for the complete coating of the fourth layer. The subsequent coating seems to be almost double of the previous one. To further characterize its water absorption property, we calculate the sorptivity of the material which is a property commonly utilized to characterize the liquid transport in porous medium. The sorptivity of the material is determined as $S = V/A\sqrt{t}$, where V represents the cumulative volume of liquid absorbed over a time period t and A denotes the cross-sectional area of the material which is partially submerged in the liquid pool. The sorptivity of GNPs-coating is compared with those of porous mediums such as aerated concrete, gypsum plaster, clay brick, mortar and concrete brick²⁹⁹, tabulated in Figure 6.6(b). A sorptivity of $34 \text{ mm} \cdot \text{min}^{-1/2}$ was obtained for GNPs-coating which is 9.7 times greater than that of the Gypsum plaster. As a result, the capillary pumping effect presumed in the water transport of porous medium is insufficient to elucidate the accelerated water absorption property of GNPs-coating. The exceptional sorptivity of GNPs-coating evidences the existence of frictionless nanocapillaries which allow rapid water permeation, beyond those of porous materials. We hereby introduce sorptivity as a unique parameter which can be utilized for better characterization of water permeability in carbon-based coatings.

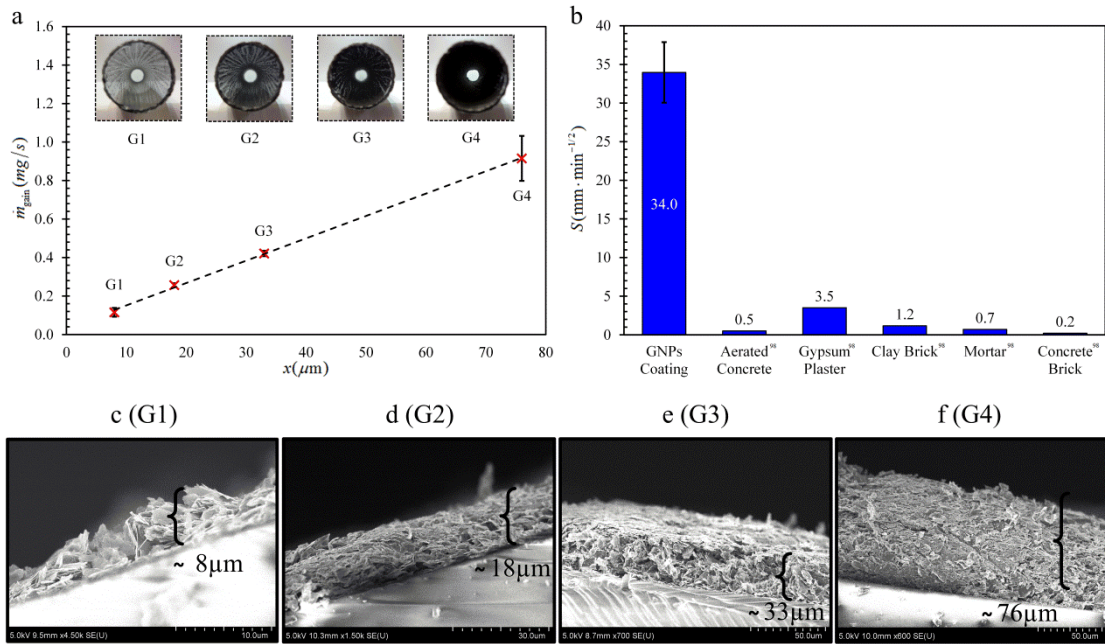


Figure 6.6| Water permeability of GNPs-coatings. (a) Rate of water mass gain \dot{m}_{gain} for various thicknesses of GNPs-coated glass tubes. The insets depict the surface morphologies of GNPs-coated glass tubes with various coating's thicknesses. (b) Sorptivity of GNPs-coating and various porous materials. The high water transport capability of GNPs-coating is attributed to the unimpeded flow of water molecules through the embedded nanocapillaries. Cross-sectional views of GNPs-coatings illustrating (c) one-coating GNPs-coated glass tube with a thickness of 8 μm , (d) two-coating GNPs-coated glass tube with a thickness of 18 μm , (e) three-coating GNPs-coated glass tube with a thickness of 33 μm and (f) four-coating GNPs-coated glass tube with a thickness of 76 μm . The water permeability of GNPs-coating enhances with the increase of coating's thickness. The layered-structure of the GNPs-coating allows the frictionless permeation of water molecules through smooth, hydrophobic carbon walls, resembling the wetting behaviour of superwetting materials.

The time-lapse images of water permeation through three-coating GNPs-coated glass tube are shown in Figure 6.7(a). Under normal atmospheric condition, water permeation was immediately observed when GNPs-coated tube was in contact with water. Over a time frame of 5 minutes, a height of 18 mm was achieved from the initial height of 3 mm. Although the permeability of the coating gradually diminished over time, a fully-wetted GNPs-coating (100 mm in length) was obtained after 43 minutes. The vigorous interaction between oxygenated functionalities and water molecules

initiates the intercalation of water molecules through the layered structure of GNPs-coating. As water molecules experience frictionless flow across non-oxidized region, it is indicative of maintaining large area of non-oxidized region for rapid water permeation. No additional external force is required to sustain the continuous water flow. On the other hand, the initial driving force behind water permeation strongly depends on the oxygenated functionalities which pull the water molecules into the layered structures. Nonetheless, the water molecules are pinned against the oxygenated functionalities, impeding the motion of water molecules. Thus, to achieve an optimized permeation rate, a balanced amount of both non-oxidized regions and oxidized regions is crucial for rapid water permeation. Apart from the pinning force, water permeation across GNPs-coating in the vertical direction is also limited by the gravitational force. This is in accordance with the observation of gradually reducing water permeability when the wetted length increases (Figure 6.7(a)).

In general, water molecules interact differently between hydrophilic glass wall and hydrophobic carbon-walled nanocapillaries. Water permeation across glass interface can be resembled with the capillary action in capillary tube. Driven by the hydrostatic pressure, water molecules are capable of travelling upwards through the capillary tube (Figure 6.7(b))³⁰⁰. The resultant surface tension force induced by the liquid cohesion force while the adhesion force between liquid and solid wall pulls the fluid upward. Acting on the opposite direction, the downward body (gravitational) force increases with the increasing volume of liquid column. The elevation of liquid column becomes stagnant when the cohesion and adhesion forces are equal and the gravitational force holds the liquid in place. While water molecules are being pulled along the glass surface *via* capillary action, water molecules adjacent to the hydrophobic nanocapillaries experience frictionless slip flow. The adhesion force from the capillary action is substituted with the repulsive force as water penetrates through the hydrophobic nanocapillaries (Figure 6.7(c)). The water molecules are not in contact with the hydrophobic carbon walls which form frictionless passages for water molecules. The GNPs are orderly stacked, allowing the water molecules to travel in the interlayer between two graphene sheets. The rapid water permeation is attributed to the frictionless interaction between the carbon wall and the well-ordered hydrogen bonds of water molecules^{250, 285, 301}. The water molecules slit through the atomically smooth hydrophobic carbon walls which form a network of nanocapillaries throughout the

coating. As the body force of water increases with its volume, the capillary action and boundary slip are eventually balanced by the gravitational force. Thus, in conjunction with the optimized populations of oxygenated functionalities, rapid water permeation across GNPs-coating is observed. GNPs-coating with the fascinating water permeability can be well-suited to enhance phase-change heat transfer in thermal management system, specifically for the enhancement of TPCT. To this end, a TPCT coated with different thicknesses of GNPs-coating was tested to determine the thermal performance enhancement.

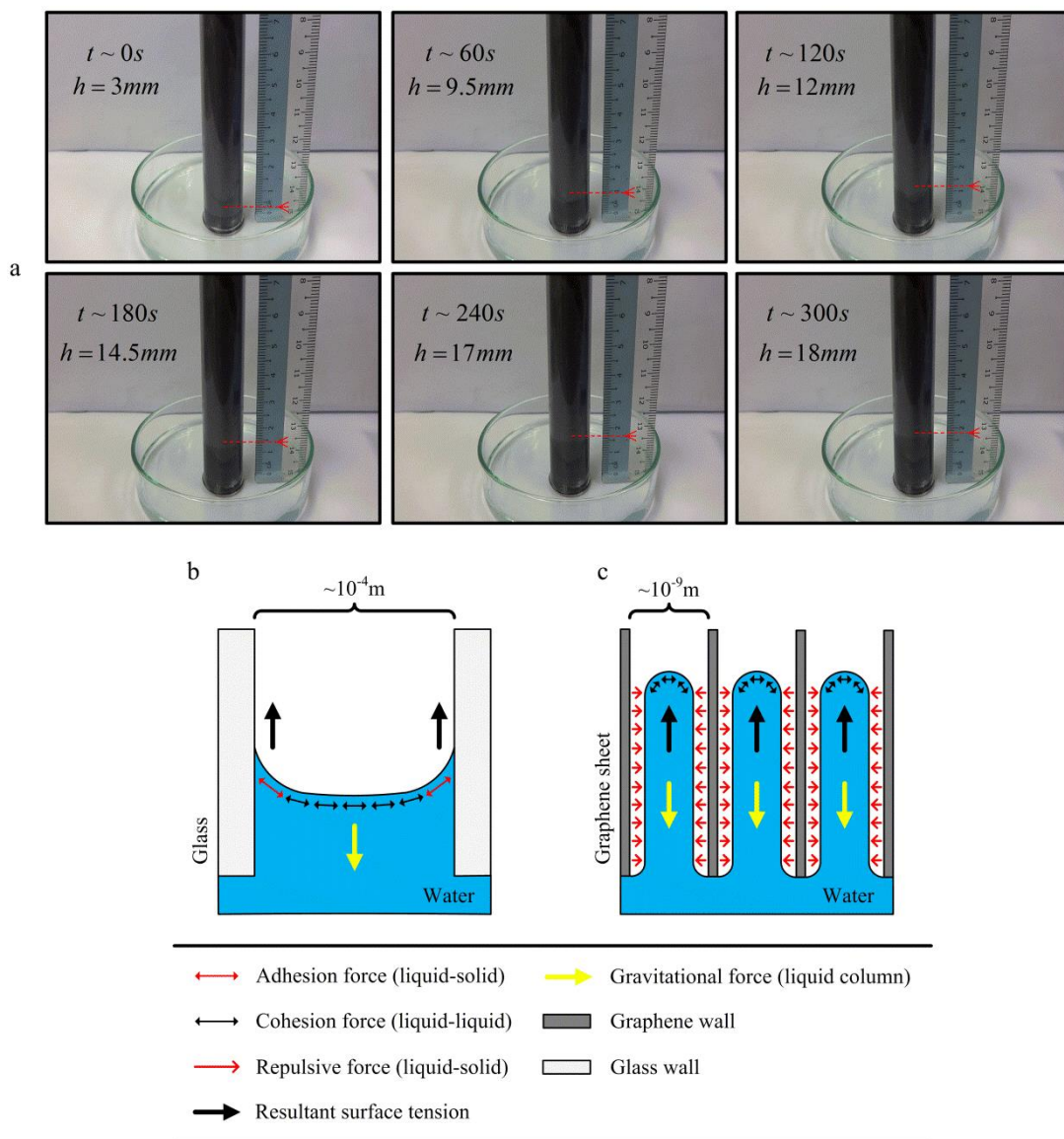


Figure 6.7| Water permeation across GNPs-coating. (a) Time-lapse images illustrating the water permeation across a three-coating GNPs-coated glass tube over a

time span of 5 minutes. The water permeability decreases gradually with increasing wetted length. Nevertheless, full water permeation across the GNPs-coating was observed after 43 minutes. **(b)** Schematic illustration of the capillary action in a capillary tube. **(c)** Schematic illustration of the driving forces which enable the water permeation across nanocapillaries of GNPs-coating. The cohesion force and the repulsive force engender the detachment of water molecules from the smooth hydrophobic carbon walls, and a frictionless flow passage is established.

6.3.4 Thermal performance enhancement in GNPs-coated TPCT

To quantify the overall thermal performance of a TPCT, we evaluate the effective thermal conductance, $k_{\text{eff}} = (\dot{Q}_a L) / (A_c \Delta T)$, which characterizes the heat conduction capability of GNPs-coated specimen, with L being the distance between the two measured temperatures, A_c the cross section area of the evacuated glass tube and $\Delta T = T_{\text{evap}} - T_{\text{cond}}$ the temperature difference. The thickness of the GNPs-coating ranges from 8 to 76 μm , denoted as G1 to G4 according to the number of coating defined in Figure 6.6. Figure 6.8 depicts the effective thermal conductance of GNPs-coated TPCTs with various thicknesses for different heat transport rate, \dot{Q}_a . The effective thermal conductance of the uncoated TPCT (G0) serves as a benchmark for comparing the enhancement in thermal performance of GNPs-coated TPCTs. The increase in k_{eff} is intrinsically attributed to the enhancement of either evaporation strength at the evaporator or circulation effectiveness of condensate back to the evaporator or of both. Basically, the effective thermal conductance of coated TPCT is higher than that of uncoated TPCT (G0). A maximum increase of 106.8% in k_{eff} can be obtained for a three-coating GNPs-coated TPCT at $\dot{Q}_a = 6.64 \text{ W}$, compared to the uncoated one. When \dot{Q}_a increases to 40.0 W, the increase of k_{eff} reduces to 22.7%. We can observe that k_{eff} increases with coating thickness up to three-coating thickness (G3), while k_{eff} of four-coating TPCT (G4) is lower than that of three-coating TPCT but still higher than that of the uncoated TPCT (G0).

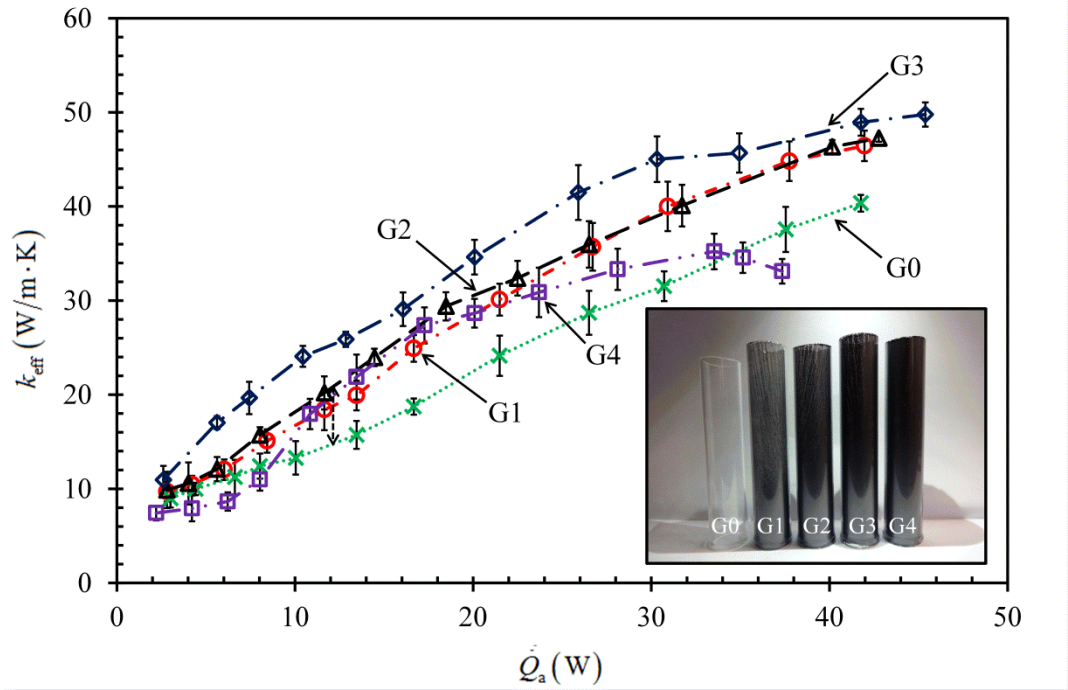


Figure 6.8 | Evaluation of thermal performance enhancement in GNPs-coated TPCTs. Effective thermal conductance k_{eff} of GNPs-coated TPCTs with various thicknesses for different heat transport rate \dot{Q}_a . G0 represents the uncoated TPCT used as a baseline for comparison while G4 represents the four-coating GNPs-coated TPCT. The inset shows the photographic view of the GNPs-coated glass tubes utilized for the fabrication of the TPCTs.

Graphene-based coatings are often positioned as excellent heat conduction medium due to its high thermal conductivity nature^{51, 52}. However, this only applies to a single-layer graphene⁵¹. In practice, graphene-based coatings obtained from scalable methods, such as thermal and chemical reduction of GO¹⁸¹ or thermal exfoliation of expandable graphite^{163, 201, 302}, yield significantly lower thermal conductivity as compared to pristine graphene. The covalent sp^2 bonding between the carbon atoms results in high in-plane thermal conductivity of pristine graphene⁵². As the layered structure of graphene is governed by the cross-plane van der Waals force, the cross-plane heat transfer is ineffective as compared to the in-plane heat transfer and hence the heat flow in GNPs is anisotropic. The weak thermal coupling between the graphitic planes and the adjacent substrate also limits the heat transfer⁵⁶. Therefore, the increase of k_{eff} is not entirely attributed to the increase in thermal conductivity of GNPs-coating. To justify this, we conducted simple heat conduction experiments to examine the

effective thermal conductance of uncharged GNP-coated TPCTs where the working fluids were evacuated from the TPCTs to exclude the two-phase heat transfer process. Figure 6.9 illustrates the effective thermal conductance of uncharged TPCT with different GNP-coating thickness. The effective thermal conductance of GNP-coated TPCTs are marginally higher than that of uncoated TPCT, with a maximum difference of 7%, showing that GNPs inherently has significantly lower thermal conductivity as compared to the pristine graphene with high in-plane thermal conductivity²⁰⁸. The contribution of thermal conductivity of GNPs to the thermal performance enhancement of TPCT is insignificant and it is postulated that the performance enhancement and the effects of GNP-coating are associated with two-phase heat transfer process, similar to our discussion in Chapter 4.

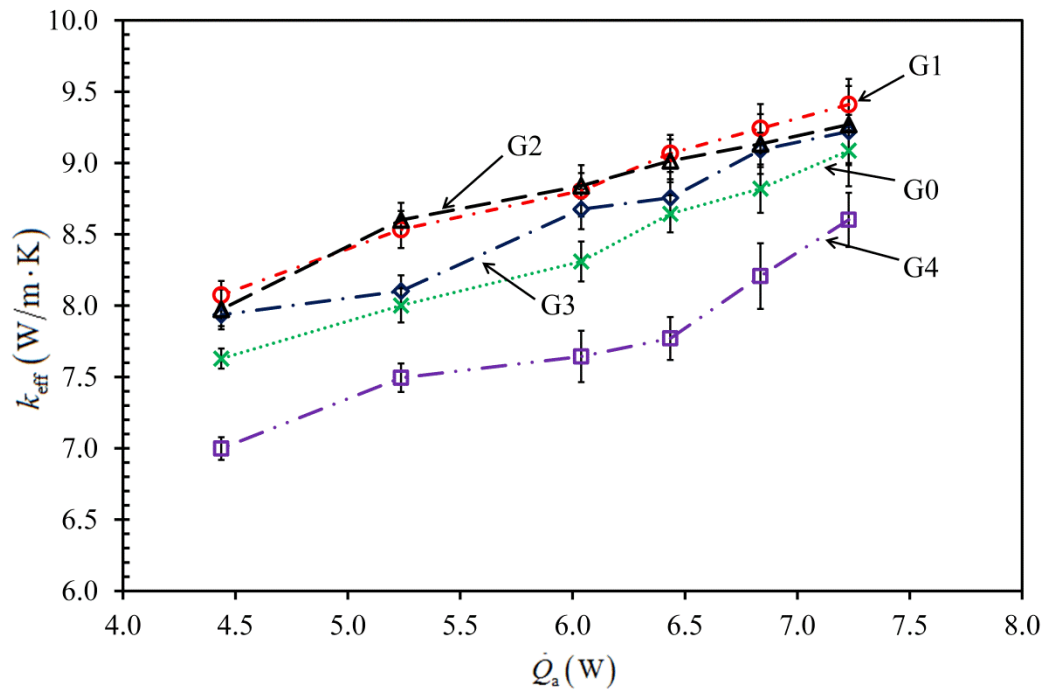


Figure 6.9 | Effective thermal conductance of uncharged GNP-coated TPCTs with different GNP-coating thickness. In the absence of the effective phase-change heat transfer, only marginal enhancement can be obtained from the GNP-coated TPCTS.

We have discussed earlier in Figure 6.6 that the water permeation rate of GNP-coating increases with its thickness but this trend is not exactly reflected in the effective thermal conductance (Figure 6.8), which is an overall performance indicator of TPCT. As the performance of TPCT is essentially governed by the processes of evaporation (at the evaporator section), condensation (at the condenser section) and circulation of

condensate (from condenser to evaporator), the occurrence of water permeation in GNPs-coating impacts these processes individually in different manners and degrees. To investigate the impact of water permeation in GNPs-coating on the strength of evaporation, we evaluate the average evaporator heat transfer coefficient, \bar{h}_e , as a function of heat input to the TPCT, as depicted in Figure 6.10(a). Similar trends of \bar{h}_e are observed in Figure 6.10(a) compared to those of k_{eff} in Figure 6.8. Therefore, the performance of a TPCT is dominated by the evaporation process. It can be observed that \bar{h}_e enhances in GNPs-coated TPCTs. For the three-coating TPCT (G3), an overall enhancement of 97% and 63% can be achieved at a \dot{Q}_a of 20 W and 40 W, respectively, as compared to the uncoated TPCT. As depicted in Figure 6.10(b), on account of water intercalation in the GNPs-coating, the effective evaporation region is extended to the wall surface, above the liquid-vapour interface (highlighted with red colour), as compared to the uncoated TPCT. As water intercalates between the carbon interlayers, a thin film of water materializes at the GNPs-coating. On account of increased surface area, this filmwise evaporation is more effective than that of a pool of water²⁹⁰. Even in an antigravity direction, with the unique property of fast water permeation of laminated graphene structures, the water thin film formed at the GNPs-coating can be sustained and continuously replenished from the pool of water. The fast water permeation in the antigravity direction is mainly driven by the net evaporation prevailing on the GNPs-vapour interface. With the application of heat, the evaporation of water is enabled by the high kinetic energy, breaking the hydrogen bond of water molecules at the interface³⁰³. Water molecules are agitated and diffuse into all directions. As vapour is constantly drawn away from the evaporator and condenses in the condenser, the rate of diffusion from the liquid phase through the interface is greater than that from the vapour phase back to the interface. Hence net evaporation is transpiring, inducing a low pressure at the coating-vapour interface. The resultant pressure gradient between the water pool and the interface drives the water molecules into the GNPs-coating, enabling them to slip through the atomically smooth carbon passages formed among the interlayers of stacked graphene sheets.

Similar to the effective thermal conductance, we can observe that \bar{h}_e increases with increasing coating thickness up to three-coating thickness and decreases for higher

coating thickness. It is obvious that the variation of \bar{h}_e for four-coating GNPs-coated TPCT (G4) manifests in three different regimes - Regime I ($\dot{Q}_a < 6.23$ W), Regime II ($6.23 \text{ W} < \dot{Q}_a < 28.29$ W) and Regime III ($\dot{Q}_a > 28.29$ W). For a small \dot{Q}_a in Regime I, \bar{h}_e is independent of \dot{Q}_a . The fact that \bar{h}_e of G4 is lower than that of G0 in this regime is caused by a significant increase in the water film thickness at GNPs-coating where the role of filmwise evaporation at GNPs thin film is essentially insignificant at a low heat input. In addition, a low heat input is incapable to drive evaporation from a significantly larger coating-vapour interfacial area and hence the evaporation strength deteriorates compared to that of an uncoated TPCT, where evaporation takes place at the liquid-vapour interface of water pool. In Regime II for higher \dot{Q}_a , \bar{h}_e increases with \dot{Q}_a and approaches an asymptotic value at high heat input. We can observe that in this regime, \bar{h}_e of G4 is lower than that of G3 and comparable to that of G2, despite the fact of the highest water permeability prevailing in the four-coating GNPs-coated surface, as discussed in Figure 6.6. When the GNPs-coating is too thick, the significance of filmwise evaporation of G4 is decreased and thus the evaporation enhancement due to GNPs-coating is reduced compared to that of G3. Therefore, there exists an optimal thickness of GNPs-coating that maximizes the overall evaporation strength of a TPCT.

When the heat input is further increased in Regime III, the filmwise evaporation becomes more intense, increasing the water permeation rate through GNPs-coating and subsequently incurring depletion of the water pool, which is evidenced by a drastic increase in the surface temperature measured at the bottom part of evaporator. The evaporator surface temperature of G4 was recorded as 237.2°C at a heat input of 37.7 W, compared to the evaporator surface temperature of G3 which is merely 183.5°C at a heat input of 45.8 W. In such circumstance, dryout transpires at the evaporator section and a subsequent small increase in heat input induces a dramatic temperature increase³⁰⁴. The TPCT is operated under an overloaded condition, where the temperature at the evaporator end increases sharply^{4, 12} and the strength of evaporation declines, with a decreased value of \bar{h}_e . This explains the decaying trend of \bar{h}_e with increasing \dot{Q}_a and the diminishing effect of GNPs-coating thickness on \bar{h}_e enhancement in Regime III.

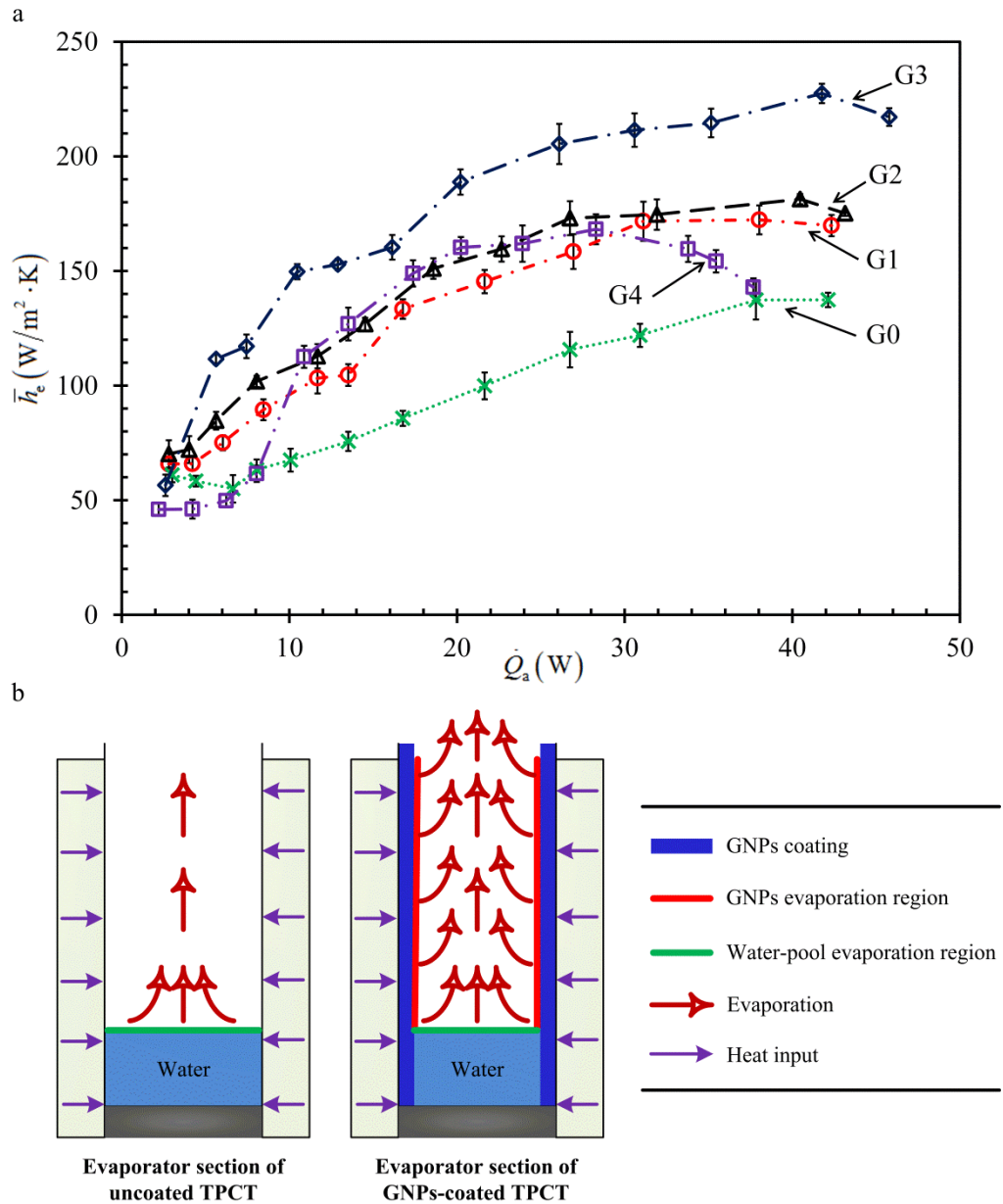


Figure 6.10| (a) Average evaporator heat transfer coefficient \bar{h}_e of GNP-coated TPCTs with different coating thickness. The introduction of GNP-coating across TPCT significantly enhanced the average evaporator heat transfer coefficient. Nevertheless, reduction in thermal performance was obtained from the thickest coating of four-coating GNP-coated TPCT, representing a limitation in increasing coating thickness. (b) Schematic illustration of effective evaporation region of GNP-coated TPCT versus uncoated TPCT. The excellent water permeability of GNP-coating dramatically increases the effective evaporation region, extending across the evaporator section while inducing filmwise evaporation.

The sustained evaporation of liquid in a TPCT is replenished by circulation of condensate from the condenser section where the vapour release the latent heat of vaporization at the saturation temperature and condensate is formed on a low-temperature surface. As discussed in Chapter 3, surface functionalization to induce low surface energy at condenser section promotes dropwise condensation for enhancing the performance of TPCT^{17, 73, 79, 297}. In fact, the surface wetting characteristics for optimum condensation and condensate circulation are dichotomous – hydrophilic surface facilitates the droplet nucleation (enhancing condensation) while superhydrophobic surface is favourable for rapid droplet removal (enhancing circulation of condensates)¹⁸. Here, to investigate the impact of water permeation in GNPs-coating on the performance of condensation in the condenser section, we compare the performance of fully-coated TPCTs and half-coated TPCTs with GNPs-coating of same thickness. Only the inner surface of evaporator section is coated with GNPs in the half-coated TPCTs while the condenser section is remained uncoated. Using the uncoated TPCT (G0) as a baseline for comparison, Figure 6.11(a) depicts the effective thermal conductance of TPCT with different GNPs-coating thicknesses (G1 and G3) as a function of heat input, \dot{Q}_a . The effective thermal conductance of half-coated TPCTs (G1_{Evap} and G3_{Evap}) is lower than that of fully-coated TPCTs (G1 and G3). The discrepancy in performance is attributed to the absence of GNPs-coating in the condenser. The function of GNPs-coating is twofold in enhancing condensation in a TPCT. The GNPs-coating behaving as a hydrophilic surface improves droplet nucleation during condensation and its fast water permeation property augments the circulation of condensates back to the evaporator. To determine the contribution of GNPs-coating at the condenser section on the overall performance enhancement of a TPCT, we plot the parameter, $\lambda = (k_{\text{eff}} - k_{\text{eff},0}) / k_{\text{eff},0}$, as a function of \dot{Q}_a , for fully-coated and half-coated TPCTs with different GNPs-coating thickness (G1, G3, G1_{Evap} and G3_{Evap}), as shown in Figure 6.11(b). The subscript “0” denotes the value evaluated for the case of uncoated TPCT (G0). By definition, λ can be regarded as the performance enhancement ratio due to the contribution of GNPs-coating, based on the performance of uncoated TPCT. All performance enhancement ratios are modelled with respect to the heat input by constructing new data points within the range of 3 W to 40 W using linear interpolation method. We can observe that λ increases from low heat input to a maximum value, beyond which λ decreases with increasing heat input. For

fully-coated TPCTs, the maximum performance enhancement amounts to 31.1% and 76.8% for one-coating (G1) and three-coating (G3) GNPs-coated TPCTs, respectively, signifying that the contribution of GNPs-coating increases with its thickness. For half-coated TPCTs, the maximum performance enhancement is recorded as 16.7% and 43.6% for one-coating ($G1_{\text{Evap}}$) and three-coating ($G3_{\text{Evap}}$) GNPs-coated TPCTs, respectively. The discrepancy in performance enhancement between fully-coated and half-coated TPCTs escalates when the heat input increases, indicating that the role of GNPs-coating at condenser wall magnifies at higher heat input. Intuitively, it can be deduced that the enhancement of performance is attributed to the enhanced condensation and circulation of condensates at the condenser section. However, the effect of GNPs-coating at condenser wall on the strength of evaporation in the evaporator section should not be overlooked.

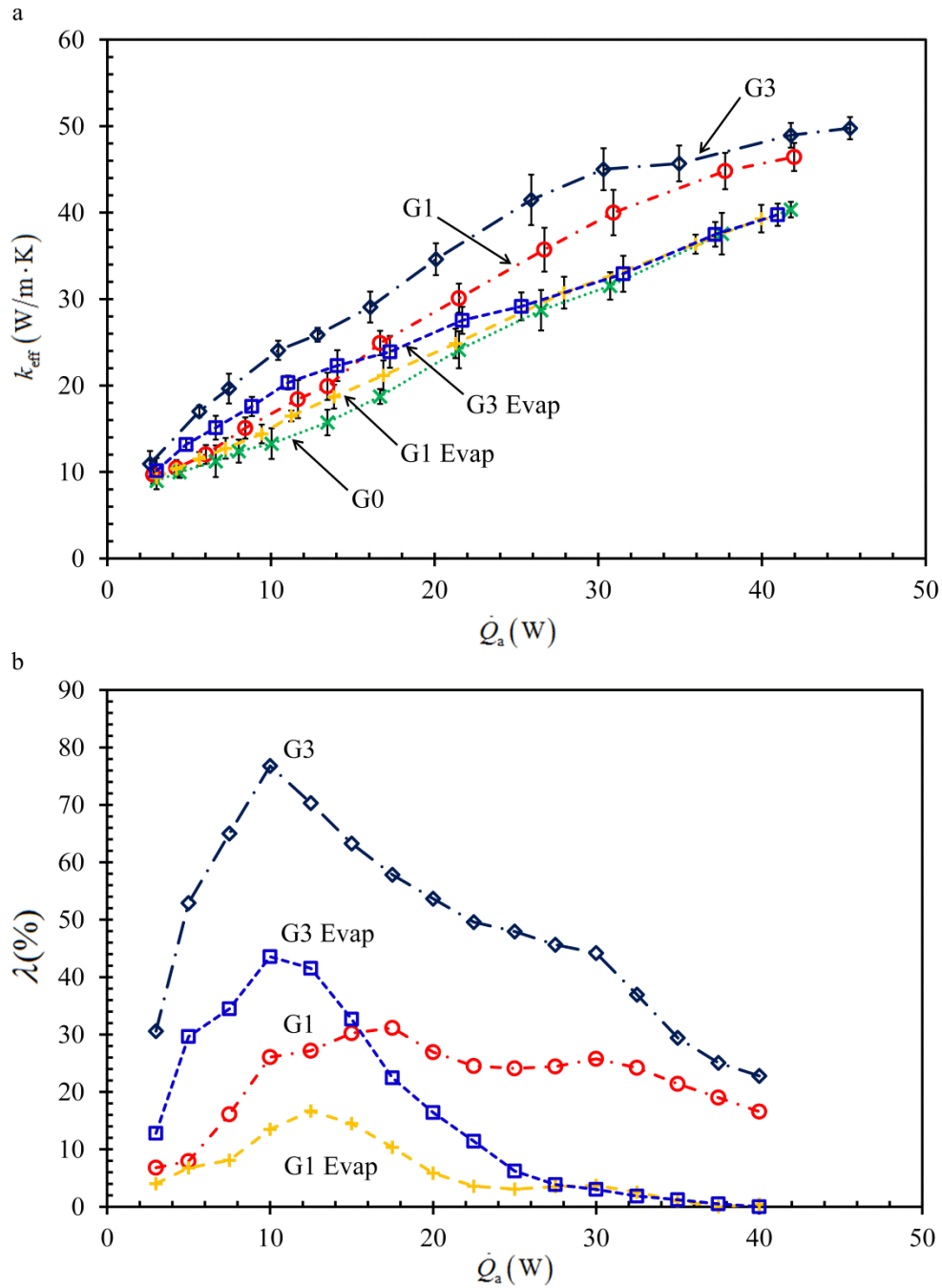


Figure 6.11| Condensation and circulation of condensates enhancements with GNPs-coating. **(a)** Effective thermal conductance of fully-coated and half-coated GNPs TPCTs with different thickness as a function of heat input, \dot{Q}_a . **(b)** Performance enhancement ratio λ of fully-coated and half-coated GNPs TPCTs with different coating thickness, as a function of \dot{Q}_a . The performance enhancement ratio is defined as the augmentation in thermal performance based on that of the uncoated one.

To this end, we evaluate the average evaporator heat transfer coefficient, \bar{h}_e , for the half-coated TPCTs and compare with the fully-coated counterparts as a function of \dot{Q}_a in Figure 6.12. The similar trends of \bar{h}_e as compared to those of k_{eff} in Figure 6.11(a) signify the dominance of evaporation over condensation in the performance enhancement of a TPCT. Therefore, the GNPs-coating at condenser wall not only affects the condensation and circulation of condensate at the condenser section, but also significantly impacts the strength of evaporation in the evaporator section. Significant increase in \bar{h}_e of fully-coated TPCTs (G1 and G3) compared to that of half-coated TPCTs (G1_{Evap} and G3_{Evap}) evidences the effect of GNPs-coating at condenser wall on the strength of evaporation in the evaporator section. The large difference in overall performance, k_{eff} , between fully-coated and half-coated TPCTs, as observed in Fig. 6.11(a), is not entirely due to the enhancement in condensation and circulation of condensate in the condenser section. The circulation of liquid water sustained by the fast water permeation action of GNPs-coating is the main determinant affecting the thermal performance of a TPCT. At high heat input, the evaporator section is depleted of liquid if the circulation rate of condensate is insufficient to overcome the evaporation rate. In such circumstance, dryout will take place at the evaporator section and the TPCT is operated under overloaded condition, where the effective strength of evaporation deteriorates and hence the effective thermal conductance declines. At high heat input ($\dot{Q}_a > 27.8 \text{ W}$), the very small overlapping values of λ for half-coated TPCTs (G1_{Evap} and G3_{Evap}) signify the insignificance of GNPs-coating at evaporator wall due to the occurrence of dryout and therefore the performance enhancement compared to uncoated TPCT is very marginal.

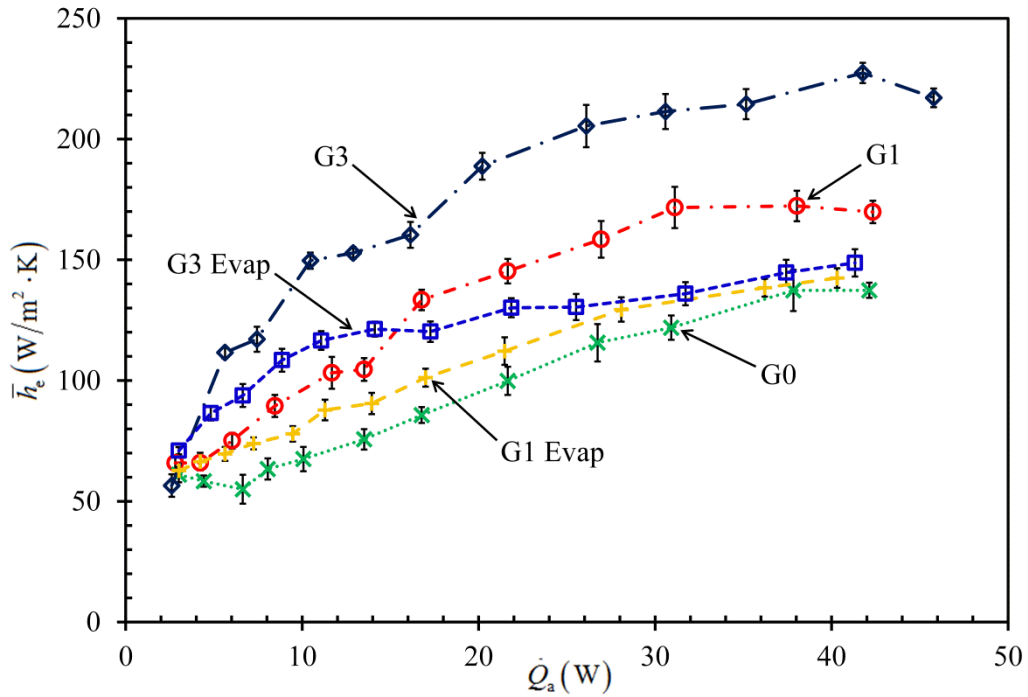


Figure 6.12 Average evaporator heat transfer coefficient \bar{h}_e of half-coated and fully-coated GNPs TPCTs with different coating thickness as a function of \dot{Q}_a . Augmentations condensation and circulation of condensates also enhance the heat transport capability of the TPCT, leading to the overall increase in thermal performance at high heat input.

Figure 6.13 depicts the schematic of conceptual view of working mechanism of GNPs-coating coated on the evaporator and condenser walls of a TPCT. In the evaporator section, the GNPs-coating is partially submerged in the liquid pool. Due to the capillary action of the wall surface, water molecules are heaved through the GNPs-coating off the liquid pool to the sides. The hydrophobic, atomically smooth carbon walls of GNPs provide frictionless nano-passages (interconnecting networks at nanoscale) for the transport of water molecules, which can be regarded as nanocapillaries. At nanoscale, capillary force is principally more intense and dominates over gravitational force, allowing water molecules to slip through the nanocapillaries in an antigravity direction. The effective evaporation region is extended to the wall surface above the liquid-vapour interface. As water intercalates in the GNPs-nanocapillaries, formation of water thin film given rise to a larger surface area for evaporation and facilitating more effective evaporation with higher latent heat being absorbed than that in a pool of water. Simultaneously the fast water permeation action is also driven by the

filmwise evaporation at the GNPs-vapour interface, where a pressure gradient is imposed across the GNPs-coating, driving the water molecules upwards from the water pool. Even though it is in an antigravity direction, water molecules are continuously replenished from the pool of water through the operation of fast water permeation in the graphene structure. At high heat input, the evaporation rate and hence the water permeation rate are so intense that the water pool is dried out, subsequently jeopardizing the strength of evaporation and hence the overall performance of TPCT. On the other hand, the resultant vapour flow is driven upwards to the condenser section by the vapour pressure gradient^{3, 4}. At the sub-cooled condenser section, condensation occurs at the GNPs-coating by releasing the latent heat to the surroundings. Attributed to its hydrophilic characteristic, GNPs-coating improves the droplet nucleation during condensation. On top of the gravitational force, the liquid pressure gradient inside the GNPs-coating drives the condensate downwards back to the evaporator section *via* the fast water permeation property of GNPs-coating. On the way to the evaporator, before the condensate reaches the water pool at the bottom of the evaporator, a large portion of the condensate is being evaporated and hence enhancing the effective filmwise evaporation rate and the circulation rate at the same time. Even at high heat input, the condensate can be replenished for evaporation directly from the condenser section and hence suppressing the occurrence of dryout in the evaporator. This explains the large discrepancies in the strength of evaporation and the overall thermal performance of the fully-coated and half-coated TPCTs, as discussed in Figure 6.12 earlier. In conclusion, in enhancing the thermal performance of a TPCT, GNPs-coating provides a synergistic interaction among its three key processes, namely the evaporation, the condensation and the circulation of condensate, leading to an absolute favourable environment for phase-change heat transfer.

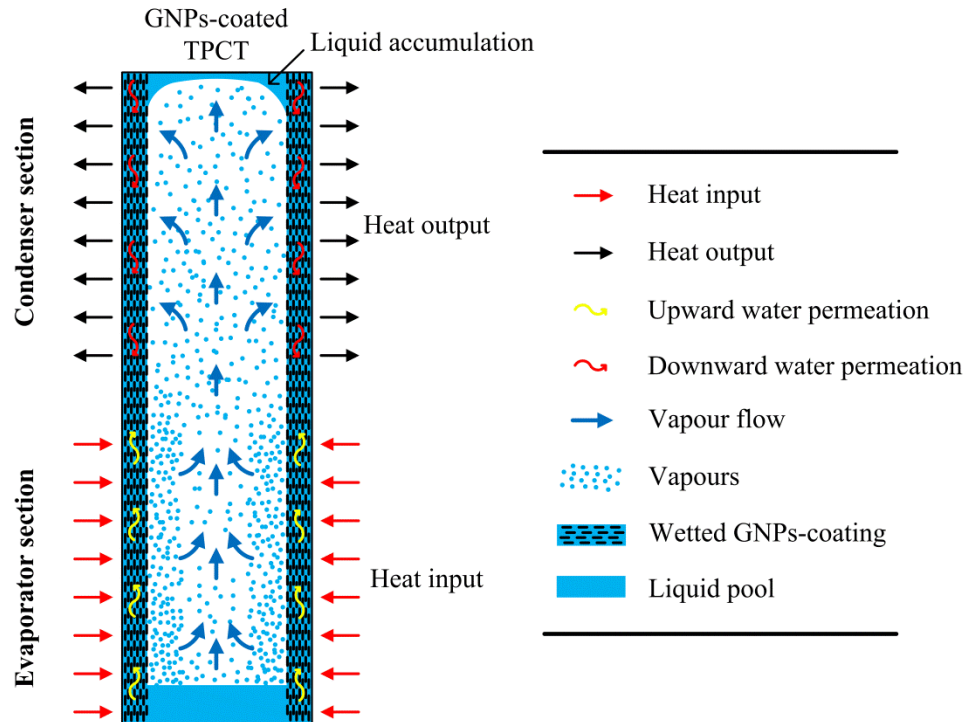


Figure 6.13| Schematic illustration of the driving mechanism of functionalized GNPs-coating coated across the TPCT. The operating principles which govern the thermal performance of the TPCT are significantly enhanced with the water permeation effect across GNPs-coating. In the evaporator section, thin film evaporation strengthens the evaporation at low heat input. The circulation of the condensates is also enhanced, relying not only on the existing gravitational force, but also on the efficient water permeation across GNPs-coating. Continuous water permeation across TPCT is driven by the imposed pressure gradient *via* effective filmwise evaporation.

6.4 Conclusions

This study demonstrated an unprecedented approach in enhancing the TPCT with the introduction of GNPs-coating across the evaporator section as well as the condenser section. Exceeding the water permeability of GO deposition, GNPs-coating with its implicit characteristic of rapid water permeation significantly augments the vital processes governing the operation of TPCT. The optimized ratio of non-oxidized to oxidized regions endows GNPs-coating with excellent water permeability. Water molecules intercalating through the layered structure of GNPs-coating experiences more frictionless flow as compared to their counterpart of GO-coating. Evaporation is enhanced with the induced thin film evaporation and the effective distribution of water molecules across GNP-coated evaporator surface for dryout prevention. GNPs-coating is endowed with unique surface characteristics. The circulation of condensates is enhanced through rapid water permeation while the nucleation of condensed droplets is promoted by its hydrophilic surface characteristic. Together with the induced filmwise evaporation, GNPs-coating is positioned as an excellent functionalized surface coating for phase-change heat transfer enhancement in TPCT.

Chapter 7

Conclusions and future work

7.1 Conclusions

In this thesis, several carbon-based materials are employed to enhance the thermal performance of TPCTs *via* surface functionalization. As the operation of the TPCT relies on evaporation and condensation, Chapter 3 focuses on enhancing the condensation heat transfer while Chapter 4 aims to enhance the evaporation heat transfer. A more detailed analysis on the anomalous enhancement in evaporation with GO deposition is conducted in Chapter 5. Attributing the fast water permeation property of graphene-based materials to the dramatic phase-change heat transfer enhancement, Chapter 6 extends the investigation on thermal performance enhancement of TPCT using GNPs-coating with greater water permeability. Chapter 6 also introduces a new approach in enhancing both evaporation and condensation in TPCT without the need of two different functionalized surfaces. Conclusions for each chapter are summarized as follows:

Chapter 3 investigates the coupled effects of contact forces and vibrations on the thermal performance of TPCTs. By applying a hydrophobic layer across the condenser surface, effective thermal resistance is reduced due to the increased falling rate of the condensed droplets and the induced dropwise condensation. The increased falling rate also indirectly augments the strength of evaporation. With the introduction of high-acceleration vibration to the hydrophobic coated TPCT, reductions of 5.2% to 21.9% in the effective thermal resistance are achieved. For nanofluid, the effects of contact force and vibration on the reduction in effective thermal resistance are similar. However, substantial increase in the heat transfer coefficient augmentation ratios is obtained with the utilization of nanoparticles, exceeding 35.2% and 47.7% for the cases without and

with vibration, respectively, in a coated TPCT. The marginal increase in the circulation effectiveness is contributed to the formation of elongated liquid jets and entrained droplets from the liquid-vapour interface induced by the high-acceleration vibration.

Chapter 4 focuses on enhancing the evaporation strength of a TPCT with the utilization of GO/water nanofluid. GO deposition formed across the evaporator wall dramatically enhances the phase-change heat transfer. Unlike metallic nanoparticles deposition, GO deposition with its unique water permeation characteristic endows filmwise evaporation across the evaporator surface and effectively expands the evaporation region. Matter of fact, similar phase-change heat transfer enhancement was observed in other studies using GO nanofluid. Nevertheless, the enhancement has often been attributed to the fictitious high thermal conductive nature of the deposited layer. Herein, the missing link between the anomalous phase-change heat transfer enhancement and the fast water permeation effect of GO deposition has been established. The finding also demonstrates the temperature dependence of water permeation across GO deposition. Surface functionalization with GO deposition illustrates great potential in the development of novel graphene-based thermal management system.

Chapter 5 presents a new approach in enhancing the vaporization of water on heated surface beyond the Leidenfrost point. The unique water vapour permeability of GO-coated layer effectively impedes the formation of vapour barrier between the liquid-solid interface, resulting in the complete vaporization of water droplet under superheated surface condition. The simplified surface functionalization approach for phase-change heat transfer enhancement and Leidenfrost state suppression utilizes GO nanofluid as coating solution, which can be directly deposited onto any heated surface, forming a uniform layer of GO deposition. Instead of the perceived enhanced surface wettability and high thermal conductive nature of GO-coated layer, the enhanced water vaporization is attributed to the effective dissipation of water vapour molecules *via* nanocapillaries embedded across the GO-coated layer. The driving mechanisms governing its water vapour permeability are also identified. This approach provides new alternative in the practical utilization of graphene-based technology for heat transfer applications while removing the technological hurdles experienced in graphene heat conduction.

Chapter 6 demonstrates a novel approach in enhancing the overall phase-change heat transfer of TPCT using GNPs-coating with high water permeability. Characterization of GNPs-coating reveals its optimized ratio of oxygenated functionalities to sp^3 C-C bonding for efficient water transport. Interestingly, GNPs-coating with its implicit characteristic of rapid water permeation yields extraordinary phase-change heat transfer enhancement when coupled with a TPCT. By applying a thin film of GNPs-coating across the TPCT, a twofold enhancement in the thermal conductance is obtained. Conventionally, diverse surface wetting characteristic is required for the enhancements in both evaporation and condensation. Revolutionized the conventional approaches, GNPs-coating is capable of enhancing both phase-change heat transfer processes. The rapid water permeability of GNPs-coating enhances the evaporation with the extended evaporation region and the induced thin film evaporation. On the other hand, enhanced droplets nucleation and accelerated circulation of condensates are also determined from the GNPs-coated condenser section. GNPs-coating manifests a great potential in applications of highly effective phase-change heat transfer devices.

7.2 Recommendations for future work

While the utilization of carbon-based surface functionalization approaches has demonstrated extraordinary enhancement in the phase-change heat transfer processes, several phenomena still remain unidentified and require further investigation. In particular, the fundamental mechanism behind the fast water permeation in GO deposited layers as proposed in several literatures remains questionable. Fast water permeation has been attributed to the increased interlayer distance of the layered GO structure with the presence of oxygenated functional groups, allowing the intercalation of water molecules. Nevertheless, our study indicates that the interlayer distance has less influence on its water permeability as GNPs-coating with graphite-like interlayer distance endows greater permeability than GO-coating. The water permeability of carbon-based coatings is more likely to be influenced by its chemical structures, i.e. the populations of non-oxidized regions and oxidized regions. This postulation is strengthened by the XPS analysis of GNPs-coating and GO-coating, in which GNPs-coating exhibiting higher populations of non-oxidized regions over oxidized regions, providing more frictionless surface for water transport. Future study will be conducted

to further justify our postulation by comparing graphene-based coatings with different chemical structures. In conjunction with the molecular dynamics (MD) simulation, comparative studies can be conducted in determining the water permeability across several graphene-based deposited layers which include GO, rGO, GNPs and carbon nanotubes. Moreover, aided by the MD simulation, the hydrophilicity of various oxygenated functionalities can be evaluated which will provide better understanding and control over its resulting water permeability. Optimized graphene-based coating with high water permeability can be materialized for greater enhancement in phase-change heat transfer. Several governing factors which influence its water permeability will also be evaluated experimentally in terms of production method of precursor material, solvent of suspension, coating technique, curing temperature and base material for surface deposition.

In the practical implementation of graphene-based coatings in real-life application, our future study also aims to develop novel and simple approach in enhancing conventionally available phase-change heat transfer devices. Boiler system which is commonly used in various industries for steam generation will be an ideal candidate for the implementation of graphene-based functionalized surface coatings. Effective water vaporization can be obtained from the heated surface while preventing the occurrence of dryout, reducing the risk of system meltdown due to excessive heat accumulation.

References

1. Moore, A.L. & Shi, L. Emerging challenges and materials for thermal management of electronics. *Materials Today* **17**, 163-174 (2014).
2. Pop, E. Energy dissipation and transport in nanoscale devices. *Nano Res.* **3**, 147-169 (2010).
3. Faghri, A. *Heat pipe science and technology*. Washington DC, USA: Taylor & Francis, 1995.
4. Peterson, G.P. *An introduction to heat pipes modeling, testing and applications*. New York, USA: John Wiley & Sons Inc., 1994.
5. Jiao, B., Qiu, L.M., Zhang, X.B. & Zhang, Y. Investigation on the effect of filling ratio on the steady-state heat transfer performance of a vertical two-phase closed thermosyphon. *Appl. Therm. Eng.* **28**, 1417-1426 (2008).
6. Jouhara, H. & Robinson, A.J. Experimental investigation of small diameter two-phase closed thermosyphons charged with water, fc-84, fc-77 and fc-3283. *Appl. Therm. Eng.* **30**, 201-211 (2010).
7. Noie, S.H. Heat transfer characteristics of a two-phase closed thermosyphon. *Appl. Therm. Eng.* **25**, 495-506 (2005).
8. Jouhara, H. & Meskimmon, R. Experimental investigation of wraparound loop heat pipe heat exchanger used in energy efficient air handling units. *Energy* **35**, 4592-4599 (2010).
9. El-Genk, M.S. & Saber, H.H. Determination of operation envelopes for closed, two-phase thermosyphons. *Int. J. Heat Mass Transf.* **42**, 889-903 (1999).
10. Hussein, H.M.S., El-Ghetany, H.H. & Nada, S.A. Performance of wickless heat pipe flat plate solar collectors having different pipes cross sections geometries and filling ratios. *Energy Convers. Manage.* **47**, 1539-1549 (2006).
11. Nguyen-Chi, H. & Groll, M. Entrainment or flooding limit in a closed two-phase thermosyphon. *J. Heat Recov. Syst.* **1**, 275-286 (1981).
12. Reay, D. & Kew, P. *Heatpipes, theory, design and applications, fifth edition*. Burlington: Butterworth-Heinemann, 2006.
13. Chen, S.J., Reed, J.G. & Tien, C.L. Reflux condensation in a two-phase closed thermosyphon. *Int. J. Heat Mass Transf.* **27**, 1587-1594 (1984).
14. Gross, U. Reflux condensation heat transfer inside a closed thermosyphon. *Int. J. Heat Mass Transf.* **35**, 279-294 (1992).
15. Pan, Y. Condensation heat transfer characteristics and concept of sub-flooding limit in a two-phase closed thermosyphon. *Int. Commun. Heat Mass Transf.* **28**, 311-322 (2001).
16. Betz, A.R., Xu, J., Qiu, H. & Attinger, D. Do surfaces with mixed hydrophilic and hydrophobic areas enhance pool boiling? *Appl. Phys. Lett.* **97**, 141909 (2010).
17. Chen, X. et al. Nanograsped micropyramidal architectures for continuous dropwise condensation. *Adv. Funct. Mater.* **21**, 4617-4623 (2011).
18. Patankar, N.A. Supernucleating surfaces for nucleate boiling and dropwise condensation heat transfer. *Soft Matter* **6**, 1613-1620 (2010).
19. Drelich, J., Chibowski, E., Meng, D.D. & Terpilowski, K. Hydrophilic and superhydrophilic surfaces and materials. *Soft Matter* **7**, 9804-9828 (2011).
20. Rahimi, M., Asgary, K. & Jesri, S. Thermal characteristics of a resurfaced condenser and evaporator closed two-phase thermosyphon. *Int. Commun. Heat Mass Transf.* **37**, 703-710 (2010).
21. Carey, V.P. *Liquid-vapor phase-change phenomena: An introduction to the thermophysics of vaporization and condensation processes in heat transfer equipment*. New York: Hemisphere Publishing Corporation, 1992.
22. Kang, M.-G. Experimental investigation of tube length effect on nucleate pool boiling heat transfer. *Annals of Nuclear Energy* **25**, 295-304 (1998).

23. Kim, S.J., Bang, I.C., Buongiorno, J. & Hu, L.W. Effects of nanoparticle deposition on surface wettability influencing boiling heat transfer in nanofluids. *Appl. Phys. Lett.* **89**, 153107 (2006).
24. Kim, H.D. & Kim, M.H. Effect of nanoparticle deposition on capillary wicking that influences the critical heat flux in nanofluids. *Appl. Phys. Lett.* **91**, 014104 (2007).
25. Tang, Y., Tang, B., Qing, J., Li, Q. & Lu, L. Nanoporous metallic surface: Facile fabrication and enhancement of boiling heat transfer. *Appl. Surf. Sci.* **258**, 8747-8751 (2012).
26. Lee, C.Y., Zhang, B.J. & Kim, K.J. Morphological change of plain and nano-porous surfaces during boiling and its effect on nucleate pool boiling heat transfer. *Exp Therm Fluid Sci* **40**, 150-158 (2012).
27. El-Genk, M.S. & Ali, A.F. Enhanced nucleate boiling on copper micro-porous surfaces. *International Journal of Multiphase Flow* **36**, 780-792 (2010).
28. Young Lee, C., Hossain Bhuiya, M.M. & Kim, K.J. Pool boiling heat transfer with nano-porous surface. *Int. J. Heat Mass Transf.* **53**, 4274-4279 (2010).
29. Xu, P., Li, Q. & Xuan, Y. Enhanced boiling heat transfer on composite porous surface. *Int. J. Heat Mass Transf.* **80**, 107-114 (2015).
30. Zhang, B.J., Kim, K.J. & Yoon, H. Enhanced heat transfer performance of alumina sponge-like nano-porous structures through surface wettability control in nucleate pool boiling. *Int. J. Heat Mass Transf.* **55**, 7487-7498 (2012).
31. Tang, Y. et al. Pool-boiling enhancement by novel metallic nanoporous surface. *Exp Therm Fluid Sci* **44**, 194-198 (2013).
32. Yang, Y., Ji, X. & Xu, J. Pool boiling heat transfer on copper foam covers with water as working fluid. *Int. J. Therm. Sci.* **49**, 1227-1237 (2010).
33. Li, S., Furberg, R., Toprak, M.S., Palm, B. & Muhammed, M. Nature-inspired boiling enhancement by novel nanostructured macroporous surfaces. *Adv. Funct. Mater.* **18**, 2215-2220 (2008).
34. Wang, C.H. & Dhir, V.K. On the gas entrapment and nucleation site density during pool boiling of saturated water. *J. Heat Transf.* **115**, 670-679 (1993).
35. Dhir, V.K. Boiling heat transfer. *Annual Review of Fluid Mechanics* **30**, 365-401 (1998).
36. Kurihara, H.M. & Myers, J.E. The effects of superheat and surface roughness on boiling coefficients. *AIChE Journal* **6**, 83-91 (1960).
37. Bankoff, S.G. Entrapment of gas in the spreading of a liquid over a rough surface. *AIChE Journal* **4**, 24-26 (1958).
38. Attinger, D. et al. Surface engineering for phase change heat transfer: A review. *MRS Energy & Sustainability - A Review Journal* **1**, null-null (2014).
39. Lu, Y.-W. & Kandlikar, S.G. Nanoscale surface modification techniques for pool boiling enhancement—a critical review and future directions. *Heat Transfer Eng* **32**, 827-842 (2011).
40. Li, C. & Peterson, G.P. Parametric study of pool boiling on horizontal highly conductive microporous coated surfaces. *J. Heat Transf.* **129**, 1465-1475 (2007).
41. Chen, R. et al. Nanowires for enhanced boiling heat transfer. *Nano Lett.* **9**, 548-553 (2009).
42. Li, C. et al. Nanostructured copper interfaces for enhanced boiling. *Small* **4**, 1084-1088 (2008).
43. Ahn, H.S., Jo, H.J., Kang, S.H. & Kim, M.H. Effect of liquid spreading due to nano/microstructures on the critical heat flux during pool boiling. *Appl. Phys. Lett.* **98**, 071908 (2011).
44. Wang, C.H. & Dhir, V.K. Effect of surface wettability on active nucleation site density during pool boiling of water on a vertical surface. *J. Heat Transf.* **115**, 659-669 (1993).
45. Wei, J.J. & Honda, H. Effects of fin geometry on boiling heat transfer from silicon chips with micro-pin-fins immersed in fc-72. *Int. J. Heat Mass Transf.* **46**, 4059-4070 (2003).

46. Ujereh, S., Fisher, T. & Mudawar, I. Effects of carbon nanotube arrays on nucleate pool boiling. *Int. J. Heat Mass Transf.* **50**, 4023-4038 (2007).
47. Ahn, H.S. et al. Pool boiling experiments on multiwalled carbon nanotube (mwcnt) forests. *J. Heat Transf.* **128**, 1335-1342 (2006).
48. Sathyamurthi, V., Ahn, H.S., Banerjee, D. & Lau, S.C. Subcooled pool boiling experiments on horizontal heaters coated with carbon nanotubes. *J. Heat Transf.* **131**, 071501-071501 (2009).
49. Nam, Y. & Ju, Y.S. Bubble nucleation on hydrophobic islands provides evidence to anomalously high contact angles of nanobubbles. *Appl. Phys. Lett.* **93**, 103115 (2008).
50. Chu, K.-H., Enright, R. & Wang, E.N. Structured surfaces for enhanced pool boiling heat transfer. *Appl. Phys. Lett.* **100**, 241603 (2012).
51. Balandin, A.A. et al. Superior thermal conductivity of single-layer graphene. *Nano Lett.* **8**, 902-907 (2008).
52. Balandin, A.A. Thermal properties of graphene and nanostructured carbon materials. *Nat. Mater.* **10**, 569-581 (2011).
53. Zurutuza, A. & Marinelli, C. Challenges and opportunities in graphene commercialization. *Nat. Nano* **9**, 730-734 (2014).
54. Yan, Z., Liu, G., Khan, J.M. & Balandin, A.A. Graphene quilts for thermal management of high-power gan transistors. *Nat. Commun.* **3**, 827 (2012).
55. Shahil, K.M., Goyal, V. & Balandin, A. Thermal properties of graphene: Applications in thermal interface materials. *ECS Transactions* **35**, 193-199 (2011).
56. Pop, E., Varshney, V. & Roy, A.K. Thermal properties of graphene: Fundamentals and applications. *MRS Bull.* **37**, 1273-1281 (2012).
57. Park, S.D. et al. Effects of nanofluids containing graphene/graphene-oxide nanosheets on critical heat flux. *Appl. Phys. Lett.* **97**, 023103 (2010).
58. Ahn, H.S. et al. A novel role of three dimensional graphene foam to prevent heater failure during boiling. *Sci. Rep.* **3** (2013).
59. Ahn, H.S. et al. Enhanced heat transfer is dependent on thickness of graphene films: The heat dissipation during boiling. *Sci. Rep.* **4** (2014).
60. Incropera, F.P., Lavine, A.S., Bergman, T.L. & DeWitt, D.P. *Principles of heat and mass transfer*. Wiley, 2013.
61. Yongji, S., Dunqi, X., Jifang, L. & Siexong, T. A study on the mechanism of dropwise condensation. *Int. J. Heat Mass Transf.* **34**, 2827-2831 (1991).
62. Graham, C. & Griffith, P. Drop size distributions and heat transfer in dropwise condensation. *Int. J. Heat Mass Transf.* **16**, 337-346 (1973).
63. Lee, S. et al. A dropwise condensation model using a nano-scale, pin structured surface. *Int. J. Heat Mass Transf.* **60**, 664-671 (2013).
64. Coulson, S.R., Woodward, I., Badyal, J.P.S., Brewer, S.A. & Willis, C. Super-repellent composite fluoropolymer surfaces. *The Journal of Physical Chemistry B* **104**, 8836-8840 (2000).
65. Nishino, T., Meguro, M., Nakamae, K., Matsushita, M. & Ueda, Y. The lowest surface free energy based on -cf₃ alignment. *Langmuir* **15**, 4321-4323 (1999).
66. Wenzel, R.N. Surface roughness and contact angle. *The Journal of Physical and Colloid Chemistry* **53**, 1466-1467 (1949).
67. Cassie, A.B.D. & Baxter, S. Wettability of porous surfaces. *Transactions of the Faraday Society* **40**, 546-551 (1944).
68. Roach, P., Shirtcliffe, N.J. & Newton, M.I. Progress in superhydrophobic surface development. *Soft Matter* **4**, 224-240 (2008).
69. Feng, X.J. & Jiang, L. Design and creation of superwetting/antiwetting surfaces. *Adv. Mater.* **18**, 3063-3078 (2006).
70. Barthlott, W. & Neinhuis, C. Purity of the sacred lotus, or escape from contamination in biological surfaces. *Planta* **202**, 1-8 (1997).
71. Otten, A. & Herminghaus, S. How plants keep dry: A physicist's point of view. *Langmuir* **20**, 2405-2408 (2004).

72. Gao, X. & Jiang, L. Biophysics: Water-repellent legs of water striders. *Nature* **432**, 36-36 (2004).
73. Chen, C.-H. et al. Dropwise condensation on superhydrophobic surfaces with two-tier roughness. *Appl. Phys. Lett.* **90**, 173108 (2007).
74. Dorrer, C. & Rühe, J. Condensation and wetting transitions on microstructured ultrahydrophobic surfaces. *Langmuir* **23**, 3820-3824 (2007).
75. Narhe, R.D. & Beysens, D.A. Water condensation on a super-hydrophobic spike surface. *EPL (Europhysics Letters)* **75**, 98 (2006).
76. Narhe, R.D. & Beysens, D.A. Growth dynamics of water drops on a square-pattern rough hydrophobic surface. *Langmuir* **23**, 6486-6489 (2007).
77. Narhe, R.D. & Beysens, D.A. Nucleation and growth on a superhydrophobic grooved surface. *Phys. Rev. Lett.* **93**, 076103 (2004).
78. Varanasi, K.K., Hsu, M., Bhate, N., Yang, W. & Deng, T. Spatial control in the heterogeneous nucleation of water. *Appl. Phys. Lett.* **95**, 094101 (2009).
79. Dietz, C., Rykaczewski, K., Fedorov, A.G. & Joshi, Y. Visualization of droplet departure on a superhydrophobic surface and implications to heat transfer enhancement during dropwise condensation. *Appl. Phys. Lett.* **97**, 033104 (2010).
80. Miljkovic, N., Enright, R. & Wang, E.N. Effect of droplet morphology on growth dynamics and heat transfer during condensation on superhydrophobic nanostructured surfaces. *ACS Nano* **6**, 1776-1785 (2012).
81. Jung, Y.C. & Bhushan, B. Wetting behaviour during evaporation and condensation of water microdroplets on superhydrophobic patterned surfaces. *Journal of Microscopy* **229**, 127-140 (2008).
82. Rykaczewski, K. et al. How nanorough is rough enough to make a surface superhydrophobic during water condensation? *Soft Matter* **8**, 8786-8794 (2012).
83. Lafuma, A. & Quere, D. Superhydrophobic states. *Nat. Mater.* **2**, 457-460 (2003).
84. Miljkovic, N., Enright, R., Maroo, S.C., Cho, H.J. & Wang, E.N. Liquid evaporation on superhydrophobic and superhydrophilic nanostructured surfaces. *J. Heat Transf.* **133**, 080903-080903 (2011).
85. He, B., Patankar, N.A. & Lee, J. Multiple equilibrium droplet shapes and design criterion for rough hydrophobic surfaces. *Langmuir* **19**, 4999-5003 (2003).
86. Bico, J., Marzolin, C. & Quéré, D. Pearl drops. *EPL (Europhysics Letters)* **47**, 220 (1999).
87. Li, X.-M., Reinhoudt, D. & Crego-Calama, M. What do we need for a superhydrophobic surface? A review on the recent progress in the preparation of superhydrophobic surfaces. *Chem. Soc. Rev.* **36**, 1350-1368 (2007).
88. Wier, K.A. & McCarthy, T.J. Condensation on ultrahydrophobic surfaces and its effect on droplet mobility: Ultrahydrophobic surfaces are not always water repellent. *Langmuir* **22**, 2433-2436 (2006).
89. Cheng, Y.-T., Rodak, D.E., Angelopoulos, A. & Gacek, T. Microscopic observations of condensation of water on lotus leaves. *Appl. Phys. Lett.* **87**, 194112 (2005).
90. Cheng, Y.-T. & Rodak, D.E. Is the lotus leaf superhydrophobic? *Appl. Phys. Lett.* **86**, 144101 (2005).
91. Daniel, S., Chaudhury, M.K. & Chen, J.C. Fast drop movements resulting from the phase change on a gradient surface. *Science* **291**, 633-636 (2001).
92. Waowaew, N., Terdtoon, P., Maezawa, S., Kamonpet, P. & Klongpanich, W. Correlation to predict heat transfer characteristics of a radially rotating heat pipe at vertical position. *Appl. Therm. Eng.* **23**, 1019-1032 (2003).
93. Chang, S.W. & Lin, C.Y. Thermal performance of rotating two-phase thermosyphon disc. *Int. J. Heat Mass Transf.* **62**, 40-54 (2013).
94. Wangnipparnto, S., Tiansuwan, J., Kiatsiriroat, T. & Wang, C.C. Performance analysis of thermosyphon heat exchanger under electric field. *Energy Convers. Manage.* **44**, 1163-1175 (2003).

95. Heris, S.Z., Mohammadpur, F. & Shakouri, A. Effect of electric field on thermal performance of thermosyphon heat pipes using nanofluids. *Mater. Res. Bull.* **53**, 21-27 (2014).
96. Fornalik, E., Filar, P., Tagawa, T., Ozoe, H. & Szmyd, J.S. Effect of a magnetic field on the convection of paramagnetic fluid in unstable and stable thermosyphon-like configurations. *Int. J. Heat Mass Transf.* **49**, 2642-2651 (2006).
97. Abou-Ziyan, H.Z., Helali, A., Fatouh, M. & El-Nasr, M.M.A. Performance of stationary and vibrated thermosyphon working with water and r134a. *Appl. Therm. Eng.* **21**, 813-830 (2001).
98. Murshed, S.M.S., Leong, K.C. & Yang, C. Enhanced thermal conductivity of tio2—water based nanofluids. *Int. J. Therm. Sci.* **44**, 367-373 (2005).
99. Eastman, J.A., Choi, U.S., Li, S., Thompson, L.J. & Lee, S. Enhanced thermal conductivity through the development of nanofluids. *MRS Online Proceedings Library* **457**, null-null (1996).
100. Liu, M.S., Lin, M.C.C., Huang, I.T. & Wang, C.C. Enhancement of thermal conductivity with cuo for nanofluids. *Chemical Engineering and Technology* **29**, 72-77 (2006).
101. Hwang, Y., Park, H.S., Lee, J.K. & Jung, W.H. Thermal conductivity and lubrication characteristics of nanofluids. *Current Applied Physics* **6**, **Supplement 1**, e67-e71 (2006).
102. Yu, W., Xie, H., Chen, L. & Li, Y. Investigation of thermal conductivity and viscosity of ethylene glycol based zno nanofluid. *Thermochimica Acta* **491**, 92-96 (2009).
103. Eastman, J.A., Choi, S.U.S., Li, S., Yu, W. & Thompson, L.J. Anomalously increased effective thermal conductivities of ethylene glycol-based nanofluids containing copper nanoparticles. *Appl. Phys. Lett.* **78**, 718-720 (2001).
104. Lee, J.-H. et al. Effective viscosities and thermal conductivities of aqueous nanofluids containing low volume concentrations of al₂o₃ nanoparticles. *Int. J. Heat Mass Transf.* **51**, 2651-2656 (2008).
105. Trisaksri, V. & Wongwises, S. Critical review of heat transfer characteristics of nanofluids. *Renew. Sust. Energy Rev.* **11**, 512-523 (2007).
106. Buschmann, M.H. Nanofluids in thermosyphons and heat pipes: Overview of recent experiments and modelling approaches. *Int. J. Therm. Sci.* **72**, 1-17 (2013).
107. Heris, S.Z., Mohammadpur, F., Mahian, O. & Sahin, A.Z. Experimental study of two phase closed thermosyphon using cuo/water nanofluid in the presence of electric field. *Experimental Heat Transfer* **28**, 328-343 (2014).
108. Liu, Z.H., Yang, X.F. & Guo, G.L. Effect of nanoparticles in nanofluid on thermal performance in a miniature thermosyphon. *Journal of Applied Physics* **102**, 013526 (2007).
109. Khandekar, S., Joshi, Y.M. & Mehta, B. Thermal performance of closed two-phase thermosyphon using nanofluids. *Int. J. Therm. Sci.* **47**, 659-667 (2008).
110. Liu, Z. & Zhu, Q. Application of aqueous nanofluids in a horizontal mesh heat pipe. *Energy Convers. Manage.* **52**, 292-300 (2011).
111. Xue Fei, Y., Zhen-Hua, L. & Jie, Z. Heat transfer performance of a horizontal micro-grooved heat pipe using cuo nanofluid. *Journal of Micromechanics and Microengineering* **18**, 035038 (2008).
112. Liu, Z.-H., Li, Y.-Y. & Bao, R. Thermal performance of inclined grooved heat pipes using nanofluids. *Int. J. Therm. Sci.* **49**, 1680-1687 (2010).
113. Kamyar, A., Ong, K.S. & Saidur, R. Effects of nanofluids on heat transfer characteristics of a two-phase closed thermosyphon. *Int. J. Heat Mass Transf.* **65**, 610-618 (2013).
114. Noie, S.H., Heris, S.Z., Kahani, M. & Nowee, S.M. Heat transfer enhancement using al₂o₃/water nanofluid in a two-phase closed thermosyphon. *International Journal of Heat and Fluid Flow* **30**, 700-705 (2009).
115. Do, K.H., Ha, H.J. & Jang, S.P. Thermal resistance of screen mesh wick heat pipes using the water-based al₂o₃ nanofluids. *Int. J. Heat Mass Transf.* **53**, 5888-5894 (2010).

116. Hung, Y.-H., Teng, T.-P. & Lin, B.-G. Evaluation of the thermal performance of a heat pipe using alumina nanofluids. *Exp Therm Fluid Sci* **44**, 504-511 (2013).
117. Huminic, G., Huminic, A., Morjan, I. & Dumitrache, F. Experimental study of the thermal performance of thermosyphon heat pipe using iron oxide nanoparticles. *Int. J. Heat Mass Transf.* **54**, 656-661 (2011).
118. Huminic, G. & Huminic, A. Heat transfer characteristics of a two-phase closed thermosyphons using nanofluids. *Exp Therm Fluid Sci* **35**, 550-557 (2011).
119. Tsai, C.Y. et al. Effect of structural character of gold nanoparticles in nanofluid on heat pipe thermal performance. *Mater. Lett.* **58**, 1461-1465 (2004).
120. Paramatthanuwat, T., Boothaisong, S., Rittidech, S. & Booddachan, K. Heat transfer characteristics of a two-phase closed thermosyphon using de ionized water mixed with silver nano. *Heat Mass Transfer* **46**, 281-285 (2010).
121. Kang, S.-W., Wei, W.-C., Tsai, S.-H. & Yang, S.-Y. Experimental investigation of silver nano-fluid on heat pipe thermal performance. *Appl. Therm. Eng.* **26**, 2377-2382 (2006).
122. Kang, S.-W., Wei, W.-C., Tsai, S.-H. & Huang, C.-C. Experimental investigation of nanofluids on sintered heat pipe thermal performance. *Appl. Therm. Eng.* **29**, 973-979 (2009).
123. Naphon, P., Assadamongkol, P. & Borirak, T. Experimental investigation of titanium nanofluids on the heat pipe thermal efficiency. *Int. Commun. Heat Mass Transf.* **35**, 1316-1319 (2008).
124. Naphon, P., Thongkum, D. & Assadamongkol, P. Heat pipe efficiency enhancement with refrigerant–nanoparticles mixtures. *Energy Convers. Manage.* **50**, 772-776 (2009).
125. Baojin, Q., Li, Z., Hong, X. & Yan, S. Heat transfer characteristics of titanium/water two-phase closed thermosyphon. *Energy Convers. Manage.* **50**, 2174-2179 (2009).
126. Peng, Y., Huang, S. & Huang, K. Experimental study on thermosiphon by adding nanoparticles to working fluid. *Huagong Xuebao/Journal of Chemical Industry and Engineering (China)* **55**, 1768-1772 (2004).
127. Ma, H.B. et al. Effect of nanofluid on the heat transport capability in an oscillating heat pipe. *Appl. Phys. Lett.* **88**, 143116 (2006).
128. Ma, H.B. et al. An experimental investigation of heat transport capability in a nanofluid oscillating heat pipe. *J. Heat Transf.* **128**, 1213-1216 (2006).
129. Xue, H.S., Fan, J.R., Hu, Y.C., Hong, R.H. & Cen, K.F. The interface effect of carbon nanotube suspension on the thermal performance of a two-phase closed thermosyphon. *Journal of Applied Physics* **100**, 104909 (2006).
130. Shanbedi, M., Zeinali Heris, S., Baniadam, M. & Amiri, A. The effect of multi-walled carbon nanotube/water nanofluid on thermal performance of a two-phase closed thermosyphon. *Experimental Heat Transfer* **26**, 26-40 (2013).
131. Liu, Z.-h., Yang, X.-f., Wang, G.-s. & Guo, G.-l. Influence of carbon nanotube suspension on the thermal performance of a miniature thermosyphon. *Int. J. Heat Mass Transf.* **53**, 1914-1920 (2010).
132. Zeinali Heris, S., Fallahi, M., Shanbedi, M. & Amiri, A. Heat transfer performance of two-phase closed thermosyphon with oxidized cnt/water nanofluids. *Heat Mass Transfer*, 1-9 (2015).
133. Shanbedi, M., Heris, S.Z., Baniadam, M., Amiri, A. & Maghrebi, M. Investigation of heat-transfer characterization of eda-mwcnt/di-water nanofluid in a two-phase closed thermosyphon. *Industrial & Engineering Chemistry Research* **51**, 1423-1428 (2012).
134. Hernández Battez, A. et al. CuO, ZnO and ZnO nanoparticles as antiwear additive in oil lubricants. *Wear* **265**, 422-428 (2008).
135. Sunqing, Q., Junxiu, D. & Guoxu, C. Wear and friction behaviour of CaCO₃ nanoparticles used as additives in lubricating oils. *Lubrication Science* **12**, 205-212 (2000).
136. You, S.M., Kim, J.H. & Kim, K.H. Effect of nanoparticles on critical heat flux of water in pool boiling heat transfer. *Appl. Phys. Lett.* **83**, 3374-3376 (2003).

137. Xie, H., Yu, W., Li, Y. & Chen, L. Discussion on the thermal conductivity enhancement of nanofluids. *Nanoscale Res. Lett.* **6**, 124 (2011).
138. Kim, H. Enhancement of critical heat flux in nucleate boiling of nanofluids: A state-of-art review. *Nanoscale Res. Lett.* **6**, 415 (2011).
139. Kim, S.J., Bang, I.C., Buongiorno, J. & Hu, L.W. Surface wettability change during pool boiling of nanofluids and its effect on critical heat flux. *Int. J. Heat Mass Transf.* **50**, 4105-4116 (2007).
140. Hsu, C.-C. & Chen, P.-H. Surface wettability effects on critical heat flux of boiling heat transfer using nanoparticle coatings. *Int. J. Heat Mass Transf.* **55**, 3713-3719 (2012).
141. Coursey, J.S. & Kim, J. Nanofluid boiling: The effect of surface wettability. *International Journal of Heat and Fluid Flow* **29**, 1577-1585 (2008).
142. Wen, D., Corr, M., Hu, X. & Lin, G. Boiling heat transfer of nanofluids: The effect of heating surface modification. *Int. J. Therm. Sci.* **50**, 480-485 (2011).
143. Das, S.K., Putra, N. & Roetzel, W. Pool boiling characteristics of nano-fluids. *Int. J. Heat Mass Transf.* **46**, 851-862 (2003).
144. Bang, I.C. & Heung Chang, S. Boiling heat transfer performance and phenomena of al₂o₃-water nano-fluids from a plain surface in a pool. *Int. J. Heat Mass Transf.* **48**, 2407-2419 (2005).
145. Yang, X.-F. & Liu, Z.-H. Application of functionalized nanofluid in thermosyphon. *Nanoscale Res. Lett.* **6**, 1-12 (2011).
146. Kwark, S.M., Moreno, G., Kumar, R., Moon, H. & You, S.M. Nanocoating characterization in pool boiling heat transfer of pure water. *Int. J. Heat Mass Transf.* **53**, 4579-4587 (2010).
147. Kwark, S.M., Kumar, R., Moreno, G., Yoo, J. & You, S.M. Pool boiling characteristics of low concentration nanofluids. *Int. J. Heat Mass Transf.* **53**, 972-981 (2010).
148. Novoselov, K.S. et al. Electric field effect in atomically thin carbon films. *Science* **306**, 666-669 (2004).
149. Choi, W., Lahiri, I., Seelaboyina, R. & Kang, Y.S. Synthesis of graphene and its applications: A review. *Critical Reviews in Solid State and Materials Sciences* **35**, 52-71 (2010).
150. Lee, C., Wei, X., Kysar, J.W. & Hone, J. Measurement of the elastic properties and intrinsic strength of monolayer graphene. *Science* **321**, 385-388 (2008).
151. Bolotin, K.I. et al. Ultrahigh electron mobility in suspended graphene. *Solid State Communications* **146**, 351-355 (2008).
152. Morozov, S.V. et al. Giant intrinsic carrier mobilities in graphene and its bilayer. *Phys. Rev. Lett.* **100**, 016602 (2008).
153. Cai, W., Zhu, Y., Li, X., Piner, R.D. & Ruoff, R.S. Large area few-layer graphene/graphite films as transparent thin conducting electrodes. *Appl. Phys. Lett.* **95**, 123115 (2009).
154. Ghosh, S. et al. Extremely high thermal conductivity of graphene: Prospects for thermal management applications in nanoelectronic circuits. *Appl. Phys. Lett.* **92**, 151911 (2008).
155. Yu, A., Ramesh, P., Itkis, M.E., Bekyarova, E. & Haddon, R.C. Graphite nanoplatelet-epoxy composite thermal interface materials. *The Journal of Physical Chemistry C* **111**, 7565-7569 (2007).
156. Liang, Q., Yao, X., Wang, W., Liu, Y. & Wong, C.P. A three-dimensional vertically aligned functionalized multilayer graphene architecture: An approach for graphene-based thermal interfacial materials. *ACS Nano* **5**, 2392-2401 (2011).
157. Yavari, F. et al. Enhanced thermal conductivity in a nanostructured phase change composite due to low concentration graphene additives. *The Journal of Physical Chemistry C* **115**, 8753-8758 (2011).
158. Shahil, K.M.F. & Balandin, A.A. Graphene-multilayer graphene nanocomposites as highly efficient thermal interface materials. *Nano Lett.* **12**, 861-867 (2012).
159. Zhu, Y. et al. Graphene and graphene oxide: Synthesis, properties, and applications. *Adv. Mater.* **22**, 3906-3924 (2010).

160. Zhu, Y., James, D.K. & Tour, J.M. New routes to graphene, graphene oxide and their related applications. *Adv. Mater.* **24**, 4924-4955 (2012).
161. Wei, D. & Liu, Y. Controllable synthesis of graphene and its applications. *Adv. Mater.* **22**, 3225-3241 (2010).
162. Wei, D. & Kivioja, J. Graphene for energy solutions and its industrialization. *Nanoscale* **5**, 10108-10126 (2013).
163. Park, S. & Ruoff, R.S. Chemical methods for the production of graphenes. *Nat. Nano* **4**, 217-224 (2009).
164. Xuekun, L., Minfeng, Y., Hui, H. & Rodney, S.R. Tailoring graphite with the goal of achieving single sheets. *Nanotechnology* **10**, 269 (1999).
165. Somani, P.R., Somani, S.P. & Umeno, M. Planer nano-graphenes from camphor by cvd. *Chemical Physics Letters* **430**, 56-59 (2006).
166. Kim, K.S. et al. Large-scale pattern growth of graphene films for stretchable transparent electrodes. *Nature* **457**, 706-710 (2009).
167. Li, X. et al. Large-area synthesis of high-quality and uniform graphene films on copper foils. *Science* **324**, 1312-1314 (2009).
168. Ago, H. et al. Epitaxial chemical vapor deposition growth of single-layer graphene over cobalt film crystallized on sapphire. *ACS Nano* **4**, 7407-7414 (2010).
169. Kwon, S.-Y. et al. Growth of semiconducting graphene on palladium. *Nano Lett.* **9**, 3985-3990 (2009).
170. Loginova, E., Bartelt, N.C., Feibelman, P.J. & McCarty, K.F. Factors influencing graphene growth on metal surfaces. *New Journal of Physics* **11**, 063046 (2009).
171. Muñoz, R. & Gómez-Aleixandre, C. Review of cvd synthesis of graphene. *Chemical Vapor Deposition* **19**, 297-322 (2013).
172. Gao, Z., Zhang, Y., Fu, Y., Yuen, M.M.F. & Liu, J. Thermal chemical vapor deposition grown graphene heat spreader for thermal management of hot spots. *Carbon* **61**, 342-348 (2013).
173. Bae, S. et al. Roll-to-roll production of 30-inch graphene films for transparent electrodes. *Nat. Nano* **5**, 574-578 (2010).
174. Kobayashi, T. et al. Production of a 100-m-long high-quality graphene transparent conductive film by roll-to-roll chemical vapor deposition and transfer process. *Appl. Phys. Lett.* **102**, 023112 (2013).
175. Berger, C. et al. Electronic confinement and coherence in patterned epitaxial graphene. *Science* **312**, 1191-1196 (2006).
176. Berger, C. et al. Ultrathin epitaxial graphite: 2d electron gas properties and a route toward graphene-based nanoelectronics. *The Journal of Physical Chemistry B* **108**, 19912-19916 (2004).
177. Hass, J. et al. Highly ordered graphene for two dimensional electronics. *Appl. Phys. Lett.* **89**, 143106 (2006).
178. Hibino, H. et al. Microscopic thickness determination of thin graphite films formed on SiC from quantized oscillation in reflectivity of low-energy electrons. *Physical Review B* **77**, 075413 (2008).
179. Taisuke, O. et al. Morphology of graphene thin film growth on $\text{SiC}(0001)$. *New Journal of Physics* **10**, 023034 (2008).
180. Emtsev, K.V. et al. Towards wafer-size graphene layers by atmospheric pressure graphitization of silicon carbide. *Nat. Mater.* **8**, 203-207 (2009).
181. Dreyer, D.R., Park, S., Bielawski, C.W. & Ruoff, R.S. The chemistry of graphene oxide. *Chem. Soc. Rev.* **39**, 228-240 (2010).
182. Paredes, J.I., Villar-Rodil, S., Martínez-Alonso, A. & Tascón, J.M.D. Graphene oxide dispersions in organic solvents. *Langmuir* **24**, 10560-10564 (2008).
183. Cote, L.J., Kim, F. & Huang, J. Langmuir-blodgett assembly of graphite oxide single layers. *J. Am. Chem. Soc.* **131**, 1043-1049 (2009).
184. Buchsteiner, A., Lerf, A. & Pieper, J. Water dynamics in graphite oxide investigated with neutron scattering. *The Journal of Physical Chemistry B* **110**, 22328-22338 (2006).
185. Rummeli, M.H. et al. Graphene: Piecing it together. *Adv. Mater.* **23**, 4471-4490 (2011).

186. Stankovich, S. et al. Synthesis of graphene-based nanosheets via chemical reduction of exfoliated graphite oxide. *Carbon* **45**, 1558-1565 (2007).
187. Shin, H.-J. et al. Efficient reduction of graphite oxide by sodium borohydride and its effect on electrical conductance. *Adv. Funct. Mater.* **19**, 1987-1992 (2009).
188. Dua, V. et al. All-organic vapor sensor using inkjet-printed reduced graphene oxide. *Angewandte Chemie International Edition* **49**, 2154-2157 (2010).
189. Su, Y. et al. Impermeable barrier films and protective coatings based on reduced graphene oxide. *Nat. Commun.* **5** (2014).
190. Wang, G. et al. Facile synthesis and characterization of graphene nanosheets. *The Journal of Physical Chemistry C* **112**, 8192-8195 (2008).
191. Fan, X. et al. Deoxygenation of exfoliated graphite oxide under alkaline conditions: A green route to graphene preparation. *Adv. Mater.* **20**, 4490-4493 (2008).
192. McAllister, M.J. et al. Single sheet functionalized graphene by oxidation and thermal expansion of graphite. *Chemistry of Materials* **19**, 4396-4404 (2007).
193. Schniepp, H.C. et al. Functionalized single graphene sheets derived from splitting graphite oxide. *The Journal of Physical Chemistry B* **110**, 8535-8539 (2006).
194. Shao, Y., Wang, J., Engelhard, M., Wang, C. & Lin, Y. Facile and controllable electrochemical reduction of graphene oxide and its applications. *Journal of Materials Chemistry* **20**, 743-748 (2010).
195. Guo, H.-L., Wang, X.-F., Qian, Q.-Y., Wang, F.-B. & Xia, X.-H. A green approach to the synthesis of graphene nanosheets. *ACS Nano* **3**, 2653-2659 (2009).
196. Harima, Y. et al. Electrochemical reduction of graphene oxide in organic solvents. *Electrochimica Acta* **56**, 5363-5368 (2011).
197. Ramesha, G.K. & Sampath, S. Electrochemical reduction of oriented graphene oxide films: An in situ raman spectroelectrochemical study. *The Journal of Physical Chemistry C* **113**, 7985-7989 (2009).
198. Zhou, M. et al. Controlled synthesis of large-area and patterned electrochemically reduced graphene oxide films. *Chemistry – A European Journal* **15**, 6116-6120 (2009).
199. An, S.J. et al. Thin film fabrication and simultaneous anodic reduction of deposited graphene oxide platelets by electrophoretic deposition. *The Journal of Physical Chemistry Letters* **1**, 1259-1263 (2010).
200. Kuila, T., Mishra, A.K., Khanra, P., Kim, N.H. & Lee, J.H. Recent advances in the efficient reduction of graphene oxide and its application as energy storage electrode materials. *Nanoscale* **5**, 52-71 (2013).
201. Cai, M., Thorpe, D., Adamson, D.H. & Schniepp, H.C. Methods of graphite exfoliation. *Journal of Materials Chemistry* **22**, 24992-25002 (2012).
202. Li, X., Wang, X., Zhang, L., Lee, S. & Dai, H. Chemically derived, ultrasmooth graphene nanoribbon semiconductors. *Science* **319**, 1229-1232 (2008).
203. Li, X. et al. Highly conducting graphene sheets and langmuir-blodgett films. *Nat. Nano* **3**, 538-542 (2008).
204. Janowska, I. et al. Microwave synthesis of large few-layer graphene sheets in aqueous solution of ammonia. *Nano Res.* **3**, 126-137 (2010).
205. Liu, Z., Robinson, J.T., Sun, X. & Dai, H. Pegylated nanographene oxide for delivery of water-insoluble cancer drugs. *J. Am. Chem. Soc.* **130**, 10876-10877 (2008).
206. Yang, Y., Liu, W. & Asheghi, M. Thermal and electrical characterization of cu/cofe superlattices. *Appl. Phys. Lett.* **84**, 3121-3123 (2004).
207. Timo, S., Brian, R.B., Niklas, C.S. & Dimos, P. An electrical method for the measurement of the thermal and electrical conductivity of reduced graphene oxide nanostructures. *Nanotechnology* **20**, 405704 (2009).
208. Mu, X., Wu, X., Zhang, T., Go, D.B. & Luo, T. Thermal transport in graphene oxide – from ballistic extreme to amorphous limit. *Sci. Rep.* **4**, 3909 (2014).
209. Callaway, J. Model for lattice thermal conductivity at low temperatures. *Physical Review* **113**, 1046-1051 (1959).
210. Berman, R., Simon, F.E. & Wilks, J. Thermal conductivity of dielectric crystals: The ω process. *Nature* **168**, 277-280 (1951).

211. Ren, S.Y. & Dow, J.D. Thermal conductivity of superlattices. *Physical Review B* **25**, 3750-3755 (1982).
212. Seol, J.H. et al. Two-dimensional phonon transport in supported graphene. *Science* **328**, 213-216 (2010).
213. Jang, W., Chen, Z., Bao, W., Lau, C.N. & Dames, C. Thickness-dependent thermal conductivity of encased graphene and ultrathin graphite. *Nano Lett.* **10**, 3909-3913 (2010).
214. Wang, Z. et al. Thermal transport in suspended and supported few-layer graphene. *Nano Lett.* **11**, 113-118 (2011).
215. Serov, A.Y., Ong, Z.-Y. & Pop, E. Effect of grain boundaries on thermal transport in graphene. *Appl. Phys. Lett.* **102**, 033104 (2013).
216. Subrina, S., Kotchetkov, D. & Balandin, A.A. Heat removal in silicon-on-insulator integrated circuits with graphene lateral heat spreaders. *Electron Device Letters, IEEE* **30**, 1281-1283 (2009).
217. Subrina, S., Kotchetkov, D. & Balandin, A.A. in Thermal and Thermomechanical Phenomena in Electronic Systems (ITherm), 2010 12th IEEE Intersociety Conference on 1-5 (2010).
218. Han, N. et al. Improved heat dissipation in gallium nitride light-emitting diodes with embedded graphene oxide pattern. *Nat. Commun.* **4**, 1452 (2013).
219. Song, N.-J. et al. Thermally reduced graphene oxide films as flexible lateral heat spreaders. *J. Mater. Chem. A* **2**, 16563-16568 (2014).
220. Botas, C. et al. Critical temperatures in the synthesis of graphene-like materials by thermal exfoliation–reduction of graphite oxide. *Carbon* **52**, 476-485 (2013).
221. Kong, Q.-Q. et al. Hierarchical graphene–carbon fiber composite paper as a flexible lateral heat spreader. *Adv. Funct. Mater.* **24**, 4222-4228 (2014).
222. Hou, Z.-L. et al. Flexible graphene–graphene composites of superior thermal and electrical transport properties. *ACS Appl. Mater. Inter.* **6**, 15026-15032 (2014).
223. Yu, H., Li, L. & Zhang, Y. Silver nanoparticle-based thermal interface materials with ultra-low thermal resistance for power electronics applications. *Scripta Materialia* **66**, 931-934 (2012).
224. Dong, H., Fan, L. & Wong, C.P. in Proceedings - Electronic Components and Technology Conference 1451-1454 (2005).
225. Fan, L., Su, B., Qu, J. & Wong, C.P. in Proceedings - Electronic Components and Technology Conference 148-154 (2004).
226. Xu, Y., Chung, D.D.L. & Mroz, C. Thermally conducting aluminum nitride polymer-matrix composites. *Composites Part A: Applied Science and Manufacturing* **32**, 1749-1757 (2001).
227. Jones, W.E., Chiguma, J., Johnson, E., Pachamuthu, A. & Santos, D. Electrically and thermally conducting nanocomposites for electronic applications. *Materials* **3**, 1478 (2010).
228. Felba, J. in Nano-bio- electronic, photonic and mems packaging (eds. Wong, C.P., Moon, K.-S. & Li, Y.) 277-314 (Springer US, 2010).
229. Biercuk, M.J. et al. Carbon nanotube composites for thermal management. *Appl. Phys. Lett.* **80**, 2767-2769 (2002).
230. Yu, A., Itkis, M.E., Bekyarova, E. & Haddon, R.C. Effect of single-walled carbon nanotube purity on the thermal conductivity of carbon nanotube-based composites. *Appl. Phys. Lett.* **89**, 133102 (2006).
231. Wei, Z. et al. Nanoscale tunable reduction of graphene oxide for graphene electronics. *Science* **328**, 1373-1376 (2010).
232. Erickson, K. et al. Determination of the local chemical structure of graphene oxide and reduced graphene oxide. *Adv. Mater.* **22**, 4467-4472 (2010).
233. Choucair, M., Thordarson, P. & Stride, J.A. Gram-scale production of graphene based on solvothermal synthesis and sonication. *Nat. Nano* **4**, 30-33 (2009).
234. Hernandez, Y. et al. High-yield production of graphene by liquid-phase exfoliation of graphite. *Nat. Nano* **3**, 563-568 (2008).

235. Wei, N., Lv, C. & Xu, Z. Wetting of graphene oxide: A molecular dynamics study. *Langmuir* **30**, 3572-3578 (2014).
236. Kim, J.M., Kim, T., Kim, J., Kim, M.H. & Ahn, H.S. Effect of a graphene oxide coating layer on critical heat flux enhancement under pool boiling. *Int. J. Heat Mass Transf.* **77**, 919-927 (2014).
237. Zhang, L., Fan, L., Yu, Z. & Cen, K. An experimental investigation of transient pool boiling of aqueous nanofluids with graphene oxide nanosheets as characterized by the quenching method. *Int. J. Heat Mass Transf.* **73**, 410-414 (2014).
238. Lee, S.W., Kim, K.M. & Bang, I.C. Study on flow boiling critical heat flux enhancement of graphene oxide/water nanofluid. *Int. J. Heat Mass Transf.* **65**, 348-356 (2013).
239. Zhang, L. et al. Enhanced critical heat flux during quenching of extremely dilute aqueous colloidal suspensions with graphene oxide nanosheets. *J. Heat Transf.* **135**, 054502-054502 (2013).
240. Ahn, H.S., Kim, J.M., Kaviani, M. & Kim, M.H. Pool boiling experiments in reduced graphene oxide colloids. Part i – boiling characteristics. *Int. J. Heat Mass Transf.* **74**, 501-512 (2014).
241. Ahn, H.S., Kim, J.M. & Kim, M.H. Experimental study of the effect of a reduced graphene oxide coating on critical heat flux enhancement. *Int. J. Heat Mass Transf.* **60**, 763-771 (2013).
242. Ahn, H.S., Kim, J.M., Kaviani, M. & Kim, M.H. Pool boiling experiments in reduced graphene oxide colloids part ii – behavior after the chf, and boiling hysteresis. *Int. J. Heat Mass Transf.* **78**, 224-231 (2014).
243. Ong, W.-J., Tan, L.-L., Chai, S.-P., Yong, S.-T. & Mohamed, A.R. Surface charge modification via protonation of graphitic carbon nitride (g-c₃n₄) for electrostatic self-assembly construction of 2d/2d reduced graphene oxide (rgo)/g-c₃n₄ nanostructures toward enhanced photocatalytic reduction of carbon dioxide to methane. *Nano Energy*.
244. Ong, W.-J., Tan, L.-L., Chai, S.-P. & Yong, S.-T. Graphene oxide as a structure-directing agent for the two-dimensional interface engineering of sandwich-like graphene-g-c₃n₄ hybrid nanostructures with enhanced visible-light photoreduction of co₂ to methane. *Chem. Commun.* **51**, 858-861 (2015).
245. Talyzin, A.V., Luzan, S.M., Szabó, T., Chernyshev, D. & Dmitriev, V. Temperature dependent structural breathing of hydrated graphite oxide in h₂o. *Carbon* **49**, 1894-1899 (2011).
246. Lerf, A. et al. Hydration behavior and dynamics of water molecules in graphite oxide. *J. Phys. Chem. Solids*. **67**, 1106-1110 (2006).
247. Luzan, S.M. & Talyzin, A.V. Hydration of graphite oxide in electrolyte and non-electrolyte solutions. *The Journal of Physical Chemistry C* **115**, 24611-24614 (2011).
248. Talyzin, A.V. et al. Colossal pressure-induced lattice expansion of graphite oxide in the presence of water. *Angewandte Chemie International Edition* **47**, 8268-8271 (2008).
249. Lee, Y. et al. Non-framework cation migration and irreversible pressure-induced hydration in a zeolite. *Nature* **420**, 485-489 (2002).
250. Nair, R.R., Wu, H.A., Jayaram, P.N., Grigorieva, I.V. & Geim, A.K. Unimpeded permeation of water through helium-leak-tight graphene-based membranes. *Science* **335**, 442-444 (2012).
251. Andrikopoulos, K.S. et al. The effect of thermal reduction on the water vapor permeation in graphene oxide membranes. *Adv. Mater. Inter.* **1**, 1400250 (2014).
252. Boukhvalov, D.W., Katsnelson, M.I. & Son, Y.-W. Origin of anomalous water permeation through graphene oxide membrane. *Nano Lett.* **13**, 3930-3935 (2013).
253. Talyzin, A.V., Hausmaninger, T., You, S. & Szabo, T. The structure of graphene oxide membranes in liquid water, ethanol and water-ethanol mixtures. *Nanoscale* **6**, 272-281 (2014).
254. Park, K., Noh, K.-J. & Lee, K.-S. Transport phenomena in the thin-film region of a micro-channel. *Int. J. Heat Mass Transf.* **46**, 2381-2388 (2003).

255. Wang, H., Garimella, S.V. & Murthy, J.Y. Characteristics of an evaporating thin film in a microchannel. *Int. J. Heat Mass Tranf.* **50**, 3933-3942 (2007).
256. Wang, H., Garimella, S.V. & Murthy, J.Y. An analytical solution for the total heat transfer in the thin-film region of an evaporating meniscus. *Int. J. Heat Mass Tranf.* **51**, 6317-6322 (2008).
257. Hong, S.-J., Li, Y.-F., Hsiao, M.-J., Sheng, Y.-J. & Tsao, H.-K. Anomalous wetting on a superhydrophobic graphite surface. *Appl. Phys. Lett.* **100**, 121601 (2012).
258. Rafiee, J., Rafiee, M.A., Yu, Z.-Z. & Koratkar, N. Superhydrophobic to superhydrophilic wetting control in graphene films. *Adv. Mater.* **22**, 2151-2154 (2010).
259. Ahn, H.S., Kim, J.M. & Kim, M.H. Experimental study of the effect of a reduced graphene oxide coating on critical heat flux enhancement. *Int. J. Heat Mass Tranf.* **60**, 763-771 (2013).
260. Wan, S., Pu, J., Zhang, X., Wang, L. & Xue, Q. The tunable wettability in multistimuli-responsive smart graphene surfaces. *Appl. Phys. Lett.* **102**, 011603 (2013).
261. Lau, K.K.S. et al. Superhydrophobic carbon nanotube forests. *Nano Lett.* **3**, 1701-1705 (2003).
262. Kempers, R., Robinson, A.J., Ewing, D. & Ching, C.Y. Characterization of evaporator and condenser thermal resistances of a screen mesh wicked heat pipe. *Int. J. Heat Mass Tranf.* **51**, 6039-6046 (2008).
263. Chol, S. Enhancing thermal conductivity of fluids with nanoparticles. *ASME-Publications-Fed* **231**, 99-106 (1995).
264. Das, S.K., Choi, S.U.S. & Patel, H.E. Heat transfer in nanofluids—a review. *Heat Transfer Eng* **27**, 3-19 (2006).
265. Saidur, R., Leong, K. & Mohammad, H. A review on applications and challenges of nanofluids. *Renew. Sust. Energy Rev.* **15**, 1646-1668 (2011).
266. Imura, H., Sasaguchi, K., Kozai, H. & Numata, S. Critical heat flux in a closed two-phase thermosyphon. *Int. J. Heat Mass Tranf.* **26**, 1181-1188 (1983).
267. Wasan, D.T. & Nikolov, A.D. Spreading of nanofluids on solids. *Nature* **423**, 156-159 (2003).
268. Holman, J.P. *Experimental methods for engineers*. Boston: McGraw-Hill, 2001.
269. Yoshimitsu, Z., Nakajima, A., Watanabe, T. & Hashimoto, K. Effects of surface structure on the hydrophobicity and sliding behavior of water droplets. *Langmuir* **18**, 5818-5822 (2002).
270. Blossey, R. Self-cleaning surfaces, virtual realities. *Nat. Mater.* **2**, 301-306 (2003).
271. Chakraborty, M., Ghosh, A. & DasGupta, S. Enhanced microcooling by electrically induced droplet oscillation. *RSC Adv.* **4**, 1074-1082 (2014).
272. Peterson, G. & Bage, B. Entrainment limitations in thermosyphons and heat pipes. *J. Energ. Resour.* **113**, 147-153 (1991).
273. Shatto, D., Besly, J. & Peterson, G. Visualization study of flooding and entrainment in a closed two-phase thermosyphon. *J. Thermophys. Heat Tr.* **11**, 579-581 (1997).
274. Baby, T.T. & Ramaprabhu, S. Experimental investigation of the thermal transport properties of a carbon nanohybrid dispersed nanofluid. *Nanoscale* **3**, 2208-2214 (2011).
275. Wang, F. et al. Surfactant-free ionic liquid-based nanofluids with remarkable thermal conductivity enhancement at very low loading of graphene. *Nanoscale Res. Lett.* **7**, 314 (2012).
276. Cicero, G., Grossman, J.C., Schwegler, E., Gygi, F. & Galli, G. Water confined in nanotubes and between graphene sheets: A first principle study. *J. Am. Chem. Soc.* **130**, 1871-1878 (2008).
277. Huang, H. et al. Ultrafast viscous water flow through nanostrand-channelled graphene oxide membranes. *Nat. Commun.* **4**, 2979 (2013).
278. Han, Y., Xu, Z. & Gao, C. Ultrathin graphene nanofiltration membrane for water purification. *Adv. Funct. Mater.* **23**, 3693-3700 (2013).
279. Zhu, J. et al. Pseudonegative thermal expansion and the state of water in graphene oxide layered assemblies. *ACS Nano* **6**, 8357-8365 (2012).

280. Tong, W.L., Tan, M.K., Chin, J.K., Ong, K.S. & Hung, Y.M. Coupled effects of hydrophobic layer and vibration on thermal efficiency of two-phase closed thermosyphons. *RSC Adv.* **5**, 10332-10340 (2015).
281. Ong, W.-J. et al. Synergistic effect of graphene as a co-catalyst for enhanced daylight-induced photocatalytic activity of $\text{Zn}_{0.5}\text{Cd}_{0.5}\text{S}$ synthesized via an improved one-pot co-precipitation-hydrothermal strategy. *RSC Adv.* **4**, 59676-59685 (2014).
282. Grab, T., Gross, U., Franzke, U. & Buschmann, M.H. Operation performance of thermosyphons employing titania and gold nanofluids. *Int. J. Therm. Sci.* **86**, 352-364 (2014).
283. Liu, Z.-H. & Li, Y.-Y. A new frontier of nanofluid research – application of nanofluids in heat pipes. *Int. J. Heat Mass Transf.* **55**, 6786-6797 (2012).
284. Zhang, W., Shen, R., Lu, K., Ji, A. & Cao, Z. Nanoparticle enhanced evaporation of liquids: A case study of silicone oil and water. *AIP Adv.* **2**, 042119 (2012).
285. Wei, N., Peng, X. & Xu, Z. Understanding water permeation in graphene oxide membranes. *ACS Appl. Mater. Inter.* **6**, 5877-5883 (2014).
286. Li, Q., Liu, C. & Fan, S. Thermal boundary resistances of carbon nanotubes in contact with metals and polymers. *Nano Lett.* **9**, 3805-3809 (2009).
287. Shen, B., Zhai, W. & Zheng, W. Ultrathin flexible graphene film: An excellent thermal conducting material with efficient emi shielding. *Adv. Funct. Mater.* **24**, 4542-4548 (2014).
288. Duchemin, L., Popinet, S., Josserand, C. & Zaleski, S. Jet formation in bubbles bursting at a free surface. *Physics of Fluids (1994-present)* **14**, 3000-3008 (2002).
289. Andrikopoulos, K.S. et al. The effect of thermal reduction on the water vapor permeation in graphene oxide membranes. *Adv. Mater. Inter.* **1**, 1-8 (2014).
290. Tong, W.L., Ong, W.-J., Chai, S.-P., Tan, M.K. & Mun Hung, Y. Enhanced evaporation strength through fast water permeation in graphene-oxide deposition. *Sci. Rep.* **5** (2015).
291. Forster, H.K. & Zuber, N. Dynamics of vapor bubbles and boiling heat transfer. *AIChE Journal* **1**, 531-535 (1955).
292. Ng, B.T., Hung, Y.M. & Tan, M.K. Suppression of the leidenfrost effect via low frequency vibrations. *Soft Matter* **11**, 775-784 (2015).
293. Kim, H.W. et al. Selective gas transport through few-layered graphene and graphene oxide membranes. *Science* **342**, 91-95 (2013).
294. Talbot, L., Cheng, R.K., Schefer, R.W. & Willis, D.R. Thermophoresis of particles in a heated boundary layer. *Journal of Fluid Mechanics* **101**, 737-758 (1980).
295. Würger, A. Leidenfrost gas ratchets driven by thermal creep. *Phys. Rev. Lett.* **107**, 164502 (2011).
296. Gu, W. et al. Graphene sheets from worm-like exfoliated graphite. *Journal of Materials Chemistry* **19**, 3367-3369 (2009).
297. Rafiee, J. et al. Wetting transparency of graphene. *Nat. Mater.* **11**, 217-222 (2012).
298. Wenzel, R.N. Resistance of solid surfaces to wetting by water. *Industrial & Engineering Chemistry* **28**, 988-994 (1936).
299. Hall, C. & Hoff, W.D. *Water transport in brick, stone and concrete*. Taylor & Francis, 2011.
300. Munson, B.R., Rothmayer, A.P. & Okiishi, T.H. *Fundamentals of fluid mechanics, 7th edition*. John Wiley & Sons, Incorporated, 2012.
301. Wei, N., Peng, X. & Xu, Z. Breakdown of fast water transport in graphene oxides. *Phys. Rev. E* **89**, 012113 (2014).
302. Loh, K.P., Bao, Q., Ang, P.K. & Yang, J. The chemistry of graphene. *Journal of Materials Chemistry* **20**, 2277-2289 (2010).
303. Nagata, Y., Usui, K. & Bonn, M. Molecular mechanism of water evaporation. *Phys. Rev. Lett.* **115**, 236102 (2015).
304. Peterson, G.P. & Ma, H.B. Temperature response of heat transport in a micro heat pipe. *J. Heat Transf.* **121**, 438-445 (1999).

Appendix A

Journal paper in RSC Advances

Tong, W.L., Tan, M.K., Chin, J.K., Ong, K.S. & Hung, Y.M. Coupled effects of hydrophobic layer and vibration on thermal efficiency of two-phase closed thermosyphons. *RSC Advances* 5, 10332-10340 (2015).

Cite this: *RSC Adv.*, 2015, 5, 10332

Coupled effects of hydrophobic layer and vibration on thermal efficiency of two-phase closed thermosyphons

Wei Li Tong,^a Ming K. Tan,^a Jit Kai Chin,^b K. S. Ong^c and Yew Mun Hung^{*a}

Condensed droplets in a two-phase closed thermosyphon (TPCT) are subject to two competing forces: contact line pinning force between the droplet and the wall of the TPCT and the body force due to gravity. Either reducing the contact line pinning force or increasing the body force can lead to significant enhancement in the heat transport capability. This study aims to scrutinize the coupled effects of hydrophobic surface coating at the condenser wall and high-acceleration induced vibration on the thermal efficiency of a TPCT. We explore an approach to reduce the contact line pinning force by applying a thin layer of hydrophobic coating, which also facilitates dropwise condensation to further increase the heat transport capability. The body force of the condensed droplets can be increased by introducing a low-frequency ($f \sim 10^2$ Hz) high-acceleration ($\xi \sim 10^3 \text{ m s}^{-2}$) vibration. The formation of elongated liquid jets and entrainment of droplets induced by the high-acceleration vibration counteracts the enhancing effect from the increased body force of condensed droplets. Nanofluid with distinguished thermo-physical properties is charged to the TPCT to further enhance the thermal efficiency. By incorporating the coupled effects of hydrophobic layer and vibration, we can obtain a maximum augmentation in the heat transfer coefficient exceeding 47.7%. The factors contributing to the enhancement of thermal efficiency of a TPCT are identified and the underlying physical significance of the coupled effects is delineated.

Received 15th November 2014
Accepted 5th January 2015

DOI: 10.1039/c4ra14589e

www.rsc.org/advances

Introduction

Since its inception in the early twentieth century, two-phase closed thermosyphon (TPCT) has been employed extensively in cooling or heating related applications due to its effective heat transport capability, passive operation, and, also its simplicity in design and operation.¹ This two-phase heat transfer device offers significant advantages over other cooling devices, providing an economical yet reliable solution to the demanding heat removal challenges in thermal management. Typical terrestrial applications of TPCT range from the cooling of automobile engines, heat exchanger of solar heating system and industrial refrigeration system to electronics cooling for computer processors. Essentially, a basic TPCT consists of a tube filled with a working fluid in low-pressure (vacuum) condition to reduce saturation temperature. The tube is divided into three sections: evaporator, adiabatic section, and condenser. It relies on the phase-change processes, namely

evaporation and condensation, and the circulation of working fluid to function as heat transfer equipment. The heat applied to the evaporator section diffuses toward the liquid-vapor interface where it is taken up as the latent heat of evaporation by the liquid phase. The resultant vapor flows through the adiabatic section toward the condenser section, where the vapor condenses and the heat is dissipated to the surroundings. The thermal efficiency of a TCPT is governed by several pertinent parameters such as the fluid properties and the filling ratio of the working fluid,^{2,3} evaporator to condenser length ratio,⁴ inclination angle,⁵ operating limitations⁶ and the structure geometry.⁷ On the other hand, the maximum heat transport capacity of a thermosyphon can be limited by a number of operating limitations such as dry-out limit, burn-out or boiling limit, sonic limit and entrainment limit.^{8–10}

Condensation occurs at the saturation temperature when the vapor comes into contact with a cool surface at the condenser section where the condensate is formed. The latent heat of vaporization is released through the condenser wall surface. Depending on the condition of the surface, condensation may occur either in filmwise or dropwise mode. Film condensation primarily takes place on clean and uncontaminated surfaces while dropwise condensation materializes on non-wettable surfaces.¹¹ Dropwise condensation is superior to film condensation as the heat transfer rate of the former is more than an

^aSchool of Engineering, Monash University, 46150 Bandar Sunway, Malaysia. E-mail: hung.yew.mun@monash.edu^bFaculty of Engineering, University of Nottingham Malaysia Campus, Jalan Broga, 43500 Semenyih, Selangor, Malaysia^cFaculty of Engineering and Green Technology, Universiti Tunku Abdul Rahman, 31900 Kampar, Perak, Malaysia

order of magnitude larger than that of the latter.^{11–13} The condensation in TPCT is a typical example of film condensation where thick liquid condensate layers cover the surface, incurring a larger thermal resistance to heat transfer between the vapor and the surface.^{4,14} It is a common practice to utilize non-wettable (hydrophobic) surface coating with low surface energy to promote dropwise condensation. A multistage process is involved in the mechanism of dropwise condensation which includes nucleation of initial droplet, droplet growth, droplets coalesce, departure of droplet and coalesce of more droplets as the droplet sweeps downward.¹⁵ The enhancement of surface refreshment rate and droplet removal stimulates continuous condensation and consequently augments both the heat and mass transfer coefficients.¹⁶ Therefore, it is desirable to achieve dropwise condensation on the condenser surface of a TPCT for thermal efficiency enhancement.

The sustained evaporation of liquid in a TPCT is replenished by the circulation of condensate from the condenser section. A deficient circulation rate induces the occurrence of flooding at the condenser section, impeding the performance of TPCT. The flooding phenomenon in TPCT has been extensively investigated.^{17–19} Major factors such as heat input, thermo-physical properties of the vapor, vapor velocity and the critical aspect ratio (defined as the radius over length) incur adverse effect on the circulation of the condensates.^{18,19} Under high evaporation rate, extreme vapor velocity, and small critical aspect ratio, the countercurrent interfacial shear acting on the condensate surface prevents the circulation back to the evaporator. As a result, accumulation of condensate in the condenser greatly reduces the condensation heat transfer. The evaporator section is subsequently depleted with working fluid. Thus, circulation of the condensate is vitally important in the heat transfer mechanism of TPCTs.

As the condensed liquids accumulate and increase in size at the condenser, two dominant competing forces – body force F_b and contact force F_c – exert on these condensed liquids. The bond number, $Bo \equiv F_b/F_c$, is used to characterize this force balance. When the body force becomes larger than the contact line pinning, *i.e.*, $F_b > F_c$ or $Bo > 1$, the condensed liquids fall to the evaporator, completing a loop circulation from evaporator to condenser. There have been many attempts to enhance the circulation of the working fluid. For instance, wick structure can be inserted in the TPCT to assist the flow of condensed liquids *via* capillary force. Alternatively, the circulation rate can be improved by introducing centrifugal force,^{20,21} electrokinetic force,^{22,23} magnetic force,²⁴ or, vibration force.²⁵ Amongst these approaches, inducing vibration on the TPCT is considered the most convenient approach to integrate with the conventional TPCT design. By inducing vibrations, the body force of the condensed liquids is increased due to the increase in acceleration, *i.e.*, $F_b \propto m_t \ddot{\xi}$, where m_t is the mass of the fluids/droplets, and $\ddot{\xi}$ is the acceleration. However, very few prior studies dealt explicitly with the effect of vibration on the circulation effectiveness of a TPCT. Up to date, the only relevant study was focused on low-frequency vibrations ($f \sim 10^0$ Hz).²⁵ While improved performance was observed, the increase of body force exerted on the liquids was only in a very

small order of magnitude as a result of accelerations in the order of $\ddot{\xi} \sim 10^{-3} \text{ m s}^{-2}$.

This study aims to scrutinize the combined effects of hydrophobic surface coating at the condenser wall and high-acceleration induced vibration ($\ddot{\xi} \sim 10^3 \text{ m s}^{-2}$) on the thermal efficiency of a mini TPCT for electronic equipment cooling. As both approaches reduce the contact forces between the condensed liquids and the TPCT wall, the circulation effectiveness inside a TPCT is expected to be substantially enhanced. We propose a well-defined parameter for the falling rate of condensed droplets and the strength of evaporation to elucidate their relationship. To ensure these approaches are working on different working fluids, water and silver-oxide nanofluid are employed. The use of nanofluid, which is essentially a base fluid with nanoparticle suspension,²⁶ has been reported to be able to enhance the heat transfer characteristic of the conventional fluids.^{27,28} Nanofluid poses distinct thermal and hydrodynamic characteristics from the conventional fluid associated with its distinguished transport properties such as thermal conductivity, heat capacity, viscosity and surface tension. It is instructive to investigate the coupled effects of the hydrophobic surface at condenser wall and the high-acceleration induced vibration on the nanofluid judging from the prominent changes induced in its thermo-physical properties. In this study, imperative information is obtained from the exposition of the size and distribution of condensate droplets in the analysis of circulation effectiveness. The underlying physical significance of the coupled effects of hydrophobic layer and vibration on the thermal efficiency is outlined.

Experimental investigation

Preparation of hydrophobic coating

Teflon AF-1600 amorphous fluoroplastics which was purchased from DuPont, Inc. is used to form a hydrophobic layer in TPCT. The hydrophobic coating is deposited onto the inner section of a standard glass tube *via* spin-coating technique to assure the uniformity of the coating. A total of 10 millilitres of Teflon solution is gently flushed through the glass tube which is then spin coated at a constant speed of 1500 rpm for 30 minutes. Subsequently, the coated glass tube is heated in a furnace with a gradual increase in temperature to a maximum of 250 °C for 30 minutes. Finally, a uniform thin transparent layer of hydrophobic coating on the inner wall surface of TPCT is obtained.

Experimental setup

A schematic diagram of the experimental setup is illustrated in Fig. 1. The setup includes a mini TPCT, electrical heater, water cooling jacket, vibrator and measuring instruments. The TPCT is fabricated with a glass tube of inner diameter of $d_i = 13.5$ mm and length of $L = 110$ mm. The glass tube is sealed by using a rubber stopper connected with an access valve for charging of working fluid into the tube [see Fig. 1(a)]. To ensure the TPCT is airtight, epoxy is applied at all connections.

Two different types of working fluid are selected: distilled water and a nanofluid. For nanofluid preparation, silver-oxide

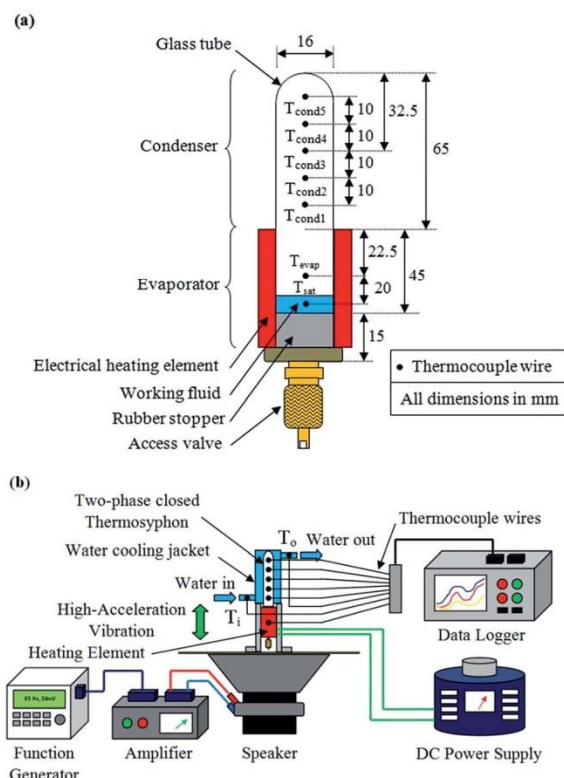


Fig. 1 (a) Schematic diagram of the basic components of a two-phase closed thermosyphon (TPCT). (b) Experimental setup for the thermal efficiency evaluation of TPCT.

(Ag₂O) nanoparticles (Sigma-Aldrich, Inc.) with an average particle size of 30 nm and volume fraction of 1% are dispersed in deionized water under mild ultrasonication treatment. The mixtures are ultrasonicated (20 kHz, 700 W) with an ultrasonic processor (Q700 Sonicator®, Qsonica, LLC.) for 5 hours with fluid temperature maintained below 80 °C to prevent evaporation. The TPCT is charged with 1 ml of working fluid, which is equivalent to 16.67% of volume fill ratio. It is a common practice to charge the TPCT with a volume fill ratio which is in the range of 13.5–20%.^{2,29} This range of fill ratio is considered as the optimal fill ratio in which case there is neither dryout nor flooding taking place in the TPCT. Once the working fluid is charged into the tube, the pressure within the tube is reduced using a vacuum pump, which is connected to the access valve, as shown in Fig. 1(a). The pressure in the tube prior to heating is maintained at 0.2 Pa for all tests. The evaporator section is heated with an electrical heating element, whereas the condenser section is cooled with a water cooling jacket, as depicted in Fig. 1(b).

The experiments are conducted in a controlled environment with a room temperature maintained at 26 °C with a fluctuation of ± 1.5 °C. Power input to the electrical heater is controlled by a DC power supply (EA-PSI 8160-04 LCD, EA Elektro-Automatik). Surface temperature on the TPCT is measured using six type-T thermocouple wires with an overall accuracy of 2%, which are

connected to a MIDI logger (GL820, Graphtec Co.), with an accuracy of 0.05%. Fig. 1(a) shows the locations of the thermocouple wires. For each test, the temperatures are recorded for 60 minutes, with an interval of two seconds between each recording. To investigate the effect of vibrations, the TPCT is positioned on a vibrating plate excited by a speaker (vibrator), which is connected to an amplifier and a function generator, as shown in Fig. 1(b). The TPCT is placed atop a thin plate attached to a speaker (TD 8", Motivity®), to provide lateral vibration to the system. The signal generated by the function generator (TG5011, Thurlby Thandar Instruments limited) is amplified by an amplifier (LZY-22, Mini-Circuits®) before it is transmitted to the speaker. The frequency of excitation is 63 Hz.

Thermal efficiency of TPCT

The thermal efficiency of a TPCT is governed by the circulation effectiveness and the strength of latent heat of evaporation of the working fluid. The thermal efficiency of a TPCT can be quantified with the performance indicators such as the effective thermal resistance R_{eff} and the average evaporator heat transfer coefficient \bar{h}_e . Lower thermal resistance indicates better overall thermal performance while larger value of evaporator heat transfer coefficient manifests higher strength of latent heat of evaporation. The overall thermal performance can be characterized using the effective thermal resistance which is obtained by evaluating the axial temperature drop, $\Delta T = T_{\text{evap}} - T_{\text{cond}}$, along the longitudinal direction of TPCT for a heat input. The effective thermal resistance is calculated as:

$$R_{\text{eff}} = \frac{T_{\text{evap}} - T_{\text{cond}}}{\dot{Q}_a} \quad (1)$$

where T_{evap} is the temperature at the evaporator, T_{cond} is the temperature at the condenser, and \dot{Q}_a is the heat transport rate of the TPCT. Notably, T_{cond} is taken here as the averaged temperatures measured across the condenser section. The heat transport rate, \dot{Q}_a , which is calculated based on the principle of energy conservation whereby the net heat transported across the TPCT is equivalent to the heat dissipated from the condenser section. The total convection heat transfer of the water flowing across the water jacket is determined as $\dot{Q}_a = \dot{m}c_p(T_o - T_i)$, where \dot{m} represents the mass flow rate of the water flow, c_p is the specific heat capacity of water. T_i and T_o denote the inlet and outlet water temperatures of the cooling jacket mounted onto the condenser section.

The average evaporator heat transfer coefficient, \bar{h}_e , is used to quantify the strength of evaporation, given by $\bar{h}_e = \dot{Q}_a / \pi d L_e (T_{\text{evap}} - T_{\text{sat}})$, where T_{sat} is the saturation temperature of the working fluid, d is the inner diameter of the TPCT and L_e is the axial length of the evaporator section. During the experiments, the heat input is kept at a constant value and the evaporator heat transfer coefficient augmentation ratio can be expressed as:

$$\eta = \frac{\bar{h}_e}{\bar{h}_{e,0}} = \frac{(T_{\text{evap},0} - T_{\text{sat},0})}{(T_{\text{evap}} - T_{\text{sat}})} \quad (2)$$

Paper

where $\bar{h}_{e,0}$ is the average evaporator heat transfer coefficient for the case of uncoated TPCT using water as working fluid. To scrutinize the heat transfer enhancement at the evaporator section, η is the relative comparison of the evaporator heat transfer coefficients by using the value of uncoated TPCT as the basis for comparison. The heat transfer is enhanced when η is greater than unity and *vice versa*.

Evaluation of static contact angle

The static contact angle θ_s between the liquid and the substrate under different conditions are measured using a standard goniometer (Model 590, Ramé-Hart Instrument Co.) under atmospheric pressure and a room temperature of 26 °C. Table 1 shows the results of the contact angle measurements under different conditions. For glass coated with a thin hydrophobic layer, the contact angle is slightly lower for nanofluid ($\theta_s \approx 118^\circ$) as compared to the distilled water ($\theta_s \approx 120^\circ$). With the addition of surfactant to the distilled water on the hydrophobic surface, the static contact angle decreases ($\theta_s \approx 73^\circ$). The reduction in static contact angle of the nanofluid was studied by Wasan and Nikolov.³⁰ It was found that the nanoparticles near the liquid-contact line tend to increase the spreading of the nanofluid, resulting in the decrease of the static contact angle.

Results and discussion

Effect of hydrophobic surface

Fig. 2 shows the plots of the effective thermal resistances R_{eff} as a function of heat transport rate, \dot{Q}_a , for three different contact forces between the working fluid and the TPCT wall: water on bare glass ($\theta_s \approx 24^\circ$), water added with surfactant on coated glass ($\theta_s \approx 73^\circ$), and, water on coated glass ($\theta_s \approx 120^\circ$), representing the cases for high, mid, and low contact force, respectively. In the cases of low and mid contact force, R_{eff} is lower compared to that of high contact force. At $\dot{Q}_a = 15.5$ W, for the cases of low and mid contact force, R_{eff} records a reduction of 16.9% and 11.4%, respectively. A smaller R_{eff} indicates a higher heat transport capability of the TPCT. The reduction in the R_{eff} can be attributed to the presence of hydrophobic coating that lowers the contact force F_c , which then facilitates the falling of condensed droplets back to the evaporator. It is observed that by reducing the contact force F_c between the condensed droplets and the wall of TPCT, the effective thermal resistance R_{eff} is

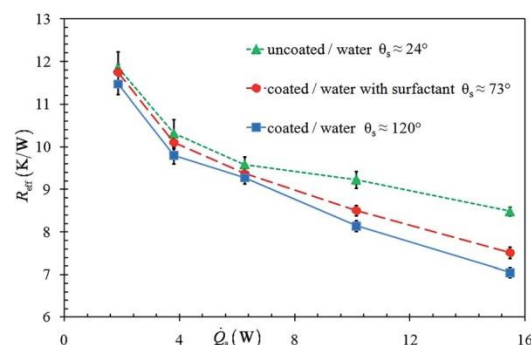







Fig. 2 Effective thermal resistance, R_{eff} , as a function of heat transport rate, \dot{Q}_a , for three different cases: water on uncoated glass ($\theta_s \approx 24^\circ$), water added with surfactant on coated glass ($\theta_s \approx 73^\circ$), and, water on coated glass ($\theta_s \approx 120^\circ$).

further reduced due to the enhanced circulation of the working fluid.

On the other hand, the strength of evaporation is observed to be indirectly affected by the contact force, as shown in Fig. 3, which depicts the evaporator heat transfer coefficient augmentation ratios η for two cases: water added with surfactant on coated glass ($\theta_s \approx 73^\circ$), and, water on coated glass ($\theta_s \approx 120^\circ$), using the case of water on bare glass ($\theta_s \approx 24^\circ$) as the baseline for comparison. For the range of heat transport rate under investigation, we can observe that the enhancement of heat transfer coefficient increases with the decrease in the contact force. For the case of smaller contact force (water on coated glass), the enhancement in the heat transfer coefficient can exceed 20.4% at high heat transport rate. It is shown that the enhancement in circulation effectiveness and strength of evaporation is inherently simultaneous.

The size and distribution of the droplets are important factors in governing the mechanism of condensation heat transfer in a TPCT. We shall, therefore, be concerned with the size and distribution of the droplets in the following. Fig. 4(a)

Table 1 Static contact angle measurement for two different working fluids: distilled water and nanofluid, on glass surfaces with and without the hydrophobic coating

				
Water on uncoated glass	Water with surfactant on coated glass	Water on coated glass	Nanofluid on uncoated glass	Nanofluid on coated glass
$\theta_s = 24^\circ$	$\theta_s = 73^\circ$	$\theta_s = 120^\circ$	$\theta_s = 40^\circ$	$\theta_s = 118^\circ$

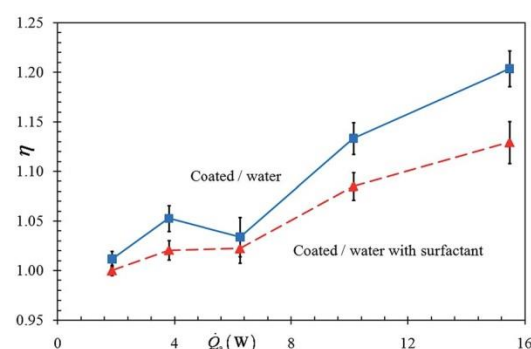


Fig. 3 Evaporator heat transfer coefficient augmentation ratio, η , as a function of heat transport rate, \dot{Q}_a , for two different cases: water added with surfactant on coated glass ($\theta_s \approx 73^\circ$) and water on coated glass ($\theta_s \approx 120^\circ$).

and (b) show the time-lapse images of the morphology of condensed droplets on the interior wall of the uncoated and coated TPCT with the hydrophobic layer, respectively. Evidently, the diameters of the condensed droplets on the coated glass tube are observed to be significantly smaller than those on the uncoated glass. We also note that dropwise condensation is prevalent in the former while film condensation occurs in the latter. As observed in Fig. 4(b) for dropwise condensation, when the droplet size increases to a diameter of 650 μm (as indicated with an arrow), the droplet starts to detach from the wall surface and move downwards coalescing with other droplets. The sliding speed increases as more droplets are combined. Subsequently, nucleation of new droplets can be observed as illustrated in the dashed circles. This shows that the surface refreshment rate (departure rate of condensed droplets on a hydrophobic surface) is high, allowing a continuous dropwise condensation to occur on the wall surface. On the contrary, Fig. 4(a) illustrates the droplet growth cycle of an uncoated glass surface. The departure diameter is found to be larger than that of the hydrophobic surface. The largest droplet diameter is measured to be more than 2500 μm with no sign of droplet departure. It has been shown that the typical droplet departure diameter on an uncoated glass surface under film condensation is between 2 mm to 3 mm.¹² Continuous coalescence of neighbouring droplets forms non-circular droplets, indicating a weak three-phase contact line with a large contact angle hysteresis.^{31,32} The large droplets on the wall surface form a thermal barrier which inhibits the condensation of the vapour, and hence reducing the overall condensing heat transfer coefficient. Furthermore, large droplets which occupy the surface reduce the area for vapour condensation, hindering the droplet growth rate in a TPCT.

To have a detailed view on the size and distribution of droplets on the mechanism of condensation, we quantify the average diameter range and the number of droplets condensing on the TPCT wall surface. SigmaScan® Pro (Systat Software, CA, USA) is used for image processing and analysis of droplet distribution and droplet size. Fig. 5(a) and (b) depict the average droplet count, N , as a function of droplet diameter, D , for the uncoated and coated surfaces, respectively. The diameters of the condensed droplets on the uncoated glass tube (100 μm –2500 μm) are observed to be significantly larger than those on the coated glass (50 μm –650 μm).

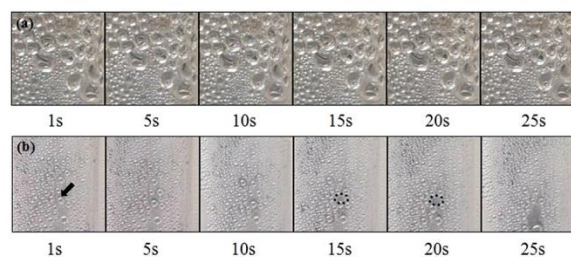


Fig. 4 Time-lapse images of the morphology of condensed droplets on the interior wall of the (a) uncoated TPCT, and, (b) coated TPCT.

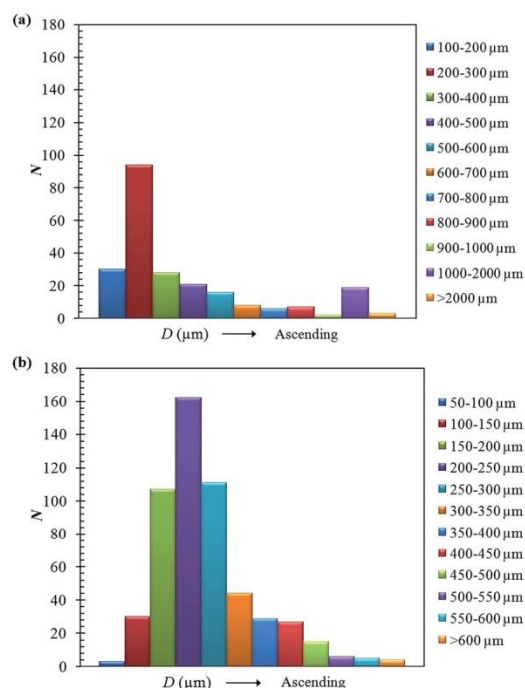


Fig. 5 Average droplet count, N , as a function of droplet diameter, D , for the (a) uncoated and (b) coated surfaces.

To scrutinize the droplet distribution over the entire wall surface of the condenser, we use the total surface area of condenser as the basis for comparison. A relative comparison parameter between the covering surface area of droplet, A_d , and the total surface area, A_t , is quantified as $\delta = A_d/A_t$. The δ value is evaluated by analyzing the marked surface area covered by the droplets on the condenser wall using SigmaScan® Pro image processing software. At a fixed heat transport rate of 15.5 W, high definition images are taken continuously for every minute during the steady state of the experiments. To ensure the accuracy of the measurement of randomly distributed droplets on the surface, a total of 24 images from 3 independent sets of experiment are analyzed. The surface area covered by the droplets, A_d , on a specific region on the condenser wall with an area of $A_t = 10 \text{ mm} \times 10 \text{ mm}$, is marked. By setting a reference length scale, SigmaScan® Pro is used to measure the total surface area covered by the droplets. The δ value is calculated based on the statistical mean of a sample size of 24. It is found that at an instant of steady operation of a TPCT, we measure $\delta = 33.7\%$ for the coated hydrophobic surface and $\delta = 67.7\%$ for the uncoated surface. This attests the fact that the hydrophobic surface which repels water molecules yields higher circulation rate for the condensate from the condenser to the evaporator. In addition, the hydrophobic surface provides larger liquid-free and sub-cooled surface for nucleation of new droplets and hence the condensation rate is enhanced.

As the condensate liquids accumulate and increase in size at the condenser, two dominant competing forces - body force F_b

and the contact line pinning force F_c exert on these condensed liquids. The shear force at the liquid–vapor interface F_s is assumed to be negligible. This point has been justified by comparing the order of magnitude of the interfacial shear force and that of the body force in an independent set of experiments. By virtue of low relative velocities associated with the vapor flow and the droplet motion, it is found that the body force F_b is at least 10^4 times of the shear force F_s . Therefore, together with the assumption of a uniform vapor temperature, the interfacial shear force acting on the surface of the liquid droplet can be neglected. To characterize the two dominant forces acting on a droplet, the bond number is used and it is given by $Bo \equiv \rho_l g \ell^2 / \gamma(\cos \theta_A - \cos \theta_R) \equiv F_b / F_c$, where ρ_l is the liquid density, g is the gravitational acceleration, ℓ is the characteristic length defined as the radius of droplet, γ is the coefficient of interfacial surface tension, θ_A is the advancing contact angle and θ_R is the receding contact angle of the droplet. When the body force becomes larger than the contact line pinning force, *i.e.*, $F_b > F_c$ or $Bo > 1$, the condensed liquids fall to the evaporator, completing a loop circulation from evaporator to condenser. The contact line pinning force increases with the decrease of contact angle. The decrease in static contact angle greatly affects the dynamic behavior of the droplet. The contact line of the three phases (solid, liquid, and vapor) deteriorates with the decrease of the static contact angle, increasing the contact area of the droplet.³¹ As a result, the contact line can be easily deformed, resulting in an increase of contact angle hysteresis. Contact angle hysteresis is defined as the difference between the advancing and the receding angles. High contact angle hysteresis impedes the movement of the droplet and higher external force is required for the droplet to overcome the pinning force F_c . Hence, for the droplet to depart, accumulation in size is required to increase the body force F_b . As noted earlier that $Bo \equiv F_b / F_c$ and the liquids start to fall back to the evaporator when $F_b > F_c$. Therefore, by reducing the F_c , the condensed droplets begin to fall back to the evaporator at a smaller body force. Since the body force is directly proportional to the volume of the condensed liquid, *i.e.*, $F_b = mg = \rho Vg$, for the TPCT coated with the hydrophobic layer, the diameter of the condensed droplets should be much smaller than those without coating. This is consistent with the experimental images shown in Fig. 4 for condensed droplets on the interior wall of the TPCT with and without the hydrophobic coating. The diameters of the condensed droplets on the uncoated glass tube are observed to be significantly larger (100 μm –2500 μm) than those on the coated glass (50 μm –650 μm), inferring that the former is film condensation whereas the latter is dropwise condensation. For film condensation, a thick layer of condensed liquid covers the wall surface, lowering the heat transfer rate. On the other hand, dropwise condensation allows for more continuous condensation to occur on the wall surface. This in turn results in high surface refreshment rate, *i.e.* the departure rate of condensed droplets, thereby improving the resultant heat transfer rate. It has been shown that the heat transfer coefficient for dropwise condensation is an order of magnitude higher than that for film condensation.¹² Therefore, the hydrophobic surface not only improves the circulation by increasing the falling rate of

condensed droplets, it also facilitates the formation of dropwise condensation, which further improves the heat transport capability of the TPCT.

To elucidate the relationship of the falling rate of condensed droplets and the strength of evaporation, in the uncoated and coated TPCT, we recast the experimental data in terms of a new dimensionless number

$$\Psi \equiv \frac{Bo}{Ja} \equiv \frac{\rho_l g \ell^2}{\gamma(\cos \theta_A - \cos \theta_R)} \frac{h_{fg}}{c_p(T_{\text{evap}} - T_{\text{sat}})} \quad (3)$$

where Ja is the Jakob number, defined as¹¹ $Ja = c_p(T_{\text{evap}} - T_{\text{sat}})/h_{fg}$, with h_{fg} being the latent heat of vaporization and c_p the specific heat capacity. In the context of present work, a larger Jakob number represents the case of higher sensible heat absorbed from the evaporator and hence a more intense evaporation rate, whereas, a larger Bond number represents the case of higher falling rate of condensed droplets to the evaporator. The plots of Ψ as a function of heat transport rate \dot{Q}_a for uncoated and coated TPCTs are shown in Fig. 6. At each fixed heat transport rate, the Ψ for the coated (hydrophobic) TPCT is higher than that for the uncoated (hydrophilic) TPCT, indicating the falling rate of condensed droplets in the coated TPCT is higher than that in the uncoated TPCT. On the other hand, as the heat transport rate is proportional to the heat input power of the heater, for both uncoated and coated TPCT, the Ψ reduces with the increase of the heat input power due to the increase in the evaporation rate (higher Ja).

Coupled effects of hydrophobic surface and high-acceleration vibration

As discussed earlier, to further increase the circulation rate, we can either reduce the contact force F_c by introducing a thin layer of hydrophobic coating (Fig. 2), or, increase the body force F_b by inducing vibrations. Fig. 7 shows the experimental results of the effect of vibrations on the effective thermal resistance. The results show that for all cases, the effective thermal resistance R_{eff} is reduced once the vibration is introduced. The reduction

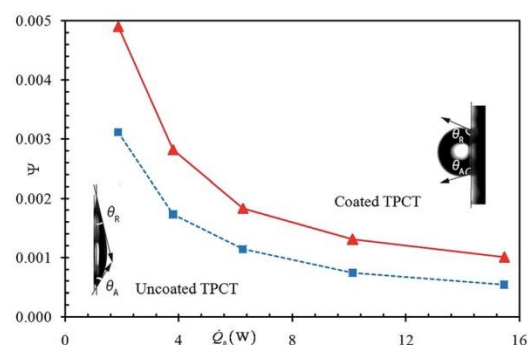


Fig. 6 Relation between the dimensionless number and the heat transport rate for coated (hydrophobic) and uncoated (hydrophilic) TPCTs. The insets show the estimation of the advancing angle and receding angle for a sessile droplet on hydrophobic and hydrophilic substrates.

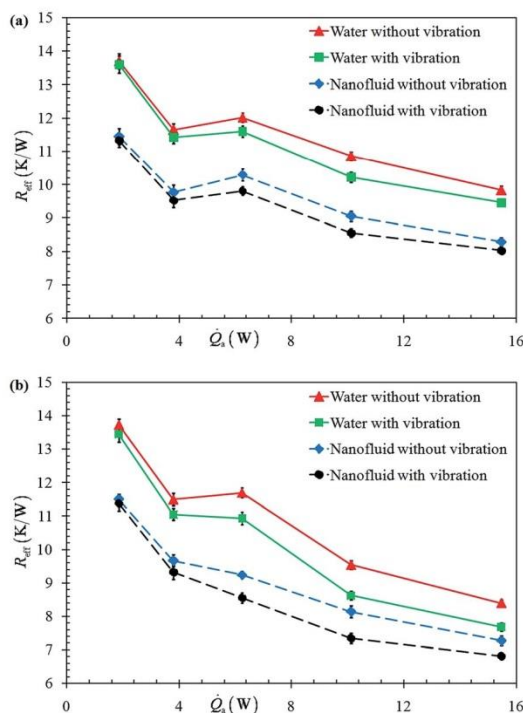


Fig. 7 Effect of vibration on the effective thermal resistance of (a) uncoated TPCT and (b) coated TPCT using water and nanofluid as working fluid.

in R_{eff} is within the range of 1.9–5.8% for uncoated hydrophilic TPCT, as depicted in Fig. 7(a). Interestingly, for coated hydrophobic TPCT shown in Fig. 7(b), the reduction in R_{eff} which ranges from 5.2% to 21.9% is almost triple to that of the uncoated TPCT. The reduction in R_{eff} is attributed to the increase in the rate of falling of condensed droplets to the evaporator. When the TPCT tube is subjected to vibratory force, the body force increases due to the additional acceleration generated by the vibrating plate, *i.e.*, $F_b \approx m(g + \ddot{\xi})$. For a 63 Hz excitation with surface displacement in the order of 10^{-3} m, the estimated surface acceleration is in the order of $\ddot{\xi} \sim 10^3 \text{ m s}^{-2}$, which is two orders of magnitudes higher than the gravitational acceleration $g \sim 10^1 \text{ m s}^{-2}$, therefore the falling rate of droplets is enhanced. As these droplets slide along the condenser wall, more liquid-free sub-cooled surfaces are available for the nucleation of new condensate droplets. In light of its distinguished thermophysical properties, Ag_2O -water nanofluid is also used as a working fluid in the uncoated and coated TPCTs. The results demonstrate a similar trend of improvement, as shown in Fig. 7(a) and (b). Under similar experiment conditions (uncoated with vibration), the TPCT filled with nanofluid as working fluid has lower thermal resistance as compared to the TPCT filled with water; the reduction in thermal resistance is in the range of 18.3–21.2%.

The effect of vibration on the strength of evaporation is investigated and the evaporator heat transfer coefficient augmentation ratios are evaluated using eqn (2) and plotted as a

function of heat transport rate for both uncoated and coated TPCTs in Fig. 8. As discussed earlier, the contact force between the droplets and the condenser wall is associated with the circulation effectiveness of condensate. We observe that the effect of vibration on the strength of evaporation is also prevalent although it is not dominant. This observation is congruous with a recent study investigating the effect of electrically induced droplet oscillation on evaporation.³³ However, interestingly, it is observed that the suspension of nanoparticles significantly augments the heat transfer coefficient augmentation ratio which characterizes the strength of evaporation, for both cases without and with vibration. The increases in heat transfer coefficient are observed to exceed 35.2% and 47.7% for the cases without and with vibration, respectively, in a coated TPCT, as depicted in Fig. 8(b). This augmentation is attributed to the deposition of nanoparticles on the evaporator surface which significantly enhances the nucleate boiling mechanism and surface wettability.^{34–36} The effect of deposition of nanoparticles on the performance enhancement is worth further investigation.

Despite these favorable factors enhancing the circulation of the condensate, the maximum reductions in thermal resistance R_{eff} are only about 12.1% and 14.3% for water charged TPCT and nanofluid charged TPCT, respectively. It is evident that the effect of vibration on the improvement of overall circulation rate is not as significant as predicted. To investigate the

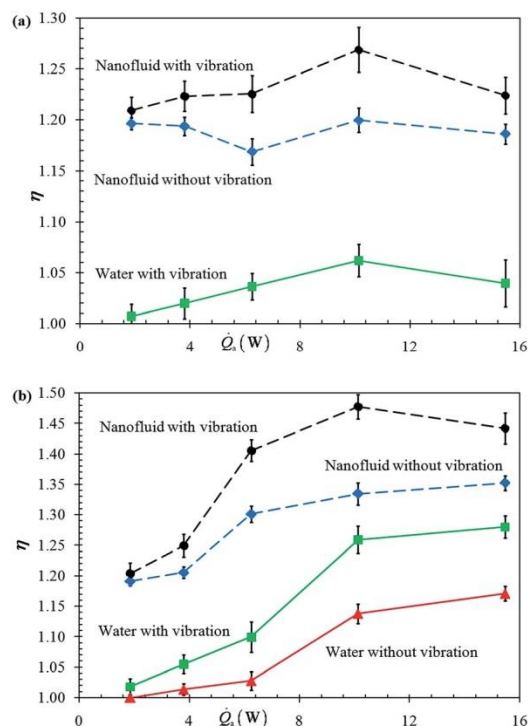


Fig. 8 Effect of vibration on the evaporator heat transfer coefficient augmentation ratios of (a) uncoated TPCT and (b) coated TPCT using water and nanofluid as working fluid.

underlying physical justification of the marginal increase in the circulation effectiveness rendered by the high-acceleration vibration, a digital high-speed camera (Phantom Miro M 310, Vision Research™) coupled with a long-distance microscope is employed to record the high-speed events of transient phenomena in the TPCT with particular attention paid to the liquid–vapor interfacial structure. It is observed that in addition to higher body force experienced by the condensed droplets at the evaporator, the high acceleration induced by the vibrator generates elongated liquid jets which subsequently break up into multiple droplets, as illustrated in Fig. 9. The diameter of these droplets is between 2 to 3 mm. Based on the images recorded at 1000 frames per second, the estimated jet Weber number We_j is approximately 100, indicating a strong inertial force dominating the jet motion. The jet Weber number is defined as $We_j \equiv \rho U_j^2 R_j / \gamma$, where R_j is the radius of the jet, and U_j is the velocity of the jet. The excitation from the vibration induces large surface waves at the liquid–vapor interface at the evaporator section, creating instabilities in the liquid flow. This leads to the formation of elongated liquid jets which eventually break up into finer droplets. The droplets formed from the breakup of the elongated jets are observed to be entrained in the vapor flow and returned to the condenser. This entrainment of liquid droplets induced by the high-acceleration vibration can be analogous to the typical entrainment phenomenon caused by high shear forces developed at the liquid–vapor interface due to the high relative velocity between the counter-current liquid and vapor flows when the axial heat flux imposed on a TPCT is substantially high.^{8,37,38} The latter which is associated with the entrainment limit in the operation of a TPCT provokes a depletion of liquid supply to the evaporator, incurring a local dry-out at the evaporator and flooding at the condenser if the entrainment is sufficiently intense.⁸ When the entrained droplets deposit on the condenser wall surface, the thermal resistance increases and the condensation heat transfer deteriorates. Consequently, the axial heat flux and the performance of the TPCT decline. In the present study, the vibration-induced entrainment of droplets acts in a similar manner in returning the liquid back to the condenser, impeding the

circulation rate of the condensate. Up to this point, the marginal increase in the circulation effectiveness rendered by the high-acceleration vibration can be reasoned out. The high-acceleration vibration yields two opposing effects on the liquid circulation effectiveness in a TPCT. The increase in the rate of falling of condensed droplets to the evaporator is apparent and explicit while the entrainment of droplets back to the condenser is a subtle phenomenon. The former is viable in enhancing the circulation effectiveness while the latter generates an adverse effect that counteracts with the enhancing effect of the increased falling rate of condensed droplets, inhibiting the circulation rate. The observation of liquid jets and entrained droplets provides valuable experimental insights into the physical process of the liquid–vapor interaction induced by the high-acceleration vibration in a TPCT.

Conclusions

We have studied the effects of contact force and vibration on the thermal efficiency of TPCTs. By comparing the experimental results for uncoated (hydrophilic) glass tube and coated (hydrophobic) glass tube, the reduction in the effective thermal resistance R_{eff} , which is used to characterize the overall thermal performance, is between 3.2% and 16.9%. This reduction is primarily due to the increase in the falling rate of the condensed droplets and the formation of dropwise condensation. The strength of evaporation which is characterized by the evaporator heat transfer coefficient augmentation ratio is observed to be indirectly affected by the contact force. The enhancement in the circulation effectiveness and the strength of evaporation is inherently simultaneous. The high-acceleration vibration ($\xi \sim 10^3 \text{ m s}^{-2}$) on the TPCT also reduces the R_{eff} ; the reduction is between 1.9% and 5.8%. By combining both the effects of contact force and vibration, the total reduction of R_{eff} is between 5.2% and 21.9%. For nanofluid, the effects of contact force and vibration on the reduction in R_{eff} are similar. However, it is observed that the utilization of nanoparticles substantially increases the heat transfer coefficient augmentation ratios, exceeding 35.2% and 47.7% for the cases without and with vibration, respectively, in a coated TPCT. Interestingly, the observation of elongated liquid jets and entrained droplets from the liquid–vapor interface induced by the high-acceleration vibration delineates the underlying physical justification of the marginal increase in the circulation effectiveness. This observation provides valuable experimental insights into the physical process of the liquid–vapor interaction phenomena induced by the high-acceleration vibration in a TPCT. To eliminate the entrainment of droplets back to the condenser which impedes the circulation rate of the condensate, high-frequency and low-acceleration vibrations ($f > 100 \text{ kHz}$) can be employed in the future investigation.

Acknowledgements

The authors would like to thank the financial support by Green Electronics, Advanced Engineering Platform, Monash University Malaysia.

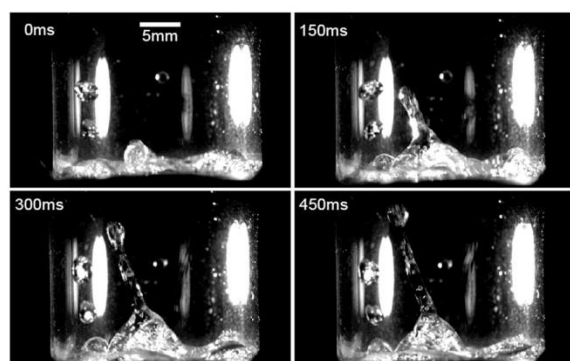


Fig. 9 Elongated liquid jet generated at the evaporator due to the strong vibration. The jet breaks up into multiple finer droplets which are entrained in the vapor flow.

Notes and references

- 1 G. S. H. Lock, *The tubular thermosyphon – variation on a theme*, Oxford University Press, 1992.
- 2 B. Jiao, L. M. Qiu, X. B. Zhang and Y. Zhang, *Appl. Therm. Eng.*, 2008, **28**, 1417–1426.
- 3 H. Jouhara and A. J. Robinson, *Appl. Therm. Eng.*, 2010, **30**, 201–211.
- 4 S. H. Noie, *Appl. Therm. Eng.*, 2005, **25**, 495–506.
- 5 H. Jouhara and R. Meskimon, *Energy*, 2010, **35**, 4592–4599.
- 6 M. S. El-Genk and H. H. Saber, *Int. J. Heat Mass Transfer*, 1999, **42**, 889–903.
- 7 H. M. S. Hussein, H. H. El-Ghetany and S. A. Nada, *Energy Convers. Manage.*, 2006, **47**, 1539–1549.
- 8 H. Nguyen-Chi and M. Groll, *J. Heat Recovery Syst.*, 1981, **1**, 275–286.
- 9 D. Reay and P. Kew, *Heatpipes, Theory, Design and Applications*, Butterworth-Heinemann, Burlington, 5th edn, 2006.
- 10 G. P. Peterson, *An Introduction to Heat Pipes Modeling, Testing and Applications*, John Wiley & Sons Inc., New York, USA, 1994.
- 11 F. P. Incropera, A. S. Lavine, T. L. Bergman and D. P. DeWitt, *Principles of heat and mass transfer*, Wiley, 2013.
- 12 X. Chen, J. Wu, R. Ma, M. Hua, N. Koratkar, S. Yao and Z. Wang, *Adv. Funct. Mater.*, 2011, **21**, 4617–4623.
- 13 N. A. Patankar, *Soft Matter*, 2010, **6**, 1613–1620.
- 14 R. Kempers, A. J. Robinson, D. Ewing and C. Y. Ching, *Int. J. Heat Mass Transfer*, 2008, **51**, 6039–6046.
- 15 S. Yongji, X. Dunqi, L. Jifang and T. Siexong, *Int. J. Heat Mass Transfer*, 1991, **34**, 2827–2831.
- 16 S. Lee, H. K. Yoon, K. J. Kim, S. Kim, M. Kennedy and B. J. Zhang, *Int. J. Heat Mass Transfer*, 2013, **60**, 664–671.
- 17 S. J. Chen, J. G. Reed and C. L. Tien, *Int. J. Heat Mass Transfer*, 1984, **27**, 1587–1594.
- 18 U. Gross, *Int. J. Heat Mass Transfer*, 1992, **35**, 279–294.
- 19 Y. Pan, *Int. Commun. Heat Mass Transfer*, 2001, **28**, 311–322.
- 20 N. Waowaew, P. Terdtoon, S. Maezawa, P. Kamonpet and W. Klongpanich, *Appl. Therm. Eng.*, 2003, **23**, 1019–1032.
- 21 S. W. Chang and C. Y. Lin, *Int. J. Heat Mass Transfer*, 2013, **62**, 40–54.
- 22 S. Wangnipparnto, J. Tiansuwan, T. Kiatsiriroat and C. C. Wang, *Energy Convers. Manage.*, 2003, **44**, 1163–1175.
- 23 S. Z. Heris, F. Mohammadpur and A. Shakouri, *Mater. Res. Bull.*, 2014, **53**, 21–27.
- 24 E. Fornalik, P. Filar, T. Tagawa, H. Ozoe and J. S. Szmyd, *Int. J. Heat Mass Transfer*, 2006, **49**, 2642–2651.
- 25 H. Z. Abou-Ziyan, A. Helali, M. Fatouh and M. M. A. El-Nasr, *Appl. Therm. Eng.*, 2001, **21**, 813–830.
- 26 S. Chol, *Am. Soc. Mech. Eng.*, 1995, **231**, 99–106.
- 27 S. K. Das, S. U. S. Choi and H. E. Patel, *Heat Transfer Eng.*, 2006, **27**, 3–19.
- 28 R. Saidur, K. Leong and H. Mohammad, *Renewable Sustainable Energy Rev.*, 2011, **15**, 1646–1668.
- 29 H. Imura, K. Sasaguchi, H. Kozai and S. Numata, *Int. J. Heat Mass Transfer*, 1983, **26**, 1181–1188.
- 30 D. T. Wasan and A. D. Nikolov, *Nature*, 2003, **423**, 156–159.
- 31 Z. Yoshimitsu, A. Nakajima, T. Watanabe and K. Hashimoto, *Langmuir*, 2002, **18**, 5818–5822.
- 32 R. Blossey, *Nat. Mater.*, 2003, **2**, 301–306.
- 33 M. Chakraborty, A. Ghosh and S. DasGupta, *RSC Adv.*, 2014, **4**, 1074–1082.
- 34 V. Trisaksri and S. Wongwises, *Renewable Sustainable Energy Rev.*, 2007, **11**, 512–523.
- 35 S. M. You, J. H. Kim and K. H. Kim, *Appl. Phys. Lett.*, 2003, **83**, 3374–3376.
- 36 S. J. Kim, I. C. Bang, J. Buongiorno and L. W. Hu, *Appl. Phys. Lett.*, 2006, **89**, 153107.
- 37 G. Peterson and B. Bage, *J. Energy Resour. Technol.*, 1991, **113**, 147–153.
- 38 D. Shatto, J. Besly and G. Peterson, *J. Thermophys. Heat Transfer*, 1997, **11**, 579–581.

Appendix B

Journal paper in Scientific Reports

Tong, W.L., Ong, W.-J., Chai, S.-P., Tan, M.K. & Hung, Y.M. Enhanced evaporation strength through fast water permeation in graphene-oxide deposition. *Scientific Reports* 5, 11896 (2015).

SCIENTIFIC REPORTS

OPEN

Enhanced Evaporation Strength through Fast Water Permeation in Graphene-Oxide Deposition

Wei Li Tong¹, Wee-Jun Ong², Siang-Piao Chai², Ming K. Tan¹ & Yew Mun Hung¹

Received: 19 March 2015

Accepted: 03 June 2015

Published: 23 June 2015

The unique characteristic of fast water permeation in laminated graphene oxide (GO) sheets has facilitated the development of ultrathin and ultrafast nanofiltration membranes. Here we report the application of fast water permeation property of immersed GO deposition for enhancing the performance of a GO/water nanofluid charged two-phase closed thermosyphon (TPCT). By benchmarking its performance against a silver oxide/water nanofluid charged TPCT, the enhancement of evaporation strength is found to be essentially attributed to the fast water permeation property of GO deposition instead of the enhanced surface wettability of the deposited layer. The expansion of interlayer distance between the graphitic planes of GO deposited layer enables intercalation of bilayer water for fast water permeation. The capillary force attributed to the frictionless interaction between the atomically smooth, hydrophobic carbon structures and the well-ordered hydrogen bonds of water molecules is sufficiently strong to overcome the gravitational force. As a result, a thin water film is formed on the GO deposited layers, inducing filmwise evaporation which is more effective than its interfacial counterpart, appreciably enhanced the overall performance of TPCT. This study paves the way for a promising start of employing the fast water permeation property of GO in thermal applications.

Since the early discovery of graphene in 2004¹, it has attracted substantial interest due to its unique electrical, physical and thermal properties. The honeycomb lattice arrangement of the carbon atoms with a single atomic layer thick structure enables the superior thermal conducting characteristics of graphene. The thermal conductivity of a single layer graphene is reported ranging from 4840 W/m·K to 5300 W/m·K, outrunning that of carbon nanotube². Despite an extensive amount of research work devoted to graphene, only a handful of studies related to its thermal applications have been reported^{3–5}. The poor thermal interaction between graphene layer and adjacent substrate⁶ is a hindrance to the development of thermal applications but the biggest deterrent has undoubtedly been the complex synthesis method in producing large area of graphene sheet^{4,5,7}. While graphene is one single layer of graphite, graphene oxide (GO), a functionalized graphene derivative which contains flakes of monolayer and few-layered graphene, can be prepared with a gentle sonication of graphite oxide in various solvents for facile and mass production^{8,9}. In light of the presence of oxygen functionalities, GO has excellent solubility and stable dispersion in water and other organic solvents while retaining some of the superior properties of graphene^{10,11}.

Recently, fast water vapor transport across laminated GO membrane while blocking even the smallest gas atom of helium has been discovered by Geim and co-workers¹². Anomalous high permeation of water through GO laminates having vacant spaces formed between non-oxidized regions of graphene sheets was observed. Two factors contribute to this unusual water permeation – the capillary driven force and the remarkable boundary slip of ultralow-friction passage. The oxidized regions act as spacers

¹Mechanical Engineering Discipline, School of Engineering, Monash University, 47500 Bandar Sunway, Malaysia.

²Multidisciplinary Platform of Advanced Engineering, Chemical Engineering Discipline, School of Engineering, Monash University, 47500 Bandar Sunway, Malaysia. Correspondence and requests for materials should be addressed to Y.M.H. (email: hung.yew.mun@monash.edu)

to form a network of nanocapillaries that vigorously interact with the intercalating water while the two-dimensional graphene nanocapillaries allow low-friction flow of monolayer water. Water flowing through the empty region between the pristine graphene sheets experiences an ultra-fast, low-friction flow similar to those reported in the water permeation of carbon nanotubes¹³. The fast water transport confined in the nanocapillary is ascribed to the frictionless interaction between the atomically smooth, hydrophobic carbon wall and the well-ordered hydrogen bonds of water molecules^{12,14,15}. For GO membranes immersed in liquid water, the mechanism of fast water permeation is not limited to non-oxidized regions¹⁶, based on the fact that no interconnecting network forms in these regions for water permeation¹⁷. Water intercalation through an immersed GO membrane engenders expansion of the interlayer distance between the graphitic planes^{16,18,19}. As the interlayer distance expanded over 9–10 Å, the first water monolayer was found to be attached firmly to the oxidized region while the second water monolayer manifests its rapid movement in a translational motion^{20,21}. The behavior of water intercalation of GO membranes was observed to be similar to that of GO powders^{16,21}. It was also suggested that fast water permeation could be attributed to the permeation across defective holes laid across the GO sheets¹⁶. By virtue of vigorous oxidation of precursor graphite and sonication treatment, GO sheets were introduced with high percentage of defective sites, allowing the permeation of water molecules across the graphitic plane. The mechanism of fast water permeation was also studied *via* theoretical modeling^{12,22,23}. It is yet conclusive to fully comprehend the underlying physical phenomenon of the anomalous fast water permeation of GO.

In view of the excellent properties measured in experiments, GO is a promising candidate for replacing metallic oxide nanoparticles in the preparation of nanofluid – a fluid containing nanoparticles suspensions^{24,25}. Characterizations of graphene based nanofluid show extraordinary thermal conductivity enhancement with a small dosage of graphene^{26,27}. The choice of working fluid has been a key area of interest in enhancing the performance of cooling devices. The exponential growth in heat generation of electronics devices in light of the trend of multi-functionalization and miniaturization necessitates development of highly efficient cooling devices. Two-phase closed thermosyphon (TPCT) has been used extensively for thermal management due to its excellent heat transport capability and reliability^{28,29}. A TPCT is essentially an evacuated tube charged with volatile working fluid, divided into three sections: evaporator, adiabatic section, and condenser. Working on the principle of phase-change heat transfer, the working fluid in the TPCT evaporates and absorbs latent heat from the heated evaporator section. The resultant vapor travels upwards through thermal buoyancy and condensation occurs at the sub-cooled condenser wall by releasing the latent heat to the surroundings. The condensate is then circulated back to the evaporator section *via* gravitational force and the cycle is perpetuated. The thermal efficiency of a TPCT is thus governed by the phase-change heat transfer processes namely evaporation and condensation, as well as circulation of condensate. As the suspension of nanoparticles in a base fluid is deemed to enhance the thermophysical properties, nanofluid was utilized as working fluid to improve the performance of TPCT^{30–32}. However, the increase in thermal conductivity of nanofluid is not the sole factor in contributing heat transfer enhancement for phase-change processes, other predominant factors are also prevalent. Prior studies showed that nanoparticles agglomerate and segregate from the base fluid, forming thin porous layers on the inner surface of the evaporator^{31,33,34}. In general, nanoparticles deposition on the heated surface is found to have significantly enhanced the surface wettability and nucleate boiling mechanism, thus increasing the evaporating heat transfer coefficient^{35–38}. The performance augmentation of nanofluid-filled TPCT is elementally attributed to the surface modification of nanoparticles deposition instead of the increase in thermal conductivity³¹.

In this work, we introduce GO/water nanofluid as a working fluid to enhance the performance of a mini TPCT. As TPCT is a phase-change heat transfer device, its performance is dominated by evaporation process which occurs from a heated surface where a liquid vaporizes into a gaseous phase. The latent heat of vaporization is absorbed through the evaporator wall surface and the evaporation strength varies depending on the condition of the surface^{39,40}. For the sake of maintaining high evaporation rate and achieving a high heat transfer rate, high surface temperature, large surface area, and low intermolecular strength of molecules are favorable conditions. Due to the distinguished physical properties of GO, the mechanism of evaporative heat transfer enhancement from GO deposition is hypothesized to be distinct from that of conventional metallic or non-metallic oxide nanoparticles. The fast water permeation property of GO inspires its application in enhancing the evaporation via surface functionalization. The GO deposition on the evaporator surface provides nanocapillaries (interconnecting networks at nanoscale) that draw the liquid water off the liquid pool to the sides of wall, giving rise to a larger surface area for evaporation and facilitating a higher evaporation rate. Notably, at nanoscale, capillary force is more intense and dominates over gravitational force, allowing liquid to flow in an antigravity direction. By comparing the performance of GO nanofluids to that of metallic oxide nanofluids, we scrutinize the mechanism of heat transfer enhancement in TPCTs. In addition, based on the structural studies of GO membrane in water of prior investigations^{12,16,19}, we are able to comprehend the heat transfer characteristics induced by different thicknesses of GO deposition. We illustrate the experimental setup in the following section, characterize the nanofluids by examining the effective thermal conductivity and viscosity, and demonstrate the effects of the anomalous characteristics of GO deposition in TPCTs.

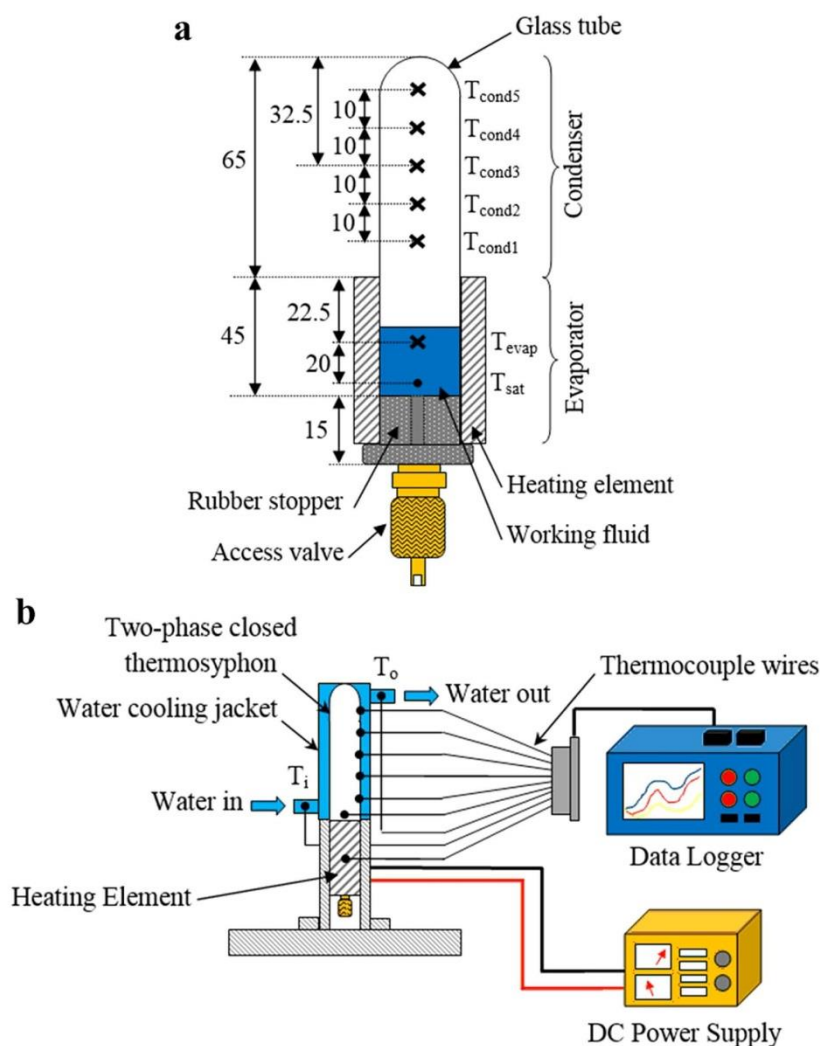


Figure 1. (a) Schematic diagram of a TPCT with temperature measurement points. (b) The experimental setup for the evaluation of performance of nanofluid charged TPCT.

Methods

Experimental Setup and Data Reduction. A schematic diagram of the experimental setup is illustrated in Fig. 1. Briefly, the apparatus includes a TPCT, electrical heater element, water cooling jacket, data logger and direct-current (DC) power supply. The TPCT was fabricated using standard laboratory glass tube with an inner diameter of 13.5 mm and a length of 110 mm. The glass tube was sealed using a rubber stopper, which was embedded with an access valve. To ensure the glass tube was airtight, high strength epoxy was applied at all connections³². A 1 ml of working fluid, equivalent to 16.7% of fill ratio, was charged into the TPCT through the access valve. Two different types of working fluids were prepared: silver oxide (SO) nanofluids (solutions with weight ratios of 0.01% and 0.5%), and GO nanofluids (solutions with weight ratios of 0.01%, 0.025%, 0.05%, 0.075% and 0.1%). SO nanofluids refer to aqueous solutions with suspension of SO nanoparticles of diameter 30 nm (Sigma Aldrich), whereas GO nanofluids refer to aqueous solutions with suspension of graphite oxide. The graphite oxide was synthesized using the high purity graphite powder of size 45 μm (Sigma Aldrich); the protocol for synthesizing the graphite oxide powder is described in the next section, followed by the preparation of graphite oxide nanofluids. Once the charging was completed, the absolute pressure in the glass tube was reduced to 0.2 Pa using a vacuum pump. The evaporator section of the TPCT was in direct contact with a uniform electrical heating element, whereas the condenser section was cooled *via* a water cooling jacket, as shown

in Fig. 1(b). The electric power input to the electrical heating element was controlled by adjusting the switch on the DC power supply. To minimize the heat loss from the electrical heating element to the surrounding, several layers of insulating materials were wrapped around the element. For performance analysis of the TPCT, the axial temperature distribution of the TPCT was measured using six type-T thermocouple wires, which were all connected to a data acquisition system. The liquid saturation temperature, T_{sat} , was also measured by inserting a type-T thermocouple wire into the bottom section of the evaporator. In each test, the temperatures were recorded for a duration of 60 minutes and at a sampling rate of 2 readings per second.

Using the measured temperatures, the overall thermal performance can be characterized using the effective thermal resistance, given by

$$R_{\text{eff}} = \frac{\Delta T}{\dot{Q}_a} \quad (1)$$

where \dot{Q}_a is the heat transport rate, $\Delta T = T_{\text{evap}} - T_{\text{cond}}$ is the axial temperature difference between the evaporator and the condenser, with T_{evap} the temperature at the evaporator and T_{cond} the temperature at the condenser. We note here that $T_{\text{cond}} = (T_{\text{cond}1} + T_{\text{cond}2} + T_{\text{cond}3} + T_{\text{cond}4} + T_{\text{cond}5})/5$, is the average temperature of the condenser and \dot{Q}_a is calculated based on the principle of energy conservation, i.e., the net heat transported across the TPCT is equivalent to the heat dissipated from the condenser section, $\dot{Q}_a = \dot{m}c_p(T_o - T_i)$, with the assumption of a well-insulated water cooling jacket. Two thermocouples are employed to measure the inlet and outlet water temperatures, T_i and T_o . Here, \dot{m} is the water mass flow rate and c_p is the specific heat capacity.

The average evaporator heat transfer coefficient, $\bar{h}_e = \dot{Q}_a / \pi d L_e (T_{\text{evap}} - T_{\text{sat}})$, is used to quantify the strength of evaporation, where T_{sat} is the saturation temperature of the working fluid in the evaporator, d and L_e are the inner diameter and length of the evaporator, respectively. During the experiments, under a constant heat input, the evaporator heat transfer coefficient augmentation ratio is given by

$$\eta = \frac{\bar{h}_e}{\bar{h}_{e,0}} = \frac{(T_{\text{evap},0} - T_{\text{sat},0})}{(T_{\text{evap}} - T_{\text{sat}})} \quad (2)$$

where $\bar{h}_{e,0}$ is the average heat transfer coefficient of deionized (DI) water charged TPCT. Here, η represents the relative comparison of the heat transfer coefficients by using the value of DI water charged TPCT as the basis for comparison. Enhancement in heat transfer at the evaporator can be noticed with η exceeding the value of one and vice versa.

Synthesis of Graphite Oxide. Graphite oxide powder was synthesized *via* the modified Hummers' method with the following procedures^{41,42}. 3 g of graphite powder (Sigma Aldrich, <45 μm , >99.99%) was added into an 80 °C mixture containing 12 ml of concentrate H_2SO_4 (Chemolab supplies, 95–97%), 2.5 g of P_2O_5 (Sigma Aldrich, $\geq 98\%$) and 2.5 g of $\text{K}_2\text{S}_2\text{O}_8$ (Sigma Aldrich, $\geq 99\%$). The mixture was then stirred for 4.5 hours and cooled to room temperature before diluted with 500 ml of DI water. The mixture was continuously washed with DI water until the pH of the filtrate became neutral. The product was dried at 70 °C overnight. The pre-oxidized graphite was re-dispersed into 120 ml of cold concentrated H_2SO_4 together with 15 g of KMnO_4 (Sigma Aldrich, $\geq 99\%$). The mixture was then stirred for 2 hours with the temperature kept below 20 °C. Next, the mixture was diluted with 250 ml of DI water in an ice bath to keep the temperature below 50 °C. After 2 hours of stirring, the solution was diluted again with 700 ml of DI water. 20 ml of H_2O_2 (R&M Chemicals, 30%) was further added into the final mixture which was then washed with 1 l of HCL (Merck, 37% diluted to 10%) followed by DI water for several times to completely remove the acid content. After filtration, the graphite oxide was air-dried at a temperature of 60 °C for 24 hours. The graphite oxide was then grounded into fine powder form. The X-ray diffraction (XRD) spectrum of GO powder indicates a peak at 9.1° corresponding to an interlayer distance of 9.72 Å, which is consistent with those of prior studies^{16,19}.

Preparation of GO and SO nanofluids. In order to obtain the final product of GO nanofluid, graphite oxide powder was dispersed in DI water and underwent ultrasonication treatment. Through sonication process, graphite oxide suspended in the aqueous solution exfoliates to yield a large distribution of nanometer-sized GO sheets. GO nanofluids were prepared with five concentrations measured by the weight of graphite oxide powder added to the dispersion (Supplementary Fig. S1). The weight percentages were maintained at 0.01 wt%, 0.025 wt%, 0.05 wt%, 0.075 wt% and 0.1 wt%. The mixtures were ultrasonicated (20 kHz, 700 W) with an ultrasonic liquid processor (Q700 Sonicator®, Qsonica, LLC.) for 5 hours with fluid temperature maintained below 80 °C to prevent evaporation. To quantify the superiority of the GO nanofluid, SO nanofluid was prepared in two concentrations of 0.01 wt% and 0.5 wt%. Similar ultrasonication treatment was used for the preparation of SO nanofluids to ensure the homogeneity.

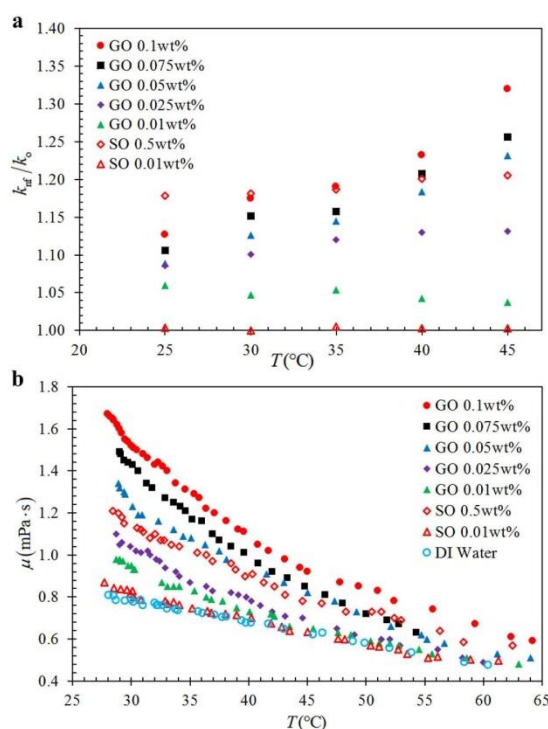


Figure 2. (a) Effective thermal conductivity enhancement ratio, and (b) viscosity, of GO and SO nanofluids as a function of temperature for different nanofluid concentration.

Characterization of GO and SO nanofluids. The heat transfer capability of a TPCT is governed by thermophysical properties such as the thermal conductivity and the viscosity of working fluid. The thermal conductivity of the nanofluid was measured using thermal property analyzer (KD2Pro, Decagon Devices, Inc., Canada) with an uncertainty of $\pm 5\%$. The device measured the thermal conductivity using transient hot wire method with a probe sensor of 60 mm in length and 1.3 mm in diameter. Thermal bath was used to prevent temperature fluctuation and all samples were measured at the temperatures ranging from 25 $^{\circ}C$ to 45 $^{\circ}C$. Prior to the taking of measurements, the KD2 Pro device was calibrated with glycerol. Ten measurements were taken for each sample at the targeted temperature to ensure the accuracy and reliability. The measured thermal conductivities of the GO and SO nanofluids were compared with thermal conductivities of the base fluid (DI water) measured under the same conditions.

Figure 2(a) shows the thermal conductivity enhancement ratios of GO and SO nanofluids as a function of nanofluid concentration and temperature. The thermal conductivity enhancement ratio is defined as k_{nf}/k_o where k_o is the thermal conductivity of the based fluid and k_{nf} is the thermal conductivity of the nanofluid. The SO nanofluid with 0.01 wt% has nearly no enhancement for the range of temperature from 25 $^{\circ}C$ to 45 $^{\circ}C$. However, the GO nanofluids achieve an overall enhancement in thermal conductivity. Different trends in the change of enhancement ratio at different temperatures are observed for SO and GO nanofluids. At a high GO content of 0.1 wt%, the enhancement ratio increases exponentially. However, the enhancement ratio of 0.5 wt% SO nanofluid remains almost constant at different temperatures. The constant enhancement ratio with the increase of temperature implies that the base fluid has more dominant effect on the increase in thermal conductivity rather than the thermal transport behavior associated with the suspended nanoparticles. The thermal transport mechanisms such as micro-convection due to Brownian motion, ballistic phonon transport and clustering effect of nanoparticles are among those commonly affecting the increase in thermal conductivity of nanofluids⁴³. Nevertheless, the factors affecting the thermal conductivity of GO nanofluids are distinguishable. For GO nanofluids, strong temperature dependence of thermal conductivity enhancement ratio is observed in the concentrations of 0.05 wt%, 0.075 wt% and 0.1 wt%. This can be attributed to the high thermal conductivity nature and the high surface area to volume ratio of GO sheets. As GO sheets have significantly larger contact area with the fluid molecules, the contact resistance at the graphene-fluid interface is substantially reduced. In light of high thermal conductivity nature of GO sheets, the thermal energy can be effectively transported across the solid-fluid interface, creating an excellent heat conduction path. Due

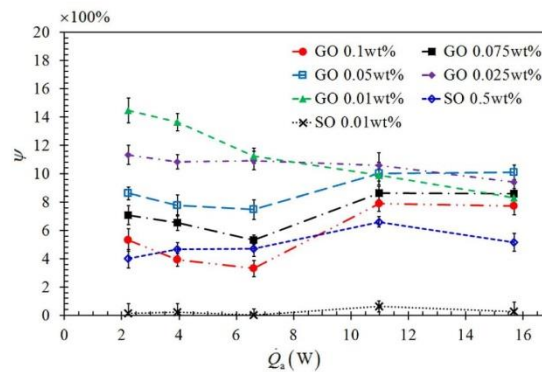


Figure 3. Variations of ΔT reduction ratio, $\psi = (\Delta T_{nf} - \Delta T_o) / \Delta T_o$ of GO and SO nanofluids charged TPCTs as a function of \dot{Q}_a , with the nanofluid concentration being a parameter.

to the high thermal conductivity and the 2D structure of GO sheets, a substantial thermal conductivity enhancement is attainable even at a low concentration of GO. On the other hand, the viscosity increases with concentration of nanoparticles. Figure 2(b) depicts the viscosities of the GO and SO nanofluids at different concentrations. The viscosity decreases with increasing temperature. At higher temperatures (above 60 °C), the viscosities of nanofluids rapidly decrease and approach the viscosity of base fluid (DI water). As the TPCT operates at temperatures higher than 60 °C, the effect of increase in viscosity on the thermal performance of TPCT can be deemed to be marginal.

Surface Morphology of Nanoparticles Deposition. During the two-phase heat transfer process, a thin layer of nanoparticles was observed depositing on the heated evaporator surface. A variation in color or color intensity of the deposition was clearly noted for different weight percentages and different nanofluids. Samples of the deposition were prepared by gently breaking the glass structure of TPCT to obtain the wall of evaporator section where the deposition took place. To assure the consistency of the results, the samples were obtained at a location 5 mm from the bottom of the evaporator. Observation of surface morphology of deposited layers was carried out using a SU-8010 field emission scanning electron microscope (FESEM, Hitachi Ltd., Japan). Static contact angle θ_s between DI water and the deposition was measured using a standard goniometer (Model 590, Ramé-Hart Instrument Co.) under atmospheric pressure and a room temperature of 26 °C.

Results and Discussion

Performance comparison of GO and SO nanofluids. The temperature difference, $\Delta T = T_{\text{evap}} - T_{\text{cond}}$, manifests itself as a convenient indicator in quantifying the heat transport rate along the axial direction. In accordance with the Fourier's law of heat conduction, under the same heat transfer rate, smaller ΔT indicates higher heat transport capability of the specimen. A low ΔT infers a low thermal resistance across the evaporator and condenser sections. We observe that ΔT of a GO-nanofluid charged TPCT is lower than that of a DI water charged TPCT. Figure 3 shows the variations of ΔT reduction ratio, $\psi = (\Delta T_{nf} - \Delta T_o) / \Delta T_o$ of GO and SO nanofluids charged TPCTs as a function of \dot{Q}_a , with the nanofluid concentration being a parameter. Here, ΔT_o is the temperature difference of the base fluid (DI water) charged TPCT, ΔT_{nf} is the temperature difference of the nanofluid charged TPCT, and ψ is regarded as a comparison of the change in ΔT of nanofluid charged TPCT with ΔT of a base fluid charged TPCT, indicating an enhancement in the performance of a nanofluid charged TPCT. The GO nanofluids charged TPCTs have higher ΔT reduction ratios than that of SO nanofluids charged TPCTs. At a very high concentration of SO (0.5 wt%), the performance of TPCT is comparable with that of 0.1 wt% GO nanofluid charged TPCT. This shows that the GO nanofluid TPCTs outperform the SO nanofluid ones. For GO nanofluid TPCTs charged with higher concentrations (0.05 wt%, 0.075 wt% and 0.1 wt%), we observe that ψ decreases with increasing \dot{Q}_a at low \dot{Q}_a and starts to increase when \dot{Q}_a exceeds 6.5 W. This indicates that the GO nanofluid TPCTs perform better at a higher heat input, which will be discussed later.

To evaluate the overall performance of TPCT, the effective thermal resistance, R_{eff} , which is a function of ΔT is analyzed. Figure 4a,b depict the variations of R_{eff} with \dot{Q}_a , for different concentrations of GO and SO nanofluids charged TPCTs, respectively. The effective thermal resistance of the DI water ($\phi = 0$) charged TPCT is used as a benchmark to illustrate the enhancement in thermal performance of nanofluid charged TPCTs. A lower R_{eff} indicates higher performance. The decrease in R_{eff} is essentially attributed to the enhancement of either evaporation strength at the evaporator or circulation effectiveness of condensed liquid back to the evaporator or of both. Basically the effective thermal resistance decreases

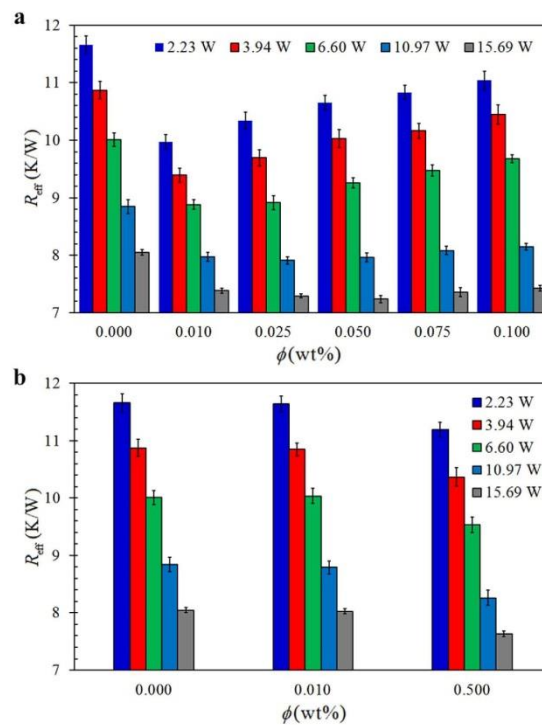


Figure 4. Effective thermal resistance, R_{eff} , as a function of nanoparticles weight ratio, ϕ , of (a) GO nanofluids, and (b) SO nanofluids, charged TPCTs at different \dot{Q}_a .

with increasing \dot{Q}_a . We observe that R_{eff} of GO nanofluid TPCTs is overall lower than that of DI water charged TPCT while R_{eff} of SO nanofluid TPCTs is only marginally lower than that of DI water charged TPCT even at high concentration of SO. Hence, comparatively the GO nanofluid TPCTs outperform the SO nanofluid TPCTs. Remarkably, for the case of GO nanofluids, R_{eff} increases with GO concentration ϕ at low \dot{Q}_a (2.23 W, 3.94 W and 6.6 W) and becomes independent of ϕ at high \dot{Q}_a (10.97 W and 15.69 W). Referring to Fig. 2(a) which shows that the effective thermal conductivity of nanofluid increases with GO concentration, we expect that R_{eff} of TPCT should decrease with increasing GO concentration. However, the finding in Fig. 4(a) is contrary to what was anticipated based on the characterization of effective thermal conductivity of GO nanofluid as discussed in Fig. 2(a). In this regard, the reduction of R_{eff} is not entirely attributed to the increase in effective thermal conductivity of GO nanofluid. Other factors might have contributed to this unusual result. As mentioned, nanoparticles agglomerate in the base fluid and thin porous layers are formed on the inner surface of the evaporator. The nanoparticles deposition manifests significant enhancement in the surface wettability and nucleate boiling mechanism^{31,33,34}. To this end, in what follows, we investigate the underlying physical significance of GO deposition and its anomalous characteristics in affecting the thermal performance of TCPT.

Fast Water Permeation Property of GO Deposition. To exclusively elucidate the role of thermal conductivity of nanoparticles deposition on the evaporator wall surface, we first examine the effective thermal conductance of uncharged TPCTs that had been coated with GO and SO during the experiments. The working fluids were evacuated from the TPCTs to exclude the two-phase heat transfer process. Simple heat conduction experiments were conducted. The primary objective is to examine the heat conduction contribution of the nanoparticle deposited layer. Except for the specimens, the experimental setup is identical to that in Fig. 1(b). The thermal conductance which can be considered as the effective thermal conductivity of specimen is calculated as $k^* = (\dot{Q}_a L) / (A_c \Delta T)$, where L is the distance between the two measured temperatures, A_c is the cross section area of the evacuated glass tube and $\Delta T = T_{evap} - T_{cond}$ is the temperature difference. Figure 5(a) depicts the results of the heat conduction experiments. Although the thermal conductance of GO deposition is slightly higher than that of SO deposition, they are only marginally higher (with a maximum of 6%) than that of the uncoated surface. This is not surprising as GO intrinsically has significantly lower thermal conductivity as compared to the

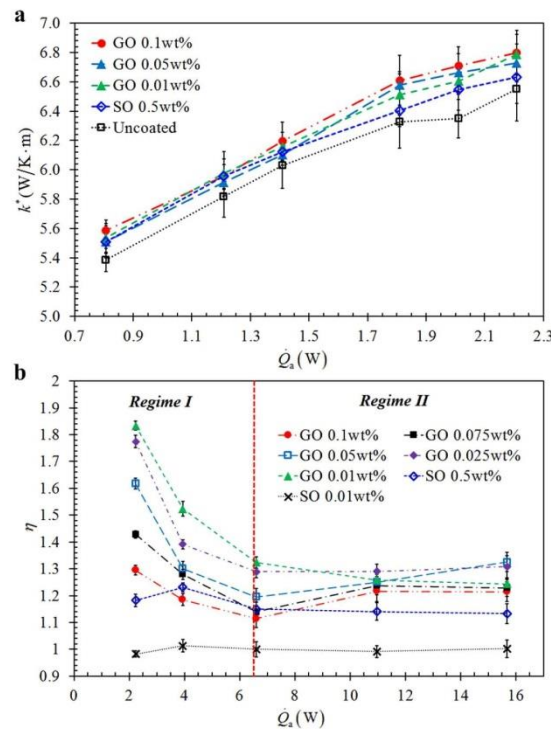


Figure 5. (a) Thermal conductance of uncharged TPCTs coated with thin GO and SO nanoparticles depositions as a function of \dot{Q}_a during the heat conduction experiments. (b) The evaporator heat transfer coefficient augmentation ratio, η , as a function of \dot{Q}_a with nanoparticles weight ratio as a parameter. Two distinct regimes – $\dot{Q}_a < 6.5$ W and $\dot{Q}_a > 6.5$ W can be clearly identified.

pristine graphene with high in-plane thermal conductivity nature^{7,43}. Due to the introduction of oxygenated functional groups and defects in GO during vigorous oxidation process, in-plane heat transfer through lattice vibrations is impeded^{7,44}. High in-plane thermal conductivity of graphene is attributed to the covalent sp^2 bonding between the carbon atoms and the heat flow is anisotropic⁷. On the other hand, the layered structure of GO is governed by the cross-plane van der Waals force and the repulsive electrostatic force which is induced by the negatively charged functional groups^{6,45}. As a result, the cross-plane heat transfer is ineffective as compared to the in-plane heat transfer. In fact, based on non-equilibrium molecular dynamics simulations, the thermal conductivity of GO with an oxygen coverage of 20% was estimated to be 8.8 W/m.K which is three orders of magnitude lower than the thermal conductivity of pristine graphene⁴³. In addition, at the interface between the glass substrate and the adjacent GO sheets, poor van der Waals coupling limits the heat transfer⁶ and a high thermal resistance (hence a low thermal conduction) is induced between the GO sheets and the glass substrate. This shows the insignificant contribution of thermal conductivity of the GO deposition, which is essentially associated with heat conduction, to the thermal performance enhancement of TPCT. Hence we postulate that the performance enhancement and the effects of GO deposition are entailed by the two-phase heat transfer process.

As mentioned earlier, the two-phase heat transfer in a TPCT is governed by the evaporation process and the circulation of condensate. As the nanoparticles deposition takes place at the evaporator section, the evaporation process is convinced to be uniquely contributing to the performance enhancement. It has been pointed out that the thermal performance enhancement of a nanofluid-charged TPCT is essentially attributed to the formation of nanoparticles deposition on the heated surface which modifies the surface wettability and enhances the nucleate boiling mechanism^{35–38}. We analyze the strength of evaporation by evaluating the evaporator heat transfer coefficient augmentation ratio, η , as defined in Eq (2). Figure 5(b) plots η as a function of \dot{Q}_a for different GO and SO concentrations. It can be observed that the average evaporator heat transfer coefficient, \bar{h}_e , enhances in TPCTs with GO deposition, with a minimum of 11.4% and a maximum of 83.3% of enhancement as compared to the uncoated TPCT (charged with DI water). For SO deposition, no \bar{h}_e enhancement is observed for low SO concentration (0.01wt%) and even at a high SO concentration (0.5 wt%), the enhancement is relatively small compared to that of

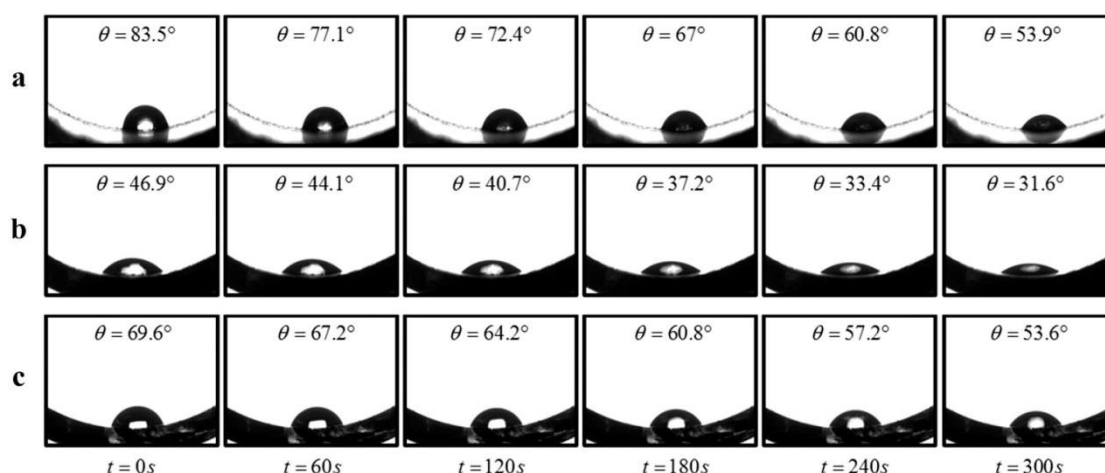


Figure 6. Time-lapse images of a 2 μ l water droplet residing on (a) 0.1 wt% GO deposited layer, (b) 0.5 wt% SO deposited layer, and (c) uncoated glass surface, over a time span of 5 minutes. For each 60-s interval, the corresponding contact angle is recorded and depicted.

GO deposition. This discrepancy between TPCTs with GO and SO deposited layers is likely due to the distinct surface morphologies and characteristics of the depositions.

To this end, we investigate the surface wettability of deposited layer with a DI water droplet (2 μ l) through measurement of its static contact angle on the substrate to observe how water spreads out. A low contact angle manifests high surface wettability which induces a higher evaporation rate as the liquid-solid contact area increases. Figure 6 displays the variations of contact angle on GO, SO deposited layers and uncoated glass surface over a time frame of 300 seconds. Although the GO deposition is the most hydrophobic (with the highest contact angle among the three cases), its decrease in contact angle over the time of 300 seconds is the highest with a rate of 0.099°/s. On the other hand, SO deposition which is the most hydrophilic (with the smallest contact angle) indicated a decrease in contact angle with a rate of 0.051°/s. For the uncoated glass surface, the contact angle decreases with a rate of 0.053°/s. The contact angle reduction rate of GO deposition is more than 1.9 times higher than that of SO deposition. As compared to the uncoated surface, the evaporation enhancement of SO deposited TPCTs is due to the enhanced hydrophilicity of SO deposition. Of particular interest is the case of GO deposition. The anomalous enhancement in evaporation strength with GO deposited layer which is more hydrophobic than uncoated glass surface is contrary to the intuitive understanding. The factor of surface wettability is insufficient to explain this unusual phenomenon. In this case the unique fast water permeation property of GO comes into play. During the contact angle measurement of water droplet on GO deposition, for a longer time span, we observed that the contact angle continuously and gradually contracts over time and eventually the water droplet was completely absorbed into the GO deposited layer which is comparable to a sponge-like material. To ascertain the cause of the evaporation enhancement of GO deposition, in an individual experiment conducted under standard atmosphere, we compared the evaporation rates of water droplets on GO coated surface and uncoated surface with a surface temperature of 130°C (see Supplementary Movie M1). The evaporation rate of the former is 4 times of that of the latter, justifying the role of the fast water permeation in GO deposition in enhancing the evaporation strength of a heated surface.

Here we illustrate the nanoparticle depositions schematically. Referring to Fig. 7(a,i), The SO deposition is observed depositing in the submerged region and the effective evaporation region is only limited to the liquid-vapor interface. On the other hand, GO deposition spreads out across the evaporator wall above the liquid-vapor interface. The negatively charged hydroxyl groups at the edges of immersed GO sheets generate strong repulsive force between each individual GO sheet⁴⁵. Concurrent with the upward liquid and vapor flows, the deposited GO sheets are spread across the wall surface covering substantially larger surface area. By virtue of water intercalation in the GO deposition, the effective evaporation region is extended to the wall surface where the GO sheets deposited, above the liquid-vapor interface (highlighted with red color) as depicted in Fig. 7(a,ii). As water intercalates between the GO interlayers, a thin film of water forms at the GO deposited layer. Evaporation occurs in a thin film is more effective than that in a pool of water due to larger surface area of the former. Even though it is in an antigravity direction, the water thin film formed at the GO deposition is continuously replenished from the pool of water through the operation of water permeation in the GO structure. In what follows, we denote the evaporation taking place at the GO deposited layer as filmwise evaporation.

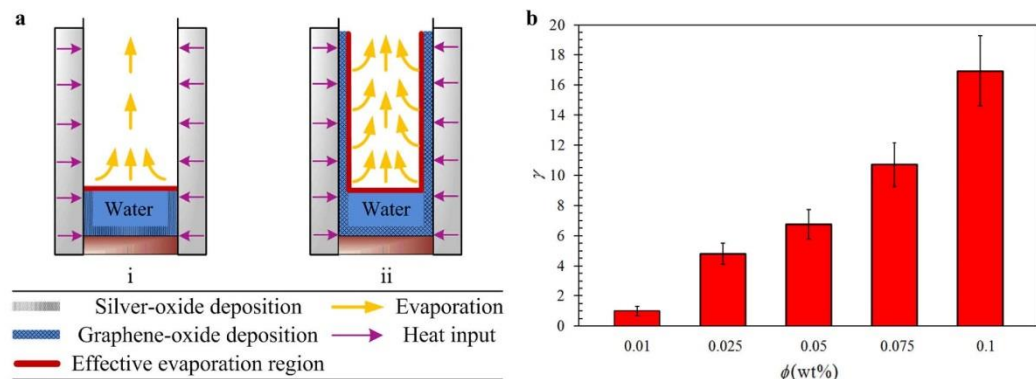


Figure 7. (a) Schematic illustration of evaporation process occurring at the effective region of a TPCT with (i) SO deposition, and (ii) GO deposition. In light of the fast water permeation effect, the effective evaporation region for TPCT with GO deposition is significantly extended across the evaporator wall surface (highlighted with red color) where filmwise evaporation is induced. (b) Relative deposition thicknesses of various GO nanofluid concentrations. The average thickness of 0.01 wt% GO deposition is used as a baseline for comparison.

To gain better insight into the mechanism of water permeation of GO deposition on the evaporator wall, we examine the surface morphologies of the deposited layers. FESEM was used to capture images of the deposited layers. Figures 8a,b,c,d illustrate the FESEM images of 0.5 wt% SO, 0.01 wt% GO, 0.05 wt% GO, and 0.1 wt% GO deposited layers, respectively. It is observed in Fig. 8(a) that spherically structured SO nanoparticles agglomerated and deposited disorderly on the surface. Although such deposition enhances the surface wettability, the enhancement of evaporation strength is not profound as discussed earlier. On the other hand, the GO depositions consist of well distributed, closely-packed layered structure of GO sheets which are responsible for the property of fast water permeation. For higher concentration of GO deposition (Fig. 8d), relatively thicker strands that can be easily distinguished from those of lower concentration (Fig. 8b) are observed. It is implied that the thickness of the GO layers depends on the nanofluid concentration.

To compare the GO deposition thicknesses of various nanofluid concentrations, we estimate the relative deposition thickness as $\gamma = t_1/t_0$, where t_1 is the average thickness of GO deposition and t_0 is the average thickness of 0.01 wt% GO deposition (lowest concentration) which is used as a baseline for comparison. The average thickness was approximated from the FESEM cross-section image of GO deposition which was then analyzed using the SigmaScan® Pro (Systat Software, CA, USA) image processing software. For each concentration, a total of 15 cross-section images from 5 independent sets of experiment were captured. The average thickness of the baseline was estimated as $0.2\ \mu\text{m}$, corresponding to approximately 300 layers of GO sheets. Figure 7(b) depicts the relative deposition thickness of various GO nanofluid concentrations. The GO deposition thickness increases with nanofluid concentration and the thickness of 0.1 wt% GO deposition is 17 times of that of 0.01 wt% GO deposited layer.

It has been reported that water intercalation through GO membrane results in the expansion of the interlayer distance between the graphitic planes^{16,18,19}. The X-ray diffraction (XRD) analysis of the hydrated GO membrane showed an increase in the interlayer distance from $7.7\ \text{\AA}$ to $12.29\ \text{\AA}$ ¹⁶, capable of intercalating bilayer of water for fast water permeation^{20,21}. Thus, the water permeability of GO membrane is appreciably enhanced when the interlayer spacing increases^{16,21}. The variation of the interlayer spacing is temperature dependent^{19,21}. Referring to Fig. 5(b), the \bar{h}_e enhancement decreases with the increase in heat input and simultaneously the operating temperature that spans from 87°C to 136°C for the GO charged TPCT. The operating temperature is below the critical temperature of 200°C where the interlayer spacing completely collapses for the minimum clearance of water monolayer ($\approx 5\ \text{\AA}$) due to excessive thermal annealing¹⁹. The decrease in the \bar{h}_e enhancement can be explained by the temperature variation which causes the structural transformation of GO deposition¹⁹, a phenomenon termed as thermohydration. As the temperature increases, structural alteration of the GO deposition takes place where the interlayer distance progressively decreases. The reduction in the interlayer distance greatly affects the water vapor permeability as less water monolayer is able to permeate through the narrowing gap. Thus, η reduction can be observed as the heat input increases.

In Fig. 5(b), it is obvious that two different regimes for the variation of η - Regime I ($\dot{Q}_a < 6.5\text{W}$) and Regime II ($\dot{Q}_a > 6.5\text{W}$) determine the evaporation enhancement for GO deposition. For a small \dot{Q}_a in Regime I, the \bar{h}_e enhancement of TPCT with GO deposition decreases with both increasing \dot{Q}_a and

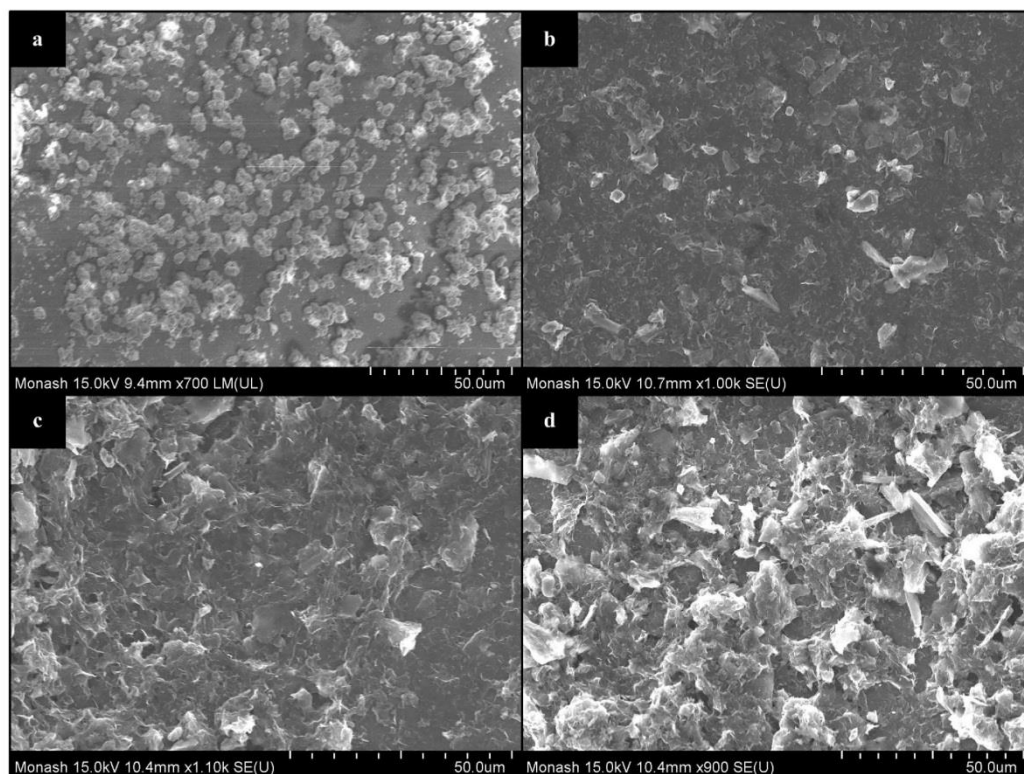


Figure 8. FESEM images of SO nanoparticles and GO sheets deposited on the glass surface of the evaporator section of TPCT: (a) 0.5 wt% SO nanoparticles, (b) 0.01 wt% GO sheets, (c) 0.05 wt% GO sheets and (d) 0.1 wt% GO sheets. The well distributed, closely-packed layered structure of GO sheets can be easily distinguished from the disorderly distributed spherical SO nanoparticles deposition. Higher concentration of GO sheets deposition is manifested in thicker strands.

GO concentration. This is intelligible that at low heat input, the evaporation rate at the liquid-vapor interface of the pool of water is relatively low while the filmwise evaporation from the extended GO thin film is vitally significant. Particularly for thinner deposited layer (lower GO concentration), the evaporation becomes more intense due to larger surface area. When the heat input increases, the contribution of evaporation at the GO deposited layer diminishes as its counterpart of the liquid-vapor interface intensifies. For thick deposited layer (high GO concentration), the effect of water permeation deteriorates, as elucidated in the following. In the oxidation process, GO sheets are attached by reactive oxygenated functional groups namely hydroxyl and carboxyl⁴¹ which enhance the hydrophilicity and act as a separation between two stacked GO sheets, allowing water molecules to travel between the interlayer of the two stacked GO sheets¹². In regions with non-oxidized graphene sheets, fast water permeation prevails as water molecules slip through the atomically smooth carbon walls. When water molecules approach the oxidized regions with oxygenated functional groups, they are pinned down due to the strong hydrophilic nature of the functional groups, impeding the in-plane water permeation effect^{12,14,46}. Stronger pinning effect prevails in thicker GO deposited layer. This explains the decreasing trend of η with increasing \dot{Q}_a and the diminishing effect of GO deposited layer thickness on \bar{h}_e enhancement.

In Regime II for higher \dot{Q}_a , except for that of the thinnest GO deposited layer (0.01 wt%), η increases with \dot{Q}_a and approaches an asymptotic value at high heat input, as depicted in Fig. 5(b). At high heat input ($\dot{Q}_a = 15\text{ W}$), the 0.05 wt% and 0.025 wt% GO depositions (of middle thicknesses) manifest the highest η . This phenomenon is a compromise between the deteriorative effects on the evaporation strength associated with the thickness of GO deposition. When the deposited layer is too thin, the filmwise evaporation is too intense for water to be replenished through permeation in GO sheets to sustain the evaporation that dryout might take place and hinder the filmwise evaporation. As the evaporation at the liquid-vapor interface is relatively intense at high heat input, the significance of filmwise evaporation is not profound and therefore the evaporation enhancement due to the deposited layer is decreased. On

the other hand, when the deposited layer is too thick, the fast water permeation deteriorates due to the water pinning effect of the hydrophilic functional groups, as discussed earlier. In this case, the effect of the thickness of GO deposition on the enhancement of evaporation is marginal at high heat input. Thus, the fast water permeation characteristics of the GO deposition which is intimately related to the structural alteration under temperature variation and deposition thickness are key factors in affecting the evaporation strength and hence the thermal performance of a GO/water nanofluid charged TPCT.

Conclusions

In summary, we demonstrated the fast water permeation effect of immersed GO deposition on the evaporation strength of a GO/water nanofluid charged TPCT. The operation of fast water permeation in the nanocapillaries was attributed to the frictionless interaction between the atomically smooth, hydrophobic carbon wall and the well-ordered hydrogen bonds of the water molecules that gives rise to capillary force which is strong enough to overcome the gravitational force to form a thin water film on the GO deposited layers. The water intercalation induces the expansion of the interlayer distance between the graphitic planes which are temperature dependent. As a result, filmwise evaporation which is more effective than its interfacial counterpart is induced and the overall performance of TPCT is greatly enhanced. This study provides important insights into the mechanism of water permeation of immersed GO that exhibits an enormous potential in thermal management applications with special relevance to the development of two-phase cooling devices.

References

1. Novoselov, K. S. *et al.* Electric field effect in atomically thin carbon films. *Science* **306**, 666–669 (2004).
2. Balandin, A. A. *et al.* Superior thermal conductivity of single-layer graphene. *Nano Lett.* **8**, 902–907 (2008).
3. Huang, X. *et al.* Graphene-based materials: Synthesis, characterization, properties, and applications. *Small* **7**, 1876–1902 (2011).
4. Zhu, Y. *et al.* Graphene and graphene oxide: Synthesis, properties, and applications. *Adv. Mater.* **22**, 3906–3924 (2010).
5. Zhu, Y., James, D. K. & Tour, J. M. New routes to graphene, graphene oxide and their related applications. *Adv. Mater.* **24**, 4924–4955 (2012).
6. Pop, E., Varshney, V. & Roy, A. K. Thermal properties of graphene: Fundamentals and applications. *MRS Bull.* **37**, 1273–1281 (2012).
7. Balandin, A. A. Thermal properties of graphene and nanostructured carbon materials. *Nat. Mater.* **10**, 569–581 (2011).
8. Choucair, M., Thordarson, P. & Stride, J. A. Gram-scale production of graphene based on solvothermal synthesis and sonication. *Nat. Nano* **4**, 30–33 (2009).
9. Hernandez, Y. *et al.* High-yield production of graphene by liquid-phase exfoliation of graphite. *Nat. Nano* **3**, 563–568 (2008).
10. Wei, N., Lv, C. & Xu, Z. Wetting of graphene oxide: A molecular dynamics study. *Langmuir* **30**, 3572–3578 (2014).
11. Paredes, J. I., Villar-Rodil, S., Martínez-Alonso, A. & Tascón, J. M. D. Graphene oxide dispersions in organic solvents. *Langmuir* **24**, 10560–10564 (2008).
12. Nair, R. R., Wu, H. A., Jayaram, P. N., Grigorieva, I. V. & Geim, A. K. Unimpeded permeation of water through helium-leak-tight graphene-based membranes. *Science* **335**, 442–444 (2012).
13. Cicero, G., Grossman, J. C., Schwegler, E., Gygi, F. & Galli, G. Water confined in nanotubes and between graphene sheets: A first principle study. *J. Am. Chem. Soc.* **130**, 1871–1878 (2008).
14. Huang, H. *et al.* Ultrafast viscous water flow through nanostrand-channelled graphene oxide membranes. *Nat. Commun.* **4**, 2979 (2013).
15. Han, Y., Xu, Z. & Gao, C. Ultrathin graphene nanofiltration membrane for water purification. *Adv. Funct. Mater.* **23**, 3693–3700 (2013).
16. Talyzin, A. V., Hausmaninger, T., You, S. & Szabo, T. The structure of graphene oxide membranes in liquid water, ethanol and water-ethanol mixtures. *Nanoscale* **6**, 272–281 (2014).
17. Erickson, K. *et al.* Determination of the local chemical structure of graphene oxide and reduced graphene oxide. *Adv. Mater.* **22**, 4467–4472 (2010).
18. Talyzin, A. V., Luzan, S. M., Szabó, T., Chernyshev, D. & Dmitriev, V. Temperature dependent structural breathing of hydrated graphite oxide in H₂O. *Carbon* **49**, 1894–1899 (2011).
19. Andrikopoulos, K. S. *et al.* The effect of thermal reduction on the water vapor permeation in graphene oxide membranes. *Adv. Mater. Inter.* **1**, 1400250 (2014).
20. Lerf, A. *et al.* Hydration behavior and dynamics of water molecules in graphite oxide. *J. Phys. Chem. Solids* **67**, 1106–1110 (2006).
21. Zhu, J. *et al.* Pseudonegative thermal expansion and the state of water in graphene oxide layered assemblies. *ACS Nano* **6**, 8357–8365 (2012).
22. Wei, N., Peng, X. & Xu, Z. Breakdown of fast water transport in graphene oxides. *Phys. Rev. E* **89**, 012113 (2014).
23. Boukhalov, D. W., Katsnelson, M. I. & Son, Y.-W. Origin of anomalous water permeation through graphene oxide membrane. *Nano Lett.* **13**, 3930–3935 (2013).
24. Eastman, J. A., Choi, S. U. S., Li, S., Yu, W. & Thompson, L. J. Anomalous increased effective thermal conductivities of ethylene glycol-based nanofluids containing copper nanoparticles. *Appl. Phys. Lett.* **78**, 718–720 (2001).
25. Prasher, R., Bhattacharya, P. & Phelan, P. E. Thermal conductivity of nanoscale colloidal solutions (nanofluids). *Phys. Rev. Lett.* **94**, 025901 (2005).
26. Baby, T. T. & Ramaprabhu, S. Experimental investigation of the thermal transport properties of a carbon nanohybrid dispersed nanofluid. *Nanoscale* **3**, 2208–2214 (2011).
27. Wang, F. *et al.* Surfactant-free ionic liquid-based nanofluids with remarkable thermal conductivity enhancement at very low loading of graphene. *Nanoscale Res. Lett.* **7**, 314 (2012).
28. Faghri, A. Heat pipe science and technology. Washington DC, USA: Taylor & Francis, (1995).
29. Peterson, G. P. An introduction to heat pipes modeling, testing and applications. New York, USA: John Wiley & Sons Inc., (1994).
30. Buschmann, M. H. Nanofluids in thermosyphons and heat pipes: Overview of recent experiments and modelling approaches. *Int. J. Therm. Sci.* **72**, 1–17 (2013).
31. Grab, T., Gross, U., Franzke, U. & Buschmann, M. H. Operation performance of thermosyphons employing titania and gold nanofluids. *Int. J. Therm. Sci.* **86**, 352–364 (2014).

32. Tong, W. L., Tan, M. K., Chin, J. K., Ong, K. S. & Hung, Y. M. Coupled effects of hydrophobic layer and vibration on thermal efficiency of two-phase closed thermosyphons. *RSC Adv.* **5**, 10332–10340 (2015).
33. Liu, Z.-H. & Li, Y.-Y. A new frontier of nanofluid research – application of nanofluids in heat pipes. *Int. J. Heat Mass Transf.* **55**, 6786–6797 (2012).
34. Zhang, W., Shen, R., Lu, K., Ji, A. & Cao, Z. Nanoparticle enhanced evaporation of liquids: A case study of silicone oil and water. *AIP Adv.* **2**, 042119 (2012).
35. You, S. M., Kim, J. H. & Kim, K. H. Effect of nanoparticles on critical heat flux of water in pool boiling heat transfer. *Appl. Phys. Lett.* **83**, 3374–3376 (2003).
36. Kim, S. J., Bang, I. C., Buongiorno, J. & Hu, L. W. Effects of nanoparticle deposition on surface wettability influencing boiling heat transfer in nanofluids. *Appl. Phys. Lett.* **89**, 153107 (2006).
37. Xie, H., Yu, W., Li, Y. & Chen, L. Discussion on the thermal conductivity enhancement of nanofluids. *Nanoscale Res. Lett.* **6**, 124 (2011).
38. Kim, H. Enhancement of critical heat flux in nucleate boiling of nanofluids: A state-of-art review. *Nanoscale Res. Lett.* **6**, 415 (2011).
39. Carey, V. P. Liquid-vapor phase-change phenomena: An introduction to the thermophysics of vaporization and condensation processes in heat transfer equipment. New York: Hemisphere Publishing Corporation, (1992).
40. Patankar, N. A. Supernucleating surfaces for nucleate boiling and dropwise condensation heat transfer. *Soft Matter* **6**, 1613–1620 (2010).
41. Ong, W.-J., Tan, L.-L., Chai, S.-P. & Yong, S.-T. Graphene oxide as a structure-directing agent for the two-dimensional interface engineering of sandwich-like graphene-g-C₃N₄ hybrid nanostructures with enhanced visible-light photoreduction of CO₂ to methane. *Chem. Commun.* **51**, 858–861 (2015).
42. Ong, W.-J. *et al.* Synergistic effect of graphene as a co-catalyst for enhanced daylight-induced photocatalytic activity of Zn_{0.5}Cd_{0.5}S synthesized via an improved one-pot co-precipitation-hydrothermal strategy. *RSC Adv.* **4**, 59676–59685 (2014).
43. Mu, X., Wu, X., Zhang, T., Go, D. B. & Luo, T. Thermal transport in graphene oxide – from ballistic extreme to amorphous limit. *Sci. Rep.* **4**, 3909 (2014).
44. Dreyer, D. R., Park, S., Bielawski, C. W. & Ruoff, R. S. The chemistry of graphene oxide. *Chem. Soc. Rev.* **39**, 228–240 (2010).
45. Cote, L. J., Kim, F. & Huang, J. Langmuir–blodgett assembly of graphite oxide single layers. *J. Am. Chem. Soc.* **131**, 1043–1049 (2009).
46. Wei, N., Peng, X. & Xu, Z. Understanding water permeation in graphene oxide membranes. *ACS Appl. Mater. Inter.* **6**, 5877–5883 (2014).

Acknowledgements

This work was supported by the eScienceFund (04-02-10-SF0113), Ministry of Science, Technology and Innovation (MOSTI), Malaysia.

Author Contributions

W.L.T., M.K.T., and Y.M.H. designed the experiments. W.L.T. performed the experiments. W.-J.O. and S.-P.C. synthesized the GO and advised on the characterization. Y.M.H. oversaw the research project. All authors discussed the results and contributed to the paper.

Additional Information

Supplementary information accompanies this paper at <http://www.nature.com/srep>

Competing financial interests: The authors declare no competing financial interests.

How to cite this article: Tong, W.L. *et al.* Enhanced Evaporation Strength through Fast Water Permeation in Graphene-Oxide Deposition. *Sci. Rep.* **5**, 11896; doi: 10.1038/srep11896 (2015).



This work is licensed under a Creative Commons Attribution 4.0 International License. The images or other third party material in this article are included in the article's Creative Commons license, unless indicated otherwise in the credit line; if the material is not included under the Creative Commons license, users will need to obtain permission from the license holder to reproduce the material. To view a copy of this license, visit <http://creativecommons.org/licenses/by/4.0/>